University of Nottingham
UK | CHINA | MALAYSIA

Apoferritin delivery of imidazotetrazine agents for targeted brain tumour therapy

Kaouthar Bouzinab
B.Sc. (Hons), M.Sc.

Thesis submitted to the University of Nottingham, United Kingdom for the degree of Doctor of Philosophy
December 2020

Abstract

Glioblastoma multiforme (GBM) is an aggressive grade IV astrocytoma. The standard of care for GBM includes surgery, radiotherapy and temozolomide (TMZ; DNA alkylating) chemotherapy. Poor TMZ accumulation at the tumour site, resistance and toxicity, limit the success of this treatment. Some modes of TMZ resistance includes drug efflux by P-glycoprotein 1 (Pgp), overexpression of *O6*-methylguanine DNA-methyltransferase (MGMT; removes cytotoxic *O6*-methylated guanine (*O6*-MeG) lesions), deficiency in base excision repair (BER; e.g. poly (ADP-ribose) polymerase (PARP); removes *N7*-methylguanine (*N7*-MeG) and *N3*-methyladenine (*N3*-MeA) lesions)) and/or deficiency in mismatch repair (MMR; leads to tolerance of *O6*-MeG lesions).

Herein, we employed a nano drug delivery system (DDS), to combat the limitations associated with TMZ. Apoferritin (AFt) has been investigated as a DDS for the delivery of various anti-cancer agents, due to its biocompatibility and its capacity to bind to transferrin receptor 1 (TfR1). TfR1 binding enables AFt (along with the drug load) to cross the blood brain barrier (BBB) and accumulate in iron hungry cancer cells that overexpress this receptor; minimising unwanted toxicity. Also, to thwart TMZ resistance, we utilised TMZ analogues such as N3-propargyl (N3P) and C8-thiazole (T25) analogues, which impart excellent anti-cancer activity irrespective of the MGMT and/or MMR status of cancer cells, and explored combinations of TMZ with inhibitors of MGMT (e.g., *O6*-Benzylguanine; *O6*-BeG) or PARP-1 (e.g., niraparib; NRP), to enhance the number of methylated lesions and cancer cell death.

Our encapsulation process *via* the ‘nanoreactor’ method garnered > 510 TMZ, N3P, T25 or *O6*-BeG molecules and > 80 molecules of NRP per AFt cage, with

encapsulation efficiencies > 60%. In addition, the protein remained intact after test agent encapsulation, with comparable size, charge, and molecular weight to AFt alone (prior to encapsulation). Moreover, *in vitro* test agent release studies for AFt-TMZ, AFt-N3P and AFt-T25, at pH 7.4, demonstrated slower test agent release in the first 3 h compared to at pH 5.5.

In vitro cytotoxicity assays revealed intriguing results with AFt-TMZ, which demonstrated significantly lower GI_{50} values in TMZ resistant U373M (MGMT +ve; 50% growth inhibition (GI_{50}) = 0.768 μM) compared to naked TMZ treatment (GI_{50} = 376 μM). Supporting studies demonstrated greater *O6*-MeG adducts, cell cycle perturbation and DNA double-strand breaks with AFt-TMZ compared to naked TMZ treatment. Additionally, environmental scanning electron microscopy (ESEM) and confocal microscopy revealed that GBM cells appeared more shrunken, with obvious blebbing (signs of apoptosis), following treatment with AFt-TMZ over TMZ. Furthermore, the T25 analogue demonstrated even greater potency when delivered inside AFt (in U373M: GI_{50} = 0.077 μM), as well as the combination of AFt-TMZ with AFt-NRP (in U373M: GI_{50} = 0.072 μM). Alone, AFt was shown to be non-toxic and imparted selective activity to the test agent, with greater anti-cancer activity seen in cancer over non-cancer cells. This was likely due to differences in TfR1 expression, where all cancer cells but the non-tumorigenic MRC-5 cells expressed TfR1.

In conclusion, test agents delivered by AFt demonstrated enhanced potency over test agent alone, in a selective and cancer specific manner. Tackling resistance with the use of TMZ analogues or inhibitors of MGMT or PARP-1 further potentiated the anti-cancer activity in TMZ resistant GBM. By overcoming TMZ resistance and toxicity, we aim to prolong patient's survival and quality of life.

Publications and conference proceedings

1. Bouzinab, K.; Thomas, N. R.; Turyanska, L.; Gershkovich, P.; Weston, N.; Ashford, M. B.; Bradshaw, T. D. Targeting brain tumours: apoferritin nanocage for delivery of novel analogues of temozolomide. *Neuro-Oncology* **2019**, *21*, iv4.

2. Bouzinab, K.; Summers, H.; Zhang, J.; Stevens, M. F. G.; Moody, C. J.; Turyanska, L.; Thomas, N. R.; Gershkovich, P.; Ashford, M. B.; Vitterso, E.; Storer, L. C. D.; Grundy, R.; Bradshaw, T. D. In search of effective therapies to overcome resistance to temozolomide in brain tumours. *Cancer Drug Resist*. **2019**, 2, 1018−1031.

3. Bouzinab, K.; Summers, H. S.; Stevens, M. F. G.; Moody, C. J.; Thomas, N. R.; Gershkovich, P.; Weston, N.; Ashford, M. B.; Bradshaw, T. D.; Turyanska, L. Delivery of Temozolomide and N3-Propargyl Analog to Brain Tumors Using an Apoferritin Nanocage. *ACS Appl. Mater*. *Interfaces* **2020**, 12, 12609-12617.

4. Bouzinab, K.; Thomas, N. R.; Turyanska, L.; Gershkovich, P.; Weston, N.; Ashford, M. B.; Bradshaw, T. D. Abstract 1727: Challenging Resistance to Temozolomide in Glioblastoma by Drug Encapsulation in Apoferritin. *Clin. Cancer Res*. **2020**, *80*, 1727–1727.

Acknowledgments

First and foremost, I would like to express my deepest gratitude to my primary supervisor Dr. Tracey D. Bradshaw (University of Nottingham, School of Pharmacy). Her support, guidance and motivation to drive this research has been a constant highlight for me throughout this Ph.D. and her encouragement and assistance in publishing papers, applying for conferences, travel grants and fellowships has allowed me to grow and better myself as a researcher. My sincere gratitude also extends to my other supervisors, firstly to Dr. Lyudmila Turyanska (University of Nottingham, Faculty of Engineering), who has also been immensely supportive throughout my Ph.D. and has always provided me with useful constructive feedback, for which I am grateful for. In addition, I would like to heartily show gratitude to my supervisors Prof. Neil R. Thomas (University of Nottingham, School of Chemistry), Dr. Pavel Gershkovich (University of Nottingham, School of Pharmacy) and Dr. Marianne B. Ashford (Advanced Drug Delivery, Pharmaceutical Sciences, R & D, AstraZeneca) for the support, encouragement, inspiration and advice throughout this project. My thanks also extend to Dr. Paul Gellert (AstraZeneca), who has been supportive and provided much needed inspiration and advice.

Next, I would like to acknowledge my funding and sponsoring body the United Kingdom Research and Innovation (UKRI): Engineering and Physical Sciences Research Council [EPSRC; grant numbers EP/L01646X/1, as well as EP/L022494/1, and EP/P031684/1], the EPSRC Centre for Doctoral Training (CDT) in Advanced Therapeutics and Nanomedicines, the University of Nottingham School of Pharmacy and AstraZeneca, for supporting my Ph.D. Furthermore, I would like to thank the American Association of Cancer Research (AACR) and the Royal Society of Chemistry (RSC) for awarding me

with travel grants to attend conferences throughout my study. In extension, I would like to thank all the management and student members of the CDT in Advanced Therapeutics and Nanomedicines from both the University of Nottingham and the University College of London (UCL), for the invaluable experiences gained throughout the four-year CDT programme. My deepest gratitude goes out to my pre-Ph.D. first mini project supervisors: Dr. Frankie Rawson (University of Nottingham) and Dr. Mischa Zelzer (University of Nottingham), and additional supervisors Prof. Snow Stolnik-Trenkic (University of Nottingham) and Dr. Giuseppe Mantovani (University of Nottingham); as well as to my second mini project supervisors: Prof. Clive Washington (AstraZeneca) and Dr. Jean-Baptiste Guilbaud (AstraZeneca), for the essentials skills and experiences gained prior to my Ph.D.

Thank you to everyone in lab C62/C64 (from the Biodiscovery Institute) for all the support, training and guidance throughout my Ph.D. Special thanks go to my lab colleagues and friends: Dr. Alastair Breen, Dr. Helen Summers, Dr. Mohannad Qazzaz, Dr. Shahadat Hossan, Haneen Abuzaid, Lenny Ferreira, Mohammed Abid, Isobel Holden, José C. Quilles Junior, Emily Vitterso, Dr. Joseph Ali, Dr. Marisa Freitas, Mustapha Musa, Maria Cassioli Amelia Hatfield and Alice Brookes. In addition, my special thanks extend to Akmal H. Bin Sabri and Rasha Khader for all the support and friendship over the years. I would also like to acknowledge the lab technicians and the Biodiscovery building support staff, as well as Boots Science Building lab technicians for all the work they do to maintain the labs; particularly my special thanks go to Ann Williams, Lee Hibbett and Paul Cooling. My thanks also go to Dr. David Onion and Nicola Croxall for help and training with flow cytometry and Dr. Robert Markus for help and training with confocal microscopy.

Furthermore, I would like to extend my gratitude to my collaborators Nicola Weston (Nanoscale and Microscale Research Centre, University of Nottingham) for carrying out the environmental scanning electron microscopy imaging, to Dr. Vahid Heravi Shargh and Dr. Beth Coyle (University of Nottingham) for our ongoing collaborative research using apoferritin formulations to target paediatric brain tumours and for our useful discussions, to Dr. Steven Shnyder for collaborating with us to carry out the *in vivo* studies (currently ongoing), and to scientists at Sygnature Discovery for PK and PD studies (currently ongoing). Most importantly, I would like to thank Prof. Malcolm F. G. Stevens and Prof. Christopher J. Moody (University of Nottingham) for allowing me to utilise the TMZ analogues for my studies and to Dr. Helen Summers for synthesising and providing me with the TMZ analogues supplies.

Finally, I would like to demonstrate my deepest gratitude and appreciation to my family for all the support and encouragement to pursue my goals, throughout these years, particularly special thanks go to my mother and father, and sisters. My gratitude also extends to my dear friends Tahne Yafai, Farida Mili and Zaheda Begum, and to Neda Yafai for the many years of friendship and support. Throughout my 8 years of University level studies, I have forged some additional friendships for which I am grateful for and my thanks extend to my friends Salma Farrah, Ulfath Shaheen, Sophia Begum and Sanna Khan.

Table of contents

Abstracts……II

Publications and conference proceedings……IV

Acknowledgements……..V

List of abbreviations……..XII

List of tables..……XVI

List of schemes..……..XVII

List of figures……XVIII

Chapter 1 - Introduction……1

1.1 Cancer……...1

1.1.1 Definition and classification……1

1.1.2 Epidemiology……...2

1.1.3 Hallmarks of cancer……6

1.1.3.1 Self-sufficiency in growth signals (to sustain chronic proliferation)……...7

1.1.3.2 Insensitivity to anti-growth signals (evading growth suppressors)……..9

1.1.3.3 Evading apoptosis……..12

1.1.3.4 Enabling replicative immortality……14

1.1.3.5 Inducing sustained angiogenesis……16

1.1.3.6 Activating invasion and metastasis……...19

1.1.3.7 Enabling hallmarks of cancer……21

1.1.3.8 Emerging hallmarks of cancer……...23

1.2 CNS-related tumours ……28

1.2.1 What are CNS tumours?……..28

1.2.2 Classification of CNS tumours and grade……..28

1.2.3 Causes of brain tumours……..30

1.2.4 Epidemiology……....31

1.3 Glioblastoma multiforme (GBM)……..34

1.3.1 What is GBM?……34

1.3.2 The site of GBM growth……36

1.3.3 Symptoms of GBM……36

1.3.4 Epidemiology……37

1.3.5 Histological features of GBM……...38
1.3.6 Hallmarks and biomarkers of GBM……40
1.3.7 Diagnosis and clinical presentation of GBM……..47
1.3.8 Treatment approach for GBM……..48
1.3.9 GBM survival rates……53

1.4 Temozolomide (TMZ)……56
1.4.1 Background of TMZ ……..56
1.4.2 Mechanism of activation of TMZ.…….....57
1.4.3 Mechanism of action of methyldiazonium cation……..59
1.4.4 Mechanism of resistance to TMZ……62
1.4.5 Mechanisms to tackle TMZ resistance……...65
1.4.6 Shortcomings in the approval of new oncology drugs……..69

1.5 Nano drug delivery systems (DDS) for GBM treatment……72
1.5.1 What are nanoparticles?…….....72
1.5.2 Important characteristics of nanoparticles as a nanomedicine……....74
1.5.3 Nanoparticles employed for GBM diagnosis and treatment…79

1.6 The use of apoferritin as a DDS……87
1.6.1 Ft function……...87
1.6.2 Ft structure……....88
1.6.3 Fe removal to generate AFt……91
1.6.4 The application of AFt……...91
1.6.5 Mechanism of achieving drug encapsulation inside AFt……..96

1.7 Project aims……....98

Chapter 2 – Materials and methods……..100
2.1 Materials……...100

2.2 Generating AFt from horse spleen Ft……104

2.3 Test agent encapsulation into AFt by nanoreactor route……105

2.4 Characterisation of AFt formulations……106
2.4.1 Bradford assay for protein concentration determination……..106
2.4.2 UV-Vis spectroscopy for test agent standard curve formation and concentration determination……..107
2.4.3 Determining efficiency of AFt encapsulation of test agents….109
2.4.4 Molecular weight determination of AFt subunit and full cage..110
2.4.5 AFt size and charge measurements……...113
2.4.6 Storage stability……115
2.4.7 *In vitro* test agent release……116

2.5 Cell culture……116
2.5.1 Reviving cell stocks……116
2.5.2 Passaging and maintaining cell lines……117
2.5.3 Protocol for freezing cells ……..……118

2.6 *In vitro* cytotoxicity testing……....118
2.6.1 MTT assay – 6 days test agent treatment……119
2.6.2 Live cell count assay – 6 days test agent treatment……124
2.6.3 Clonogenic assay – 24 h and 6 days test agent treatment…125
2.6.4 Flow cytometry: cell cycle analysis – 72 h test agent treatment……..126
2.6.5 Flow cytometry: γ-H2AX analysis – 48 and 72 h test agent treatment……..128
2.6.6 Indirect ELISA: DNA *O6*-MeG quantification – 4, 24, 72 and 144 h test agent treatment……129

2.7 Cellular characterisation……131
2.7.1 Western blot……...131
2.7.2 Flow cytometry: quantification of transferrin receptor 1……134

2.8 Cell-based imaging……..135
2.8.1 Environmental scanning electron microscopy (ESEM)……135
2.8.2 Confocal microscopy……136

2.9 Statistical analyses……..137

Chapter 3 - Apoferritin encapsulation of test agents to overcome temozolomide resistance……138
3.1 Introduction……....138

3.2 Results and Discussion……..143
3.2.1 Preparation of AFt from horse spleen Ft……..143
3.2.2 Drug stock preparation and characterisation……..150
3.2.3 AFt encapsulation of test agents……...152
3.2.4 Characterisation of formulations by DLS, ζ-potential and native-PAGE……154
3.2.5 *In vitro* test agent release studies for AFt formulations……..156
3.2.6 Storage stability of AFt formulations……158

3.3 Conclusions..……160

Chapter 4 - *In vitro* activity of horse spleen apoferritin encapsulated-temozolomide……162
4.1 Introduction……....162

4.2 Results and Discussion……..165
4.2.1 Preliminary assessment of cellular growth inhibition by TMZ and AFt-TMZ *via* MTT assay……165
4.2.2 Assessment of the number of live/dead GBM cells following exposure to TMZ and AFt-TMZ……170
4.2.3 Assessing the expression levels of cellular protein……..…171
4.2.4 The effect of TMZ and AFt-TMZ on GBM colony formation...174
4.2.5 Monitoring the changes to cell cycle and DNA damage status of GBM cells following exposure to TMZ and AFt-TMZ……..176
4.2.6 Quantifying differences in the levels of DNA *O6*-MeG following exposure to TMZ and AFt-TMZ……178
4.2.7 Monitoring the morphological changes to GBM cells after short treatment exposure……179

4.3 Conclusions..……182

Chapter 5 - *In vitro* assessment of alternative horse spleen AFt encapsulated-test agents that overcome TMZ resistance ……184
5.1 Introduction…….....184

5.2 Results and Discussion……..186
5.2.1 Preliminary assessment of cellular growth inhibition by AFt encapsulated N3P or T25 analogues *via* MTT assay…….186
5.2.2 Effect of MGMT or PARP inhibitors on AFt-TMZ activity assessed *via* MTT assay……190

5.3 Conclusions..……198

Chapter 6 – Conclusion and future directions……200
6.1 Conclusions…….....200

6.2 Future directions……..204

7- References……209

8 – Appendices……..229
8.1 Appendix I…….229
8.2 Appendix II……230
8.3 Appendix III……..231
8.4 Appendix IV……..232

List of abbreviations

% v/v	Percentage volume/volume
%DL	Drug loading percentage
%EE	Encapsulation efficiency percentage
+ve	Positive
1° Ab	Primary antibody
2° Ab	Secondary antibody
2-HG	2-hydroxyglutarate
3D	Three-dimensional
5-ALA	5-aminolevulinic acid
aAPC	Artificial antigen presenting cell
Ab	Antibody
ACN	Acetonitrile
AFt	Apoferritin
AIC	5-aminoimidazole-4-carboxamide
APAF1	Apoptotic protease activating factor 1
ATCC	American Type Culture Collection
ATP	Adenosine triphosphate
ATRX	Alpha thalassaemia mental retardation
BBB	Blood brain barrier
BBTB	Blood brain tumour barrier
BER	Base excision repair
bp	Base pair
BRCA gene	Breast cancer gene
BSA	Bovine serum albumin
C1	Initial concentration
C2	Final concentration
CAM	Cell-cell adhesion molecules
CDKN2A	Cyclin-dependent kinase inhibitor 2A
CED	Convection enhanced delivery
CGKRK	Cysteine-glycine-lysine-arginine-lysine
CNS	Central nervous system
cnx43	Connexin 43
CO_2	Carbon dioxide
CRC	Colorectal carcinoma
CSC	Cancer stem cells
CSF	Cerebrospinal fluid
CT	Computerised tomography
CTL	Cytotoxic T lymphocytes
Cys	Cysteine
D:A	Drug/ Apoferritin
$_D$[KLAKLAK]$_2$	$_D$[lysine-leucine-alanine-lysine-leucine-alanine-lysine]$_2$
DAPI	4',6-diamidino-2-phenylindole
DDS	Drug delivery system
dH_2O	Deionised water
DLS	Dynamic light scattering
DMSO	Dimethyl sulfoxide
DNA	Deoxyribonucleic acid
DNMT	Cytosine DNA-methyltransferase
DOX	Doxorubicin
DTIC	Dacarbazine
ECL	Enhanced chemiluminescence

ECM	Extracellular matrix
EGFR	Epidermal growth factor receptor
ELISA	Enzyme-linked immunosorbent assay
EMT	Epithelial-to-mesenchymal transition
EOR	Extent of resection
EPR	Enhanced permeability and retention
ESEM	Environmental scanning electron microscopy
F(ka)	Henry's function
FACS	Fluorescence activated cell sorter
FADD	FAS-associated death domain protein
FBS	Fetal bovine serum
Fe	Iron
FGF	Fibroblast growth factors
Ft	Ferritin
G0 phase	Gap 0 phase
G1 phase	Gap 1 phase
G2 phase	Gap 2 phase
G418	Geneticin
GAPDH	Glyceraldehyde 3-phosphate dehydrogenase
GBM	Glioblastoma multiforme
GEM	Genetically engineered mouse
GF	Growth factors
GF	Growth factors
GFP	Green fluorescent protein
GI	Gastrointestinal
GI_{50}	50% Growth inhibition
GLUT1	Glucose transporter 1
GS	Growth signals
Gy	Gray (unit)
h	Hours
H	Heavy
$H_2PO_4^-$	Dihydrogenphosphate
HCl	Hydrochloric acid
HCT116	Adult human colorectal carcinoma cell line
HCT116-VR	Adult human colorectal carcinoma cell line – vincristine resistant
HFSRT	Hypofractionated stereotactic radiotherapy
HIF-1α	Hypoxia-inducible factor 1-alpha
HIF-1β	hypoxia-inducible factor 1-beta
HIF-2α	Hypoxia-inducible factor *2*-alpha
His	Histidine
HPLC	High performance liquid chromatography
HR	Homologous recombination
HRP	Horseradish peroxidase
I^{125}	Iodine 125
IDH	Isocitrate dehydrogenase
IEP	Isoelectric point
IL-13Rα2	Interleukin-13 receptor α2
IMS	Industrial methylated spirits
IONP	Iron oxide nanoparticle
JNK	c-Jun NH2-terminal kinases
KPS	Karnofsky performance status
L	Light
LOH	Loss of heterozygosity
M phase	Mitosis phase

MAPK	Mitogen-activated protein kinase
MDSC	Myeloid-derived suppressor cells
MEM	Minimum essential media
MeOH	Methanol
MGMT	*O6*-Methylguanine-DNA-methyltransferase
Min	Minutes
MLH1	MutL homolog 1
MMR	Mismatch repair
MRC-5	Medical research council strain 5 (fetal lung fibroblast cell line)
MRI	Magnetic resonance imaging
MTIC	Triazene, 5-(3-methyltriazen-1-yl) imidazole-4-carboxamide
MTT	3-(4,5-dimethylthiazol-2-yl)-2,5-diphenyltetrazolium bromide
MW	Molecular weight
MWCO	Molecular weight cut-off
N3-MeA	*N3*-methyladenine
N3P	N3-propargyl analogue
N7-MeG	*N7*-methylguanine
Native PAGE	Native polyacrylamide gel electrophoresis
NEAA	Non-essential amino acids
NK	Natural killer
NLC	Nanostructured lipid carriers
NP	Nanoparticle
NP40	Nonidet-P40
NRP	Niraparib
O6-BeG	*O6*-benzylguanine
O6-MeG	*O6*-methylguanine
OS	Overall survival
PAMAM	Poly(amidoamine)
PARP	Poly (ADP-ribose) polymerase
PARylation	PolyADP-ribosylation
PBS	Phosphate-buffered saline
PD	Pharmacodynamic
PDGFR	Platelet-derived growth factor receptor
PDGFRα	Platelet-derived growth factor receptor-alpha
PDGFRβ	Platelet-derived growth factor receptor-beta
PDX	Patient-derived tumour xenograft
PE%	Plating efficiency %
PEG	Polyethylene glycol
PFS	Progression-free survival
Pgp	P-glycoprotein 1
pH	Potential of Hydrogen
PI	Propidium iodide
PI3K	Phosphoinositide 3-kinase
PK	Pharmacokinetic
PLGA	Poly(lactide-co-glycolides)
PNP	Polymeric nanoparticle
POS	Probability of success
PS	Performance status
PTEN	Phosphatase and tensin homolog
PTX	Paclitaxel
QOL	Quality of life
qPCR	Quantitative polymerase chain reaction
R^2	Coefficient of determination
RAS	Rat sarcoma

Rb	Retinoblastoma protein
RES	Resveratrol
RGD	Arginylglycylaspartic acid
RGDyK	Arginine-glycine-aspartic acid-D-tyrosine-lysine
RNaseA	Ribonuclease A
ROS	Reactive oxygen species
RPMI-1640	Roswell Park Memorial Institute 1640 media
RT	Room temperature
RTK	Receptor tyrosine kinase
s	Seconds
S phase	Synthesis phase
SAM	S-adenosylmethionine
SCARA5	Scavenger receptor class A member 5
SDS	Sodium dodecyl sulfate
SDS-PAGE	Sodium dodecyl sulfate polyacrylamide gel electrophoresis
SF%	Survival fraction %
siRNA	Small (or short) interfering ribonucleic acid
SLN	Solid lipid nanoparticles
SPIO	Superparamagnetic iron oxide
SRS	Stereotactic radiosurgery
T	Temperature
t	Time
T0	Time 0
T25	C8-thiazole analogue
TBST	Tris-buffered saline and Tween 20
TEM	Transmission electron microscopy
TERT	Telomerase reverse transcriptase
Tf	Transferrin
TfR1	Transferrin receptor 1
TfR2	Transferrin receptor 2
TGF	Transforming growth factor
TMB	Tetramethylbenzidine
TMZ	Temozolomide
Treg	Regulatory T cells
Tris	Tris(hydroxymethyl)aminomethane
TTFields	Tumour-treating fields
Tyr	Tyrosine
U118MG	Adult human glioblastoma multiforme cell line
U373M	Adult human glioblastoma multiforme cell line
U373V	Adult human glioblastoma multiforme cell line
UK	United Kingdom
UV-Vis spectroscopy	Ultraviolet/visible spectroscopy
-ve	Negative
VEGF	Vascular endothelial growth factor
VHL	Von Hippel-Lindau
WHO	World Health Organisation
γ-H2AX	Gamma-histone 2 family member X
ζ-potential	Zeta potential

List of tables

Table 1.1. The physicochemical properties of TMZ…….57

Table 1.2. Nanoparticle formulations being assessed for GBM therapy……81

Table 2.1. List of materials used for experimental studies……...100

Table 2.2. Human cell lines used for experimental studies……..103

Table 2.3. The concentration of test agents used in the MTT assay……..121

Table 2.4. The Ab used for western blot……134

Table 3.1. Summary of the AFt encapsulation of test agents. The mean values for drug:AFt (D:A) ratio, encapsulation efficiency (EE), drug loading (DL) and protein yield are shown along with the standard deviation (n = 3)……154

Table 5.1. A summary of the estimated GI_{50} values following a 6-day treatment exposure (1:1 molar ratio of TMZ+*O6*-BeG or 1:1 molar ratio AFt-TMZ+AFt-*O6*-BeG) in GBM cell line: U373M (MGMT +ve) and non-cancerous MRC 5 fibroblasts). GI_{50} values were determined for each test agent in the combination administered to cells. Values are reported as mean ± SD (n > 3)……..192

Table 5.2. A summary of the estimated GI_{50} values following a 6-day treatment exposure (5.8:1 molar ratio of TMZ+NRP or AFt-TMZ+AFt-NRP) in GBM cell line: U373M (MGMT +ve) and non-cancerous MRC 5 fibroblasts). GI_{50} values were determined for each test agent in the combination administered to cells. Values are reported as mean ± SD (n > 3)……195

Table 5.3. Combination indices calculated for different combination treatments administered to U373M and MRC-5 cells to determine synergistic, additive, or antagonistic drug interactions (using the bottom table as a key)……...197

List of schemes

Scheme 1.1. The mechanism of breakdown of TMZ **1** to release active methyldiazonium cation **5**……58

Scheme 1.2. Interaction of methyldiazonium cation **5** with the O6-position of guanine to generate *O6*-MeG DNA adduct……60

List of figures

Figure 1.1. Pie Charts representing the distribution of all cancer cases (total: 18.1 million cases) and deaths (total: 9.6 million deaths) worldwide, in 2018……...3

Figure 1.2. The number of new cases and deaths of the most common cancers worldwide, in 2018……...4

Figure 1.3. Pie Charts representing the distribution of all cancer cases (total: 372611 cases) and deaths (total: 167508 deaths) in the UK, in 2017……...4

Figure 1.4. The number of new cases and deaths of the most common cancers in the UK, in 2017……5

Figure 1.5. The MAPK pathway……9

Figure 1.6. The cell cycle……..11

Figure 1.7. The intrinsic and extrinsic pathways that activate apoptosis……13

Figure 1.8. Maintenance of telomere length in normal vs cancer cells……..15

Figure 1.9. Tumour promoting sustained angiogenesis……...18

Figure 1.10. Invasion and metastasis of cancer cells……20

Figure 1.11. Tumour promoting inflammation……22

Figure 1.12. Normal vs cancer cell energy metabolism……25

Figure 1.13. Cancer cell evasion of immune destruction by going through the process of cancer immunoediting……27

Figure 1.14. Pie Charts representing the distribution of CNS-related cancer cases (total: 11886 cases) and deaths (total: 5342 deaths) in the UK, in 2017……31

Figure 1.15. Pie Charts representing the distribution of primary CNS (benign and malignant) tumours by main histology groups, in England, between the period of 1995–2003……33

Figure 1.16. Brain cells……35

Figure 1.17. Different regions of the brain and their roles in the body……36

Figure 1.18. Distribution of GBM cases in England between 2007-2011……...38

Figure 1.19. The histological features of GBM……...39

Figure 1.20. Verhaak classification system of GBM……..40

Figure 1.21. Convection enhanced delivery (CED)……...53

Figure 1.22. A Kaplan–Meier plot showing survival (months) according to treatment type for patients with GBM (England; 2007–2010)……..55

Figure 1.23. The chemical structure of TMZ……..56

Figure 1.24. The breakdown and elimination of TMZ by-products……..59

Figure 1.25. The most common methylated adducts formed from methyldiazonium cation alkylation of DNA purine bases……..59

Figure 1.26. The DNA damage signalling pathway……..61

Figure 1.27. The MGMT Cys145S–*O6*-MeG DNA substrate complex (PDB code: 1T38)……63

Figure 1.28. Mechanism of removal of methyl group from *O6*-MeG by MGMT, to restore guanine……..64

Figure 1.29. Parent TMZ alongside analogues of TMZ bearing N3- and/or C8-group substitutions……68

Figure 1.30. Schematic representation of the EPR effect……73

Figure 1.31. Schematic showing the various types of nanoparticles……..74

Figure 1.32. A schematic demonstrating the formation of a protein corona around a nanoparticle……78

Figure 1.33. Amphiphilic block co-polymer–coated iron oxide nanoparticles (IONPs; red; 10 nm core size)……..80

Figure 1.34. Materials for *ex vivo* expansion of T cells……..85

Figure 1.35. Horse spleen Ft (PDB: 4V1W)……90

Figure 1.36. The common routes of AFt encapsulation of test agents……97

Figure 2.1. Primary amino acid sequences of horse spleen Ft L-subunit (entry code: P02791) and H-subunit (entry code: Q8MIP0) obtained from UniProtKB……108

Figure 3.1. The chemical structures of test agents……140

Figure 3.2. Conversion of Ft to AFt……143

Figure 3.3. Standard curves from Bradford assay……..145

Figure 3.4. UV-vis spectra of Ft and AFt showing the presence and absence of the Fe peak……..146

Figure 3.5. Protein separation by PAGE……..148

Figure 3.6. The stability of Ft, AFt and AFt (Sigma-Aldrich) monitored through hydrodynamic size measurements by DLS and ζ-potential……...150

Figure 3.7. The standard curves of TMZ and TMZ analogues (N3P and T25), as well as *O6*-BeG and NRP obtained by UV-vis spectroscopy……151

Figure 3.8. AFt size, charge and MW characterisation……...155

Figure 3.9. Time-dependent test agent release at 37 °C under two buffered conditions, pH 5.5 (0.1 M NaOAc) and pH 7.4 (1X PBS)……156

Figure 3.10. AFt-TMZ, AFt-N3P and AFt-T25 stability monitored at storage conditions (*T* = 4 °C; pH 5.5)…..……...159

Figure 4.1. Concentration-dependent growth inhibition profiles from MTT assays……...166

Figure 4.2. A summary of estimated GI_{50} values for TMZ and AFt-TMZ (6-day treatment exposure) in all studied cell lines…….169

Figure 4.3. *In vitro* cell viability assessment of U373V (MGMT -ve) and U373M (MGMT +ve)…….171

Figure 4.4. Cellular characterisation of protein expression……172

Figure 4.5. Flow cytometric quantification of cell surface TfR1 expression (through quantification of the fluorescence of R-PE conjugated on an anti-TfR1 1° Ab) in U373V, U373M, HCT116 and MRC-5 cells……..174

Figure 4.6. *In vitro* characterisation of cell proliferation proficiency following treatment……..175

Figure 4.7. Mechanism of action of TMZ compared to AFt delivered TMZ (AFt-TMZ) in GBM: MGMT +/−ve cells, as assessed by flow cytometry……...177

Figure 4.8. Indirect ELISA, DNA *O6*-MeG quantification in GBM: MGMT +/−ve cells following exposure of cells to 50 μM TMZ or AFt-TMZ……...179

Figure 4.9. Morphological changes to GBM cells (MGMT +/-ve) following 24 h treatment exposure (TMZ/AFt-TMZ; 50 μM)……181

Figure 5.1. *C*oncentration-dependent growth inhibition profiles from MTT assays……...187

Figure 5.2. Bar graphs of estimated GI_{50} values following a 6-day treatment of all studied cell lines……..189

Figure 5.3. MTT assay to assess cellular growth inhibition……191

Figure 5.4. *C*oncentration-dependent growth inhibition profiles from MTT assays……...192

Figure 5.5. MTT assay to assess cellular growth inhibition……194

Figure 5.6. *C*oncentration-dependent growth inhibition profiles from MTT assays……...195

Chapter 1 – Introduction

1.1 Cancer

1.1.1 Definition and classification

Cancer, the Latin word for crab, is a collection of related diseases in which abnormal cells divide without control and invade nearby tissues. A cancer can start almost anywhere in the human body.[1] Normally, human cells grow and divide to form new cells when the body needs them and as the cells grow old or become damaged, they die, and new cells take their place.[1] However, during cancer development, this process breaks down. Old/damaged cells survive when they should die, and new cells form when they are not needed.[1] These extra cells divide continuously to form growths called tumours.[1]

Tumours can be benign or malignant.[1] Benign tumours are non-cancerous and are simply slow-growing masses that compress rather than invade surrounding tissue.[1] On the other hand, malignant tumours are cancerous and have the potential to invade nearby tissue and spread to other parts of the body, through a process called metastasis.[1] A cancer formed at the original site is called a primary cancer and cancers that form in other sites from metastasised cancer cells are called secondary cancers.[1] Cancers are histologically categorised into the following groups:[1]

1) Carcinoma – originating from epithelial tissues on the inner or outer surface of the body, generally from endodermal/ectodermal germ layers during embryogenesis. They can invade and metastasise.
2) Sarcoma - are altered cells of mesenchymal origin in bone, muscle, or connective tissue.

3) Leukaemia - originating in the bone marrow, leading to the abnormal development of white blood cells and is generally classified into acute and chronic forms.
4) Lymphoma - originating from glands or nodes of the lymphatic system.
5) Myeloma – originating in the plasma cells of bone marrow.
6) Blastoma - originating in embryonic tissue of organs, particularly occurring in undifferentiated cells.

1.1.2 Epidemiology

As the world population continues to grow and age, and changes in socioeconomic development occurs, global cancer incidence and number of cancer deaths also increase.[2] According to the International Agency of Research on Cancer GLOBOCAN 2018 estimates of cancer incidence and mortality cases (from 185 countries, 36 cancers and 18 age groups), there were an estimated 18.1 million new cases of cancer and 9.6 million cancer-related deaths, worldwide.[2] However, when the increase in population growth and age is taken into consideration, the rate of cancer deaths has shown to slowly decline.[2] Incidence and mortality indicate the number of new cases and deaths, respectively, occurring in a specified period and geographic area and can be conveyed as an absolute number of cases per year.[2] Figure 1.1 shows the distribution in the number of cases and deaths estimated in 2018, worldwide.[2] Incidences and deaths for all cancers combined are slightly higher amongst men than women (Figure 1.1a-b).[2] In addition, the majority of cancer cases occur predominantly amongst older populations, with the number of mortality cases for 50+ age group at 87.9% and far fewer amongst the younger age groups (Figure 1.1c-d).[2] It is also apparent that the continents with the greatest population densities have the highest number of cancer incidences and mortalities, particularly in Asia, where almost 60% of the global population

reside, followed by Europe, representing ~ 9% of the global population (Figure 1.1e-f).[2]

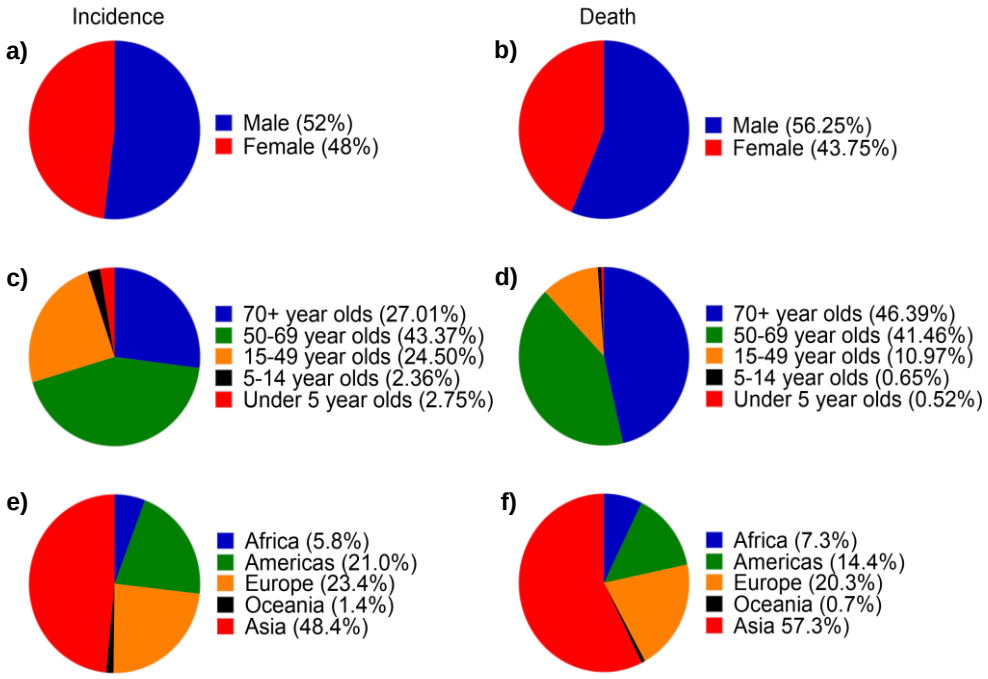

Figure 1.1. Pie Charts representing the distribution of all cancer cases (total: 18.1 million cases) and deaths (total: 9.6 million deaths) worldwide, in 2018. (a) Distribution of cancer incidences by sex (with ages and world regions combined). (b) Distribution of cancer deaths by sex (with ages and world regions combined). (c) Distribution of cancer incidences by age (with sexes and world regions combined). (d) Distribution of cancer deaths by age (with sexes and world regions combined). (e) Distribution of cancer incidences by world continents (with sexes and ages combined). (f) Distribution of cancer deaths by world continents (with sexes and ages combined). Source: GLOBOCAN 2018.[2]

Furthermore, Figure 1.2 represents the incidence and death cases (sexes combined) of the world's common cancers, in 2018.[2] Brain and central nervous system (CNS) related-cancers were one of the top 20 most diagnosed cancers worldwide and one of the leading causes of deaths.[2]

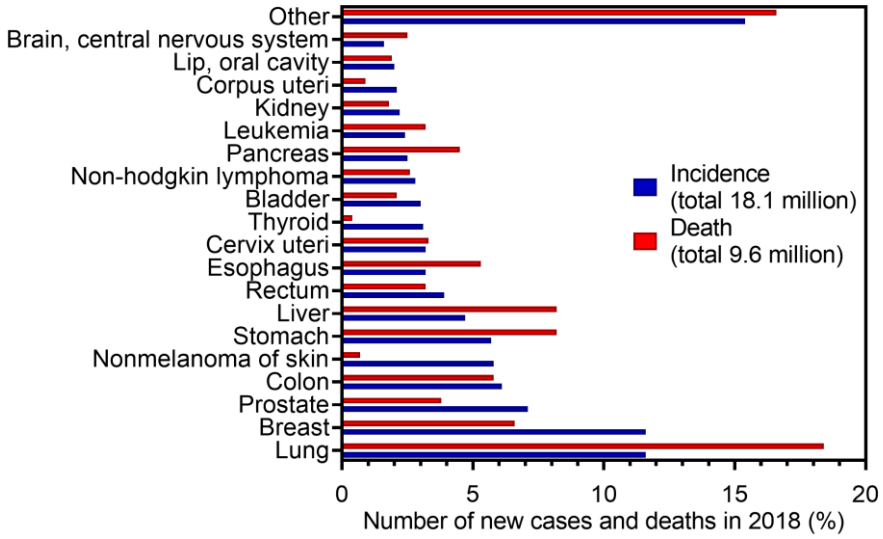

Figure 1.2. The number of new cases and deaths of the most common cancers worldwide, in 2018. Source: GLOBOCAN 2018.[2]

In the United Kingdom (UK), it was estimated in 2017, according to Cancer Research UK, that there were 372611 new cases of cancer and 167508 cancer-related deaths.[3] Of these, men were slightly more affected (Figure 1.3a-b) and again the 50+ age group fared worse with respect to cancer incidence and mortality (age 50+ comprised 95.9% of cancer mortalities; Figure 1.3c-d).[3,4]

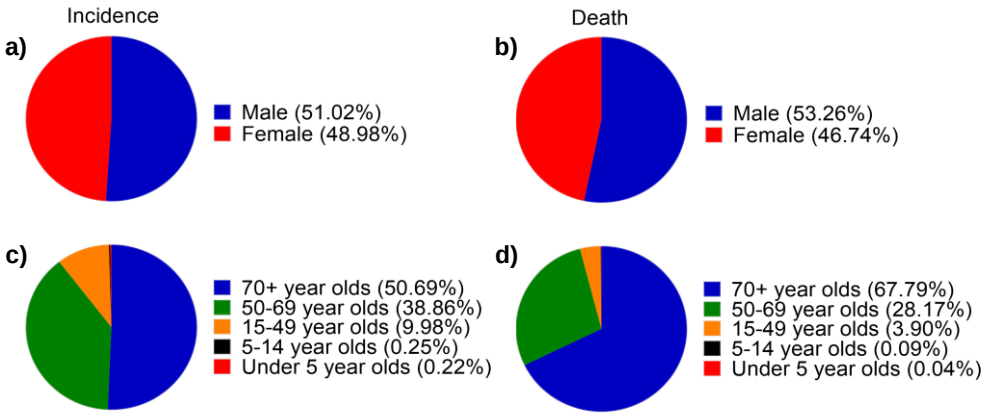

Figure 1.3. Pie Charts representing the distribution of all cancer cases (total: 372611 cases) and deaths (total: 167508 deaths) in the UK, in 2017. (a) Distribution of cancer incidences by sex (with ages combined). (b) Distribution of cancer deaths by sex (with ages combined). (c) Distribution of cancer incidences by age (with sexes combined). (d) Distribution of cancer deaths by

age (with sexes combined). Source: Cancer Research UK and World Cancer Research Fund.[3,4]

As illustrated in Figure 1.4, brain and CNS-related cancers were also one of the top 20 most diagnosed cancers in the UK and one of the leading causes of deaths.[2]

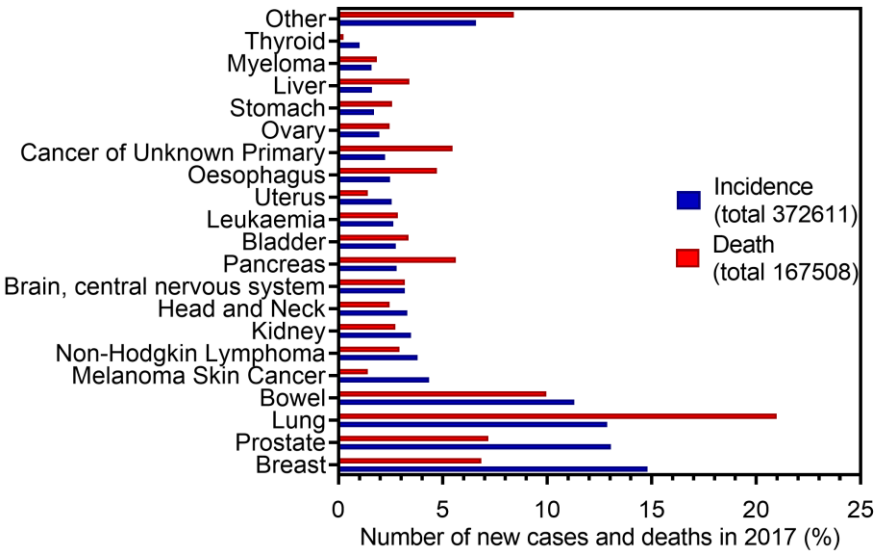

Figure 1.4. The number of new cases and deaths of the most common cancers in the UK, in 2017. Source: Cancer Research UK.[3]

Overall, there is a precedented need to further understand the characteristics of cancer behaviour and factors leading to cancer formation, to lower cancer incidence and mortality.

1.1.3 Hallmarks of cancer

The understanding of cancer traits to better aid drug design has been significantly advanced upon the description of the hallmarks of cancer by Hanahan and Weinberg through two seminal publication.[5,6] The aim of the publications was to align cancer research into a logical science, whereby the complexities of the disease would become understandable in terms of a small number of underlying principles. The authors reviews demonstrated that a small number of molecular, biochemical, and cellular traits are shared by most, if not perhaps all types of human cancers. Tumorigenesis is a multistage process. In summary, the following events take place during tumorigenesis: 1) initiation, 2) promotion, 3) progression (whereby chromosomal/genomic instability starts to increase dramatically) and 4) invasion/metastasis.

The first of the two publications published in the year 2000 titled 'The Hallmarks of Cancer' outlines six hallmarks of cancer that are acquired to permit normal cells to evolve into a neoplastic state, to become tumorigenic and eventually malignant.[5] These steps include: 1) sustaining proliferative signalling, 2) evading growth suppressors, 3) resisting cell death, 4) enabling replicative immortality, 5) inducing angiogenesis and 6) activating invasion and metastasis.[5]

Subsequently, progress in the understanding of cancer biology in the forthcoming decade rendered the publication of additional hallmarks of cancer, in 2011, in the publication entitled 'Hallmarks of Cancer: The Next Generation'.[6] These include two emerging hallmarks of cancer: 1) reprogramming/deregulation of cellular energy metabolism and 2) evading immune destruction, and two enabling hallmarks of cancer: 1) tumour-promoting inflammation and 2) genome instability and mutation.[6]

1.1.3.1 Self-sufficiency in growth signals (to sustain chronic proliferation)

Normal cells require mitogenic growth signals (GS) to transition from a quiescent to an active proliferative state.[5] Uptake of GS occur *via* transmembrane receptors.[5] GS are used to propagate normal cells in culture.[5] For tumour cells, there is a reduced dependence on exogenous growth stimulation from the neighbouring normal tissue environment, possibly due to the ability to generate their own GS – a process known as acquired GS autonomy. This is a process whereby a positive feedback loop is achieved, allowing cells to become responsive to their own synthesised GS - a procedure known as autocrine stimulation.[5]

Three common modes of achieving autonomy include: alteration to extracellular GS, alteration to the cell surface receptors involved in GS uptake and/or alteration to the intracellular pathways that translate those signals into action.[5]

Receptors of growth factors (GF), often have tyrosine kinase activities in their cytoplasmic domains and are overexpressed in many types of cancers.[5] This means that they are hyperresponsive to ambivalent levels of GF that would not normally trigger proliferation; eliciting ligand-independent signalling such as through structural alteration of receptors e.g. truncated epidermal growth factor receptor (EGFR), which lacks much of its cytoplasmic domains and thus fires constitutively.[5] Cancer cells can also switch the type of extracellular matrix (ECM) receptors (integrins) expressed, to favour ones that transmit pro-growth signals, by binding to certain ECM groups that would eventually enable signal transduction into the cytoplasm, influencing cell behaviour (shift from quiescent to active motile form), allowing entrance into active cell cycle (and causing resistance to apoptosis, described in section 1.1.3.3).[7]

Alteration to downstream cytoplasmic circuitry components that receive and process the signals emitted by ligand activated GF receptors and integrins represent the most complex mechanism of acquired GS autonomy.[5] One example includes the disruption to the mitogen-activated protein kinase (MAPK) pathway (Figure 1.5), which in normal cells is activated through binding of GF to cell surface receptors to signal the Ras-Raf-MEK-ERK cascade, where signals ultimately reaching the nucleus to activate cell proliferation.[8] The pathway is controlled by Ras GTPase.[6] However, in cancers, the disruption to the MAPK pathway often a consequence of mutations in various components of the MAPK circuitry (most commonly in Ras proteins), can lead to continuous cellular proliferation.[6]

Whilst it appears that cancer cells have an ability to achieve GS autonomy, it is also possible that contributions from normal cells present in the tumour microenvironment such as fibroblasts, endothelial cells and inflammatory cells could play a role in driving tumour cell proliferation.[5] Communication between the various types of cells occurs *via* heterotypic signalling.[5] Tumour cells may derive an ability to induce their normal neighbouring cells to release abundant levels of GS to benefit themselves.[5]

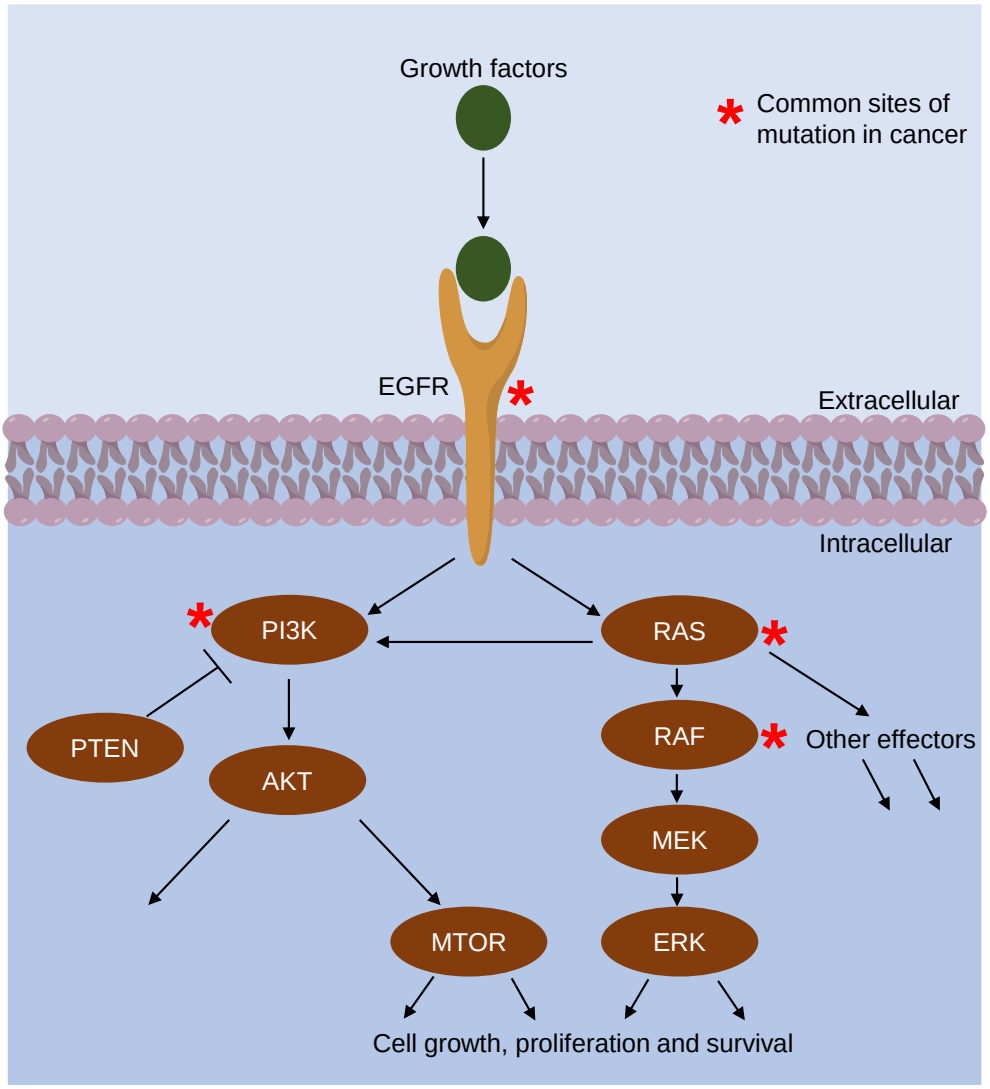

Figure 1.5. The MAPK pathway. Mutations occurring in various components of the MAPK signalling pathway can lead to sustained, chronic, cellular proliferation.[5,6]

1.1.3.2 Insensitivity to anti-growth signals (evading growth suppressors)

Multiple anti-proliferative signals such as soluble growth inhibitors, and immobilised inhibitors embedded in the ECM and on surfaces of nearby cells (within normal tissues), act by maintaining cellular quiescence and tissue homeostasis.[5] These signals are taken up by transmembrane cell surface receptors coupled to intracellular signalling circuits.[5] These signals work in two ways. Cells may be forced into the quiescent, gap 0 (G0) i.e. Pre-gap 1 (G1) phase of the cell cycle and emerge into the active phases of the cell cycle in the future (when permitted by extracellular signals), or cells can be induced

permanently to relinquish their proliferative capabilities by being induced to enter into postmitotic states; usually associated with the acquisition of specific differentiation-associated traits.[5]

Cancer cells must evade the anti-proliferative signals to proliferate indefinitely. Most of the circuitry that enables normal cells to respond to anti-growth signals are associated with the cell cycle clock - specifically components overseeing the transition of cells through the G1 phase of its growth cycle. So, whether cells sense the signals or not, is the basis for whether they become quiescent, continue to proliferate or enter into a postmitotic state.[5] At the molecular level, many anti-proliferative signals are channelled through the tumour suppressor protein called retinoblastoma protein (Rb; Figure 1.6) and its two relatives, p107 and p130.[9] Hypophosphorylated Rb (active form) blocks proliferation by binding and inhibiting E2F transcription factors (that control genes essential for the progression of cells from G1 to S phase of the cell cycle), thereby retaining cells in the G1 phase of the cell cycle.[9] Hyperphosphorylated Rb (inactive form) allow cells to transition to the S-phase of the cell cycle.[9] In cancers, loss of function of Rb through mutations, can lead to continuous proliferation and insensitivity to anti-GF.[5]

Cell proliferation depends on more than the avoidance of cytostatic anti-GS. Tissues also restrict cell multiplication by instructing cells to enter irreversibly into postmitotic differentiated states, using diverse mechanisms that are not completely understood.[5] It is apparent that tumour cells follow numerous tactics to avoid this terminal differentiation.[5] One strategy involves the c-Myc oncogene, which encodes a transcription factor.[5] During normal development, the growth stimulatory action of Myc, in association with another factor – Max,

can be supplanted by other complexes of Max i.e. complexes of Max with a group of Mad transcription factors; eliciting differentiation-inducing signals.[10] However, the overexpression of the c-Myc oncoprotein, which is seen in many tumours, can reverse this process by shifting the balance back to favour Myc-Max complexes; impairing differentiation and promoting growth.[10]

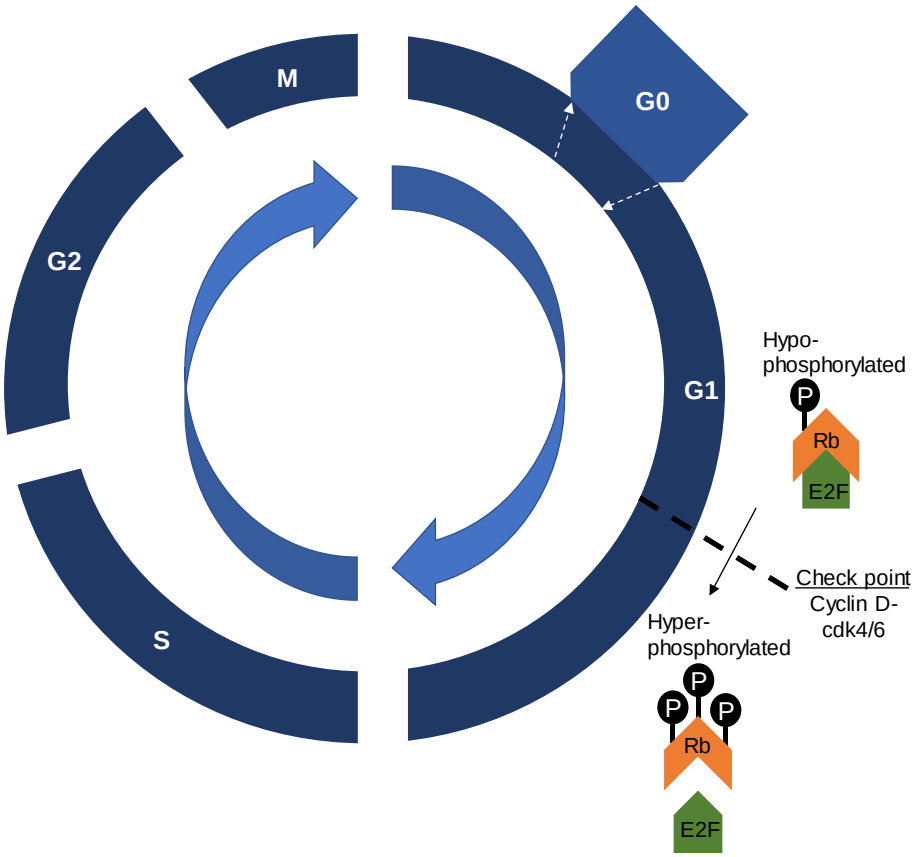

Figure 1.6. The cell cycle. In the G0- and early G1-phase of the cell cycle, proliferation *via* the transition of cells from G1- to S-phase of the cell cycle is blocked when hypophosphorylated Rb is bound to and inhibits the E2F transcription factors. When Rb is hyperphosphorylated in the late G1 phase, cells are able to transition to the S-phase of the cell cycle through the release of E2F factors, which subsequently allows for E2F-mediated gene transcription and the generation of S-phase related machinery.

1.1.3.3 Evading apoptosis

Expansion of a tumour cell population is dependent on the rates of both cell proliferation and death i.e. cell turnover.[5] Apoptosis represents one of the major mechanisms of programmed cell death and can be found present in all cells in latent form.[5] Once triggered, a series of steps occurs in the process of apoptosis, which includes cell membrane disruption, cytoplasmic and nuclear skeleton disintegration, cytosol extrusion, chromosomal degradation, and nucleus fragmentation.[11] Subsequently, shrivelled cells are engulfed by nearby macrophages.[11] Intracellular sensors are involved in monitoring the welfare of cells and activate the apoptotic pathway in response to anomalies such as deoxyribonucleic acid (DNA) damage, signalling imbalance, hypoxia, abrogation of cell-to-matrix and/or cell-to-cell adherence survival signals, etc.[12]

Many proapoptotic signals congregate on the mitochondria, which lead to the release of cytochrome C (a catalyst for apoptosis; Figure 1.7).[13] Certain members of the Bcl-2 family of proteins govern mitochondrial cell death signalling, which lead to the release of cytochrome C.[5,13] The tumour suppressor protein, p53, can cause apoptosis by upregulating the expression of a particular Bcl-2 proapoptotic protein member called Bax - in response to DNA damage, which in turn signals the release of cytochrome C from the mitochondria.[5,13] Effectors of apoptosis include a series of intracellular proteases called caspases (named as such because of their specific cysteine protease activity, whereby the cysteine in its active site nucleophilically attacks and cleaves the target protein solely after an aspartic acid residue).[14] Two caspases, caspase 8 and caspase 9 are activated by death receptors such as FAS, and by cytochrome C, respectively.[5,14] These caspases subsequently trigger other caspases, which carry out the mass proteolysis that leads to apoptosis.[5,14]

Resistance to apoptosis can be acquired by cancer cells through various methods. The most commonly occurring method is through the loss of a proapoptotic regulator e.g. *via* mutations in the *TP53* gene, resulting in the inactivation of the p53 protein.[5,15] This is seen in > 50% of human cancers.[5,15]

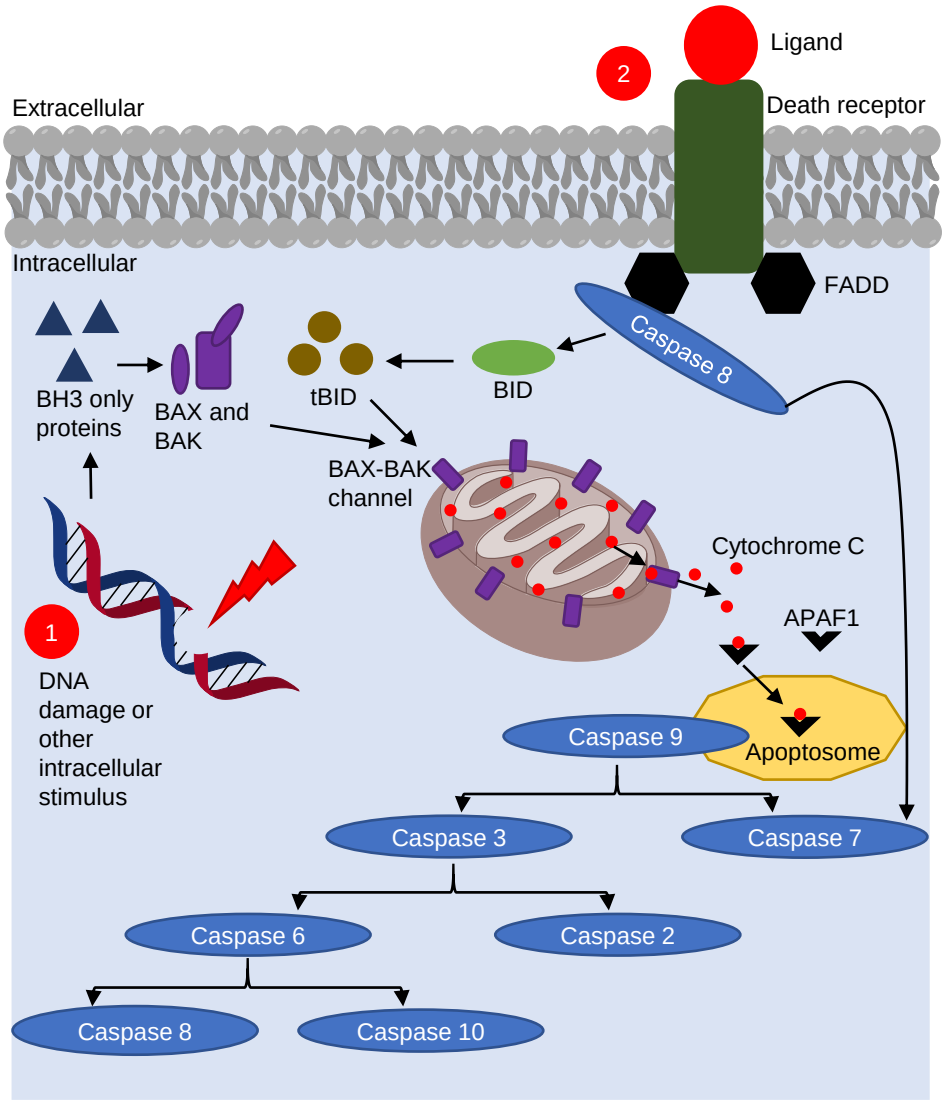

Figure 1.7. The intrinsic and extrinsic pathways that activate apoptosis. Activation of apoptosis *via* intrinsic mechanisms occur when internal stimuli like DNA damage activate BH3-only proteins, which lead to BAX or BAK activation. This leads to the generation of BAX-BAK channels in the mitochondrial outer membrane, which makes the mitochondria permeable and allows release of proapoptotic factors such as cytochrome C. Cytochrome C and its association with the apoptotic protease activating factor 1 (APAF1) forms the apoptosome - promoting the proteolytic maturation of activator caspase 9. Caspase 9 cleaves and activates other effector caspases 2, 3, 6-8, 10, eventually leading to apoptosis. Activation of apoptosis *via* extrinsic mechanisms occurs when certain ligands associate with the death receptors, which leads to the

recruitment of molecules such FAS-associated death domain protein (FADD), and then caspase 8. Caspase 8 can directly cleave and activate caspase 3 and caspase 7 and proteolytically activate BID to generate tBID, which can also promote mitochondrial membrane permeabilisation through the generation of BAX-BAK channels in the mitochondrial outer membrane. This represents the main link between the extrinsic and intrinsic apoptotic pathways.

1.1.3.4 Enabling replicative immortality

The uncoupled proliferation programme in cancer cells should enable the production of a mass population of cells creating a macroscopic tumour. However, research over the past few decades has shown that disruption to cell-to-cell signalling on its own does not guarantee massive tumour growth.[5] The intrinsic cell autonomous programme that limits cell multiplication must also be disrupted for a clone of cells to expand to a macroscopic sized tumour.[5] Hayflick has demonstrated that cells in culture have a finite replication potential and once the limit has been reached, senescence ensues (whereby cells stop dividing but are still metabolically active).[5,16]

Work carried out to disable the Rb and p53 proteins in human fibroblast cells, have managed to disable senescence and achieve continued multiplication, adding new generations of cells until they enter a second state called crisis.[5] This is characterised by massive cell death, karyotypic disorder involving end-to-end fusion of chromosomes and occasionally, development of variant cells (1 in 10^7), which has acquired immortality (the ability to multiply indefinitely without limit).[5,17] Tumour cells propagated in culture from tumours grown *in vivo*, appear as though they already possess the immortal characteristic.[5,16] It seems that at some point during tumour progression, pre-malignant cells breach their doubling limit and acquire replicative immortality.[5]

In normal cells, the ends of chromosomes, telomeres (Figure 1.8; composed of several thousand repeats of a short 6 base pair (bp) sequence element,

TTAGGG in humans) undergo shortening per each replication generation, which is counted as a loss of 50-100 bp of telomeric DNA from the ends of chromosomes, during each cell cycle round.[5] This happens when DNA polymerase is unable to completely replicate the 3' ends of chromosomal DNA during each S phase.[5] The continuous erosion of telomeres means that cells lose the ability to protect the ends of chromosomal DNA, which leads to end-to-end chromosomal fusion, karyotypic disorder and ultimately cell death.[18]

In tumours, the telomeres are protected by either upregulating the expression of the telomerase enzyme complex, which goes on to add hexanucleotide repeats to the telomere ends, or they activate a mechanism called ALT, which maintains telomeres through homologous recombination-based-interchromosomal exchanges of sequence information.[5] Both methods serve to maintain telomeres at a length beyond the threshold, allowing for unlimited replication of progeny cells.[5]

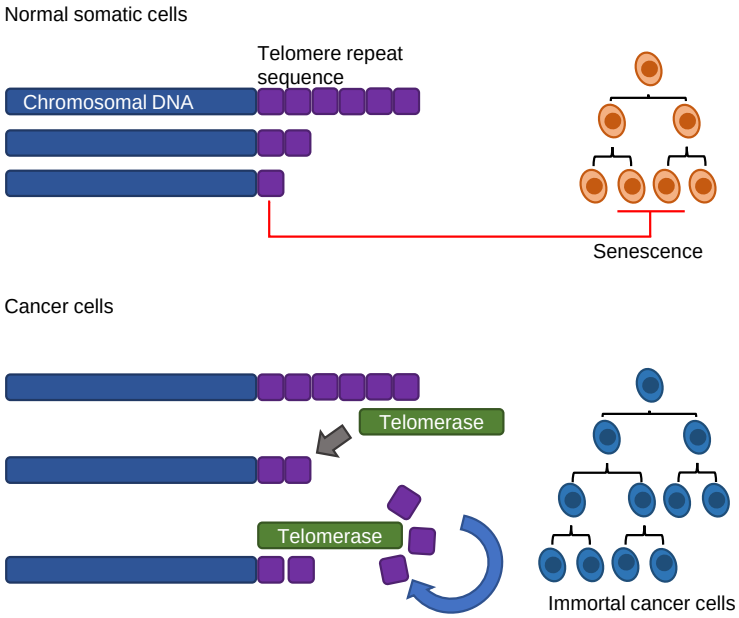

Figure 1.8. Maintenance of telomere length in normal vs cancer cells. In normal cells, telomeres undergo shortening after each replication round. In cancer cells, the telomeres are protected by enhancing the expression of the telomerase enzyme, which goes on to add hexanucleotide repeats to the telomere ends.[5]

1.1.3.5 Inducing sustained angiogenesis

It is crucial for cellular health that there is good vasculature supply of nutrients and oxygen to the tissues and efficient waste removal; as such, cells often reside within 100 μm of a capillary blood vessel.[5] Cells in early stage proliferative lesions initially lack angiogenic capabilities, which restrain their ability to expand.[5] Angiogenesis describes the process of generating new blood vessels from pre-existing vessels.[5] Contradictory positive and negative signals play a role in either encouraging or inhibiting angiogenesis.[5] Angiogenesis-initiating signals include vascular endothelial growth factor (VEGF) and acidic and basic fibroblast growth factors (FGF1/2), which all bind to tyrosine kinase receptors on endothelial cells.[5] There are more than two dozen angiogenic inducer factors and a similar number of inhibitor proteins.[5] Integrin signalling also plays a role in regulating angiogenesis.[5] Quiescent vessels express one category of integrins, and emerging capillaries express another.[5,19] Interfering with signalling from the later class of integrins can lead to the inhibition of angiogenesis.[5,19]

During tumour development, inducing and sustaining angiogenesis is acquired in a series of steps *via* an 'angiogenic switch' from vasculature dormancy (Figure 1.9).[5] It was found that angiogenesis is activated in mid-stage lesions before becoming macroscopic tumours.[5] Neovascularisation is a pre-condition to macroscopic tumour formation.[5] Tumours seem to activate the angiogenic switch by altering the levels of inducers and inhibitors of angiogenesis.[5,20] A common strategy involves altering gene transcription. It is evident that there is increased expression of VEGF and FGF1/2 in many tumours compared to original normal tissues; and in some tumours the expression of endogenous inhibitors are downregulated, such as thrombospondin-1 or β-interferon.[5] It has also been shown that loss of p53 can lead to a drop in thrombospondin-1 levels,

which releases endothelial cells from its inhibitory effects.[5] Proteases also control the availability of angiogenic inducers and inhibitors, by for example releasing them from the ECM.[5]

The *VEGF* gene is also under transcriptional control, e.g. Ras oncogene activation can lead to upregulation in the expression of VEGF.[5] *VEGF* gene is also transcriptionally activated under hypoxia. When hypoxia-inducible factor 1-alpha (HIF-1α) is not degraded, it binds to hypoxia-inducible factor 1-beta (HIF-1β) and together they comprise the HIF transcription factor.[5] Genes under control of this transcription factor include VEGF, c-MET, etc.[5] Tumour cells > 100 μm away from blood vessels become hypoxic, therefore HIF is activated. HIF-1α is degraded in the presence of oxygen – generally. However, in Von Hippel-Lindau (VHL) disease HIF-1α is not degraded and is constitutively active. VHL drives certain cancers including renal (kidney) carcinoma – characterised by high density blood vessels, hig angiogenicity and very metastatic (see section 1.1.3.6).

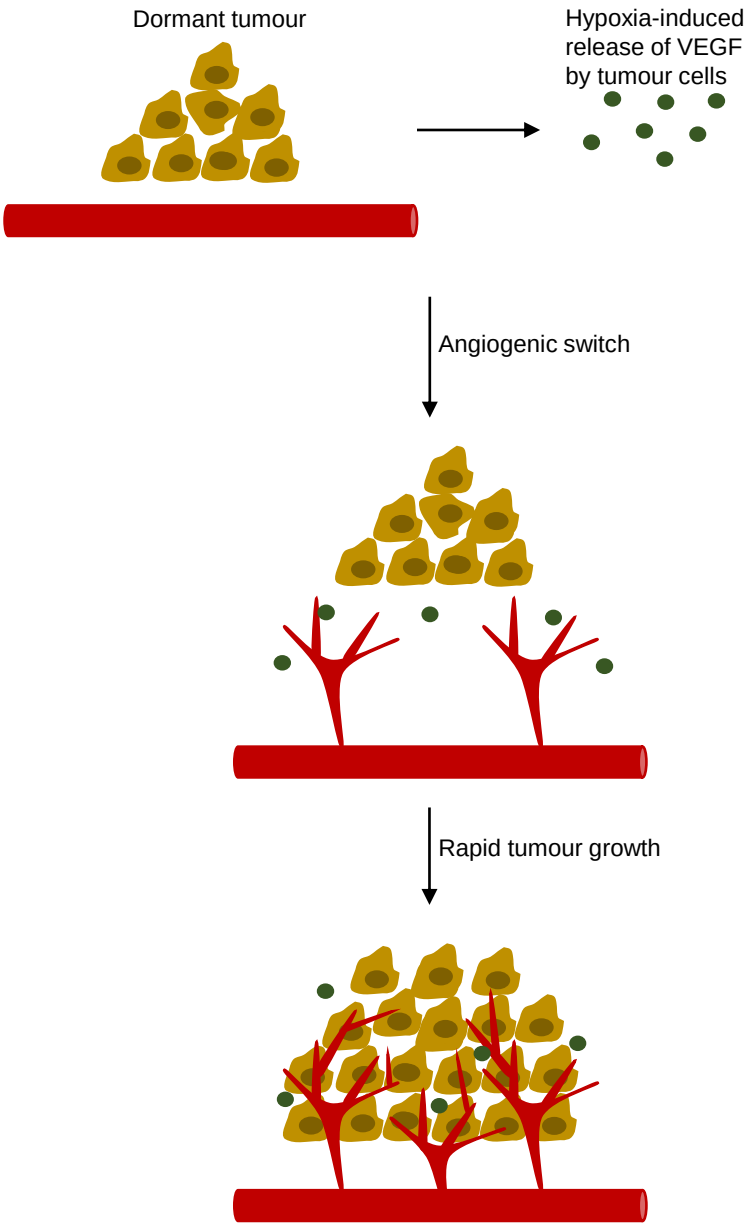

Figure 1.9. Tumour promoting sustained angiogenesis. Tumour induced angiogenesis is promoted through the expression of vascular endothelial growth factor (VEGF) and subsequent tumour mass expansion.

1.1.3.6 Activating invasion and metastasis

During the development of most human cancers, the primary tumour eventually generates cells that leave and invade nearby tissues (Figure 1.10).[5] Also, they can migrate to further locations in the body, colonise and generate new tumours, called metastases.[5] Metastastic cells spread through the body *via* cardiovascular and lymphatic systems (therefore, sustained angiogenesis is very important for metastasis *via* circulatory system). Also, invasion into lymph nodes is often a pre-requisite to lymphatic spread of e.g. breast cancer. Cancer cells escaping the primary tumour to colonise new areas, find themselves initially in terrains with plenty of nutrients and space.[5] Successful invasion and metastasis requires the acquisition of all of the five hallmarks of cancer (listed in section 1.1.3).[5]

Both invasion and metastasis utilise similar mechanistic strategies. They require physical attachment of cells to their environment and activation of extracellular proteases.[5] Proteins involved in attaching cells to their environment are altered to facilitate the activation of cellular detachment from the primary tumour.[5] These include cell-to-cell adhesion molecules (CAM), which comprise of members of the immunoglobulin and calcium-dependent cadherin families and integrins, which link cells to certain groups on the ECM.[5] These adherence interactions often relay regulatory signalling to cells.[21] Frequently, the alteration to the cancer cell-to-environment interactions involves E-cadherin, which is a homotypic cell-to-cell interaction molecule expressed widely in epithelial cells.[22] Attachment between adjacent cells by E-cadherin bridges, leads to the transmission of anti-growth and other signals through cytoplasmic contacts with β-catenin, to various intracellular signalling circuits.[22]

The activities of E-cadherin and other CAMs are lost in many epithelial cancers through mechanisms like gene mutations, transcriptional repression, or proteolysis of the extracellular domains of the cadherin protein.[22] Even changes in integrins are seen in invasive/metastatic cells.[5] To successfully colonise new sites, migrating cancer cells are required to adapt to new environments by shifting the spectrum of their displayed integrin α or β subunits.[5] Therefore, cancer cells can invade by shifting their expression of integrins from those that favour the ECM to integrins that preferentially bind to degraded components of the stroma - generated by extracellular proteases (whose genes are upregulated whilst expression of protease inhibitor genes are downregulated).[5] Cancer metastases can account for ~ 90% of cancer deaths.[5]

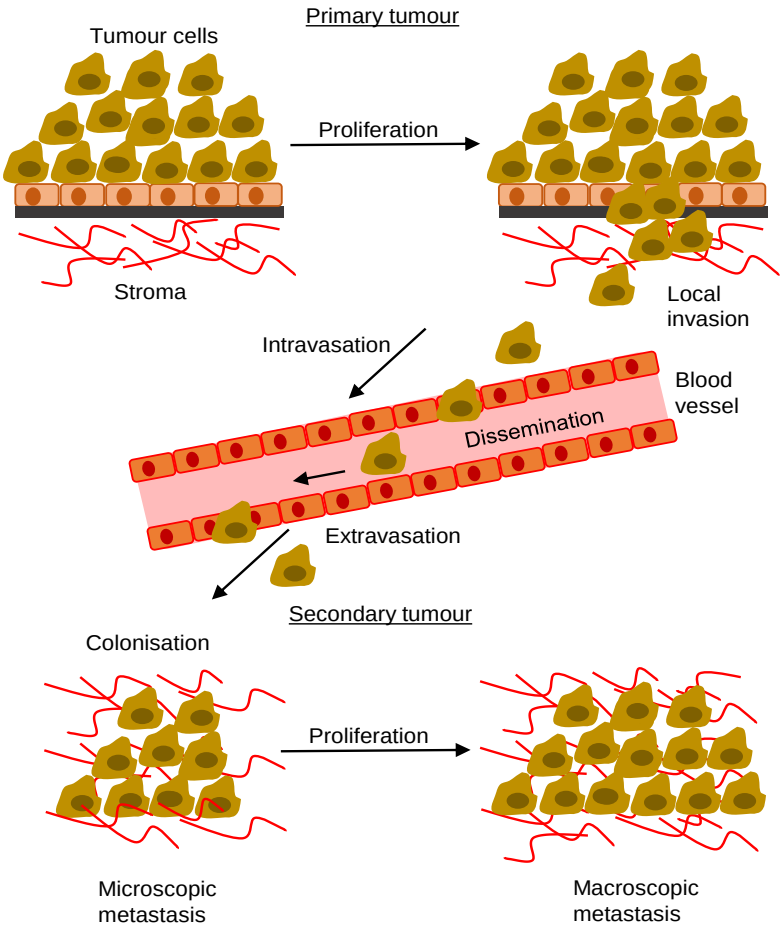

Figure 1.10. Invasion and metastasis of cancer cells.

1.1.3.7 Enabling hallmarks of cancer

The above listed six hallmarks of cancer describe acquired functionalities that drive cancer cells to thrive and spread. These acquisitions are made possible by two enabling characteristics:

1) Genome instability and mutation

The generation of certain gene mutations can impart a selective advantage for cancer cells to thrive, expand and dominate their microenvironment.[6] Usually defects in the DNA are rapidly detected and repaired; thus, the rate of spontaneous mutations during replication are kept low.[6] To orchestrate tumorigenesis, cancer cells can increase the rate of mutations to acquire mutant genes, which make cells more sensitive to mutagenic agents through the loss of genomic maintenance machinery.[6,23,24] There are various components of the genomic maintenance family, which are classed as the caretakers of the genome, that can become defective.[6,23,24] These include those that detect DNA damage, activate DNA repair pathways, directly repair DNA damage and deactivate or intercept mutagenic agents before they have the chance to damage DNA.[6,23,24] These 'caretaker' genes are much like the tumour suppressor genes regarding the ease in which deactivating mutations and epigenetic silencing can deactivate these genes and lose their function during tumorigenesis.[6]

2) Tumour-promoting inflammation

Past studies on some tumours have shown that they are often populated with infiltrative innate and adaptive immune cells.[6] It was thought that these cells may have been recruited to eradicate the cancerous cells.[6] Later, it was discovered that recruiting the immune system may also aid in the acquisition of certain hallmarks for tumorigenesis (Figure 1.11).[6] The inflammatory response may aid in the acquisition of multiple hallmarks by supplying certain molecules

to the tumour microenvironment, which includes GF that sustain proliferation, survival molecules that limit cell death, ECM-altering enzymes that aid invasion and metastasis, etc.[6,25,26] Also, inflammatory cells can release reactive oxygen species (ROS) that are mutagenic towards nearby cancer cells; shifting them towards advanced stage malignancy.[6,25,26]

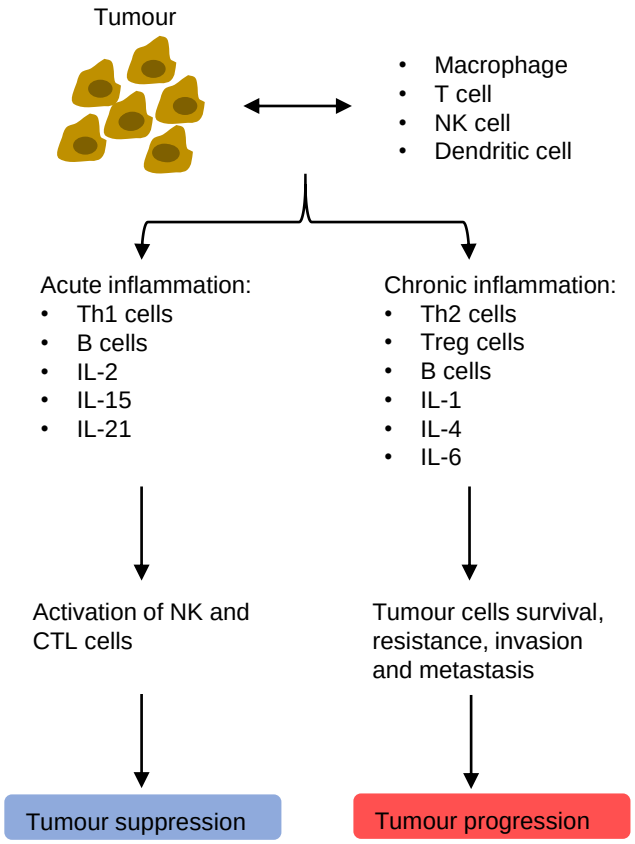

Figure 1.11. Tumour promoting inflammation. Tumour-associated inflammation leads to the release of factors promoting either tumour progression or suppression.

1.1.3.8 Emerging hallmarks of cancer

In addition to the two enabling hallmarks of cancer to materialise in the last decade, two emerging hallmarks of cancer were also recorded:

1) Reprogramming/deregulation of cellular energy metabolism

Unrestrained cell proliferation not only involves a deregulated control of cell proliferation machinery, but also alteration to energy metabolism - to aid in cellular growth and tumour expansion.[6] Normal cells, under aerobic conditions, usually favour the conversion of glucose to pyruvate, *via* the glycolysis pathway, in the cytoplasm and then to carbon dioxide (CO_2), in the mitochondria (Figure 1.12).[6] Whereas under anaerobic conditions, the glycolysis pathway is preferred, with very little amounts of pyruvate going to the mitochondria.[6]

For cancer cell metabolism, it was observed that even in the presence of oxygen, cancer cells can reprogram glucose energy metabolism solely to glycolysis, avoiding the need for mitochondrial oxidative phosphorylation to take place (Figure 1.12).[6] This kind of reprogramming requires the cancer cells to compensate for the reduced ATP production efficiency by upregulating the expression of glucose transporters, particularly glucose transporter 1 (GLUT1), to enhance the uptake of glucose into the cytoplasm.[6,27] Indeed, many types of tumours show enhanced consumption of glucose.[6] Certain activated oncogenes such as Ras and Myc, and mutations in tumour suppressor proteins such as p53 have been shown to contribute to this glycolytic fuelling.[6,27]

Also, the reliance on glycolysis can be further reinforced under hypoxia, where the response to hypoxic conditions is to upregulate glucose transporters and enzymes of the glycolytic pathway.[6,27] Independently, the Ras oncogene and hypoxia can enhance the levels of the transcription factors, HIF-1α and HIF-2α,

to upregulate glycolysis.[6] Cancer cells may prefer to rely on the glycolytic pathway for energy generation despite its lower efficiency in ATP production because the various glycolytic intermediates can lead to useful biosynthetic pathways fuelling synthesis of amino acids and nucleosides.[6,28] These are important building blocks for generating new cells.

Remarkably, some tumours have been shown to have two subpopulations of different energy metabolism profiles.[6] One subpopulation, is often composed of hypoxic cancer cells, which prefer the glucose-dependent (as fuel) metabolic pathway towards lactate production (as waste), whilst the other subpopulation often comprises of well oxygenated cells (normoxia), preferentially importing lactate (as fuel), from lactate producing cells, as their main energy source and utilising the Krebs cycle to do so.[6] These subpopulations work symbiotically to survive and grow.[6] It is worth noting that the oxygenation status of cancer cells within tumours ranges both regionally and temporally due to the chaotic organisation of the tumour vasculature.[29]

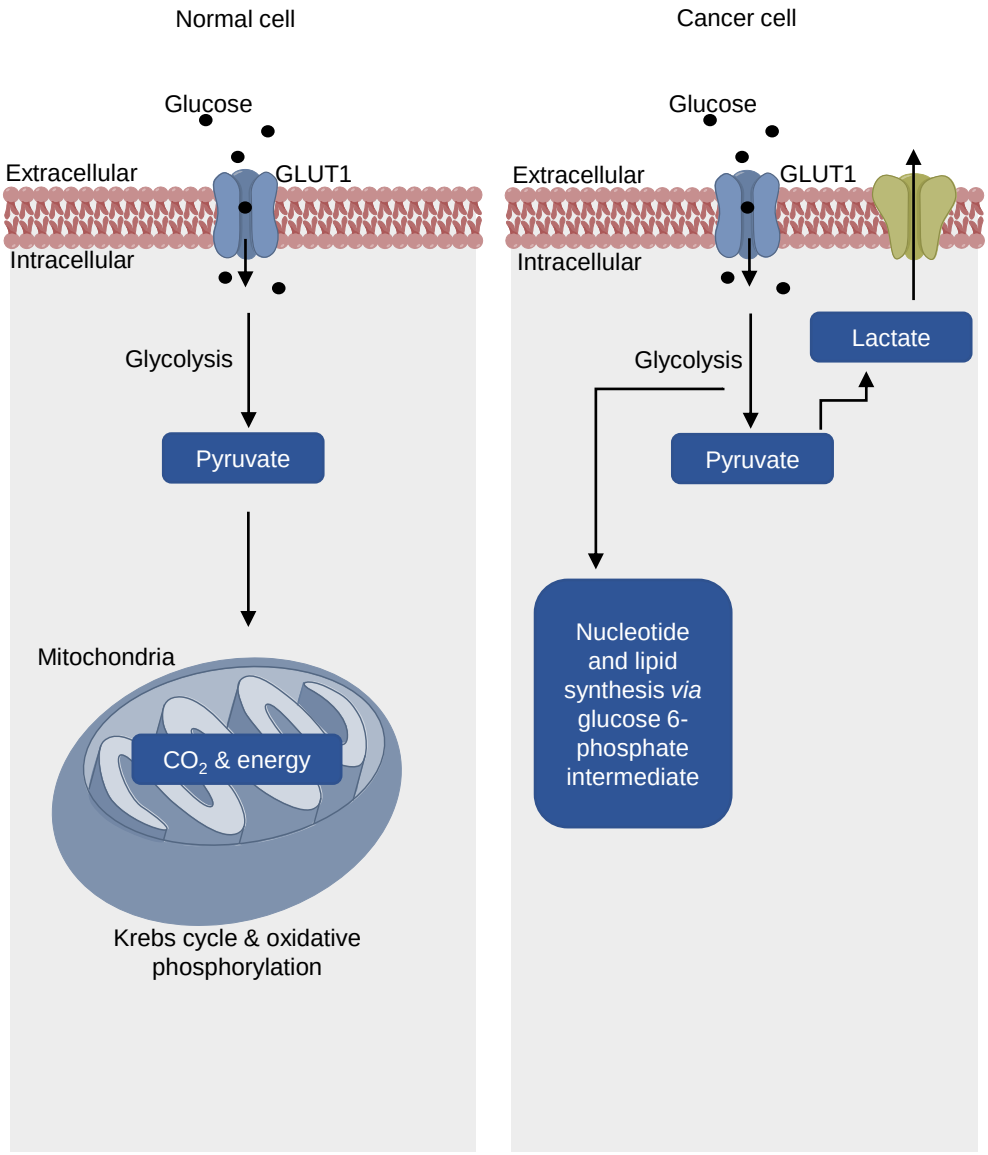

Figure 1.12. Normal vs cancer cell energy metabolism. Normal cells favour the conversion of glucose to pyruvate, *via* the glycolysis pathway, in the cytoplasm and then generate CO_2 and ATP in the mitochondria. Cancer cells, on the other hand, reprogram energy metabolism to favour solely glycolysis for continuous proliferation; upregulating the expression of GLUT1, to enhance the uptake of glucose into the cytoplasm.

2) Evading immune destruction

It was long understood that cells and tissues are maintained by the immune system, which is responsible for detecting and removing emerging cancer cells.[6] It so appears that solid tumours have managed to avoid/limit detection by the immune system in order to avoid eradication.[6] Studies have shown that tumours were more likely to develop in immunodeficient mice over

immunocompetent mice.[6,30] Deficiencies in $CD8^+$ cytotoxic T lymphocytes (CTL), $CD4^+$ Th_1 helper T cells or natural killer (NK) cells can lead to increased tumour incidences, and mice with combined deficiencies in NK and T cells, were more prone to cancer development.[6,30]

In immunocompetent hosts, immunogenic cancer cell clones are routinely removed - a process referred to as 'immunoediting' (Figure 1.13), leaving only weakly immunogenic cells to grow and form tumours.[6,30] These weakly immunogenic cells can then colonise immunodeficient and immunocompetent hosts.[6,30] For some cancer types, the presence of immune killer cells signifies a better prognosis then those with a weak anti-tumoral immune response.[6,31]

However, highly immunogenic cancer cells may develop tactics to evade immune attack by disabling components of the immune system.[6] For instance, they may paralyse infiltrating CTLs and NK cells by releasing transforming growth factor (TGF-β) or other immunosuppressive factors.[32,33] Cancer cells may also attempt to recruit inflammatory cells that are immunosuppressive agents, such as regulatory T cells (Treg) and myeloid-derived suppressor cells (MDSC), which both supress the activities of cytotoxic lymphocytes.[34,35]

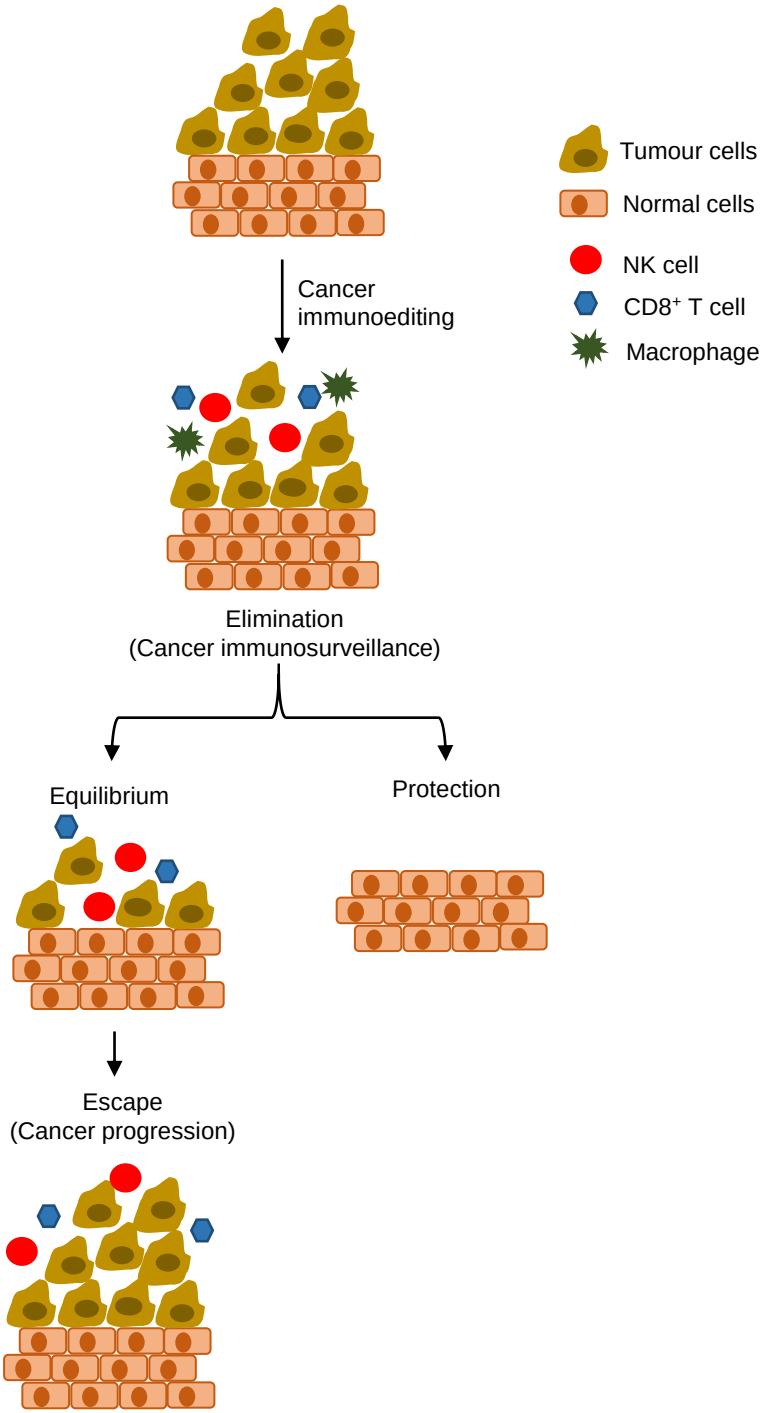

Figure 1.13. Cancer cell evasion of immune destruction by going through the process of cancer immunoediting. This process involves three steps: elimination, equilibrium and escape, to ultimately achieve continued growth.

1.2 CNS-related tumours

1.2.1 What are CNS tumours?

CNS tumours are abnormal growths that occur within any compartment of the CNS, with the majority (90%) occurring within the brain; they can affect both children and adults.[36] Once diagnosed, the burden of CNS tumours is compounded by the fact that patients require highly specialised multimodal treatment, such as access to neurosurgical care, radiation and chemotherapy, which is not widely available in many parts of the world.[36] Brain tumours are either non-cancerous (benign) or cancerous (malignant).[37] Benign brain tumours can still cause many problems in the brain, because the slow growing mass of cells expands and exerts pressure on nearby brain tissues in an area which cannot be expanded due to the skull. Brain tumours which originate in the brain are primary brain tumours, whilst secondary brain tumours are those that arise from elsewhere in the body and then metastasise to the brain.[37] In adults, secondary brain tumours (commonly from patients with breast, colon, lung or kidney cancers as well as melanomas) are more common than primary brain tumours.[38]

1.2.2 Classification of CNS tumours and grade

According to the National Brain Tumour Society, there are over 120 types of CNS tumours.[39] The 2016 World Health Organisation (WHO) classification of CNS tumours includes both phenotypic and genotypic characterisation of tumorigenesis.[40] The combined approach of classifying CNS tumours based on both their phenotype and genotype allows researchers to work on achieving better targeted therapies for patients, better classification for clinical trials, improved experimental and epidemiological studies, and opportunities for greater focused studies on less defined groups. A list of the WHO classified

CNS tumours was published in 2016, which include a variety of glial, neuronal, embryonal and many more CNS-related tumours.[40]

CNS tumours are mostly graded according to four morphological criteria: cytological atypia, mitotic activity, microvascular proliferation (endothelial cell proliferation), and necrosis (St. Anne–Mayo grading system).[41]

As such, the WHO has classified CNS tumours according to four grades, and a list of a variety of CNS tumours with grades was also published in 2016:[40]

- Grade I: Tumours do not meet any of the criteria. These tumours are slow growing, non-malignant, and associated with long-term survival.
- Grade II: Tumours meet only one criterion, i.e., only cytological atypia. These tumours are slow growing but can recur to become a higher-grade tumour. They can be malignant or non-malignant.
- Grade III: Tumours meet two criteria, i.e., anaplasia and mitotic activity. These tumours are malignant and can recur as higher-grade tumours.
- Grade IV: Tumours meet three or four of the criteria, i.e., they show anaplasia, mitotic activity with microvascular proliferation, and/or necrosis. These tumours reproduce rapidly and are very aggressive malignant tumours.

With the growing variety of CNS (mostly brain) tumours and its aggressiveness, there is a mounting need to better understand the potential risk factors which lead to the formation of these tumours.

1.2.3 Causes of brain tumours

However, the causes of brain tumours are not fully understood and very few risk factors are well proven.[42] Researchers have identified some changes that occur within brain cells that lead to brain tumour formation. These include changes in genes which govern cellular growth, division, and DNA repair. Some inherited gene changes that cause some rare, inherited syndromes like neurofibromatosis type 1 and 2, tuberous sclerosis, Li-Fraumeni syndrome, VHL syndrome, Turner syndrome, Turcot syndrome and Gorlin syndrome can increase the risk of developing some brain tumours.[42] For example, Li-Fraumeni syndrome is caused by changes in the *TP53* tumour suppressor gene, which increases the risk of developing brain tumours, like gliomas, as well as multiple other cancers.

Alternatively, there are people with no inherited syndromes that still develop brain tumours through gene changes acquired during a person's lifetime.[42] Possible causes still not fully understood or proven are, exposure to chemicals in tobacco smoke or from work environments. However, the brain is relatively protected from most cancer-causing chemicals that we may breathe in or ingest, so these factors might not play a major role in these cancers. Other potential causes include radiation. Some types of brain tumours are more common in people who have had radiotherapy, CT scans and x-rays of the head or radiation from a nuclear fallout. Additionally, the risk of getting brain tumours increases with age and races, as brain tumours are more common amongst Caucasians. Being overweight and obese also increases the risk of developing some types of cancers, including a brain tumour type called meningioma. Exposure to infections, viruses and allergens or a history of cancer, head injury or seizures are other potential causes of brain tumours. Finally, research evaluating the role of electromagnetic fields such as energy from power lines or

from mobile phone use has shown no link to an increased risk of developing brain tumours in adults, however, there is conflicting information regarding risk to children; the WHO recommends limiting mobile phone use and promotes the use of hands-free headset for both adults and children.

1.2.4 Epidemiology

In the UK, it is estimated that in 2017, according to Cancer Research UK, there were 11886 new cases of CNS-related cancers and 5342 CNS-related cancer deaths.[43] Of these, females were slightly more likely to be diagnosed with a CNS tumour, with deaths from a CNS tumour slightly higher amongst males (Figure 1.14a-b). Additionally, the 50+ age group fare worse with respect to cancer incidence and mortality (number of mortalities for 50+ years were 85.7%; Figure 1.14c-d).

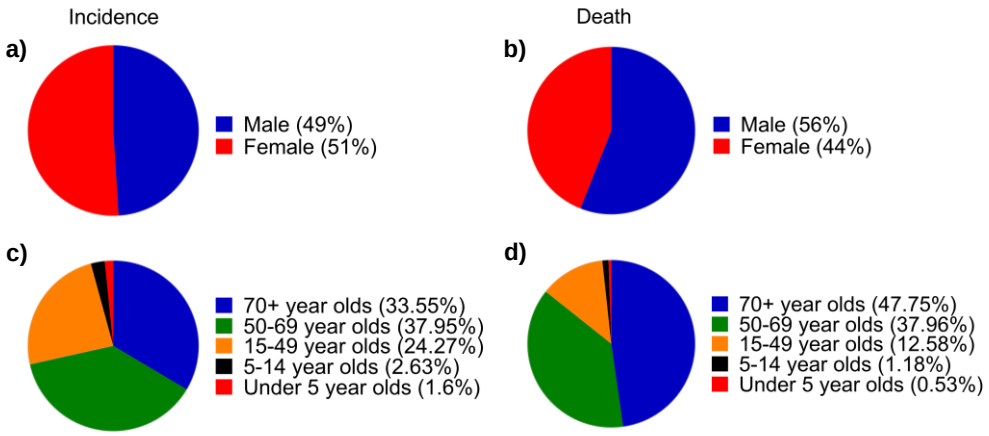

Figure 1.14. Pie Charts representing the distribution of CNS-related cancer cases (total: 11886 cases) and deaths (total: 5342 deaths) in the UK, in 2017. (a) Distribution of CNS-related cancer incidences by sex (with ages combined). (b) Distribution of CNS-related cancer deaths by sex (with ages combined). (c) Distribution of CNS-related cancer incidences by age (with sexes combined). (d) Distribution of CNS-related cancer deaths by age (with sexes combined). Source: Cancer Research UK.[43]

It has been previously shown that the epidemiology of histologically varied CNS tumours differ amongst different age groups. One published study has mapped out the distribution of primary CNS tumours (benign and malignant origins) according to their main histological group, from 54336 registrants in England, between the period of 1995-2003.[44] The distribution is presented seperately for age groups 0-14 years, 15-24 years and 25-84 years (Figure 1.15). There were 28069 male and 26267 female registered cases during that period of time. From analysis, it appears that tumours of neuroepithelial tissue origin (which include glimoas and medulloblastomas) decrease in incidence upon increasing age, whilst meningeal and unspecified tumour origins increase in incidence with increasing age.

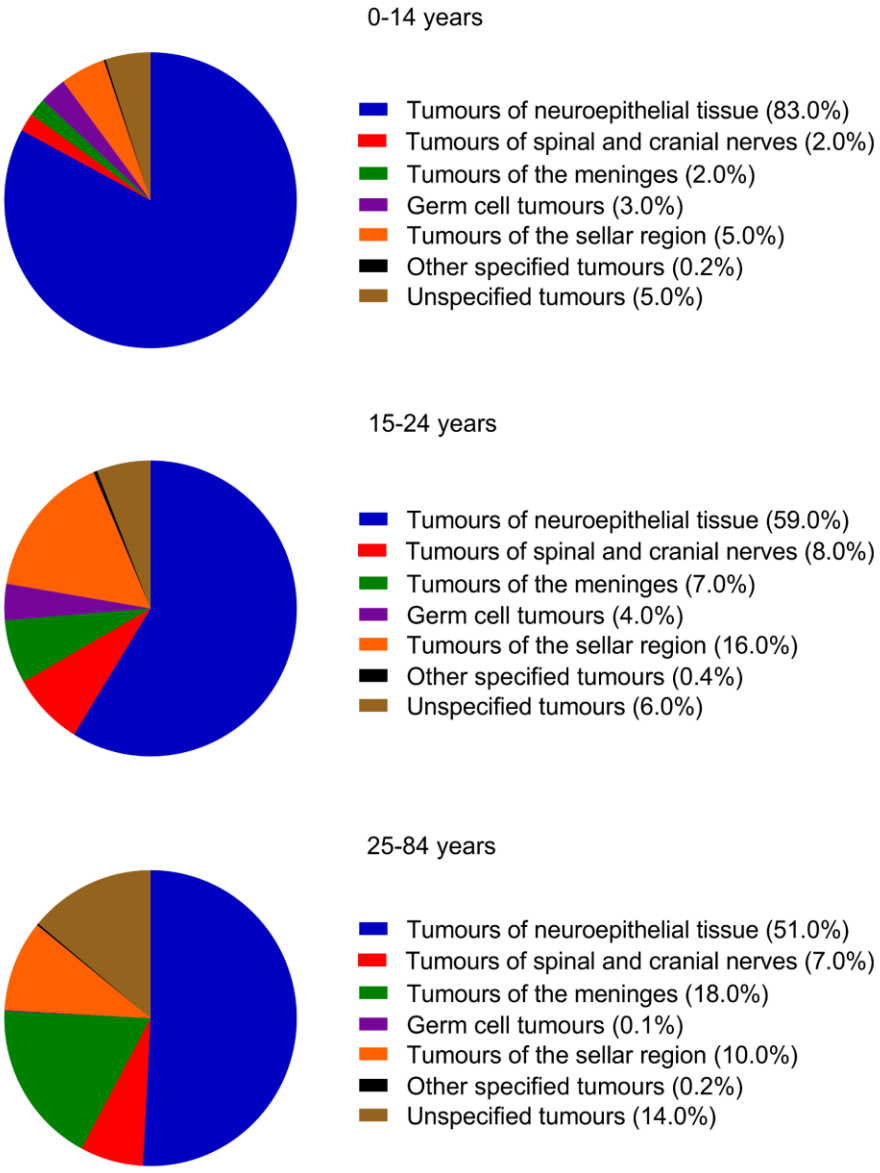

Figure 1.15. Pie Charts representing the distribution of primary CNS (benign and malignant) tumours by main histology groups, in England, between the period of 1995–2003. Total registered cases: 54336 (28069 male and 26267 female cases.[44]

1.3 Glioblastoma multiforme (GBM)

1.3.1 What is GBM?

Glioblastoma multiforme (GBM) is the most aggressive and frequently occurring, type of malignant primary astrocytoma (a type of glioma) in humans.[45] It has been designated by WHO as grade IV astrocytoma - the highest-grade classification for CNS tumours.[45] GBM can arise either as a primary tumour or secondary tumour, the latter occurring as a malignant transformation from a pre-existing lower grade astrocytoma or oligodendroglioma and/or with mutation in the isocitrate dehydrogenase (IDH) genes.[46]

These tumours are also fast growing and highly heterogeneous, with a complex makeup. As the term indicates, glioblastoma is multiforme.[47,48] It is multiforme grossly, microscopically, and genetically.[48] GBM tumours develop from star-shaped glial cells such as astrocytes and/or oligodendrocytes.[49] Astrocytes represent one of the most abundant faction of glial cells in the human adult brain. Some of the typical roles of astrocytes include blood brain barrier (BBB) maintenance (Figure 1.16a), maintenance of ion and water homeostasis etc., whilst oligodendrocytes function to myelinate CNS axons (Figure 1.16b).[50] These cells are important support systems for the maintenance of brain health.

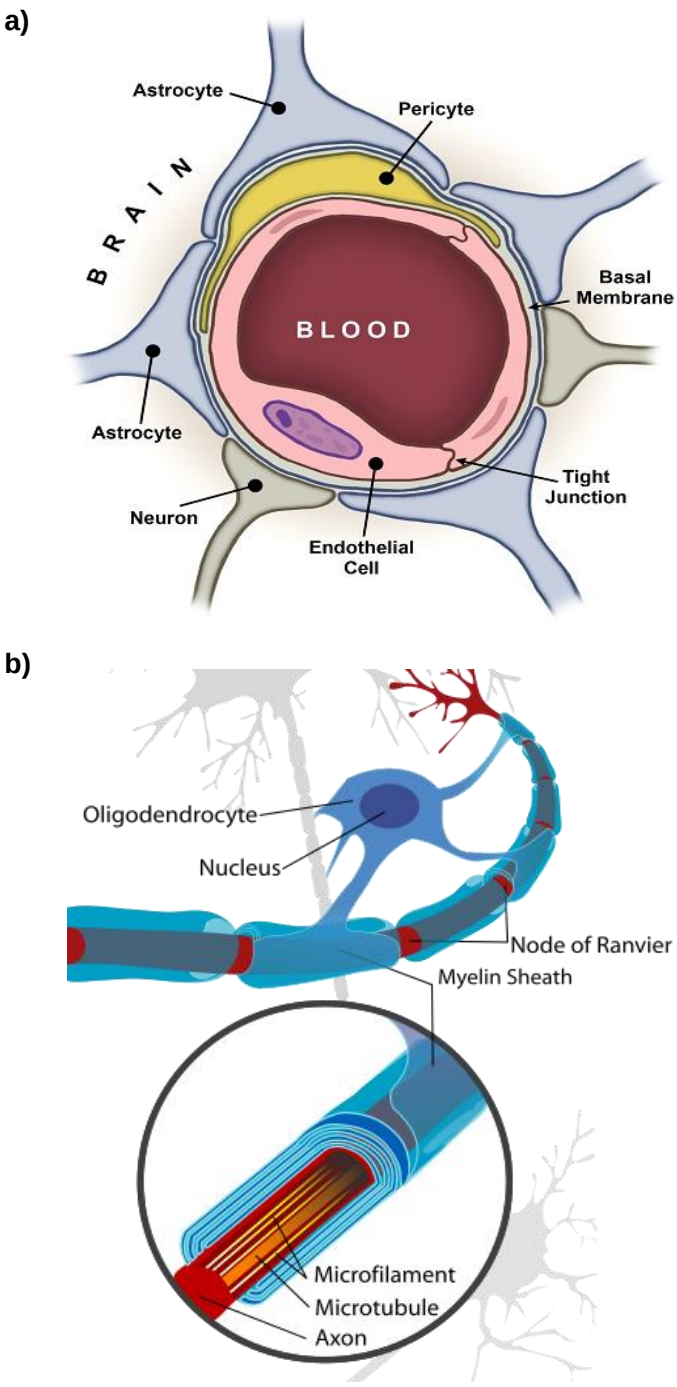

Figure 1.16. Brain cells. (a) Illustrates the BBB, with astrocytes playing a role in BBB maintenance.[51] (b) Illustrates an oligodendrocyte, whose role is to myelinate CNS axons.[52]

1.3.2 The site of GBM growth

Commonly, GBM is found in the cerebral hemisphere of the brain, with 95% of GBM cases found in the supratentorial region (frontal, temporal, parietal and occipital lobes).[47] They can also (very rarely) be found in the cerebellum, brain stem and spinal cord.[47] Figure 1.17 represents a diagram of the different regions of the brain and the important role they play in normal bodily function.

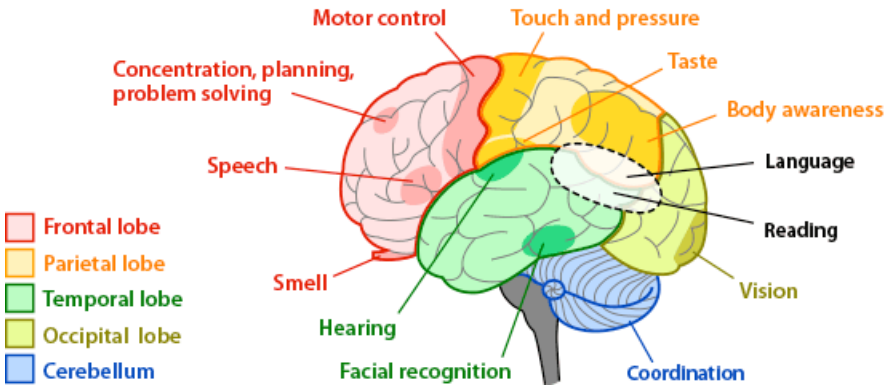

Figure 1.17. Different regions of the brain and their roles in the body.[53]

1.3.3 Symptoms of GBM

The brain represents the main coordination and command centre of the body. A tumour arising in the brain is catastrophic in the sense that as it expands (leading to brain swelling) there is a limit before it begins to impact and alter normal brain function. This is because the brain is encased by a skull which cannot expand. The severity of the tumour and its location dictates the symptoms that the patients present with.[54] These may include any of the following:

- Persistent headaches.
- Seizures.
- Loss of movement, sensation, and language or speech difficulty.
- Loss of memory.
- Loss of appetite.

- Double or blurred vision.
- Vomiting.
- Changes in mood and personality.
- Changes in the ability to learn and think.

1.3.4 Epidemiology

GBM is the most frequently occurring type of primary astrocytoma in adults. It accounts for ~ 40-60% of all primary brain tumours in adults; whereas in children, GBM accounts for only ~ 3-15% of all primary brain tumour cases.[47,55] Primary or *de novo* GBM accounts for ~ 90% of cases (mostly with a corresponding IDH–wildtype biomarker), with the over-54 age group predominating these cases.[40] The remaining 10% are IDH–mutant cases, which usually arise in younger patients.[40] The mean age of primary GBM patients is about 62 years, whilst the mean age of secondary GBM is about 45 years.[56] Primary GBM occurs more frequently in males than in females, whilst the opposite is the case for secondary GBM.[56] Histologically, primary, and secondary GBM's are mostly indistinguishable but they do differ in their genetic and epigenetic profiles.[57]

A study assessing the distribution of GBM cases in England from 2007-2011 counted 10743 patients registered with GBM (6451 males and 4292 females), in this time frame.[58] It was seen that the incidence of GBM occurring in the frontal lobe was the most common (24.9%), followed by the temporal lobe (21.8%), parietal lobe (16.7%), occipital lobe (4.8%), cerebellum (0.5%), brain stem (0.4%) and non-specified/other (30.9%). Figure 1.18 demonstrates the distribution of female and male GBM cases across different ages, ranging from 0-85+ years. Males dominate GBM cases in England, with cases increasing with age and peaking between 60 and 70 years of age.

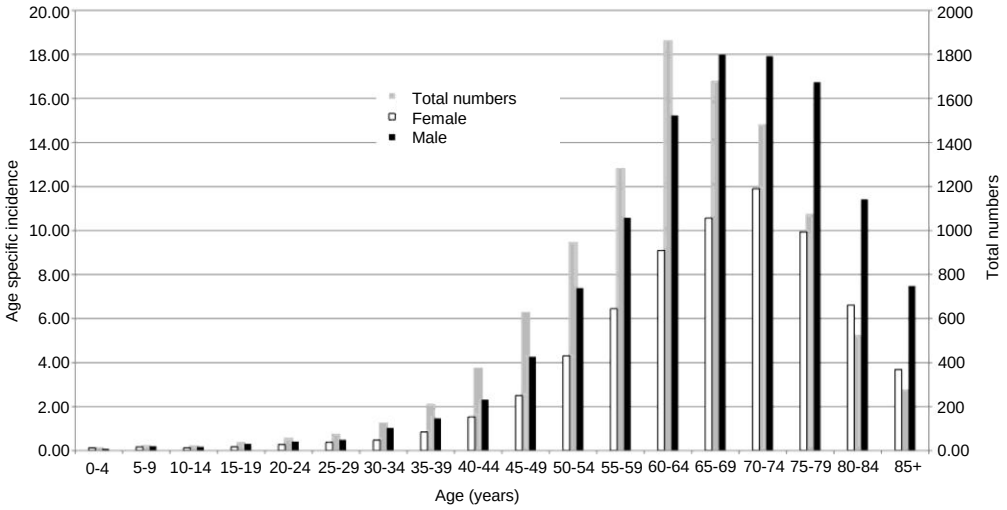

Figure 1.18. Distribution of GBM cases in England between 2007-2011. Average total numbers of patients presenting with GBM per year between 2007 and 2011 by age (right axis). Age specific incidence of patients by sex with GBM per 100,000 people (left axis).[58]

1.3.5 Histological features of GBM

Histologically, GBM resembles an anaplastic astrocytoma i.e. these tumours show pleomorphic cell populations (ranging from small, poorly differentiated cells to large, multinucleate cells; see Figure 1.19).[59] Necrotic foci are a characteristic feature of GBM.[59] Depending on the size of the necrotic area and the location, there are histologically two types of necrosis encountered. The first presents large areas of necrosis within the centre of the tumour due to insufficient blood supply (in all primary GBM). The second presents small, irregularly shaped necrotic foci surrounded by pseudopalisading areas (which are tumour cells around necrotic zones.[59] These are created by radially oriented glial cells and is a process observed in both primary and secondary GBM. Pseudopalisade areas range from 30 to 1500 µm (greatest internal width) and from 50 to 3500 µm (greatest internal length). These areas also present multiple apoptotic cells.[59]

In addition, GBM also presents the following histological features: nuclear atypia, microvascular proliferation with atypical blood vessels and increased mitotic activity.[59]

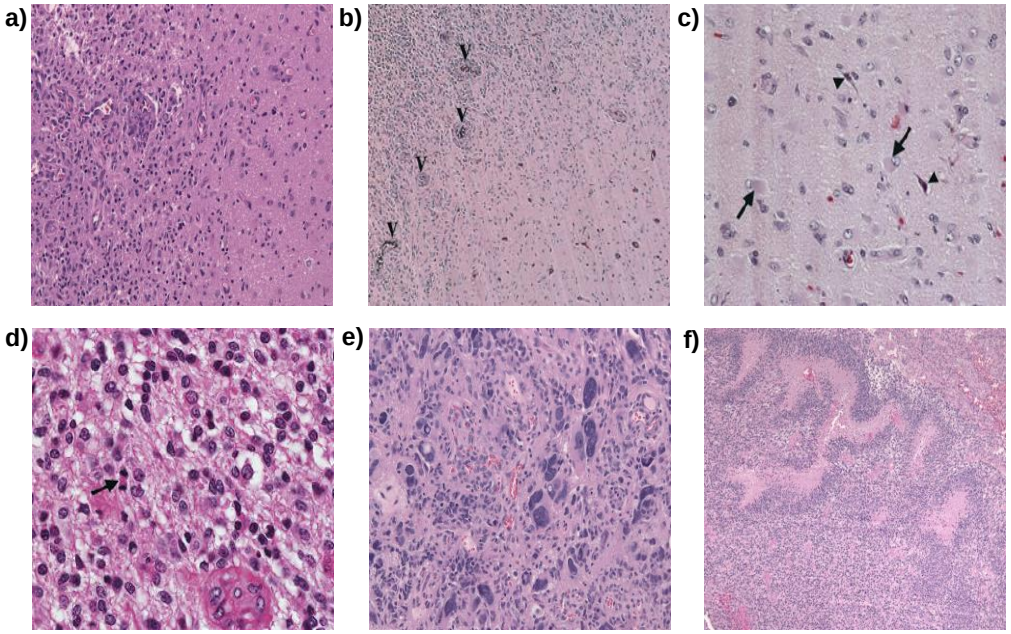

Figure 1.19. The histological features of GBM. (a) Tumour-normal brain interface in a GBM biopsy specimen also showcasing the diffuse infiltration of the tumour. (b) Another representation of the left side of the image representing the tumour area and the right side of the non-tumour area, with 'v' indicating spots of microvascular proliferation. (c) Arrow heads indicate cells with atypical nuclei and full arrows point out the reactive astrocytes. (d) Arrow indicates mitotic cells. (e) Represents extreme cell anaplasia in a GBM biopsy specimen. (f) GBM showing areas of pseudopalisading necrosis.[60,61]

1.3.6 Hallmarks and biomarkers of GBM

There are two types of GBM, namely primary and secondary GBM. The types of GBM can be further broken down by their molecular subtypes.[62] According to Verhaak's classification they are called classical, mesenchymal, proneural and neural GBM subtypes.[63] Primary GBM can be further broken down into these four molecular subtypes, whilst secondary GBM is usually classified with a proneural molecular subtype. In addition, GBM can be classified based on Phillips' classification, which include proliferative subtypes (a subtype of GBM with enriched markers of neuronal stem cells),[64] and the Jiao classification, which focuses on the variation in IDH mutations.[65] Figure 1.20 demonstrates the biomarkers that are associated with these molecular subtype classifications. It is crucial that molecular biomarkers associated with GBM are identified, so that better diagnoses and treatment is directed towards fighting GBM.

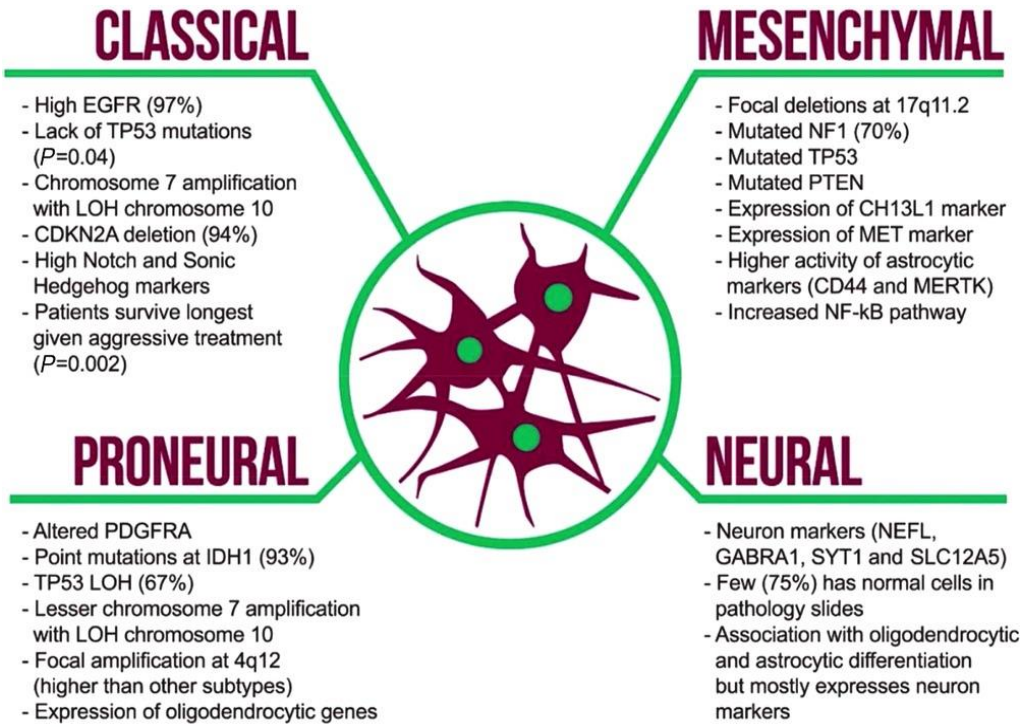

Figure 1.20. Verhaak classification system of GBM. The molecular biomarkers that are associated with the different molecular subtypes of GBM.[62]

GBM tumours are characterised of variety of complex molecular and biochemical cellular alterations. Some of the common biomarkers seen in GBM tumours, which allow for GBM characterisation, includes the following:[46,62]

1) The most significant alteration to the receptor tyrosine kinase/rat sarcoma/phosphoinositide 3-kinase (RTK/RAS/PI3K) pathway is related to EGFR.[46,62] The amplification of EGFR and the genetic rearrangement of EGFR (EGFRvIII) are common hallmarks of GBM (40–50%), especially in the classical subtype of primary GBM. EGFR codes for a tyrosine kinase receptor that is specific to certain GF. The mutation of EGFR due to histone modifications on its gene at chromosome 7p12, leads to the development of EGFRvIII, which truncates exons 2 and 7, leading to the loss of the extracellular ligand binding site. In long-term survivors of GBM, aberrations in EGFR were less frequent. Cancer proliferation is mainly controlled by key GFs and the abundance of their receptors. EGFR is an important receptor for cancers, which can activate pathways essential for GBM tumour cells to thrive, such as the RTK/RAS/PI3K pathway. The activation of this pathway (by amplified EGFR expression) leads to uncontrolled proliferation. Patients with the EGFRvIII mutation show significantly lower survival compared to patients without the mutation.

2) The p53 pathway acts on intracellular signals.[46,62] The *TP53* gene encodes for the well-known tumour suppressor protein called p53. p53 serves various roles in suppressing tumorigenesis. Mutated p53 is found in 27%–34% of GBM cases. Point mutations in the *TP53* gene have been detected at a much higher rate in secondary GBM (90%) compared to primary GBM (30%), and sometimes the mutation is absent in primary GBM. Around 10 isoforms of p53 have been discovered, resulting in different expression of p53. However, muta-

tions in *TP53* are not tumour-type specific but rather shared across a variety of tumour. Proneural GBM has a high incidence of *TP53* mutations, whilst the classical subtype entirely lacks mutations. This may suggest that mutations that promote GBM may occur early on in the process of glioma development and accumulate as the disease progresses.

3) Mutations in the protein, Rb, are more common than mutations in the *Rb* gene.[46,62] Whilst *Rb* is mutated in most cancers, only 6–11% of GBM cases show mutated *Rb*. Inactivation of the protein, Rb, can happen through cdk 4 and 6, which can phosphorylate Rb, allowing the cells to pass the G1-phase checkpoint in the cell cycle or by cyclin-dependent kinase inhibitor 2A (*CDKN2A*) gene mutation through deletion. The proteins expressed by the gene *CDKN2A* work by inhibiting cdk 4 and 6. Loss of *CDKN2A* function by mutation, indirectly inhibits the function of Rb protein.

4) Like EGFR, platelet-derived growth factor receptor (PDGFR) is a receptor stimulated by specific GF.[46,62] If overexpressed, this receptor leads to abnormal and uncontrolled cellular growth. There are different PDGFR in gliomas, including GBM, which react to different PDGFR ligands. Some of the different receptors are platelet-derived growth factor receptor-alpha (PDGFRα) and platelet-derived growth factor receptor-beta (PDGFRβ). PDGFRα serves as a prognostic biomarker for GBM, particularly for the proneural subtype. Increased PDGFRα seems to almost always coincide with the presence of IDH mutations (93%) , which is coincidentally present at a much higher rate in secondary GBM. PDGFR proteins have been shown to be expressed in low-grade diffuse astrocytoma and highly in high-grade secondary GBM tumours.

5) The enzyme *O6*-methylguanine-DNA methyltransferase (MGMT) is a determinant biomarker for successful/unsuccessful treatment of GBM.[46,62] It is specifically involved in DNA repair, by removing methyl groups deposited on the O6-position of guanine, following DNA alkylating treatment. Specifically, it is implicated in temozolomide (TMZ) chemotherapeutic resistance, which is the first-in-line drug used for the treatment of GBM.[46,62] However, if the MGMT promoter is methylated, the protein is not expressed. MGMT promoter methylation occurring in some patients has been known to provide a better survival outcome in patients receiving TMZ therapy. Epidemiologically, the MGMT promoter methylation is found more considerably in secondary GBM (75%), with a strong correlation with *TP53* mutations (92%); abundant in secondary GBM and only 36% of primary GBM cases.[46,62]

6) IDH is an enzyme encoded by the *IDH* genes on chromosome 2.[46,62] Five *IDH* genes have been defined, which code for three IDH enzymes (IDH1, IDH2 and IDH3). Their primary function is within the Krebs cycle, which is to catalyse the oxidative decarboxylation process of isocitrate to alpha-ketoglutarate and CO_2. Only *IDH1* and *IDH2* are mutated in GBM, both exerting the same mutagenic effects. In contrast to the wild-type enzymatic function, IDH mutants acquire an alternative responsibility, towards catalysing the production of 2-hydroxyglutarate (2-HG), which is an oncometabolite.[46,62] 2-HG ultimately competes with alpha-ketoglutarate in activating enzymes which support DNA demethylation, generating a hypermethylation in tumour cells and ultimately tumorigenesis.[46,62] Mutant IDH expression has been shown to coincide with methylated MGMT to give a favourable prognosis for GBM patients undergoing TMZ and radiation therapy. *IDH* mutations (in *IDH1* and *IDH2*; the difference between the two mutations is the codons where the mutations are; codon R132 for *IDH1* mutation and codon R172 for *IDH2* mutation) are commonly found in

the proneural subtype of GBM, where 85% are secondary GBM and 7% are primary GBM presenting with these mutations.[46,62] Since the mutations are prominently found in secondary GBM, there is a possibility that *IDH* mutations play a significant role in glioma development and progression. A study of 1010 individuals with diffuse gliomas have shown that 70.9% of patients possessed the *IDH1* mutation, whilst only 3.1% possessed *IDH2* mutation.[46,62]

7) Loss of heterozygosity (LOH) is commonly found in malignant cancer cells.[46,62] Mostly it affects tumour suppressor genes, leading to greater incidences of tumorigenesis. Within GBM, LOH affects many chromosomes, including chromosome 9p, 10, 17p, 19q and 22. LOH 10q (specifically LOH 10q23) is observed frequently in GBM (70% of total GBM cases), mostly in primary GBM. It is thought that LOH of chromosome 10 is a good prognostic biomarker for both primary and secondary GBM, with a more specific LOH at 10q25qter accurate enough to diagnose secondary GBM. One tumour suppressor gene heavily affected by LOH 10q is the phosphatase and tensin homolog (*PTEN*) gene, which encodes for the tumour suppressor protein, PTEN. PTEN regulates the PI3K pathway and thus controls cellular proliferation. It is deactivated in 36% of GBM cases, leading to loss of the negative feedback to PI3K, which results in proliferation and decreased apoptosis.

8) The downregulation of connexin 43 (cnx43) is another biomarker of GBM.[46,62] Cnx43 normally plays a role in tight junctions between cells. Its downregulation means that there is reduced adherence and communication between the cells, allowing tissue invasion to take place. The GBM microenvironment is populated by inflammatory cells. These cells provide an alternative way for invasion to take place. Protumoural immune cells can produce ECM degrading enzymes in

the periphery, paving the way for the cancer cells to invade. Hypoxia also causes an increase in proinflammatory proteins. It has been shown that proinflammatory proteins allow cancer stem cells (CSC) to differentiate, which may drive gliomagenesis.[46,62] The epithelial-to-mesenchymal transition (EMT) process has been observed in GBM.[46,62] For this to happen, E-cadherin is lost, causing cells to lose polarity, and enabling cell motility. Hypoxia can also aid in EMT by recruiting myeloid cells, which then upregulate TGF-β, epidermal growth factor (EGF), PDGFRα and TWIST, and ultimately these can secrete transcription factors like N-cadherin which is required for EMT.

9) The gene, telomerase reverse transcriptase (*TERT*), which results in the expression of telomerase, has been found to be mutated in 51% of GBM cases and is abundantly expressed.[46,62] In some cases, mutations were seen in the transcriptional regulator gene, alpha thalassaemia mental retardation (*ATRX*), with mutations in *TERT* or *ATRX* not expressed in tandem. The study which discovered this, has implied that mutations in either *TERT* or *ATRX* may be responsible for telomere lengthening.[46,62] *ATRX* appeared to be expressed alongside mutated *TP53* and *IDH1* genes, which is representative of secondary GBM.

Finally, it is worth noting that one of the major characteristics of GBM is its heterogeneous nature, as the term ‘multiforme’ implies.[66,67] Different patients with tumours from the same organ are well known to differ from one another, which is known as inter-tumoural heterogeneity. As discussed, GBM is divided into various sub-groups based on differences in biomarkers. However, even within the tumour, there are a variety of cell populations and this is known as intra-tumoural heterogeneity. The co-existence of different cell groups within the same tumour maybe due to fluctuations in the microenvironment or

selective pressure imparted by chemotherapy and radiotherapy. Therefore, certain interactions between different tumour clones can be favoured or disfavoured to give an evolutionary advantage. Intra-tumoural heterogeneity is responsible for tumour progression, metastasis, resistance, relapse (due to poorly targeted therapies which fail to eradicate all tumour cells) and challenging diagnosis.

The microenvironment within a tumour can vary according to oxygen pressure, blood vessel density, ECM composition and GF, which may lead to phenotypic and genotypic variations of cancer cells in the tumour. Tumour cell plasticity - a non-heritable source of heterogeneity, may also explain some of the phenotypic differences between cancer cells, and can also be affected by the microenvironment.

In the context of GBM biomarkers, some studies have observed differences in MGMT expression within a GBM tumour, where in a subset of tumour cells, in specific areas, MGMT is expressed, but surrounded by cells lacking MGMT.[66] The same phenomenon is seen with EGFRvIII, where its expression is varied and limited to a subset of cells surrounded by EGFR wild type cells.[66] Regional heterogeneity has also been observed in GBM, for instance amplified EGFR cells have been found to preferentially accumulate at the invading edges of GBM tumours, in poorly vascularised environments, and amplified PDGFRα cells have been found to preferentially accumulate close to endothelial cells.[66]

1.3.7 Diagnosis and clinical presentation of GBM

Initially, a patient presenting neurological symptoms will have a physical neurological assessment, which would include a neurologic functions test (reflexes, hearing, muscle strength, eye and mouth movement, balance and coordination, sense of touch and smell, alertness etc.).[45,68,69] If a tumour is suspected, the patient will have imaging scans and laboratory tests conducted to observe any CNS-related abnormalities. These include magnetic resonance imaging (MRI) and computerised tomography (CT) scans to determine tumour size, type, and location.[45,68,69] A tumour visualised with a CT scan would appear as a hypointense area in comparison to adjacent brain tissue, and would usually show a midline shift due to moderate to severe oedema. Ideally however, MRI scans allows for better soft tissue contrast to determine the complexity and the heterogeneity of the tumour. Hypointense lesions are seen on T1– weighted MRI scans, whilst hyperintense lesions are visualised in proton density weighted and T2-weighted images. Usually MRI scans of malignant glioma tumours enhanced with gadolinium demonstrate a central area of necrosis, surrounded by white matter oedema. Exact diagnosis is then confirmed through a biopsy.[45,68,69]

Tumour staging can also be carried out to determine if a tumour has migrated beyond the site of its origin.[69] For CNS tumours, staging is determined from a CT scan or MRI images, or by assessing the cerebrospinal fluid (CSF).[69] A sample of CSF is examined in a laboratory to ascertain the presence of tumour cells.[69] The CSF can also be studied for the presence of tumour biomarkers.[69] Particularly after surgery, the occurrence of tumour cells/biomarkers in the CSF would indicate tumour spread.[69]

Patients with GBM may clinically present different signs and symptoms, produced by the following: 1) brain tissue destruction because of necrosis, giving rise to symptoms such as focal neural deficit and cognitive impairments.[45] The signs and symptoms depend on the location of the tumour in the brain. 2) Increased intracranial pressure due to an increase in tumour size and oedema surrounding the tumour, which results in a shift in the intracranial contents, leading to headaches.[45] 3) Depending on the tumour location patients may also present with seizures usually with a focal onset, which could be simple partial, complex partial or generalised seizures.[45]

1.3.8 Treatment approach for GBM

The current treatment plan for newly diagnosed GBM patients is maximum surgical resection followed by radiotherapy (60 gray (Gy) in 30 fractions) and concomitant and adjuvant TMZ (75 mg/m^2/day for 6 weeks) chemotherapy.[70] Subsequently, patients are given six maintenance cycles of TMZ (150–200 mg/m^2/day for the first 5 days of a 28-day cycle.[70]

Prior to the operation, an evaluation of the medical condition of the patient, imaging and lab studies of the tumour, neuropsychological evaluation and the use of corticosteroid and anti-epileptic drugs are considered.[70] Steroids are used to control cerebral oedema and symptoms of intracranial hypertension, which improve the brain's condition for surgical resection. Anti-epileptic drugs, however, should not be used prophylactically. If patients with brain tumours have not had a seizure, reducing and discontinuing anti-convulsants after the first week of the operation is fitting. Patients that will be operated with cortical stimulation, in an asleep–awake–asleep custom, need special consideration, because of the possibility of patients developing stimulation-induced seizures.

The aims for carrying out surgery are to achieve maximal surgical resection, obtain tissue specimen for diagnosis, improve the chances of achieving greater efficacy with complimentary treatment to delaying clinical deterioration and improve patient quality of life (QOL).[70] Strong predictors of a good outcome are reliant on the patient, but also on the extent of resection (EOR), which is an important treatment-related predictor. Longer life expectancy is often associated with patients who undergo a more extensive, gross total resection, allowing for the longest survival to be achieved in patients who undertake surgery followed by radiotherapy and concomitant and maintenance TMZ chemotherapy. Yet a balance must be struck between aggressive tumour removal and the preservation of brain function, so maximal safe surgical resection must be carried out. A post-operative MRI would be needed to assess the EOR within 72 h of surgery rather than 72 h after surgery due to inflammatory post-operative variations.[70] It has been suggested that ≥ 98% EOR is essential for significantly improving survival.[70] However, one group has shown that resections of even 78% of the tumour volume, along with chemoradiotherapy, have prognostic rewards.[70] Some researchers have additionally shown that the amount of residual volume may be more important than the EOR.[70]

Tumours found within eloquent cortex are more surgically challenging because of the higher risk of post-operative neurological deficits.[70] Mapping *via* intraoperative electrical stimulation in awake craniotomy, provides decreased risk of developing novel neurological deficits and still achieve maximal EOR. To enhance EOR and progression-free survival (PFS), tumour margins can be visualised better with fluorescent agents, such as 5-aminolevulinic acid (5-ALA).[70]

Alternative chemotherapeutic agents have been explored. Biodegradable carmustine (nitrosourea; DNA alkylating agent) wafers can be implanted into the tumour site after tumour resection, for the treatment of GBM.[70] However, the use of carmustine wafers is controversial because of the questionable survival benefit and potential adverse side effects and infection risks associated with its application. Additionally, since GBM is highly vascularised, anti-angiogenic therapeutics are a sought-after chemotherapeutic strategy. The monoclonal antibody (Ab) - bevacizumab binds to all forms of VEGF including circulating VEGF-A, and prevents its interaction with the VEGF receptor, thereby inhibiting its biological activity.[70] Ultimately, this leads to reduced endothelial proliferation and vascular growth within the tumour, which should impede tumour growth. Again, however, there are concerns associated with the use of bevacizumab, namely a decline in patient QOL and neurocognitive function. Trials have demonstrated that the combination of bevacizumab with standard radiotherapy–TMZ therapy, for the treatment of newly diagnosed GBM, led to improved median PFS, but no increase in overall survival (OS).[70]

Upon GBM recurrence, treatment options include supportive care, re-operation, re-irradiation, systemic therapies, and combined modality therapy. EOR at re-operation does improve OS.[70] However, survival benefit is dependent on the patient and tumour characteristics, and so these need to be considered before pursuing a second surgery. The most reliable prognostic factor is a favourable performance status (PS; Karnofsky performance status (KPS) score of ≥ 70), which is associated with significantly improved PFS and OS, following rescue therapy.[70] Younger age (< 60 years) is the second most frequently reported prognostic factor linked with improved survival.[70] Maximal tumour volume resection is still the goal even for second surgeries. It remains critical that the

eloquent brain areas are preserved and that neurological deterioration after second surgery is avoided, as this may lessen the expected survival benefit.[70]

In younger patients with a good PS, focal re-irradiation (stereotactic radiosurgery (SRS) or hypofractionated stereotactic radiotherapy (HFSRT)) for recurrent GBM may improve their outcome compared to supportive care or systemic therapy alone.[70] As most GBM recurrences occur after being irradiated with a high dose, re-irradiation with doses and margins used for treatment of newly diagnosed GBM may lead to increased toxicity. Therefore, SRS or HFSRT is often employed to limit the volume of re-irradiation used.

Brachytherapy has also been assessed for the treatment of recurrent GBM, which includes a sharp dose gradient.[70] Strategies involves using permanent iodine 125 (I^{125}) seeds and a silicone balloon catheter system containing I^{125} solution. Patients selected for brachytherapy are typically those with operable tumours, good PS, and small disease.

TMZ plus re-irradiation have been observed to be safe and effective. Based on some phase II clinical trials, TMZ was approved for treatment of recurrent GBM, whilst nitrosoureas were relegated to second-line therapy use.[70]

Alternatively, an emerging treatment field called tumour-treating fields (TTFields) has been hailed the “fourth cancer treatment modality”, after surgery, radiotherapy, and chemotherapy.[70] It aims to deliver a low-intensity, intermediate-frequency (200 kHz), varying the electric fields *via* four transducer arrays, which is composed of nine insulated electrodes attached to a shaved scalp and connected to a portable device. *In vitro* studies have demonstrated that TTFields arrests cell division and kills tumour cells, mainly by achieving

misalignment of microtubule subunits during division, aberrant chromosomal segregation, and cytoplasmic blebbing during anaphase. Randomised clinical trials using TTFields for recurrent GBM (EF-11) and newly diagnosed GBM (EF-14), showed favourable QOL and toxicity profiles in the EF-11 trials, which led to FDA approval, in 2011, as a therapeutic option for the treatment of recurrent GBM.[70] In October 2015, the FDA also approved TTFields for use on newly diagnosed GBM patients.[70] TTFields plus TMZ use is particularly safe, with no additional systemic toxicity observed with the addition of this technology. The most common side effects were mild to moderate skin reactions beneath the transducer arrays. However, disadvantages associated with this therapy include the fact that it requires > 18 h of usage per day and the high cost associated with using this therapeutic approach.

Despite maximal safe surgical resection and combined chemotherapy and radiotherapy, GBM still retains a poor prognostic value. To date, excluding TTFields, no new agents have been brought forward, since the approval of TMZ, that improves survival when added to standard therapy. Efforts still need to be made to prolong OS and enhance QOL for GBM patients.

Alternative, up and coming treatment methods being investigated for GBM treatment include unconventional routes of chemotherapeutic administration. One example includes the method of convection enhanced delivery (CED; Figure 1.21), which allows therapies to be infused directly into localised areas of the brain parenchyma *via* bulk interstitial flow; bypassing the BBB.[56] Additionally, infused doses of therapies do not need to be as high as those required for other administration routes such as intravenous administration. With this route treatments could potentially cover an area as large as an entire

cerebral hemisphere.[56] This is beneficial for targeting therapies to migrating/invading cancer cells.[56]

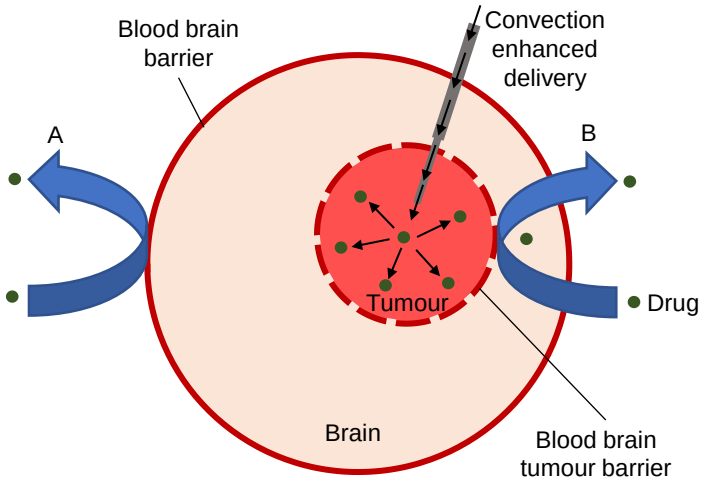

Figure 1.21. Convection enhanced delivery (CED). CED is used to deliver drugs directly to the tumour *via* a catheter, to bypass two brain barriers. A: Involves systemic delivery of drugs, which is obstructed from entering the brain by the blood brain barrier; B: Involves drug delivery obstructed by the blood brain tumour barrier.

1.3.9 GBM survival rates

Despite advances in diagnostic modalities and multidisciplinary treatment approaches, which include maximal surgical resection, followed by radiotherapy and concomitant and maintenance TMZ chemotherapy, almost all patients experience tumour progression with nearly widespread mortality. Even with the addition of bevacizumab to standard treatment, OS is not increased, yet PFS is improved. Presently, no standard of care is recognised for recurrent or progressive GBM. Potential treatments may include supportive care, re-operation, re-irradiation and combined modality therapy.

According to data collated by Brodbelt et al., little to no difference in survival outcome was observed between male and female patients with GBM that were not given treatment (data collated from a cohort of patients from England

between 2007-2010; see Figure 1.22a).[58] However, survival does seem to worsen with increasing age (see Figure 1.22b). Median survival for patients aged 20–44 was 16.2 months, for those aged 45–69 was 7.2 months, and for those aged 70+ was 3.2 months. Assessment of survival (sex and age combined) in patients receiving different treatment types show that the best survival outcome is through the combination of surgery, radiotherapy and chemotherapy (TMZ; Figure 1.22c). Median survival for patients receiving a combined therapy approach was ~ 16 months, with 30% of patients having 2-year survival and < 10% of patients surviving > 5 years.

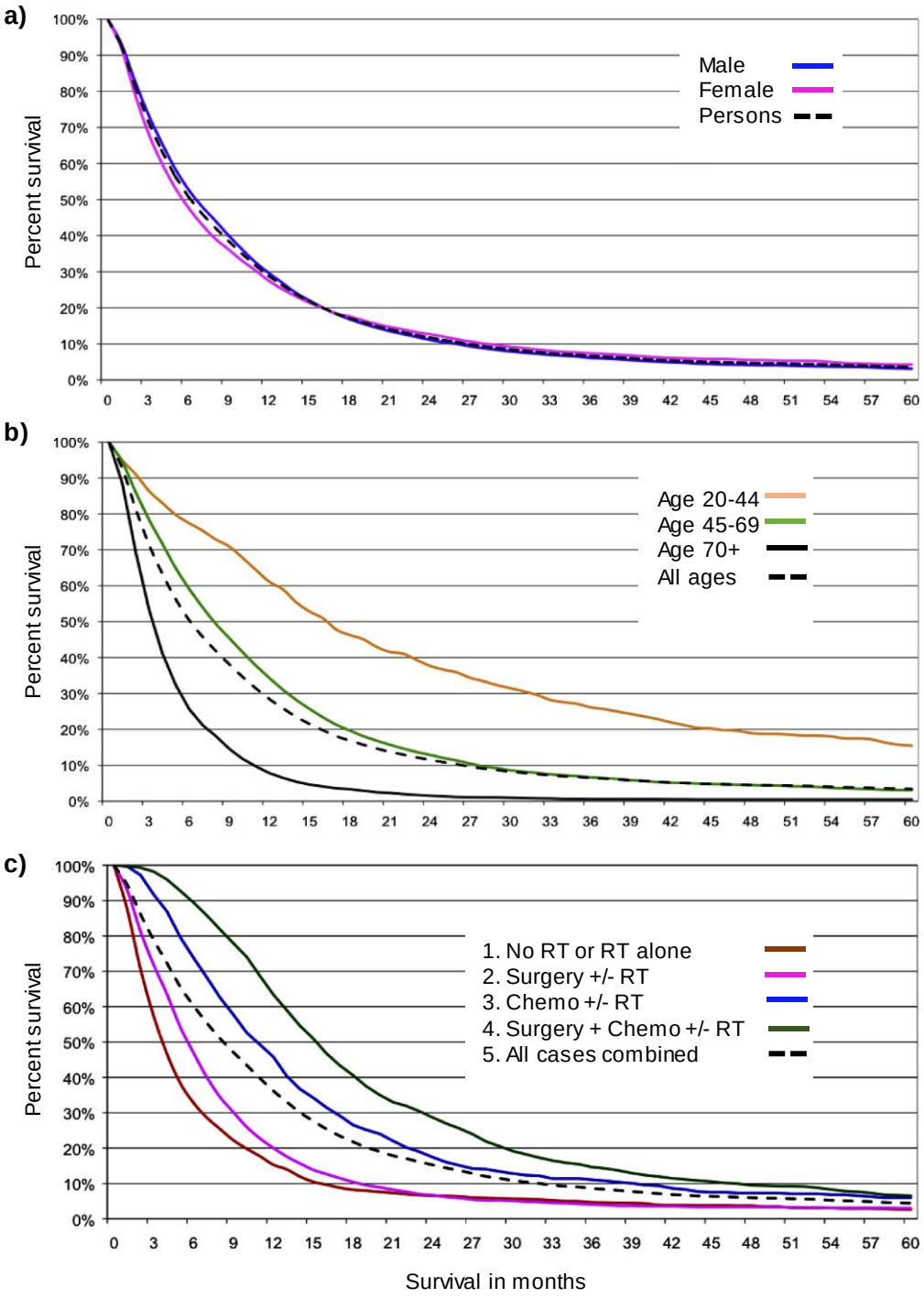

Figure 1.22. A Kaplan–Meier plot showing survival (months) according to treatment type for patients with GBM (England; 2007–2010). (a) Survival according to sex (with no treatment). (b) Survival according to age (with no treatment). (c) Survival with sex and age combined with different treatment approaches. RT: Radiotherapy. Chemo: Chemotherapy. Surgery involves any debulking procedure and does not include biopsy.[58]

1.4 Temozolomide (TMZ)

1.4.1 Background of TMZ

TMZ (trade names: Temodar/Temodal/Temodac; IUPAC name: 3-methyl-4-oxoimidazo[5-1-d][1,2,3,5]tetrazine-8-carboxamide), is an orally administered DNA alkylating prodrug discovered by Professor Malcolm Stevens and his team at Aston University, in Birmingham UK.[71,72] TMZ ($C_6H_6N_6O_2$; Figure 1.23) is used as the first-in-line chemotherapeutic agent for the treatment of GBM. It is an imidazotetrazine derivative containing an imidazole ring and is structurally and functionally like the drug dacarbazine (DTIC).[71] Specifically, TMZ is a triazene analogue of DTIC.

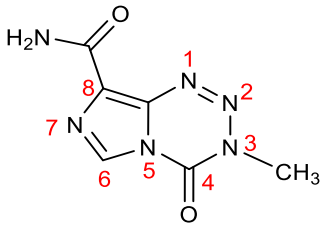

Figure 1.23. The chemical structure of TMZ.

Table 1.1 represents some of the physicochemical properties of TMZ.[71] TMZ is a small molecule, with the propensity to successfully penetrate the BBB.[72] It also has an overall neutral charge and is poorly water soluble.

Table 1.1. The physicochemical properties of TMZ.

Physicochemical properties	Values of physicochemical properties
Molecular weight (MW; g/mol)	194.15
Water solubility (mg/mL)	5.09
Calculated Log P	-0.81
Hydrogen bond acceptor count	8.00
Hydrogen bond donor count	2.00
Rotatable bonds	1.00
Topological polar surface area (Å^2)	106.00

TMZ is rapidly absorbed after oral administration across the gastrointestinal (GI) tract, with an oral bioavailability of ~ 100%.[71-74] The absorption of TMZ is only minimally affected by food (reduced by only ~ 9% when taken with food, which is not a clinically significant effect).[72] It is however, recommended to take TMZ 1 hour (h) before a meal or before going to bed to limit the possibilities of nausea and vomiting.[72] TMZ is sequestered in the plasma with a low volume of distribution of 0.4 L/kg and protein binding of 15%.[73] It has been shown to have a plasma half-life ($t_{1/2}$) of approximately 1.8 h and a clearance rate of 5.5 L/h/m^2.[73] Additionally, it appears that 38% of the administered TMZ total radioactive dose is recovered after 7 days with 37.7% found in the urine and 0.8% found in the faeces.[71,73]

1.4.2 Mechanism of activation of TMZ

The methyldiazonium cation is the active by-product of TMZ that is involved in the methylation of certain DNA bases. The mechanism of breakdown of TMZ to release the methyldiazonium cation is represented in Scheme 1.1.[74,75] The breakdown route of TMZ is a clean process consisting of four irreversible stages. First, TMZ **1** undergoes a base-catalysed hydrolytic attack (under physiological pH, at 37 °C) at the C4 position, to generate the tetrahedral molecule **2**. Subsequently, the tetrahedral complex at the N1 position is

protonated, which then ring opens to form unstable carbamic acid **3**. This spontaneously decarboxylates to form the triazene, 5-(3-methyltriazen-1-yl) imidazole-4-carboxamide (MTIC) **4**. MTIC, which has a very short $t_{1/2}$ of < 2 minutes (min), undergoes proteolytic degradation, to form the methyldiazonium cation **5** and 5-aminoimidazole-4-carboxamide (AIC) **6**. TMZ is stable at acidic pH and is absorbed across the GI tract in its intact form. However, it is unstable at pH > 7 (particularly at pH 7.4 ± 0.1) and therefore will start to breakdown in the blood.

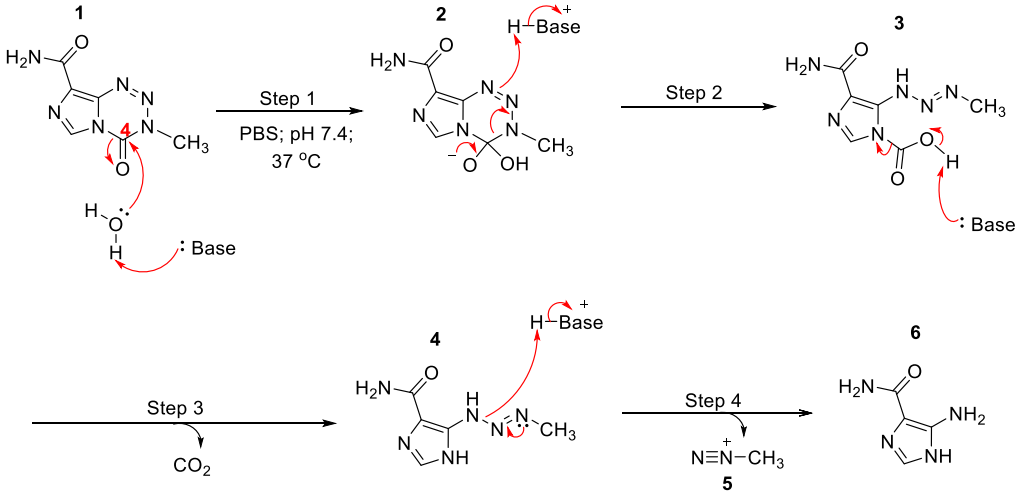

Scheme 1.1. The mechanism of breakdown of TMZ **1** to release active methyldiazonium cation **5**.

Additionally, TMZ degrades into different components which are safe and tolerable. Figure 1.24 summarises the routes by which the by-products of TMZ are eliminated. This involves AIC elimination *via* urine/faeces excretion, CO_2 and N_2 eliminated as gases and the methyldiazonium cation, which goes onto alkylate DNA.[74]

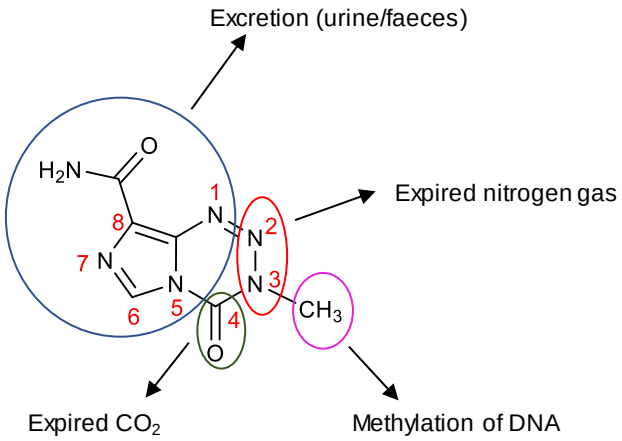

Figure 1.24. The breakdown and elimination of TMZ by-products.

1.4.3 Mechanism of action of methyldiazonium cation

The main by-product of TMZ, involved in DNA alkylation is the methyldiazonium cation, which promiscuously methylates mainly purine bases of the DNA.[74] Figure 1.25 shows the most common methylated adducts formed, which include: *N7*-methylguanine (*N7*-MeG; 70%), *N3*-methyladenine (*N3*-MeA; ~ 10%) and *O6*-methylguanine (*O6*-MeG; 5-7%).[76]

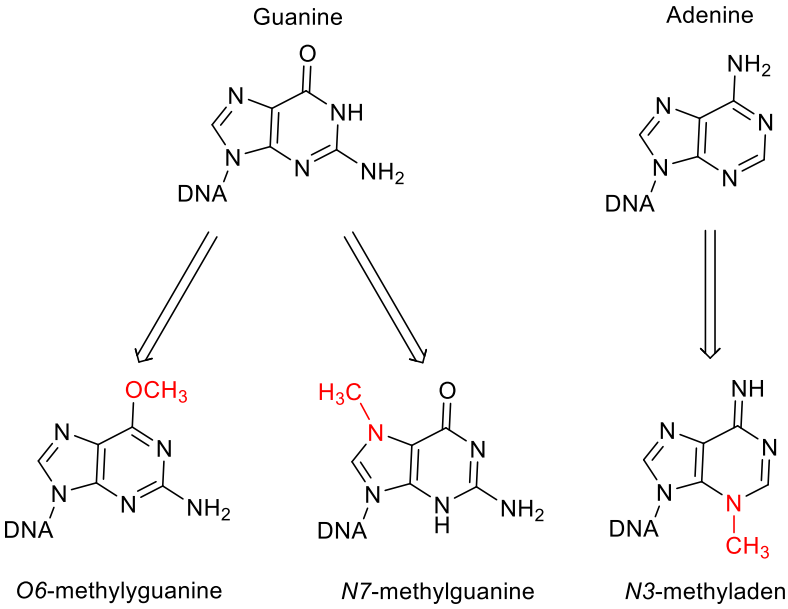

Figure 1.25. The most common methylated adducts formed from methyldiazonium cation alkylation of DNA purine bases.

Scheme 1.2 demonstrates the methylation reaction carried out by methyldiazonium cation **5**.[74] The methyldiazonium cation **5** electrophilically interacts with the most nucleophilic centres of the purine bases (especially where there are contiguous runs of guanine or adenine), releasing nitrogen gas in the process.

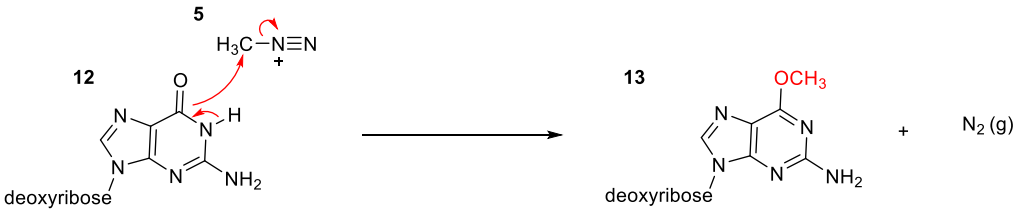

Scheme 1.2. Interaction of methyldiazonium cation **5** with the O6-position of guanine to generate *O6*-MeG DNA adduct.

N7-MeG, which is susceptible to spontaneous depurination to generate toxic and mutagenic sites, and *N3*-MeA, which is also highly toxic by blocking DNA polymerase, are however, easily repaired by the base excision repair (BER) pathway.[77,78] As such, these lesions contribute very little to the cytotoxic effects imparted by TMZ therapy. *O6*-MeG on the other hand, is highly cytotoxic.[79-82] During DNA replication, a mispairing of bases takes place, whereby thymine is paired with *O6*-MeG rather than cytosine. With a functioning mismatch repair (MMR) system, the MMR proteins only detect the thymine base in the mispairing (on the daughter strand), and subsequently removes it, whilst the *O6*-MeG base adduct remains intact. This leads to futile cycles of thymine excision and reinsertion, resulting in extensive DNA strand breaks and replication fork collapse. From this point, the ATR/CHK1 dependent signalling pathway is alerted (Figure 1.26), which signals for G2/M cell cycle arrest, predominately occurring from the second round of the cell cycle onwards. Eventually due to genomic instability, apoptosis ensues.

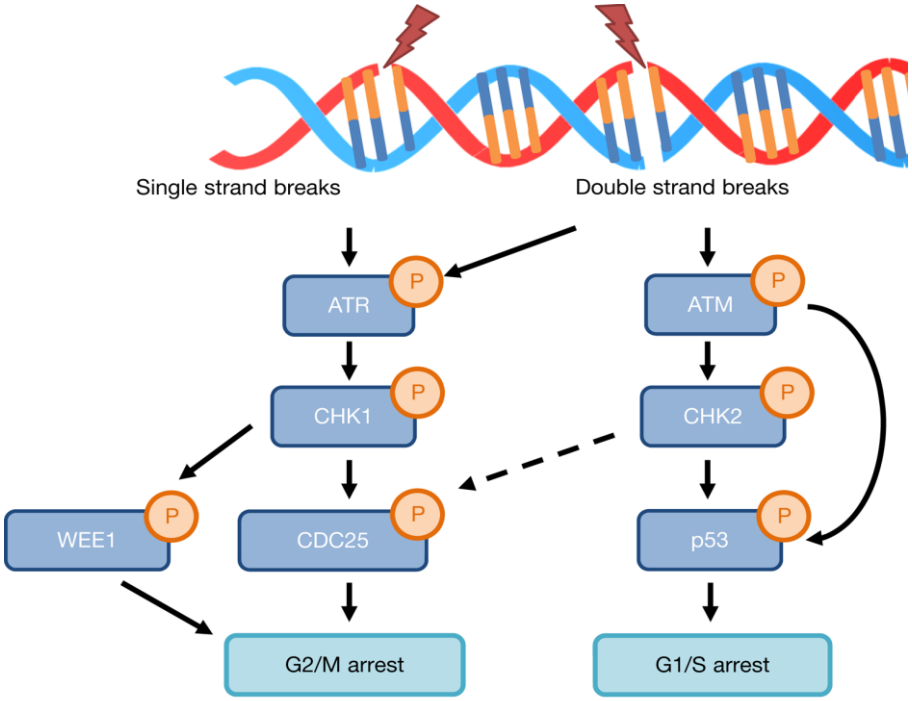

Figure 1.26. The DNA damage signalling pathway. The accumulation of DNA damage and replication stress can lead to the activation of either the ATM- or ATR-dependent signalling pathways. DNA damage in response to TMZ treatment is thought to activate the ATR pathway. Phosphorylation and thus activation of the CHK1 effector kinase by ATR ultimately results in the phosphorylation of the CDC25 phosphatases (leading to inactivation or ubiquitylation-dependent degradation). Eventually, this leads to cell-cycle arrest at the G2/M checkpoint. WEE1 is also a target of CHK1 kinase activity, leading to G2/M checkpoint activation.

Nonetheless, it was found that autophagic cell death can be another mode of cell death from TMZ treatment, in the event that GBM cells are able to evade death by apoptosis.[83,84] Autophagy following TMZ treatment, can either establish cell death or cell survival.[83] It seems however, that under starved conditions, survival of glioma cells resistant to apoptosis is usually promoted. It was found that inhibition of autophagy by co-administration of TMZ with late autophagic inhibitor, bafilomycin A1 or over activation of autophagy, hypothetically through continual doses of TMZ, can induce apoptotic cell death.[83,84]

1.4.4 Mechanism of resistance to TMZ

GBM cells are equipped with or acquire machinery to resist chemotherapy. As mentioned in the previous section, methylation at the *N7*- position of guanine and *N3*-position of adenine are quickly and efficiently recognised for removal by the BER system, *via* poly (ADP-ribose) polymerase-1 (PARP-1).[77,78] As for *O6*-MeG, there are mechanisms of resistance established to resist the effects of this adduct. Firstly, this includes repair by MGMT and secondly, some cells may tolerate the base mispairing with *O6*-MeG through mutated mismatch repair systems.[80]

MGMT is involved in the specific removal of the methyl substituent from the O6-position of guanine. Ultimately, normal guanine base is restored, thereby allowing for its natural pairing with cytosine to take place. The mechanism by which MGMT achieves this is through an extrahelical DNA process, whereby MGMT binds and expands the minor groove of the DNA, *via* the recognition helix, and then the nucleotide adduct is flipped to the exterior face of the DNA, see Figure 1.27.[85]

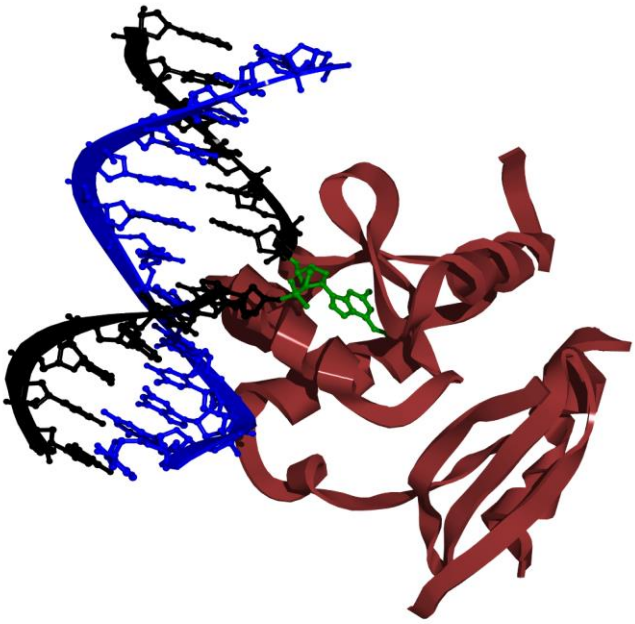

Figure 1.27. The MGMT Cys145S–*O6*-MeG DNA substrate complex (PDB code: 1T38). The *O6*-MeG adduct is coloured in green. The adduct is found outside of the DNA helix (strands separately coloured as black and blue) and buried within the core of the MGMT enzyme (coloured as maroon).

Figure 1.28 demonstrates some of the amino acids of MGMT that are involved in the demethylation process.[74,85] Initially, the reactive thiolate group of cysteine 145 (Cys145) is directly positioned opposite the methyl group of *O6*-MeG. Subsequently, histidine 146 (His146) initiates a water-mediated base catalysis process, to deprotonate the sulfhydryl group on Cys145. The thiolate anion then undergoes a nucleophilic attack to displace the methyl group and free the guanine. Additionally, tyrosine 114 (Tyr114) hydrogen bonds with the N3-position of guanine to reduce the resulting negative charge on free guanine. Overall, for every methyl group that is removed, an MGMT protein is destroyed.

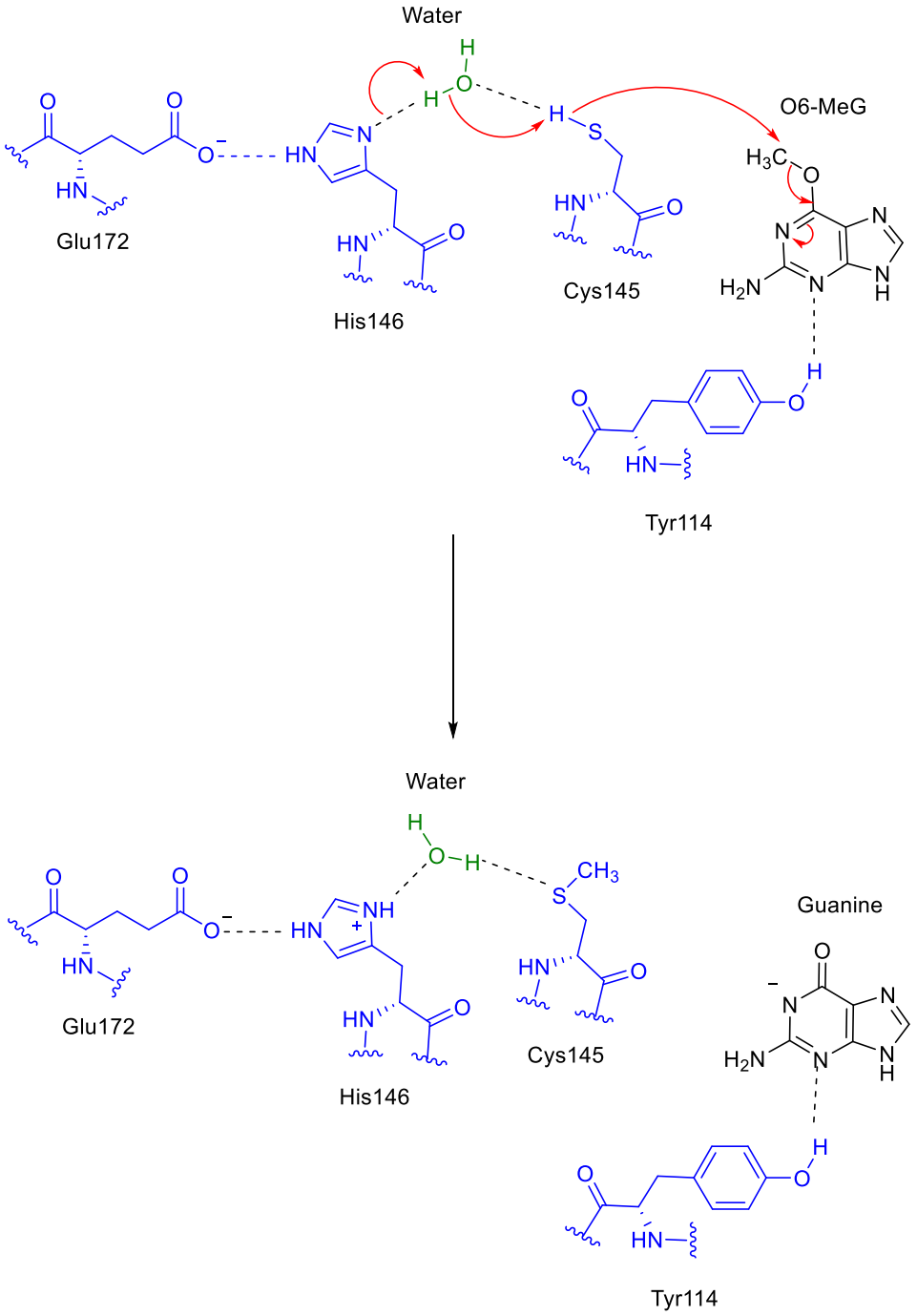

Figure 1.28. Mechanism of removal of methyl group from *O6*-MeG by MGMT, to restore guanine.

In some cases, the CpG promoter of the MGMT gene is methylated, which results in the MGMT protein not being expressed.[74] Suppression of MGMT expression in GBM tumours confers improved survival for patients treated with TMZ. However, studies have shown that treatment of GBM cells with TMZ can

also result in the inhibition of another enzyme called cytosine DNA-methyltransferase (DNMT).[74] DNMT is usually involved in transferring a methyl group from S-adenosylmethionine (SAM) to the C5-position of flipped out cytosine, of the CpG promoter. If DNMT is inhibited, methylation of the CpG promoter does not take place. Possibly, this could switch on the expression of MGMT, which then confers resistance to TMZ. This may in part explain why GBM resistance to TMZ is acquired after treatment with this alkylating agent.

1.4.5 Mechanisms to tackle TMZ resistance

With past studies showcasing various modes of inherent and acquired resistance mechanisms against TMZ in GBM, studies are now attempting to develop new approaches to overcome TMZ resistance. Some strategies of combating TMZ resistance include:

- **Combination of TMZ with PARP-1 inhibitors**.[86,87] The methylation of *N7*-guanine and *N3*-adenine represent the bulk of the methylation adducts caused by TMZ and yet they are rapidly repaired by BER. Ongoing research is taking place to explore combination treatment of BER inhibitors with TMZ, namely PARP-1 inhibitors. By inhibiting PARP-1 and combining with TMZ, the aim is to accumulate *N7*-MeG and *N3*-MeA adducts, following TMZ treatment, to enhance DNA damage, and ultimately promote cell death.

- **Combination of TMZ with MGMT inhibitors**.[86,88] Depleting MGMT would allow accumulation of *O6*-MeG adducts and ultimately enhance DNA damage and cellular arrest. *O6*-Benzylguanine (*O6*-BeG) is one example of an MGMT false substrate that irreversibly inactivates MGMT, sensitising cells to TMZ treatment.

- **Increase the likelihood of apoptosis with TMZ, through combination with late stage autophagic inhibitors**.[86,89] One example includes the additional treatment of TMZ treated cells with bafilomycin A1 (an inhibitor of autophagosome and lysosome fusion), which research has shown was able to initiate apoptosis to a greater extent than TMZ or bafilomycin A1 alone. It was shown that using a late stage autophagic inhibitor was more effective than using an early stage autophagic inhibitor. Bafilomycin A1 prevents the TMZ-induced autophagic survival response at the late stage, by activating caspase-3, and mitochondrial and lysosomal membrane permeabilisation.

- **Targeting shared biomarkers between CSC and GBM tumour bulk, in combination with TMZ therapy**.[86,90] CSCs (which have stem-cell-like properties such as self-renewal, capacity to differentiate and initiate tumour) are believed to play a role in developing resistance to chemoradiotherapy and may be the reason behind tumour recurrence. Discovering intrinsic and surface CSC biomarkers that are shared with the main GBM tumour bulk, may aid in preventing tumour recurrence. One example includes sensitising CSCs to TMZ by inhibiting c-Jun NH2-terminal kinases (JNK). JNK is commonly upregulated in GBM and the activation levels in self-renewing cells is far greater than those of differentiated cells. By inhibiting JNK, CSCs exhibit weakened stem cell properties, reduced expression of certain stem cell markers like Nestin and Sox-2, reduced ability to form tumour spheroids and enhanced levels of differentiated cell markers like GFAP and β III-tubulin. Additionally, studies have shown that the expression of MGMT was supressed when JNK was inhibited (with SP600125) and that in

combination with TMZ, SP600125 synergistically sensitised CSCs to TMZ cytotoxicity.

- **Combination of TMZ with existing treatment modalities**.[86] Currently, studies have been carried out to investigate the combinations of TMZ with bevacizumab (anti-VEGF antibody). However, no OS benefit was seen for GBM patients in two randomized clinical trials (AVAglio and RTOG0825). However, PFS was improved and it did improve certain clinical symptoms such as reducing cerebral oedema. Additionally, TTFields with TMZ therapy prolonged both PFS and OS compared to TMZ alone. TTFields may postpone repair of DNA damage by TMZ, thereby potentiating TMZ potency. However, TTFields is expensive to employ. Potentially, one could explore the combination of TMZ with a microtubule inhibitor like vincristine or jerantinine to achieve the same effect as TTFields.

- **Analogues of TMZ**.[84,91,92] To tackle the issue of TMZ resistance by MGMT and tolerance *via* MMR-deficiency, analogues of TMZ bearing alternative N3-alkyl groups have been developed. One example includes the replacement of N3-methyl with an N3-propargyl group (N3P analogue; Figure 1.29). Such modifications to generate these analogues, have shown *in vitro*, that they are able to evade recognition and removal by MGMT and exert activity irrespective of the DNA MMR status. Furthermore, substitutions at the C8-position of TMZ have created analogues with far superior pharmacokinetic (PK) and pharmacodynamic (PD) properties *in vitro*. Such analogues i.e. the C8-

thiazole analogue (T25; Figure 1.29) have demonstrated improved drug potency and $t_{1/2}$ over TMZ and N3P analogue.

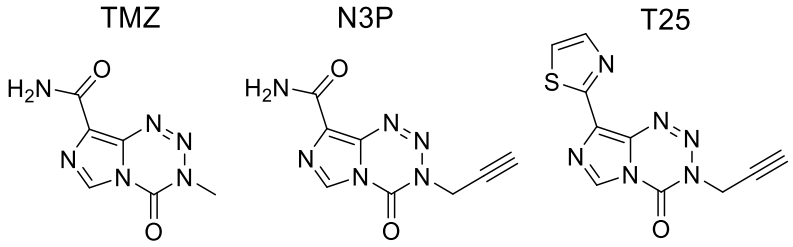

Figure 1.29. Parent TMZ alongside analogues of TMZ bearing N3- and/or C8-group substitutions.[92]

- **Delivery of TMZ inside a drug delivery system (DDS).** Studies have shown that delivering TMZ inside a GBM targeted DDS may enhance the accumulation of TMZ across the BBB and at the tumour site; ultimately increasing TMZ potency. Subsequent sections will review the various DDS that have been investigated to deliver TMZ.

1.4.6 Shortcomings in the approval of new oncology drugs

Our improved understanding of the pathophysiology of cancer has increasingly resulted in the advance of effective targeted therapies, which are more tolerable than the conventional cytotoxic drugs. Many large pharmaceutical and biotechnology companies have invested heavily in the field of oncology therapeutics in the past couple of decades.[93] However, so far, these novel therapies have shown only marginal therapeutic improvement and limited success rates for drug approval.[93] One research group have collated 406038 clinical data entries for over 21143 compounds (from 1st January 2000 – 31st October 2015) to estimate the success of these compounds in clinical trials.[94] From these entries, compounds for oncology trials have the lowest probability of success (POS) rate of only 3.4% compared to other therapeutic groups for all indication.[94]

Some of the shortcomings and reasoning behind the lack of significant therapeutic improvement has been partly due to inter- and intra-tumoral heterogeneity.[93] It may be that it will become futile and not successful long-term to prescribe a single targeted agent, when tumours have demonstrated capabilities of adapting to treatment and to evolve new ways to resist and thrive.[93] It appears combination therapy may be considered the future for oncology patients, following thorough (and continued) characterisation of the tumour.

Early on in the development process (pre-clinical phase), oncology drugs are mainly tested in established cancer cell lines propagated in tissue culture for *in vitro* studies and in immunocompromised animal models, like mice, for *in vivo* studies. Unfortunately, such models are poorly customed to predicting clinical outcomes because they have inadequate intra-tumoral heterogeneity, lack

human stroma and a competent host immune system, and generally have higher proliferation rates than those of human tumours.[93] Yet, *in vivo* studies in xenograft models remain fundamental in directing pre-clinical drug discovery and development; specifically, to rapidly assess the relationship between PK and PD measures of target variation within the tumour and to determine the efficacy and toxicity of drug.[93] Therefore, improving such models should be considered critical.

Patient-derived tumour xenograft (PDX) models implanted in immunosuppressed animals, may mimic the heterogeneity and drug responsiveness of the original tumour more closely than traditional xenograft models do.[93] But whether they can be translated to the clinical setting has yet to be seen.[93] More sophisticated spontaneous tumour models are now available that lack many of the shortcomings associated with xenograft and PDX models. For example, genetically engineered mouse (GEM) models provide an arrangement in which a tumour's drug response and resistance are determined in a microenvironment that further accurately reflects the natural niche of the disease.[93] Therefore, to improve the clinical success of oncology drugs, employing high quality pre-clinical models that recapitulate the tumour, is very much needed. No pre-clinical model is perfect, but they are useful if interrogated properly.

It is no longer acceptable to proceed with compounds that lack sufficient pre-clinical understanding into the mechanism of action for the indicated disease.[93] Rushing drugs into the clinic to fill in a pipeline can result in many patients being subjected to futile treatments with undesirable side effects. In one example, iniparib, a presumed PARP-1/2 inhibitor, was moved into phase III clinical trials based on the results of phase I and II trials and eventually failed.[93] Later studies

would reveal that iniparib was not a PARP-1/2 inhibitor but is active on cancer cells through a separate mechanism (namely the nitroso metabolite of iniparib forms adducts with many cysteine-containing proteins).[95,96] Therefore, by understanding the drug's mechanism of action, more appropriate trials could be designed with appropriate recruitment of patients most likely to benefit from these drugs.

Indeed, collaborations between industry, with capabilities in drug discovery, and academia, with deep biological knowledge, should allow for greater growth in delivering better targeted and tolerable therapies to the right patient cohorts.[97] Industries have gotten better at being more careful in licensing compounds and at identifying potential failures early on in the development process.[98] There has been an improved use of biomarkers in recent years, with companies targeting drugs to patients whom are more likely to respond positively, in clinical trials.[94] Hence, trials that were directed with the use of biomarkers in selecting patients, have shown greater success.[94] Lastly, drug delivery systems (DDS), are also being explored in oncology research as alternative treatment approaches towards improving patient response to onco-therapeutics (see section 1.5).

1.5 Nano drug delivery systems (DDS) for GBM treatment

1.5.1 What are nanoparticles?

Drug delivery systems DDS are engineered systems that are employed for the targeted delivery and/or controlled release of therapeutic agents. Specifically, DDS are utilised to overcome some of the physicochemical, PK and PD limitations that some drugs face, which result in limited efficacy and unwanted toxicity. Currently, treating cancer is complex and faces issues such as low specificity and selectivity, rapid drug clearance and biodegradation. Nanoparticles are often employed as DDS. A nanoparticle is defined as a material with a size range between 1 and 500 nm.[99] The advantages of utilising a nanoparticle as a DDS are its small size, high surface area-to-volume ratio, controlled drug release and capacity for targeting functionalisation.[99] The size range of the nanoparticles is thought to be applicable as a nanomedicine for cancer targeting because they can easily permeate the leaky vasculature of the tumour and accumulate in the tumour microenvironment due to impaired lymphatic drainage, *via* a process called the enhanced permeability and retention (EPR) effect (Figure 1.30). The possibility that the brain may not have a lymphatic system means that the EPR effect may not be seen in brain tumours.[100,101]

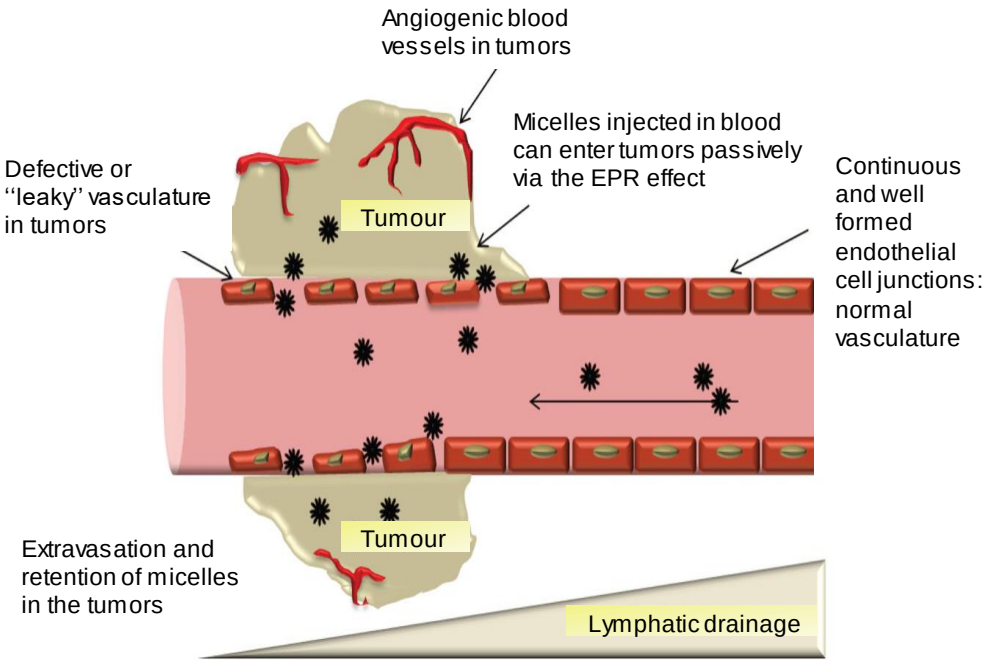

Figure 1.30. Schematic representation of the EPR effect in solid tumours. Passive targeting to tumour tissue is achieved by extravasation of nanoparticles (e.g. micelles) through the more permeable tumour vasculature and retention within the tumour due to ineffective lymphatic drainage (as shown in the schematic, where there is a decline in lymphatic drainage ability, from the normal to the tumour microenvironment). However, this mechanism may not be seen in brain tumours.[102]

At the moment, there are a wide variety of nanoparticles being investigated for cancer treatment, some of these include lipid-based, polymeric-based, inorganic, viral, drug-conjugated nanoparticles, etc. (Figure 1.31).[99,103] Several of these nanomedicines have been approved for use in the clinic, such as Doxil, a liposomal formulation of doxorubicin.[104] Nanoparticles for application as a nanomedicine can be used to carry drugs, imaging agents or both, which makes it applicable as a theragnostic agent.[99]

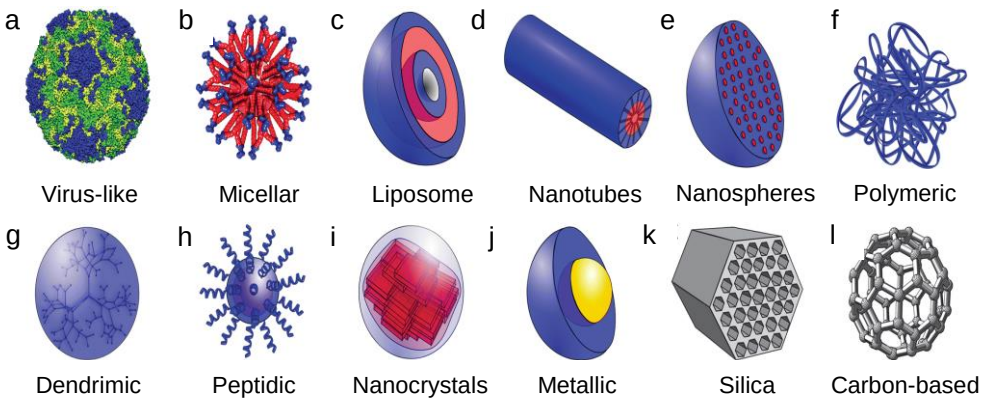

Figure 1.31. Schematic showing the various types of nanoparticles.[103]

1.5.2 Important characteristics of nanoparticles as a nanomedicine

The characteristic properties of nanoparticles such as their size, charge, shape, and surface modifications, in addition to protein corona formation and the cell cycle, have an important role in influencing the biodistribution, cellular internalisation and toxicity of these particles.[105-108]

Nanoparticle size. A decrease in nanoparticle size increases the surface area of the particles. A higher surface area allows greater diffusion of particles into the cancer cells. A smaller size also means that they are less likely to be recognised as a foreign agent by the macrophages. Larger entities are far more likely to be removed by the reticuloendothelial system. Typically, the sizes of nanoparticles (1-100 nm) are akin to the sizes of proteins (2-10 nm), DNA helix diameter (2 nm) and the thickness of the cell membrane (10 nm), which makes it possible for them to enter the cells or even enter cellular organelles. Huo et al. (2014) demonstrated that gold nanoparticles ≤ 6 nm can successfully enter the cell nucleus, whilst larger nanoparticles of 10 or 16 nm remain in the cytoplasm.[109]

It also appears that the route of entry into cells can be dictated by size. It was found that microspheres with a diameter of < 200 nm were internalised *via*

clathrin coated pits, but increasing the size to 500 nm, facilitated a caveolae-mediated internalisation process. Small nanoparticles also have less ligand-to-receptor interactions than larger nanoparticles. As such, a cluster of small nanoparticles are required to cooperate simultaneously to bind with nearby receptors to trigger membrane wrapping. On the other hand, large nanoparticles can individually group receptors to induce membrane wrapping and cellular internalisation.

There appears to be an enthalpic limit for a spherical nanoparticle at a size of around 30 nm for membrane wrapping. Nanoparticles smaller than this will not be able to efficiently drive the membrane-wrapping process, whereas nanoparticles > 60 nm in diameter would lead to receptor shortage; decreasing uptake because of the increasing entropic penalty. Many *in vitro* studies have shown that maximum cellular uptake can be achieved within the 10–60 nm range.

The distribution of nanoparticles and accumulation in a particular tissue is dependent on the relative amount of cardiac output that goes through that tissue. Organs with high blood flow like the brain, liver, kidney, heart, intestines, spleen, etc., should be exposed to higher levels of nanoparticles; so long as the nanoparticles can cross the vasculature walls. Smaller nanoparticles (< 10 nm) were found to distribute rapidly to many organs, whereas larger nanoparticles (50-250 nm) were found to greatly accumulate in the spleen, liver, and blood. There is some debate about whether this is due to the likelihood of larger particles being recognised by certain immune cells or if this is due to a simple filtration process. Some specific size limitations have been established. Nanoparticles with a diameter of < 10 nm will be rapidly eliminated by the kidneys. The glomerulus has three layers with varying pore sizes. The effective

cut-off size is ~ 10 nm. Moghimi et al. (2012) have suggested that a maximum size of ~ 150 nm, for spherical nanoparticles, should be set to avoid filtration in the spleen.[110] Additionally, micrometre sized particles appear to remain in the body much longer than particles on the nanometre scale.

Furthermore, nanoparticles of < 12 nm demonstrate faster tumour penetration rates. However, when designing a nanoparticle, a balance must be placed between circulation $t_{1/2}$ and the ability of nanoparticles to accumulate at the tumour site. Increased circulation $t_{1/2}$ will allow for increased penetration. It appears that for nanoparticles in the 40–100 nm range, circulation $t_{1/2}$ is crucial for tumour accumulation. A study examining the effects of size on biodistribution and penetration across the BBB showed that when polystyrene nanoparticles ranging in size between 25 and 500 nm were injected into rats, 3 h post injection, the biodistribution and accumulation across the BBB was greatest with the 25 and 50 nm particles. Similarly, this trend was seen with gold nanoparticles, with sizes of 15 and 50 nm nanoparticles accumulating in the brain the greatest. This suggests that smaller nanoparticles are favoured for BBB penetration and brain tumour accumulation.

Also, distribution through the tumour mass is hindered by differences in the hydrostatic pressure of the tumour. The high central tumour pressure drives fluid away from the centre of the tumour, which makes it difficult for nanoparticles to reach those areas. Nanoparticles that can reach the centre of the tumour show slow and restricted movement through the tumour ECM in a size-dependent manner. Using targeting ligands may help to enhance uptake.

Nanoparticle shape. It has been shown that elongated nanoparticles demonstrate better cellular adherence and uptake efficiency over spherical

nanoparticles, with the same size. This is because the curve shape of spherical particles reduces the number of binding sites that can interact with cell surface receptors, whereas elongated nanoparticles have a higher surface area, which allows for multivalent receptor interactions. It has also been shown that nanoparticle toxicity strongly depends on their shape. For instance, single-walled carbon nanotubes have been shown to block calcium channels more so than spherical fullerenes.

Nanoparticle charge. Positively charged nanoparticles can achieve electrostatic interactions with the negatively charged cell membranes. Hence, positively charged nanoparticles demonstrate greater intracellular uptake. However, since the glomerular basement membrane is negatively charged, cationic nanoparticles < 10 nm are more likely to be cleared than neutral or anionic nanoparticles.[99] The greater steric prevention with neutral nanoparticles, however, means that there is a lower chance of plasma protein adsorption, higher blood circulation time due to the greater ability to avoid clearance by the phagocytic system, and broader cellular uptake. Cellular uptake of nanoparticles can be increased by reducing particle aggregation. Negatively charged nanoparticles show an initial repulsive interaction which can modulate later aggregation, cluster formation and cellular uptake. According to some studies in rat brains, it appears that neutral and anionic nanoparticles resulted in less neurotoxicity than cationic nanoparticles.[99]

Protein corona. Nanoparticles in contact with a biological medium commonly result in the surface of the nanoparticle being coated with a layer of biomolecules such as lipids and especially proteins (including the major serum proteins albumin, fibrinogen, immunoglobulin G, etc.), to form what is called a protein corona (Figure 1.32). Proteins that adsorb with high affinity form a ‘hard’

corona. This is composed of tightly bound proteins that are not easily desorbed. There are proteins which also adsorb with low affinity to form a ‘soft’ corona. The presence of a corona surrounding a nanoparticle has multiple implications, which may include altered physicochemical properties in biological fluids, how the nanoparticle interacts with cells, speed of elimination, aggregation characteristics and/or hydrodynamic size, conformational change of the nanoparticle, biodistribution, complement activation, etc.

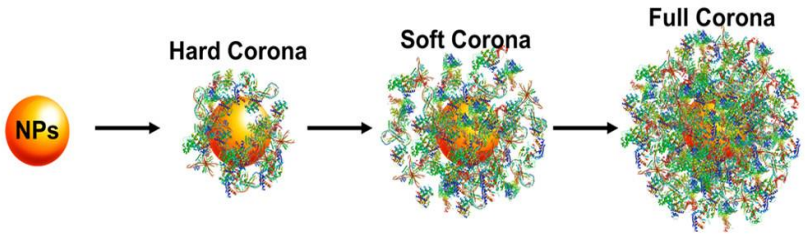

Figure 1.32. A schematic demonstrating the formation of a protein corona around a nanoparticle. First, there is the formation of a hard corona, followed by the formation of a soft corona.[111]

Nanoparticle surface modification. Coating the surface of a nanoparticle with polyethylene glycol (PEG) chains can decrease biomolecule association with PEGylated nanoparticles and increase the circulation time. It can alter the physicochemical properties of the nanoparticles and change its hydrodynamic size. Also, ligands can be introduced to enable active targeting of the nanoparticle.

Cell cycle. The position of the cell in its division cycle can affect the uptake of nanoparticles. Partly, this is because the expression of cell membrane proteins differs according to the phase of the cell cycle. As well as this, cell proliferation can reduce the concentration of nanoparticle that is internalised because cell division will divide the nanoparticles between the two daughter cells. A study looking at the uptake of a 40 nm sized carboxylated polystyrene nanoparticle in

different phases of an A549 cell cycle, demonstrated that the nanoparticles accumulated the greatest during G2/M-, followed by S- and then lastly the G0/G1-phase of the cell cycle.[112]

1.5.3 Nanoparticles employed for GBM diagnosis and treatment

Diagnosis. Currently, there are several imaging tools employed for the diagnosis of GBM, such as CT and MRI. Developing nanoparticles as delivery vehicles for contrast agents serves to enhance the tumour specificity and biocompatibility of imaging agents. So far, there have been many nanoparticles that have been tested, for imaging purposes, *in vitro*, *in vivo* and in human subjects.[113] To achieve nanoparticle specificity, such nanoparticles are coated with targeting groups on their surface. One example includes the attachment of EGFRvIII antibodies (Ab) to the surface of a multifunctional iron oxide nanoparticle, which is being investigated as an imaging agent for molecular MRI (Figure 1.33).[114] The advantage of using this nanoparticle is that it provides direct imaging of the tumour by MRI, in a selective and targeted manner. Indeed, *in vitro* studies have demonstrated enhanced MRI contrast of the tumour.[114] Additionally, ultrasmall superparamagnetic iron-oxide-based nanoparticles, tested in human subjects, have demonstrated advantages over gadolinium-based MRI contrast agents.[115] They are eliminated more slowly, reside longer in tumour cells and imaging can take place 24-72 h after administration.[115]

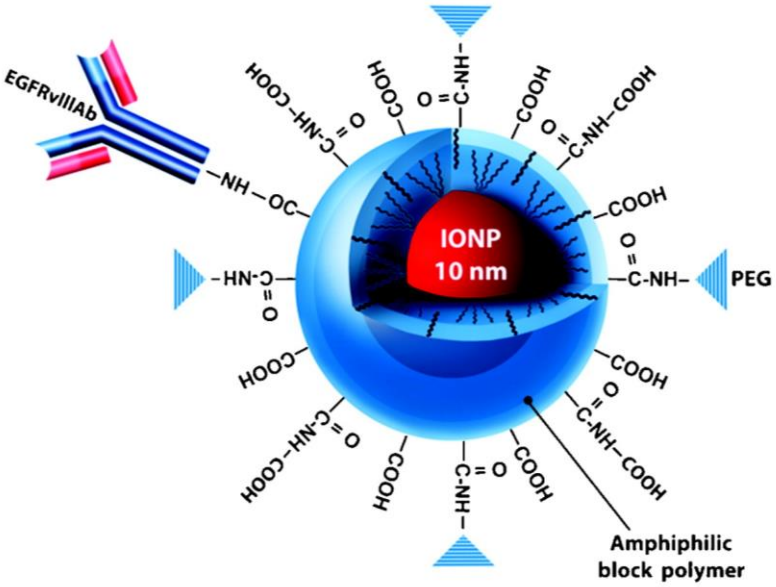

Figure 1.33. Amphiphilic block co-polymer–coated iron oxide nanoparticles (IONPs; red; 10 nm core size). The co-polymer coated IONP is conjugated to the EGFRvIII Ab, *via* -COOH of the polymer. PEG was introduced on the surface of the polymer for further stabilisation and biocompatibility of the IONP.[114]

Treatment. Nanoparticles loaded with drugs can enhance the drug circulation time, improve specificity, reduce unwanted toxicity, and achieve controlled drug release.[113] Not all brain tumours have a compromised leaky BBB, called the blood brain tumour barrier (BBTB), but it is characteristic of high-grade gliomas.[113] Therefore, we can achieve passive targeting of nanoparticles to tumours by EPR. However, a disadvantage with the EPR effect is that it relies on passive diffusion, which is hard to control.[113] In addition, tumours have a chaotic arrangement of blood vessels, which does not equally access all areas of the fast-growing tumour. This means that the nanoparticles will likely not reach some areas; so, adding targeting to the nanoparticles would facilitate an active targeting process that is more specific. Also, engineering nanoparticles to release the drug under certain stimuli such as a change in the potential of hydrogen (pH), redox state, catalysis by enzymes, or externally applied stimuli like heat, light or magnetic field, would limit toxicity and prolong drug

compliance, by enabling fewer drug administration schedules and/or lower drug doses.[113]

Different approaches have been employed in glioma treatment with nanoparticles, and assessed *in vitro*, *in vivo* or early-stage clinical trials. Some interesting nano-formulations are summarised in Table 1.2.

Table 1.2. Nanoparticle formulations being assessed for GBM therapy.[113]

Nanoparticle	Stage	Advantages
Cerebral EnGeneIC delivery vehicle (EDV) (EGFR(V)-EDV-Dox).	Clinical trial - Phase I (NCT02766699)	- Single-agent therapy - intravenous.
Nanoliposomal irinotecan.	Clinical trial - Phase I (NCT02022644)	- Single-agent therapy - intracranial.
DOX-loaded PEGylated liposomes modified with p-hydroxybenzoic acid (pHA) and c(RGDyK).[116]	*In vitro* (glioblastoma cells (U87), brain capillary endothelial cells (bEnd.3), and umbilical vein endothelial cells (HUVECs)) *In vivo* (orthotopic mouse model)	- Efficient targeting of the tested cell lines and increased doxorubicin cytotoxicity. - Passing the BBB and BBTB *in vitro* and *in vivo*. - Increased median survival.
DOX-loaded PEGylated liposomes conjugated with CB5005 peptide.[117]	*In vitro* (glioma cells U87) *In vivo* (xenograft- and intracranial-glioblastoma bearing nude mice)	- Penetrated glioma cells and delivered DOX into the nucleus. - Increased the efficiency of killing glioma cells. - *In vivo*: distributed into the brain and accumulated at tumour xenograft site. - Prolonged the survival time.
Resveratrol-loaded PEGylated liposome targeted with transferrin.[118]	*In vitro* (glioblastoma cells (U87) and neurospheres) *In vivo* (xenograft mouse model)	- Good drug-loading capacity and prolonged drug-release. - Significantly more cytotoxic and induced higher levels of apoptosis compared to free RES. - Inhibited tumour growth and prolonged survival time.
DOX- and erlotinib-loaded PEGylated liposomes, modified with transferrin and cell-penetrating peptide PFVYLI.[119,120]	*In vitro* (glioblastoma cells (U87), brain capillary endothelial cells (bEnd.3) and in vitro brain tumour model *In vivo* (orthotopic mouse model)	- Efficient internalization of drugs and higher apoptosis. - Translocation across the BBB. - Increased drug accumulation in mice brain and increase in median survival time.
PTX- and SPIO-loaded, PEGylated, PLGA-based nanoparticles.[121]	*In vitro* (glioblastoma cells (U87)) *In vivo* (orthotopic mouse model)	- Enhanced accumulation of nanoparticles in the brain. - Prolonged the median survival time. - No induced systemic toxicity.

Temozolomide loaded PNPs, SLNs, and NLCs.[122]	*In vitro* (glioblastoma cells (U87)) *In vivo* (malignant glioma-bearing mice)	- NLCs showed most efficient delivery of temozolomide and higher inhibition efficacy of tumour growth.
Epirubicin-loaded polymeric micelles decorated with cRGD.[123]	*In vitro* (glioblastoma cells (U87)) *In vivo* (orthotopic mouse model)	- Faster and higher penetration of cRGD-decorated NPs into the cells compared to non-decorated NPs. - Effective suppression of the tumour growth.
DOX- and curcumin-loaded polymeric micelles decorated with GLUT1.[124]	*In vitro* (glioblastoma cells (U87))	- Successful apoptosis enhancement due to combinatory treatment. - Deeper penetration into the 3D (three-dimensional) spheroid model.
DOX- and tamoxifen-loaded PAMAM dendrimer conjugated with transferrin.[125]	*In vitro* (glioblastoma cells (U87))	- Effective transport across the BBB.

Note: EGFR = epidermal growth factor receptor; BBB = blood brain barrier; BBTB = blood brain tumour barrier; c(RGDyK) = cyclic peptide composed of arginine-glycine-aspartic acid-D-tyrosine-lysine (RGDyK); DOX = doxorubicin; RES = resveratrol; PTX = paclitaxel; SPIO = superparamagnetic iron oxide; PLGA = poly(lactic-co-glycolic acid); PNPs = polymeric nanoparticles; SLNs = solid lipid nanoparticles; NLCs = nanostructured lipid carriers; cRGD = cyclic peptide composed of arginylglycylaspartic acid (RGD); NP = nanoparticle; GLUT1 = glucose transporter-1; PAMAM = polyamidoamine.

Liposomes are spherical nanoparticles composed of a phospholipid bilayer and a hollow core.[113] Some liposomal-based nano-formulations are currently in early-stage clinical trials for GBM therapy, these include liposomes loaded with doxorubicin (NCT02766699) or with irinotecan (NCT02022644). Studies with liposomes have also looked at combination therapy strategies. Co-delivery of two chemotherapeutics, doxorubicin and erlotinib, which act through various non-intersecting and synergistic mechanisms, to enable enhanced therapeutic efficacy and limited cancer cell drug resistance, have been loaded into liposomes modified with two targeting moieties: transferrin (Tf; for receptor-mediated endocytosis) and penetratin (a cell-penetrating peptide). Examined *in vitro* and *in vivo*, this formulation demonstrated excellent anti-glioma activity.[119,120]

Liposomes have also been successfully engineered to respond to stimuli, to induce controlled drug release. Babincova et al. devised thermosensitive magnetoliposomes with superparamagnetic iron oxide nanoparticles and doxorubicin.[126] This formulation was tested *in vitro* and *in vivo* (rat glioma C6), whereby the particles were heated to 43 °C to enable controlled release of encapsulated doxorubicin. The study demonstrated inhibition of tumour growth and complete regression.

Additionally, polymeric nanoparticles have been frequently employed as a DDS for glioma treatment. They are composed of a core polymer matrix, with therapeutic agents encapsulated or conjugated onto the surface.[113] The nanoparticles can be composed of synthetic polymers such as poly-ε-caprolactone, polylactides, polyglycolides, and the popular poly(lactide-co-glycolides) (PLGA), or with natural polysaccharides e.g. chitosan, hyaluronic acid, and corn starch.[113] Additionally, it can include proteins such as albumin, gelatin, collagen, transferrin, etc.[113] Ganipineni et al. assessed the activity of paclitaxel and superparamagnetic iron oxide-loaded PEGylated PLGA-based nanoparticles.[121] *Ex vivo* studies demonstrated enhanced accumulation of the nanoparticles in the brain glioma of orthotopic mice and *in vivo* studies demonstrated significantly prolonged median survival.

Solid lipid nanoparticles (SLN) and nanostructured lipid carriers (NLC) are nanoparticles made from natural lipids.[113] One limitation of the SLN is their restricted loading space, and so to overcome this issue, NLC were developed.[113] NLC are made up of a mixture of spatially varied solid and liquid lipids, arranged in a less perfect crystalline lattice than SLN, which provides more space for loading.[113] One group has engineered an NLC with two ligands

on its surface: lactoferrin (enables passage across BBB and receptor-mediated endocytosis into glioma cells) and arginylglycylaspartic acid (RGD) tripeptide (binds to αvβ3 which is overexpressed on neurovascular endothelial cells).[127] *In vitro* studies assessing the co-delivery of TMZ and vincristine within this NLC demonstrated synergistic activity and greater cellular uptake with the targeted over non-targeted NLC. *In vivo* studies demonstrated that the administration of the dual-targeted NLC showed the greatest tumour inhibition.

Dendrimers are small, highly branched, globular symmetrical polymeric molecules with a distinct structure.[113] Dendrimers used in biological applications can be made from different polymers, among which poly(amidoamine) (PAMAM) dendrimers are preferred.[113] PAMAM dendrimers are made of an ethylene diamine initiator core, and around this, amidoamine repeating units are radially attached.[113] A PEGylated PAMAM dendrimer conjugated with a glioma homing peptide: Pep-1 (a ligand which is specific for interleukin-13 receptor α2 (IL-13Rα2)) was developed.[128] This receptor is overexpressed in glioma cell lines. *In vitro* and *in vivo* results both show significantly enhanced penetration and accumulation of the targeted dendrimer at the tumour site.

Nanoparticles for glioma treatment have also been developed as theragnostic agents.[113] One example includes a nanoparticle consisting of iron oxide nanoworms covered with two branched chimeric peptides: one is a tumour-specific vascular homing element of cysteine-glycine-lysine-arginine-lysine (CGKRK) and the other serves as an anti-bacterial peptide drug called the membrane-perturbing proapoptotic D-amino acid peptide $_{D}$[lysine-leucine-alanine-lysine-leucine-alanine-lysine]$_2$ ($_{D}$[KLAKLAK]$_2$).[129] This drug results in mitochondrial membrane disruption, and therefore initiates apoptosis. *In vivo* studies in murine GBM models with this nanosystem, demonstrated high

tumour specificity, reduced toxicity, and tumour growth inhibition. Due to the presence of the iron oxide (an imaging agent for MRI) and drug, this nanoparticle can be utilised for both diagnostic and treatment purposes.

Finally, immunotherapy for GBM eradication is another mode of treatment that is gaining traction, particularly with the use of nanoparticles. For instance, nanoparticles have played an important role in antigen-presentation for *ex vivo* T-cell expansion e.g. by using Dynabeads composed of ferrosoferric oxide (Fe_3O_4) in a polystyrene matrix and including anti-CD3 and anti-CD28 ligands (Figure 1.34).[130]

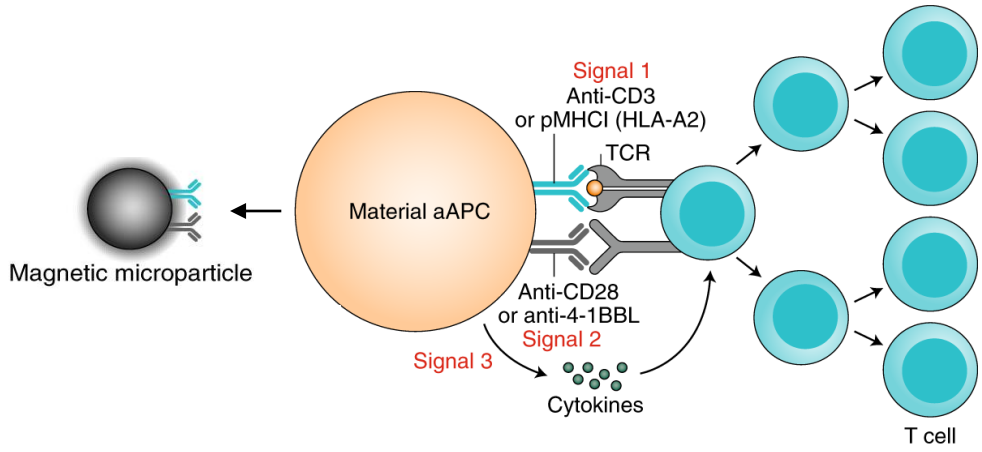

Figure 1.34. Materials for *ex vivo* expansion of T cells. One example includes employing the use of magnetic microparticles like Dynabeads (composed of ferrosoferric oxide (Fe_3O_4) in a polystyrene matrix). Such materials are coated with T cell receptor stimulatory signals like anti-CD3 and co-stimulatory signals anti-CD28, to perform as artificial antigen presenting cells (aAPCs) to stimulate T cell expansion *ex vivo* (image modified from following reference).[130]

Like many drugs, there are advantages and disadvantages associated with each of the DDS.[113,131] Liposomes for instance have the advantage of being able to incorporate both hydrophilic and hydrophobic drugs and offer good drug protection. However, depending on their size, charge, and composition, liposomes can easily be removed by the immune system and accumulate in the

liver and spleen. As for polymeric nanoparticles, they can be engineered to be biodegradable and functionalised as a theragnostic agent. Yet, one concern is that like liposomes, they require organic solvents for their preparation and there are concerns about early drug leakage. Additionally, many of these DDS are synthetic in nature and foreign to the human body, which leaves concerns associated with immunogenicity, accumulation and possible unwanted toxicity. Therefore, although there are a wide range of nanoparticles in development and assessment for glioma treatment, many have yet to go beyond pre-clinical stages and into clinical trial studies.

1.6 The use of apoferritin as a DDS

The potential of utilising a DDS native to the human body may be an attractive way forward for combating certain toxicity issues. Apoferritin (AFt; see Figure 1.35a) is a 12 nm (external diameter) sized, hollow protein cage, derived from ferritin (Ft) - an iron (Fe) transport/storage protein.[132] It has been explored for use as a DDS. One interesting advantage over other synthetic DDS is that AFt is naturally found in humans and is biocompatible and biodegradable.[132]

1.6.1 Ft function

Fe is an essential atom found in the active sites of many enzymes and in oxygen carrier proteins.[133-143] Free Fe is low because under physiological pH and oxidising conditions Fe is highly insoluble, i.e., Fe^{3+}. Uncomplexed Fe along with superoxide (to reduce Fe^{3+} to Fe^{2+}), and hydrogen peroxide, can result in a deadly mixture containing reactive hydroxyl radicals. Reactive hydroxyl radicals can cause DNA strand breaks, lipid peroxidation and degradation of other biomolecules. To defend against the toxic nature of free Fe, Fe can be captured by two proteins, extracellular Tf (which plays an important role in Fe distribution) and intracellular Ft. Fe is mainly stored intracellularly, by converting the highly toxic Fe^{2+} to the less toxic Fe^{3+}, and is sequestered in the Ft cavity.

H-subunits of AFt are responsible for the oxidation of Fe^{2+} by molecular oxygen or hydrogen peroxide at a dinuclear Fe-oxo ferroxidase center in the interior side of the capsule. L-subunits on the other hand, assists in the clearance of compounds from the ferroxidase center into the cavity, the initiation of the Fe core nucleation (by deposition of Fe^{3+} and release of protons) and mineralisation (addition of phosphates to stabilise the core). The 3-fold channels are the most likely point of entry for Fe^{2+}. The expulsion of protons

and addition of anions like dihydrogen phosphate ($H_2PO_4^-$) are believed to occur *via* the 4-fold channels. H-subunit-rich Ft in organs like the heart and brain, have high ferroxidase activity and will play a more anti-oxidant role, whereas a more L-subunit rich Ft in organs like the spleen and liver, will play a more iron storage role, as the L-subunit is believed to play an important role in generating a more stable Ft capsule and in holding more Fe than a heavily H-subunit capsule.

1.6.2 Ft structure

Ft (~ 750 kDa) is composed of a 24-polypeptide subunit protein cage called AFt (~ 480 kDa) and up to ~ 4500 Fe atoms in the cavity, stored as an inorganic ferrihydrite complex (through the oxidation of Fe^{2+} to Fe^{3+} to generate [Fe^{3+}O.OH], in addition to the inclusion of other minerals such as phosphates).[133-143] The 24 subunits are split into two subunit varieties: heavy (heart; H; MW: 21 kDa) or light (liver; L; MW: 19 kDa) polypeptide subunits. These polypeptide subunits differ because of variations in their amino acid sequence, chain length, mass, surface charge (isoelectric focusing) and immunoreactivity. The ratios of these subunits (to make up the AFt cage) can vary among different species and even between different organs within the same species. For instance, Ft in the human heart is composed of 90% (H-chain):10% (L-chain), whereas in the human liver it is 50% (H-chain):50% (L-chain) and in the spleen it is 10% (H-chain):90% (L-chain). Slight differences between different species is also seen, e.g. when comparing human spleen to horse spleen, the subunits ratio in horse spleen is 2% (H-chain):98% (L-chain).

Ft is a ubiquitous protein found in both eukaryotes (humans, other vertebrates, invertebrates, plants, fungi) and prokaryotes (bacteria). While Ft mainly exists intracellularly, some can be found in the serum. Ft from vertebrates is composed of H- and L-subunits, whilst those from plants and bacteria contain

only H-subunits. A sequence similarity of ~ 53% was found between the subunits, and yet the two subunits have different assigned roles. Also, despite slight differences in the amino acid sequences between the two subunits and even of the same subunit between different species, the 3D conformation of the subunits is very similar, apart from bacterioferritin. Mammals have three functional Ft genes: Ft (H-subunit) on human chromosome 11, which encodes cytosolic H-subunit, Ft (L-subunit) on chromosome 19, which encodes cytosolic L-subunit, and the intronless Ft (mitochondria) on chromosome 5, which encodes a precursor of the mitochondrial Ft composed of 242 amino acid residues. The H- and L-subunits are expressed under the same iron-dependent post-transcriptional control.

The AFt subunits consist of a 4-helix bundle, joined by a long loop and a smaller C-terminal helix (Figure 1.35b). Also, AFt has 14 channels of ~ 3-4 Å in diameter. Six channels are hydrophobic, which exist at the intersections created by 4 polypeptide chains and are referred to as the 4-fold channels (~ 4 Å in diameter; Figure 1.35c). They are lined with non-polar amino acids, mainly leucine. The other eight channels are hydrophilic, which exist at the intersections created by 3 polypeptide chains and are referred to as the 3-fold channels (~ 3 Å in diameter; Figure 1.35d). They are lined with polar amino acids: glutamate and aspartate residues. The interior surface of the AFt cage, like the exterior surface, is mostly negatively charged, with few areas that have extra positively charged amino acids. The walls of the 3-fold channels have a negative potential value due to the presence of glutamic acid and aspartic acid amino acid residues, which allows cations to be funnelled in for entry. On the other hand, the walls of the 4-fold channels have a positive potential value due to the presence of the amine from lysine, which result in the repulsion of cations.

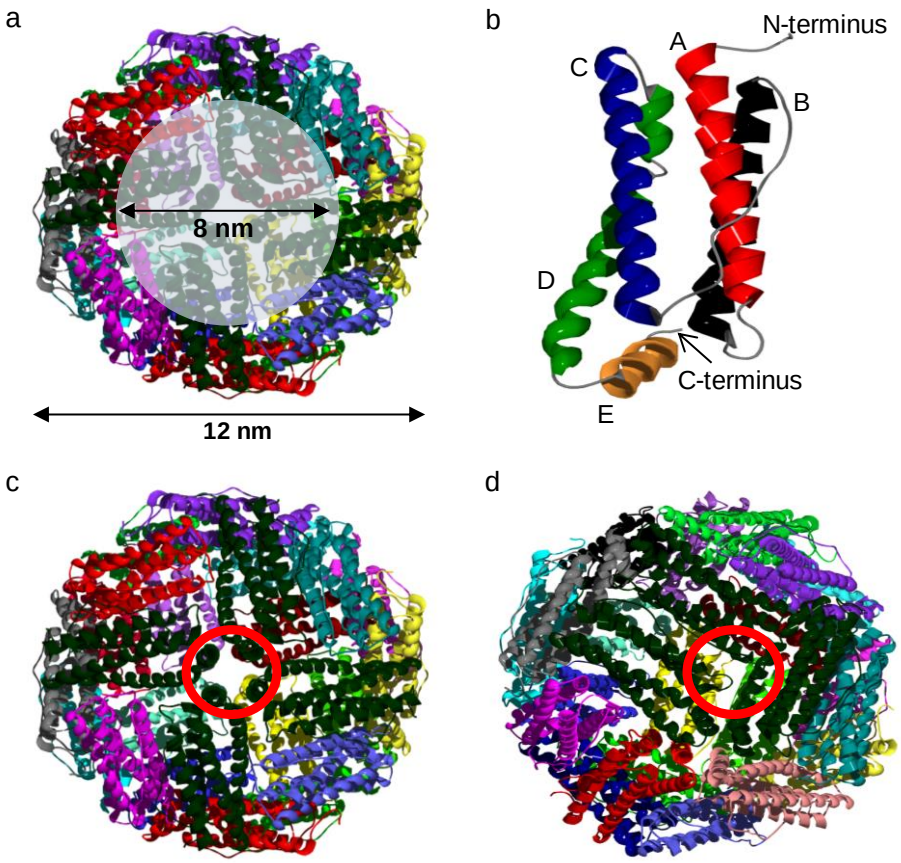

Figure 1.35. Horse spleen Ft (PDB: 4V1W). (a) Horse spleen Ft multimer (24-mer) of 8 nm core diameter and 12 nm overall diameter. (b) A single polypeptide subunit of Ft, with each helical strand coloured distinctly (helix A = red; helix B = black; helix C = blue; helix D = green and helix E = orange) and the loops and coils are coloured in grey. (c) Horse spleen Ft displaying a 4-fold channel. (d) Horse spleen Ft displaying a 3-fold channel.

1.6.3 Fe removal to generate AFt

Inside cells, the $t_{1/2}$ of endogenous Ft is about 19-24 h, under Fe deficient environments, but much longer in Fe abundant environments.[144] *In vivo*, it is postulated that Fe is released from Ft by lysosomal degradation, yet further studies are required to explore other potential avenues of Fe release from Ft i.e. by physiological reducing agents.[145,146] *In vitro*, chemical removal of Fe from Ft requires the conversion of Fe^{3+} to Fe^{2+}.[147] Examples of reducing/chelating agents explored by various groups for Fe removal from Ft includes sodium dithionite combined with *O*-phenanthroline or α-α'-bipyridine,[139] flavin mononucleotide,[148] ascorbate,[149] and thioglycolic acid.[150] Thioglycolic acid, also known as mercaptoacetic acid is commonly used for the preparation of Fe-free AFt.

1.6.4 The application of AFt

Aside from the Fe storage role typically assigned to Ft, the generation of a hollow AFt cage has many advantages and applications.[141-143,151] AFt is a natural cellular component, meaning that it is likely to be applicable as a biocompatible and non-toxic nanoparticle. AFt has a special structure, which is highly stable and water soluble. It can withstand high temperatures of ~ 75 °C for ~ 10 min and is stable in various denaturants such as sodium hydroxide, urea, and guanidinium chloride, for an appreciable period. Additionally, below pH 2, AFt disassembles into subunits but increasing the pH to 7 allows the protein to reassemble to its original size and shape, in a reproducible and uniform manner. A uniform size means that as a nanomedicine, precise control of the number of molecules encapsulated is reproducibly achieved, which ultimately is a necessary parameter for defining drug dosage. Moreover, its nano-size makes it suitable for cancer targeting by EPR, but also the H- and L-subunits have recognition sites for transferrin receptor 1 (TfR1) and Scavenger

receptor class A member 5 (SCARA5), respectively. TfR1 is overexpressed on many types of cancers, which includes GBM. Binding of AFt to TfR1 results in cellular uptake by clathrin dependent endocytosis, with its destination being the lysosomes for protein degradation and cargo release. As a result, AFt can be utilised as a naturally built-in targeted DDS, and is readily biodegradable, with an established mechanism of protein degradation and cargo release. However, one concern with AFt for nano-therapy applications is that it has been shown that excessive administration of AFt over a long period can prompt immune complex glomerulonephritis in mice.[142] There is currently a lack of evidence regarding immune responses in humans. It is ideal that a nanomedicine should go undetected by the immune system in the body. Studies will need to be carried out in humans to establish whether this may be a possible outcome.

Currently, there are a variety of applications that have been explored for AFt. Some investigated applications are listed below:

1) Drug encapsulation for treatment

AFt has been employed as a DDS for the treatment of many types of cancers. In the context of brain tumour treatment, AFt has been utilised for the encapsulation of anti-cancer drugs such as doxorubicin,[152] vincristine sulfate,[153] a conjugate of MTIC and copper,[154] and even a conjugate of TMZ and doxorubicin.[155] As such, these AFt-drug formulations have demonstrated better anti-cancer activity compared to drug alone.

2) Imaging

The superparamagnetic nature of the Fe core of Ft can allow it to be used as a *T2* enhanced MRI contrast agent.[137] However, Ft has a much lower relaxivity per iron atom compared to synthetic iron oxide nanoparticles, restricting its clinical MRI applications. To overcome this issue, one strategy involved the encapsulation of superparamagnetic iron oxide nanoparticles within AFt to create magnetoferritin, which has high relaxivity and can be used as an MRI contrast agent.[156] Gadolinium (III) complexes and manganese (oxyhydr)oxides have also been encapsulated inside AFt to create an MRI contrast agent.[157,158] Additionally, radioactive atoms such as ^{64}Cu have also been encapsulated for PET scan applications, and solution-processed lead sulfide quantum dots have been encapsulated into AFt for bioimaging purposes.[159-161] Overall, AFt is used to reduce the toxicity and improve the solubility of the imaging agents.

3) Targeted therapy

The surface of AFt provides a fitting platform for desired modifications by chemical or genetic methods for enhanced targeting or imaging purposes. The amine (amino-termini of lysine), carbonyl, and thiol (of cysteine) groups on the protein exterior are typically used as functional groups for site-specific modifications.[141] Examples of chemical modifications include carbodiimide-activated coupling of long chain (C-9, C-12, C-14) primary amines to carboxylic acid residues on the AFt surface or biotinylation of the protein shell *via* modification of amine groups initially with *N*-hydroxy-succinimide esters, to specifically link to amine groups, which can then facilitate linkage to groups such as avidin or streptavidin.[141] Fluorescence molecules like Cy5.5 have also been conjugated to AFt *via* a maleimide functional group linked to the thiol group of cysteine residues.[141] Genetic modification of the AFt surface provides an alternative method of functionalising the protein surface. For example,

recombinant H-chains have been expressed with RGD-peptides, which can bind selectively to integrin αvß3.[162]

4) Photodynamic therapy

Photosensitisers are molecules that if accumulated preferentially inside tumour cells, exert a cytotoxic effect following excitation by a light source at a suitable wavelength.[142] The photosensitiser is then promoted to an excited state and undertakes crossing with oxygen, resulting in singlet oxygen formation, which destructively attacks any organic compounds - making it highly cytotoxic.[142] AFt has been employed for the specific delivery of photosensitisers to cancer cells. For example, methylene blue-encapsulated AFt samples exhibited cytotoxic effects in MCF-7 human breast adenocarcinoma cells, when irradiated at a wavelength of 633 nm.[163]

5) Gene therapy

Recently, considerable interest has been placed on the utilisation of DDS to deliver gene silencing products such as small (or short) interfering ribonucleic acid (siRNA), to target cells for gene therapy or even as alternative means for transfecting cells over the more cytotoxic lipofectamine reagent, typically used in tissue culture assays for transfection. AFt has a negative interior surface charge, which makes it appealing for positively charged siRNA to be encapsulated. One research group has demonstrated enhanced transfection and more effective gene silencing by siRNA delivered within AFt over lipofectamine.[164]

6) Biosensor/bioassays

One example of AFt being utilised as a biosensor was carried out when AFt was genetically engineered with fused green fluorescent protein (GFP) to its C-terminus (inside AFt, but flips when a large protein is fused to it).[165] This was then chemically conjugated to DNA aptamers *via* each GFP's cysteine residues (introduced through site-directed mutagenesis). Subsequent complexes were used as fluorescent reporter probes in the aptamer-based 'sandwich' assay of the PDGF β-chain homodimer, which is a tumour biomarker.

7) Vaccine

One research group has employed *Helicobacter pylori* non-haem AFt to develop a vaccine, to produce broadly neutralizing H1N1 antibodies.[166] To do so, the haemagglutinin of the influenza virus was incorporated at the interface of adjacent subunits to form eight trimeric viral spikes on the surface of AFt. Immunisation with this nanoparticle vaccine produced one magnitude higher haemagglutination inhibition antibody titres than licensed inactivated vaccine.

8) Chimera formation

AFt can be fused to other proteins to form chimeras. The insertion of haem-agglutinin at the interface of adjacent apoferritin subunits, generates a nanoparticle with immunisation attributes.[166]

1.6.5 Mechanism of achieving drug encapsulation inside AFt

The two popular routes commonly used to load test agents inside AFt are demonstrated in Figure 1.36.[141] One route involves a direct incubation of the test agent with AFt, subsequently allowing the agent to diffuse across the channels of the AFt cage. This method is often called the 'nanoreactor' method. According to the size of the channels, this method is mostly applicable for the entrapment of small molecules. The second method involves the disassembly of the AFt cage into subunits, which occurs at lower pH values, typically at pH 2. The test agent is subsequently added to the AFt solution followed by an increase in pH to ~ 7, to facilitate the reassembly of the AFt cage around the agents. The second route is typically used for molecules that are larger in size than the channels of the AFt cage. The interior surface of AFt is negatively charged, therefore, positively charged test agents are the most likely to bind and retain well inside the cage, in addition to large sized molecules.

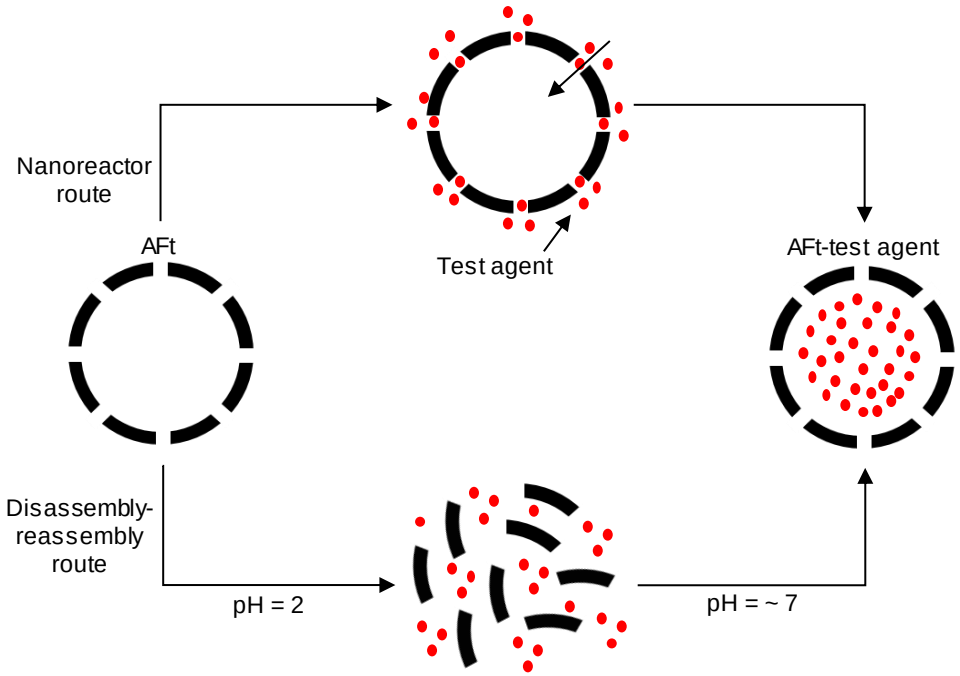

Figure 1.36. The common routes of AFt encapsulation of test agents. The nanoreactor route allows small test agents to accumulate inside AFt by diffusion across the ~ 3-4 Å sized (in diameter) channels of AFt. Alternatively, the encapsulation of larger test agents can occur *via* the disassembly-reassembly route, whereby AFt is dissociated into subunits at pH = 2 and mixed with test agents. The pH is then raised to ~ 7 to facilitate the reassembly of AFt around the test agents.

1.7 Project aims

The overall aim of the Ph.D. project is to develop alternative, novel therapies for improved treatment of high-grade brain tumours like GBM. Currently, GBM therapy is not very effective and is outdated. Also, combination of surgery, radiotherapy and TMZ chemotherapy, whilst necessary to achieve the best survival outcome fails to prolong survival beyond several months. Additionally, therapy is marred with issues of inherent and acquired drug resistance, tumour recurrence and unwanted systemic toxicity.

The Ph.D. project proposes to discover approaches towards thwarting some current TMZ chemotherapy pitfalls, namely TMZ resistance and toxicity. To do this, the project will employ the use of AFt, as a natural DDS for the encapsulation of TMZ, TMZ analogues (N3P and T25) and TMZ in combination with inhibitors of MGMT (*O6*-Benzylguanine (*O6*-BeG)) or PARP-1 (niraparib (NRP)). Utilising AFt would allow targeted drug delivery across the BBB, to GBM tumours with overexpressed TfR1, for specific and selective GBM cell uptake. By doing this, the aim is to enhance drug potency and minimise drug toxicity towards non-cancerous tissues. Overall, the aim is to prolong and improve patient survival and quality of life.

The objectives of the Ph.D. include:

1) To develop and optimise the encapsulation method for TMZ, N3P, T25, *O6*-BeG and NRP to achieve good test agent load inside AFt, and still maintain AFt capsule integrity.
2) The characterisation of AFt-test agent formulations to establish success of the test agent encapsulation.

3) The evaluation of the activity of AFt-test agent formulation, in comparison to test agent and AFt alone, against a broad spectrum of cell lines. These include TMZ-resistant and non-resistant cancer and non-cancer cell lines.
4) The investigation of (the) mechanism(s) driving the differences in the activity seen between test agent alone, AFt alone, and AFt-test agent in TMZ-resistant and non-resistant cell lines.

Chapter 2 – Materials and methods

2.1 Materials

Table 2.1. List of materials used for experimental studies.

Materials	Manufacturer/supplier
0.22 µm polyethersulfone filter	Sartorius
10 cm tissue culture treated petri dish	Thermo scientific
10x trypsin-EDTA solution	Sigma-Aldrich
16% formaldehyde-MeOH free	Thermo scientific
2-mercaptoethanol	Sigma-Aldrich
8 well µ-slide glass plate	Ibidi
clear, flat bottom polystyrene 96-well plate	Corning
Acetic acid	Fisher Scientific
Amicon ultra-4 centrifugal filter molecular weight cut-off (MWCO; 30kDa)	Merck Millipore
Blotting filter (chromatography; 3 mm) paper	GE Healthcare Whatman
Bradford reagent	Scientific Laboratory Supplies
Bromophenol blue	Sigma-Aldrich
Bovine serum albumin (BSA)	VWR
Coomassie brilliant blue G250	G Biosciences
Cryogenic vials	Scientific Laboratory Supplies
4',6-diamidino-2-phenylindole (DAPI)	Sigma-Aldrich
DTS1070 cell	Malvern Panalytical
eBioscience wash buffer 1x	Invitrogen
Enhanced chemiluminescence (ECL) reagent	GE Healthcare Amersham
FACS tubes (75x12 mm, polystyrene)	Sarstedt
Fetal bovine serum (FBS) heat inactivated, non-USA origin, sterile filtered	Sigma-Aldrich
Fisherbrand regenerated cellulose dialysis tubing (MWCO: 12-14000 Da)	Fisher Scientific
Horse spleen Ft	Sigma-Aldrich
Horse spleen AFt	Sigma-Aldrich
Geneticin (G418)	Sigma-Aldrich
Gentamicin	Scientific Laboratory Supplies

Glycerol	Sigma-Aldrich
Horse spleen Ft	Sigma-Aldrich
IgG (Total) Mouse Uncoated ELISA Kit	Invitrogen
L-glutamine	Sigma-Aldrich
MEM medium	Sigma-Aldrich
Mercaptoacetic acid	Fisher Scientific
Methylene blue	Fisher Scientific
Microsart research mycoplasma detection kit for qPCR (cat no. SMB95-1005)	Sartorius
Monoclonal primary (1°) Ab, mouse anti-human *O6*-MeG	Axxora
Mouse anti-human phospho-histone H2A.X (Ser139) 1° Ab, clone JBW301	Merck
3-(4,5-dimethylthiazol-2-yl)-2,5-diphenyltetrazolium bromide (MTT)	Alfa Aesar
Sodium chloride (NaCl)	Fisher Scientific
Tissue culture treated, clear flat bottom polystyrene 6-well plates	Corning
Sodium acetate (NaOAc)	Fisher Scientific
NativeMark protein standard	Invitrogen
MEM Non-essential Amino Acid (NEAA) Solution (100x) without L-glutamine, liquid, sterile-filtered	Scientific Laboratory Supplies
Whatman nitrocellulose membrane	GE Healthcare Amersham
Novex nativePAGE 4-16% Bis-Tris pre-cast gel	Fisher Scientific
Novex gel cassette Pre-sealed on three sides with slot pre-taped; 1.5mm	Fisher Scientific
Nonidet P-40 (NP-40)	Sigma-Aldrich
F(Ab')2-goat anti-mouse IgG, IgM (H+L) Alexa-fluor 488	Invitrogen
Phosphate-buffered saline (PBS)	Thermo Scientific, Oxoid
Penicillin/streptomycin	Sigma-Aldrich
Phalloidin-iFluor 633 conjugate	AAT Bioquest
Phosphatase inhibitor	Roche
Propidium iodide (PI)	Sigma-Aldrich
Polythene layflat tubing	Scientific Laboratory Supplies
Ponceau red S	Fisher Scientific
Pre-stained molecular weight (MW) standard (10-250 Da)	Thermo Scientific

Protamine sulfate	Sigma-Aldrich
Protease inhibitor	Roche
Blood & Cell Culture DNA mini purification kit	QIAGEN
Ribonuclease A (RNaseA)	Scientific Laboratory Supplies
Roswell Park Memorial Institute 1640 (RPMI-1640) medium	Sigma-Aldrich
Sodium dodecyl sulfate (SDS)	Thermo Scientific
Non-fat dried milk	ASDA
Slide-A-Lyzer 10 K MWCO device	Thermo Fisher Scientific
Sodium citrate	Fisher Scientific
Sterile dimethyl sulfoxide (DMSO)	Sigma-Aldrich
Sterile, cell culture Hepes buffer	Sigma-Aldrich
Sterile, cell culture sodium bicarbonate	Sigma-Aldrich
Stop solution	Invitrogen
Suprasil quartz cuvette	Hellma Analytics
T25	University of Nottingham (Helen Summers)
N3P	University of Nottingham (Helen Summers)
TGS1x0.2 Gold Slot grid	EM resolutions
Timesaver MspI restriction enzyme kit	New England Biolabs
TMZ	Sigma-Aldrich
Tris(hydroxymethyl)aminomethane (Tris)	Fisher Scientific
Triton X-100	Sigma-Aldrich
Trypan blue	Sigma-Aldrich
Tween20	Thermo Fisher Scientific
Vented T25/T75 cm^2 culture flasks	Corning
10-well comb	Invitrogen
NRP (MK-4827) tosylate	Selleckchem
O6-BeG	Sigma-Aldrich
Human anti-TfR1 R-PE conjugated 1° Ab	Invitrogen

Table 2.2. Human cell lines used for experimental studies.

Cell lines	Description	Manufacturer/supplier
U373V	GBM; MGMT -ve	Schering Plough
U373M	GBM; MGMT +ve	Schering Plough
LN-18	GBM; MGMT +ve	ATCC
HCT116	MLH1 -ve; MGMT +ve	ATCC
HCT116-VR	MLH1 -ve; MGMT +ve; P-glycoprotein 1 (Pgp) +ve	ATCC
MRC-5	Normal lung fibroblasts	ATCC

2.2 Generating AFt from horse spleen Ft

In vitro, chemical removal of Fe from Ft through either the reductive dissolution of Fe^{3+} to Fe^{2+} followed by chelation and removal of Fe^{2+} by dialysis (*via* the 3-fold protein channels) or direct chelation of Fe^{3+} and removal by dialysis have been successfully carried out.[147] The reducing/chelating agent must first penetrate the protein cage *via* the channels to react with the Fe core. Thioglycolic acid is an effective, stable reducing agent at low pH. Once the acid is deprotonated to reduce Fe^{3+} to Fe^{2+}, the dianion then complexes with the Fe and is cleared by dialysis. It is necessary that the dialysis buffer is frequently changed, and that fresh, excess acid is added after each buffer change in order to prevent the re-oxidation of Fe^{2+} to Fe^{3+}, since the rate of re-oxidation is high.[147]

Horse spleen AFt (pale yellow colour) was generated from horse spleen Ft (dark red/brown colour) *via* a reductive demineralisation process. Initially, 2L of 0.1 M sodium acetate (NaOAc) buffer was prepared, and the pH was adjusted to 5.5 with acetic acid using a Mettler Toledo pH meter. The buffer solution was then purged using nitrogen, at room temperature (RT) for 20 min. Following this, Ft (55 mg/mL) was diluted to 5.5 mg/mL with 0.1 M NaOAc buffer (pH 5.5) and the solution was subsequently transferred to a pre-wet Fisherbrand regenerated cellulose dialysis tubing (MWCO: 12-14000 Da). Ft was dialysed against 0.1 M NaOAc buffer (pH 5.5), with nitrogen constantly purged through the solution, at RT, under 300 rpm stirring. Thereafter, 0.03 M mercaptoacetic acid (3 mL) was added to the buffer and the sample was dialysed for 3 h (first 2 mL of acid for 2 h then another 1 mL of acid for an additional 1 h). A total of 6 rounds of mercaptoacetic acid additions were performed, each round proceeding after the dialysis bag was placed in freshly prepared buffer. After the final round, the

protein was dialysed against fresh buffer without acid for 1 h. The AFt solution was collected and sterilised through a sterile 0.22 µm polyethersulfone filter. AFt was then aliquoted into 1 mL fractions in microcentrifuge tubes and stored at -20 °C.

2.3 Test agent encapsulation into AFt by nanoreactor route

The following test agents: TMZ (194.15 g/mol), N3P (218.18 g/mol), T25 (258.26 g/mol), *O6*-BeG (241.25 g/mol) and NRP (salt form: 510.61 g/mol) were encapsulated into AFt by diffusion across the AFt channels into the interior core. Test agent solutions (TMZ: 10 mM, 7.2 µmol; N3P/T25/*O6*-BeG: 10 mM, 6.3 µmol; NRP: 10 mM, 0.9 µmol) were initially prepared in DMSO from dry powder stored at 2-8 °C (for TMZ and *O6*-BeG) and -20 °C (for N3P, T25 and NRP). Whilst the test agents were left to fully dissolve in DMSO on a tube roller, AFt solution (0.0045 mM, 0.009 µmol) was prepared in a glass scintillation vial containing a stir bar, by diluting the stock (thawed after removal from -20 °C) with 0.1 M NaOAc buffer (pH 5.5). The AFt solution was placed on a magnetic stirrer set to 300 rpm in a cold room at T = 2-8 °C. Test agent solution (in small volume increments) was added, every 30 min, to the AFt solution to prevent precipitation of the test agent. The solution was then ultra-filtered through an Amicon ultra-4 centrifugal filter (MWCO: 30 kDa) at 4000 *g* using the Allegra 25R centrifuge (Beckman Coulter) for 4 min. The resulting samples named as AFt-TMZ, AFt-N3P, AFt-T25, AFt-*O6*-BeG and AFt-NRP were sterilised through a sterile 0.22 µm polyethersulfone filter and stored at 2-8 °C.

Additionally, AFt-TMZ and AFt-*O6*-BeG (AFt-TMZ+AFt-*O6*-BeG), as well as AFt-TMZ and AFt-NRP (AFt-TMZ+AFt-NRP) combination mixtures were

prepared alongside TMZ and *O6*-BeG (TMZ+*O6*-BeG), and TMZ and NRP (TMZ+NRP) unencapsulated combination mixtures. First, the concentration of TMZ, *O6*-BeG and NRP encapsulated into AFt was determined. Subsequently, a 1:1 v/v solution of AFt-TMZ and AFt-*O6*-BeG or AFt-TMZ and AFt-NRP was prepared. This meant that the final molar ratio of TMZ to *O6*-BeG in solution was measured to be 1 (TMZ):1 (*O6*-BeG) and TMZ to NRP in solution was 5.8 (TMZ):1 (NRP). The resulting combination mixtures were sterilised through a sterile 0.22 µm polyethersulfone filter and stored at 2-8 °C.

2.4 Characterisation of AFt formulations

2.4.1 Bradford assay for protein concentration determination

The Bradford assay was carried out to determine the concentration of AFt.[167] Here, an acidified Coomassie Brilliant Blue G-250 (doubly protonated; brown) dye was used. In the presence of proteins, the dye first donates an electron to charged groups on the protein, which ultimately results in protein structure disruption and unravelling of hydrophobic pockets. The dye then interacts with these pockets through the binding of sulfonic acid groups in the dye to positive amine groups of amino acids such as lysine's, arginine's and to a lesser degree histidine's, tryptophan's and tyrosine's, in addition to Van der Waals interactions.[168] Bound dye (unprotonated; blue) was spectrophotometrically quantified by observing a shift in absorbance maxima from 470 nm (unbound dye) to 595 nm (bound dye).[169] The amount of blue dye measured at 595 nm was directly proportional to the amount of protein in the solution. The green form of the dye that donates an electron but does not bind protein (absorbs at 650 nm) was not quantified in this assay.

The assay was carried out in a clear, flat bottom polystyrene 96-well plate. A standard curve of known concentrations of BSA or AFt (Sigma-Aldrich) were prepared with Milli-Q water from a 10 mg/mL (BSA: 0.150 μmol; AFt: 0.023 μmol) stock. Linearity was achieved with a concentration range of 0.1–1 mg/mL. Triplicate of each sample were performed on the same plate and on three separate occasions. The samples of known and unknown concentrations (10 μL) were combined with Bradford reagent (140 μL; 1:15 dilution) to achieve a total volume of 150 μL, and the plate was placed on an orbital shaker (name of machine) for 5 min, in the dark. The absorbance of the samples was read using a PerkinElmer Envision optical accessories plate reader at λ = 595 nm. Thereafter, the absorbance was plotted on the y-axis against concentration (x-axis) to provide a linear standard curve with Equation (2.1) and $R^2 > 0.9$. Unknown sample concentrations were determined from a measured absorbance value (y) that was inserted into Equation (2.1) to generate a concentration value (x).

$$y = mx + c \tag{2.1}$$

2.4.2 UV-Vis spectroscopy for test agent standard curve formation and concentration determination

First, to obtain the concentration of AFt by absorbance readings, the Beer-Lambert Equation (2.2) was employed.[170] Proteins containing tryptophan, tyrosine and cysteine amino acids can absorb at 280 nm. The molar extinction coefficient of horse spleen AFt is reliant on the relative concentrations of the three amino acids. The theoretical calculated molar extinction coefficient of AFt assuming all cysteines were reduced was 349540 $M^{-1}\,cm^{-1}$ (22 L-subunits and 2 H-subunits, each subunit with extinction coefficients at 280 nm in water of 14440 and 15930 $M^{-1}\,cm^{-1}$, respectively, assuming all cysteines were reduced),

determined from ProtParam, using protein amino acid sequences (see Figure 2.1) obtained from UniProtKB. Both software's were accessed from ExPASy SIB Bioinformatics Resource Portal.

$$A = \varepsilon c l \quad (2.2)$$

where:
A = Absorbance
ε = Molar extinction coefficient ($M^{-1}\,cm^{-1}$)
c = Concentration (M)
l = Optical light path (cm)

L-subunit of horse spleen Ft:

MSSQIRQNYSTEVEAAVNRLVNLYLRASYTYLSLGFYFDRDDVALEGVCHFF
RELAEEKREGAERLLKMQNQRGGRALFQDLQKPSQDEWGTTLDAMKAAIV
LEKSLNQALLDLHALGSAQADPHLCDFLESHFLDEEVKLIKKMGDHLTNIQRL
VGSQAGLGEYLFERLTLKHD

H-subunit of horse spleen Ft:

MTTAFPSQVRQNYHQDSEAAINRQINLELHASYVYLSMSFYFDRDDVALKNF
AKYFLHQSHEEREHAEKLMKLQNQRGGRIFLQDIKKPDQDDWENGLKAME
CALHLEKNVNESLLELHKLATDKNDPHLCDFLETHYLNEQVKAIKELGDHVT
NLRRMGAPESGMAEYLFDKHTLGECDES

Figure 2.1. Primary amino acid sequences of horse spleen Ft L-subunit (entry code: P02791) and H-subunit (entry code: Q8MIP0) obtained from UniProtKB.

To generate a test agent standard curve, known test agent concentrations was plotted against their absorbance values to produce a linear regression standard curve. The samples of known concentrations were prepared from a stock, by weighing out known amounts of the test agent and dissolving them in DMSO (10 mM, 10 µmol). Subsequently, a range of concentrations (TMZ: 5-200 µM; N3P: 5-200 µM; T25: 5-200 µM; *O6*-BeG: 5-100; NRP: 5-75 µM) were prepared in 99:1 %v/v DMSO:NaOAc (0.1 M; pH 5.5). The absorbance of each test agent sample (1 mL) was measured using the Varian Cary 50 UV-Vis spectrophotometer (TMZ: λ = 330 nm, N3P: λ = 328 nm, T25: λ = 364 nm, *O6*-BeG: λ = 287 nm and NRP: λ = 315 nm) with a Suprasil quartz cuvette (1 cm

light path). The absorbance was later plotted on the y-axis against concentration (x-axis) to generate a linear standard curve with Equation (2.1) and $R^2 > 0.9$. Triplicate of each sample were performed on the same day and on three separate occasions. Unknown sample concentrations were determined by diluting the sample 1:100 using DMSO. The measured absorbance value obtained (y), was inserted into Equation (2.1) to generate a concentration value (x) and the value was later multiplied by its dilution factor. Additionally, a wavelength scan ranging from 200 to 1000 nm was carried out for Ft and AFt samples (2 mg/mL), to obtain absorbance peaks at different wavelengths.

2.4.3 Determining efficiency of AFt encapsulation of test agents

After calculating the concentration of test agent and AFt before and after purification (to remove unencapsulated drugs), the drug:AFt (D:A) ratio, % encapsulation efficiency (%EE), % drug loading (%DL) and % protein yield were calculated following Equations (2.3-2.6).

$$D:A = \frac{Final\ mol\ of\ drug}{Final\ mol\ of\ AFt} \tag{2.3}$$

$$\%EE = \frac{Final\ mol\ of\ drug}{Initial\ mol\ of\ drug} \times 100 \tag{2.4}$$

$$\%DL = \frac{((No.\ of\ drug\ molecules\ inside\ cage \times MW\ of\ drug) \times 100)}{((No.\ of\ drug\ molecules\ inside\ cage \times MW\ of\ drug) + MW\ of\ AFt)} \tag{2.5}$$

$$\%\ protein\ yield = \frac{Final\ mol\ of\ protein}{Initial\ mol\ of\ protein} \times 100 \tag{2.6}$$

All values are stated as mean ± SD of n = 3.

2.4.4 Molecular weight determination of AFt subunit and full cage

PAGE is a process that causes proteins to be separated according to size *via* electrophoresis, by travelling through a mesh-like gel matrix, with smaller proteins migrating faster through the gel matrix than larger proteins.[171] Protein structure and charge can also affect the run. In sodium dodecyl sulfate polyacrylamide gel electrophoresis (SDS-PAGE), the SDS (which coats the protein in negative charge) and denaturing components (heat and reducing agent) eliminate the influence of protein structure and charge, allowing proteins to be separated solely based on polypeptide chain length. As for native polyacrylamide gel electrophoresis (native-PAGE), proteins are separated in their native (non-denatured) state. Therefore, the influences of mass, charge and shape are present during the separation process. Alternatively, red native PAGE utilises ponceau red S to impart negative charge to the protein surface without denaturing the protein.[172] This allows us to monitor the run according to mass only. Other chemical agents have also been utilised to impose uniform charge on proteins without denaturation. A popular example is the blue native-PAGE technique that has been used for the separation of membrane proteins.[173] However, Ponceau Red S has been shown to bind to proteins less tightly than Coomassie Brilliant Blue and this advantageously allows the dye to be removed more easily without protein structure disruption, *via* simple washing steps.

SDS-PAGE:

Recipe:

- 10% resolving gel: 4 mL dH_2O, 3.3 mL acrylamide mix (30%), 2.5 mL Tris (1.5 M; pH 8.8), 0.1 mL SDS (10%), 0.1 mL AMPS (10%) and 0.004 mL TEMED. Total volume: 10 mL.
- 5% stacking gel: 3.4 mL dH_2O, 0.83 mL acrylamide mix (30%), 0.63 mL Tris (1.0 M; pH 6.8), 0.05 mL SDS (10%), 0.05 mL AMPS (10%) and 0.005 mL TEMED. Total volume: 5 mL.

- 4x SDS-PAGE Loading buffer: 4 mL glycerol (100%), 2.4 mL Tris (1.0 M; pH 6.8), SDS (0.8 g), bromophenol blue (4 mg), 3.1 mL dH_2O.
- Running buffer 10x: Tris (250 mM), glycine (1920 mM) and SDS (1%). Total volume: 1 L (make up volume with dH_2O).
- Running buffer 1x: A 1:10 dilution was carried out using 10x running buffer (final concentrations: Tris (25 mM), glycine (192 mM) and SDS (0.1%)). Total volume: 1 L (make up volume with dH_2O).

SDS-PAGE was carried out on Ft, AFt, AFt (Sigma-Aldrich) to monitor the purity of the protein. SDS-PAGE gels were prepared by adding the 10% resolving gel solution into the Novex gel cassette, followed by the addition of isopropanol (80 µL) to remove any air bubbles. The resolving gel was left to polymerise for ~ 30 min. The isopropanol was then removed, and the 5% stacking gel solution was added, followed by the insertion of a 10-well comb. The stacking gel was left to polymerise for ~ 30 min. Once the gel has polymerised the gel cassette was stored at 2-8 °C, for up to a week. Samples (10 µg; 15 µL) and 5 µL of the following solution: 118.75 µL of 4x SDS-PAGE loading buffer and 6.25 µL of 2-mercaptoethanol, were mixed in microcentrifuge tubes. They were further denatured under heating at 95 °C for 10 min. Each sample was then pulse centrifuged to bring down the condensation and briefly vortexed. The cassette was inserted into a XCell SureLock Mini-Cell (Invitrogen) followed by the addition of 1x running buffer (to fill entire inner chamber above the wells and a ¼ of the outer chamber). Pre-stained MW standards (10 µL) and samples (18 µL) were loaded into the wells of the gel and the run proceeded for 20 min at 90 V to allow samples to align at the bottom of the stacking gel before switching to 150 V for 35-45 min to allow protein bands to separate according to size on the resolving gel. After, the gel was stained with Coomassie brilliant blue G250 for 1 h and de-stained overnight in dH_2O, gel was imaged using Gene flow limited.

Red native-PAGE:

Recipe:

- 10x Cathode buffer: Tricine (500 mM), Bis-Tris/HCl (150 mM), 500 mL dH_2O and adjust to pH 7.0 with hydrochloric acid.
- 1x Cathode buffer: Make up to 1 L. A 1:10 dilution was carried out using 10x cathode buffer (final concentrations: Tricine (50 mM), Bis-Tris/HCl (15 mM) and add ponceau red S (0.012%).
- 10x Anode buffer: Bis-Tris/HCl (500 mM) and 1 L dH_2O. Adjust to pH 7.0 with hydrochloric acid.
- 1x Anode buffer: Make up to 1 L. A 1:10 dilution was carried out using 10x anode buffer (final concentrations: Bis-Tris/HCl (50 mM)).
- 4x native-PAGE loading buffer: glycerol (60%), Bis-Tris/HCl (200 mM; pH 7.0) and ponceau red S (0.08%).

A recent new application of red native-PAGE was used.[172,174] Here, the proteins were coated in Ponceau red S to impart a uniform negative charge, without denaturation to allow proteins to migrate only according to size. Adopting this protocol, red native-PAGE was performed on Ft, AFt, AFt (Sigma-Aldrich), AFt-TMZ, AFt-N3P, AFt-T25, AFt-*O6*-BeG and AFt-NRP to monitor protein stability/ integrity. Samples (1 µg; 15 µL) and 5 µL of 4x native-PAGE loading buffer were mixed in microcentrifuge tubes and left on wet ice. The Novex nativePAGE 4-16% Bis-Tris pre-cast gel was loaded into a XCell SureLock Mini-Cell (Invitrogen) followed by the addition of 1x cathode buffer to cover the wells in the inner chamber and 1x anode buffer to cover a ¼ of the outer chamber. Samples (18 µL) were separated alongside the NativeMark protein standard (5 µL) at 2-8 °C for 1 h at 150 V and 1 h at 250 V. The gel was stained with Coomassie brilliant blue G250 for 1 h and left to de-stain overnight in water before gel imaging.

2.4.5 AFt size and charge measurements

The average hydrodynamic nanoparticle size (from dynamic light scattering (DLS)) and zeta potential (ζ-potential) were measured for Ft, AFt, AFt (Sigma-Aldrich) AFt-TMZ, AFt-N3P, AFt-T25, AFt-*O6*-BeG and AFt-NRP. DLS measures the rate at which the intensity of scattered light fluctuates from particles undergoing Brownian motion, which is the random motion of particles when bombarded by surrounding solvent molecules, because of a laser beam hitting the particles.[175] It is known that smaller particles are pushed further by the solvent molecules and move more rapidly in solution. The speed of the particles undergoing Brownian motion is computed by DLS, generating a parameter called translational diffusion coefficient (D).[175] This parameter can be affected by sample particle size, viscosity, and temperature. To determine particle size, sample viscosity and temperature were kept constant and since the viscosity of the solvent is related to the temperature, the type of solvent and temperature were factored into the zetasizer prior to measurement. The zetasizer then calculates the hydrodynamic diameter from the translational diffusion coefficient (D) using the Stokes-Einstein equation (see Equation (2.7)).[175] The translational diffusion coefficient is dependent not only on the particle but also on the surface structure of the particle i.e. any additional surface ligands on the particle, as well as the concentration and type of ions in the medium that will form the solvent layer around the particle. Therefore, the hydrodynamic diameter of a spherical particle is that of the spherical particles itself in addition to the surface structures and solvent surrounding layer of the particle.[175]

$$D = k_B T/6\pi nr \quad (2.7)$$

where:
r = hydrodynamic radius
D = translational diffusion coefficient
k_B = Boltzmann constant
T = absolute temperature
n = viscosity

The zetasizer was primarily programmed to obtain a relative intensity weighted size distribution displayed as a plot of relative intensity of light scattered by particles (Y-axis) versus hydrodynamic size (X-axis).[175] As such, in cases when there were multiple peaks present on the plot the Mie theory was employed to convert the intensity distribution to a volume or number-based size distribution.[175] This gives a more realistic view of the importance of any additional peaks that were present. However, it was crucial that parameters such as the dispersant viscosity and refractive index of the particles and solvent were factored into the zetasizer.

Additionally, charged particles dispersed in a liquid would have a thin layer of ions of opposite charge strongly bound to its surface, known as the Stern layer.[175] A second diffuse outer layer, composed of loosely associated ions, called the diffusive ion layer is also present.[175] Collectively these two layers form what is called the electrical double layer.[175] As the particle moves in the liquid phase due to an applied electrical field, gravity and/or kinetic energy, a boundary between the ions in the diffuse layer (that move with the particle) and ions that remain with the bulk dispersant is formed. The electrostatic potential at this slipping plane boundary is the ζ-potential, which is measured using the Henry equation (see Equation (2.8)).[175] The electrophoretic mobility (which is a ratio of the particle velocity and external applied field) is the parameter measured by the zetasizer that is required to calculate the ζ-potential.[175]

$$\mu_e = (2 \times \varepsilon \times z \times (f(\kappa \times \alpha))) / (3 \times \eta) \quad (2.8)$$

Where:
μ_e = Electrophoretic mobility
ε = Dielectric constant
z = ζ-potential
$f(k \times \alpha)$ = Henry function (α is the radius of the particle and k is the Debye parameter (represents the thickness of the electric double layer). For particles in polar media the f(k x α) is approximate to its maximum value of 1.5, known as the Smoluchowski approximation.
η = absolute zero-shear viscosity of the medium

The AFt samples were diluted prior to measurement with deionised water (dH_2O; pH 7.2; AFt: 0.9 μM, 0.0009 μmol), and then measured using Malvern Zetasizer Nano ZS (measurement backscatter angle: 173°; λ = 633 nm; temperature (T) = 25 °C; refractive index of dH_2O: 1.33; refractive index of sample: 1.33; Smoluchowski model: F(ka) = 1.5). The equilibration time was 120 seconds (s) for samples placed in the zetasizer to reach a T = 25 °C prior to measurements. The number of measurements per sample was 3, with 13 runs per measurement. The samples were filtered through a sterile 0.22 μm polyethersulfone filter, prior to measurements, and measured in a disposable DTS1070 cell, first performing DLS and then ζ-potential readings. Readings were performed on three different batches.

2.4.6 Storage stability

Storage stability of AFt formulations (AFt-TMZ, AFt-N3P and AFt-T25) stored at 2-8 °C under pH 5.5 (0.1 M NaOAc) buffered conditions was monitored daily over a 7-day period. The following parameters monitored were hydrodynamic size by DLS, ζ-potential, and protein and test agent concentrations to determine D:A by Bradford assay and UV-Vis spectroscopy, respectively. Triplicate measurements were performed from three different batches.

2.4.7 *In vitro* test agent release

Release of TMZ, N3P and T25 from AFt nanocages was studied. AFt formulations (400 µL) were added into the small dialysis tube of the Slide-A-Lyzer 10 kDa MWCO device and samples were dialysed at 37 °C (and shaken at 150 rpm) against 14 mL of either pH 5.5 NaOAc buffer (0.1 M) or pH 7.4 PBS (1x). After 1, 3, 5, 7 and 24 h dialysis, 1 mL of the release medium (solution outside the dialysis tube) was extracted and measured by UV-Vis spectroscopy before returning to device to continue dialysis.

2.5 Cell culture

2.5.1 Reviving cell stocks

Cell lines (see Table 2.2) were handled under sterile conditions and work was carried out inside a BioMat^2 MDH Class II microbiological safety cabinet with a laminar flow system. The interior of the cabinet and all materials inserted into the cabinet, including gloved hands, were decontaminated with 70% industrial methylated spirits (IMS). New cell batches were retrieved from liquid nitrogen storage (-196 °C). The cell vials were defrosted immediately and quickly, using a 37 °C, pre-heated, water bath. Vials were sterilised with 70% IMS before transferring thawed cells to a T75 cm^2 culture flask containing 10 ml of pre-warmed complete growth medium with 20% FBS (see section 2.5.2 for complete growth medium recipe). Cell flasks were examined under the Nikon Eclipse TS100 inverted light microscope for signs of infection. If infection free, cell flasks were maintained in the Sanyo CO_2 incubator (at 5% CO_2, 37 °C, humid conditions). The next day, flasks were inspected again for cell viability and infection and medium was replaced with fresh pre-warmed medium to remove DMSO and dead cells. All cell lines used were tested for mycoplasma infection using Microsart research mycoplasma detection kit for qPCR and following manufacturer's instructions. Medium replacement was performed

every 2-3 days until cell coverage in the flasks reached ~ 70-80% confluency; after which 10% FBS was used to make up the complete growth medium.

2.5.2 Passaging and maintaining cell lines

Human GBM cell lines, U373V and U373M, were cultured in RPMI-1640 medium with 10% FBS, 1% NEAA, 50 µg/mL gentamicin and 400 µg/mL G418, whilst LN-18 cells were culture in DMEM medium (containing high glucose and L-glutamine) with 10% FBS and 1% penicillin/streptomycin. Human colorectal carcinoma cell lines, HCT116 and HCT116-VR were cultured in RPMI-1640 medium with 10% FBS and 1% penicillin/streptomycin. Human healthy lung fibroblast cell line, MRC-5, was cultured in MEM medium with 10% FBS, 1% NEAA, 1% penicillin/streptomycin, 2 mM L-glutamine, 10 mM Hepes buffer and 0.075% sodium bicarbonate. Cell lines were cultured in T25 cm^2 culture flasks. Passaging (to maintain normal logarithmic cell growth) was carried out when cells were ~ 70-80% confluent; once a week for U373V and U373M cells and twice a week for all other cell lines. Upon reaching 70% confluency, medium was aspirated, and cells were washed with PBS (sterilised by autoclaving) before adding 0.5 mL of 1x trypsin-EDTA solution. To ensure efficient cell detachment, trypsin was evenly spread across the surface of the flask to cover all cells and the flasks were then placed in an incubator for 3-5 min, to allow enough time for cells to detach from the flask. Detached cells were then neutralised with 4.5 mL of medium, and subsequently 300 µL of U373V/U373M cell suspensions or 0.5-1 mL for other cell suspensions were transferred to a new flask containing 6 mL of fresh new medium, pre-heated to 37 °C. Cell flasks were discontinued once they have reached passage number 30, in order to avoid genotypic and phenotypic drift. New cells were then revived from liquid nitrogen.

2.5.3 Protocol for freezing cells

Cells were cryopreserved for long term storage in liquid nitrogen. First, medium was aspirated and attached cells were washed with PBS. PBS was then removed by aspiration and subsequently 1 mL of 1x trypsin-EDTA was added to detach cells from the flask. Trypsin was evenly spread across the surface of the flask to cover all cells and the flasks were then incubated for 3-5 min. Later, 1 mL of freezing medium (90% FBS and 10% sterile DMSO; stored at 2-8 °C) was added to detached cells and homogenous cell solutions were transferred to sterile cryogenic vials (1 mL per vial). Cells were frozen gradually in a three-step process. First cryogenic vials were placed overnight at -20 °C. Subsequently, they were transferred to -80 °C for 24 h, before being transferred to its final storage destination, for long term storage, in liquid nitrogen (-196 °C).

2.6 *In vitro* cytotoxicity testing

For all *in vitro* assays, cells from flasks were harvested by trypsinisation at ~ 70-80% confluency. After deactivating the trypsin with 4.5 mL of fresh medium, the cell suspension was gently passed through a syringe with an attached 23-gauge needle, twice, to obtain a single cell suspension. Cells were counted using a haemocytometer (always counting the same six grids) and the amount of cell suspension needed was determined based on the required seeding density for the assay to be undertaken.

2.6.1 MTT assay – 6 days test agent treatment

MTT is a yellow, water-soluble tetrazolium salt that is reduced by metabolically active (healthy) cells to form purple, water-insoluble formazan crystals.[176] Formazan must be solubilised by miscible solvents such as DMSO prior to measurement by absorbance readings at 570 nm.

Formazan production is proportional to the number of metabolically viable cells. Prior to current understanding, it was assumed that MTT reduction was carried out solely in the mitochondria by the mitochondrial electron transport chain, with succinate dehydrogenase considered the major site.[177] It was later established that MTT is endocytosed, and after entering the cells, MTT reduction could occur in different locations in the cell (not just in the mitochondria), by various oxidoreductases (which utilise NAD(P)H), small reducing molecules and superoxides.[177] The formazan then exits the cell by exocytosis, forming needle-like crystals at the cell surface; thereby inhibiting further uptake of MTT (by inhibiting endocytosis).[177,178] It has since been reported that MTT reduction can be affected by multiple factors such as by the levels of glucose, its uptake rate, rate of glycolysis, levels of lactate and pyruvate and rate of endocytosis of MTT and exocytosis of formazan.[179]

Therefore, MTT incubation period and concentration was decided accordingly to allow enough time for MTT to be taken up and reduced without toxicity, as the needle-like formazan crystals kill the cells once they puncture the plasma membrane during exocytosis; inhibiting further uptake of MTT by endocytosis. Indeed, it has been reported that at the time of MTT addition, it took B12 cells at nearly 100% confluency, > 6 h to exocytose formazan, but around 3 h when cells were at stationary phase.[177] Hence, the duration of MTT incubation and concentration were decided based on the confluency state of cells at the point

of MTT addition. MTT reduction could also be affected by the growth conditions of cells, so cells were maintained under healthy conditions, with enough nutrients and correct seeding densities; the only factor affecting the cells was the drug itself. Henceforth, various experimental controls were included to conclusively ensure that any growth inhibitory effects seen, were from the test agent's activity in the cells.

Cells were seeded in a tissue culture treated, clear flat bottom polystyrene 96-well plate at the following seeding densities: U373V and U373M cells: 650 cells/well, LN-18 cells: 1000 cells/well and HCT116, HCT116-VR and MRC-5 cells: 400 cells/well. There were 5 replicates for each concentration of test agent, 16 for T0 control and 20 for cell only controls. In addition, medium only (200 µL) was added to columns 1 and 12 to serve as additional controls and to minimise medium evaporation from the plate. Cells were seeded in wells at a volume of 180 µL. Cells were treated with test agent 24 h post-seeding and incubated (37 °C; 5% CO_2) for 6 days (see table 2.3 for the concentrations of test agents used). Test agent solutions were prepared immediately before each assay at a concentration 10x greater than the final concentrations required in the well. Subsequently, 20 µL of the test agent or medium (to cell only controls) were added to each well to achieve a final volume of 200 µL per well.

Also, to assess whether the test agents or solvent/buffer reacts with MTT, three different concentrations of TMZ, AFt-TMZ, AFt, DMSO and NaOAc (0.1 M; pH 5.5), ranging from the lowest to the highest concentrations that were used in the assay to treat the cells, were incubated with MTT, for 2 h at 37 °C.

Table 2.3. The concentration of test agents used in the MTT assay.

Test agents	Final concentration range in plate (μM)					
	U373V	U373M	LN-18:	HCT116	HCT116-VR	MRC-5
TMZ	5-1000	5-1000	5-1000	5-1000	5-1000	5-1000
AFt-TMZ	0.1-50	0.01-5	0.01-5	0.1-50	0.1-50	1-150
N3P	1-500	1-500	1-500	1-500	-	1-500
AFt-N3P	0.01-5	0.01-5	0.01-5	0.1-50	-	0.1-50
T25	0.01-100	0.005-100	1-500	0.5-100	-	0.5-100
AFt-T25	0.01-50	0.005-5	0.01-5	0.1-50	-	0.1-50
O6-BeG	-	1-500	-	-	-	1-500
AFt-*O6*-BeG	-	0.01-5	-	-	-	0.05-500
NRP	-	0.172-86	-	-	-	0.172-86
AFt-NRP	-	0.00172-0.86	-	-	-	0.086-17.2
TMZ+*O6*-BeG	-	1-500 (based on TMZ)	-	-	-	1-500 (based on TMZ)
AFt-TMZ+AFt-*O6*-BeG	-	0.01-5 (based on TMZ)	-	-	-	0.05-500 (based on TMZ)
TMZ+NRP	-	1-500 (based on TMZ)	-	-	-	1-500 (based on TMZ)
AFt-TMZ+AFt-NRP	-	0.01-5 (based on TMZ)	-	-	-	0.01-5 (based on TMZ)
AFt	0.0052-1	0.0052-1	0.0052-1	0.0052-1	0.0052-1	0.0052-1
DMSO	0.01-1%	0.01-1%	0.01-1%	0.01-1%	0.01-1%	0.01-1%
0.1 M NaOAc (pH 5.5)	1-500	1-500	1-500	1-500	1-500	1-500

After 6 days of treatment or at the time of test agent introduction (24 h post-seeding; the T0 plate), the assay was terminated. Firstly, MTT reagent was prepared in PBS (2 mg/mL). The MTT solution was then added to the medium in each well (50 µL) to obtain a final concentration of 400 µg/mL. The plates were incubated for 2 h at 37 °C (5% CO_2). The medium containing non-metabolised MTT was then aspirated and the purple product (insoluble formazan) was dissolved in DMSO (150 µL). The plates were placed on an orbital shaker for 5 min and the absorbance was read at λ = 570 nm on a Perkin Elmer Envision plate reader. Four individual repeats were carried out for each test agent.

Absorbance values obtained by Wallac Envision manager software (version 1.12) were exported to Microsoft Excel. Graphs with absorbance values of formazan were plotted against the test agent concentration values. The estimated concentration that causes 50% growth inhibition (GI_{50}) was later determined for each test agent after calculating the GI_{50} absorbance using Equation (2.9). Thereafter, the GI_{50} concentration value was calculated by interpolation (see Equation (2.10)).

$$GI_{50}A = \left(\frac{\left(\begin{matrix} Mean\ A\ of\ control\ (cell\ only)\ - \\ Mean\ A\ of\ control\ (T0) \end{matrix} \right)}{2} \right) + Mean\ A\ of\ control\ (T0)$$

(2.9)

$$Estimated\ GI_{50}\ concentration\ (\mu M) = ((((W - GI_{50}\ A) / (W - X)) \times (Y - Z)) + Z)$$

(2.10)

Where:
A = Absorbance
W = High absorbance (absorbance data point just above the GI_{50} absorbance)
X = Low absorbance (absorbance data point just below the GI_{50} absorbance)
Y = High concentration (concentration of the absorbance data point just above the GI_{50} absorbance)
Z = Low concentration (concentration of the absorbance data point just below the GI_{50} absorbance)

Additionally, the combination index (see Equation (2.11)) was calculated for the following combination treatments TMZ+*O6*-BeG, AFt-TMZ+AFt-*O6*-BeG TMZ+NRP and AFt-TMZ+AFt-NRP, using estimated GI_{50} values for each test agent in the mixture, to determine whether the combination of test agents reaps synergistic or antagonistic drug interactions.[180-182]

$$Combination\ index = (((D_1)/(D_{X1})) + ((D_2)/(D_{X2}))) + ((\alpha((D_1) \times (D_2)))/((D_{x1})/(D_{X2})))$$

(2.11)

Where:
D_1 = GI_{50} concentration of test agent no.1 when in combination with D_2
D_{X1} = GI_{50} concentration of test agent no.1 alone
D_2 = GI_{50} concentration of test agent no.2 when in combination with D_1
D_{X2} = GI_{50} concentration of test agent no.2 alone
α = 0 for mutually exclusive or 1 for mutually non-exclusive modes of drug action; for our calculations we used α = 1.

2.6.2 Live cell count assay – 6 days test agent treatment

Trypan blue was used as a stain to distinguish between live and dead cells. Trypan blue can only be taken up by dead cells. Dead cells have porous membranes (live cells have an intact membrane), and so the dye can enter and accumulate in the cytoplasm.[183]

U373V/M cells were harvested, counted, and seeded in tissue culture treated, clear flat bottom polystyrene 6-well plates at a seeding density of $1x10^4$ cells/well (2 mL per well). After 24 h, medium was aspirated and fresh medium was replaced for cell only controls, whilst wells designated for treatment were treated with 2 mL of 50 μM TMZ or AFt-TMZ (concentration based on TMZ) and 0.057 μM of AFt (equivalent to concentration of AFt in the AFt-TMZ 50 μM solution), for 6 days (37 °C; 5% CO_2). After 6 days, cells were trypsinised and collected by centrifugation (1200 rpm, 5 min, 4 °C). Live cells were counted using a haemocytometer under a brightfield light microscope, with trypan blue used (following manufacturer's instructions) to exclude dead cells (those that have taken up the stain). Under a brightfield light microscope, only dead cells display a blue colour (due to the accumulated dye), and so the remaining non-stained cells (live cells) were counted. Three replicates of each sample were performed on the same day and at least 3 independent repeats also.

2.6.3 Clonogenic assay – 24 h and 6 days test agent treatment

The clonogenic cell survival assay, also known as the colony formation assay, is an *in vitro* cell survival assay which looks at the ability of single cells to grow (proliferate) into a large colony or a clone (usually established as ≥ 50 cells per colony).[184] These cells are said to be clonogenic. The test was carried out to assess whether every cell seeded could undergo unlimited division after treatment (which for the case with TMZ treatment should cause cell reproductive death as a result of damage to chromosomes), to produce a large progeny. This assay has been established to test the effect of radiation and chemotherapy.[184] Only a fraction of seeded cells retains the capacity to produce colonies. Therefore, plating efficiency (PE; colony forming efficiency) was determined, which refers to the percentage of cells seeded at a low seeding density that give rise to colonies (see Equation (2.12)).[184] From this, the survival fraction (SF) was quantified using the PE of treated wells and untreated wells (see Equation (2.13)).[184]

U373V/M cells were harvested, counted, and subsequently seeded in tissue culture treated, clear flat bottom polystyrene 6-well plates at a seeding density of 400 cells/well (2 mL per well). After 24 h, medium was aspirated and fresh medium was replaced for cell only controls, whilst wells designated for treatment were treated with 2 mL of 1, 10 and 50 μM TMZ and AFt-TMZ (concentration based on TMZ) and 0.057 μM AFt (equivalent to concentration of AFt in the AFt-TMZ 50 μM solution), for 24 h or 6 days (37 °C; 5% CO_2). Thereafter, medium containing test agent was removed, cells were washed with PBS and fresh medium (2 mL) was introduced into wells. Plates were further incubated until colonies reached ≥ 50 cells in control wells. Once so, assays were terminated by aspirating the medium and colonies were washed with ice-cold PBS twice (2x 1 mL), fixed with ice-cold 100% methanol (MeOH; 1 mL) for

15 min and then stained with 1 mL of 0.05% methylene blue (5% methylene blue stock diluted with 1:1 dH_2O:MeOH solution to make 0.05% solution for the assay) for 10 min. After 10 min, the methylene blue stain was aspirated, and the wells were washed with tap water several times before the plates were left to air dry. Duplicate repeats for each test agent were performed on 3 independent attempts. Colonies were later manually counted and recorded. The PE% and SF% were then calculated following Equations (2.12 and 2.13).

$$PE\% = \left(\frac{Number\ of\ colonies\ counted}{Number\ of\ cells\ plated}\right) x\ 100 \quad (2.12)$$

$$SF\% = \left(\frac{PE\%\ of\ treated\ sample}{PE\%\ of\ untreated\ control}\right) x\ 100 \quad (2.13)$$

2.6.4 Flow cytometry: cell cycle analysis – 72 h test agent treatment

The cell suspension is taken up by a flow cytometer using sheath fluid to hydrodynamically focus the cell suspension through a small nozzle.[185] The tiny stream of fluid pushes the cells past the laser beam one cell at a time.[185] Light scattered from the cells or particles is detected as they pass the laser beam. A detector in front of the light beam measures the forward scatter (FS; correlates with cell size) and several detectors on the side measure the side scatter (SS; proportional to the granularity of cells).[185] In addition, fluorescence detectors are present, which measure the fluorescence emitted from positively stained cells.[185] In our studies, some cells were not stained to serve as negative controls. Different cell populations can be accounted for by the flow cytometer based on their size and granularity e.g. it can detect different components in blood samples. For our study, the cells were from the same population and therefore the detectors simply detected differences in size that were due to cellular aggregation or dust.

Propidium iodide (PI) dye is often used for cell cycle analysis. PI binds to DNA in a stoichiometric manner i.e. the amount of bound stain is proportional to the amount of DNA present in the cell.[186] So, cells in the S-phase of the cell cycle which have more DNA than cells in the G1-phase, would take up more dye and display higher fluorescence intensity.[186] Cells would continue to fluoresce more brightly until they have doubled their DNA content. As such, the fluorescence intensity of cells in G2 will be approximately twice as high as those in G1.[186]

U373V/M, were seeded in 6-well plates at a seeding density of $1x10^5$ cells/well, following cell collection by trypsinisation and then counting. The following day, cells were treated for 72 h with 50 µM TMZ or AFt-TMZ (concentration based on TMZ) and 0.057 µM AFt (equivalent to concentration of AFt in the AFt-TMZ 50 µM solution). Floating and attached cells (collected by trypsinisation) were collected into FACS tubes and pelleted by centrifugation (1200 rpm, 5 min, 4 °C). The supernatant was discarded by decantation (which applies for all other centrifugation steps in this assay). Following on, the pellet was washed once with ice-cold PBS (1 mL), and the pellet was disrupted by a rapid, short pulse (< 5 s) with a vortex and pelleted again by centrifugation (1200 rpm, 5 min, 4 °C). Cells were later stored overnight at 2-8 °C, in the dark, after resuspending the cell pellet with 500 µL of hypertonic fluorochrome solution (0.1% sodium citrate, 0.1% triton X-100, 50 µg/mL PI and 0.1 mg/mL RNaseA in dH_2O). The mean fluorescence from 10000 gated events was computed using the Beckman Coulter FC500 flow cytometer. The data were later extracted and analysed using Weasel v3.0.2 software. Three replicates of each sample were performed on the same day and at least 3 independent repeats also.

2.6.5 Flow cytometry: γ-H2AX analysis – 48 and 72 h test agent treatment

For γ-H2AX foci analysis, U373V/M cells were harvested by trypsinisation, counted, and then seeded in 10 cm tissue culture treated petri dishes at $5x10^5$ cells/dish. Following overnight incubation, the dishes were treated with TMZ, AFt-TMZ (50 μM and 100 μM) and AFt vehicle (0.057 and 0.1 μM; equivalent to concentration of AFt in the AFt-TMZ 50 and 100 μM solution, respectively) for 48 and 72 h. Floating and attached cells (collected by trypsinisation) were collected into FACS tubes and pelleted by centrifugation (1200 rpm, 5 min, 4 °C). The supernatant was discarded by decantation (which applies for all other centrifugation steps in this assay). Cell pellets were fixed for 5 min at RT with the addition of 0.5 mL of 1% formaldehyde (prepared from 16% formaldehyde-MeOH free solution diluted with PBS). Pellets were disrupted by a rapid, short pulse (< 5 s) with a vortex (which was done in this manner for all stages that required the pellet to be disrupted). Subsequently, 0.5 mL of 0.4% triton X-100 (diluted from stock with PBS) was added for cell permeabilisation, and incubated for another 5 min at RT. The cells were pelleted, and blocking was performed to prevent non-specific binding of the Ab, through the addition of 1 mL of 1% FBS (in PBS) for 30 min incubation at RT on a plate shaker (Amersham). After incubation, cells were collected by centrifugation and stained with 200 μL of mouse, anti-human phospho-histone H2A.X (Ser139) primary (1°) Ab, clone JBW301 (1:3333) for 1.5 h on the shaker at RT, in the dark. Cells were then washed once with the addition of 1% FBS (1 mL) and then pelleted, followed by the addition of 200 μL of F(ab')2-goat anti-mouse IgG, IgM (H+L) Alexa-fluor 488 secondary (2°) Ab (1:1750) for 1 h on the shaker at RT, in the dark. Again, cells were washed once with 1% FBS (1 mL) and pelleted, followed by the addition of 500 μL of PBS. Subsequently, the fluorescence of 10000 mean gated events was obtained using the Beckman Coulter FC500 flow

cytometer. Data was processed using Weasel v3.0.2 software. Three replicates of each sample were performed on the same day and at least 3 independent repeats also.

2.6.6 Indirect ELISA: DNA *O6*-MeG quantification – 4, 24, 72 and 144 h test agent treatment

An indirect colorimetric ELISA assay much like western blot, uses a 1° Ab directed to the target of interest (in this case DNA *O6*-MeG) and uses a secondary (2°) Ab conjugated to an enzyme for detection.[187] A 96-well microplate ELISA setup is advantageous as it negates the step for transfer of sample from gel to membrane for Ab incubation and detection. However, the western blot technique does have the added advantage of separating proteins by size; enabling further characterisation of the protein of interest. Nevertheless, the western blot technique cannot be applied for the detection of DNA samples. So, ELISA was carried out instead, using single-stranded, digested DNA affixed to the surface of a microwell plate coated with protamine sulfate.[187]

Indirect ELISA was carried out for DNA *O6*-MeG quantification in U373V and M cells. Briefly, cells were harvested by trypsinisation, counted and seeded in 6-well plates at 0.1-1x10^5 cells/well. On the following day, medium was aspirated and cells were exposed to 50 µM TMZ or AFt-TMZ for 4, 24, 72 and 144 h. Cells were frozen down following step 2.5.3 until treatment of 144 h was completed in order to perform DNA extraction for all samples at the same time. The purification of DNA from frozen cells was carried out with QIAGEN Blood & Cell Culture DNA mini purification kit, following the manufacturer's procedure. Subsequently, double stranded DNA (1 µg; quantified using Nanodrop UV-Vis 2000) was digested with the Timesaver MspI restriction enzyme kit (the

positions where the enzyme cuts to generate shorter DNA fragments are denoted by the forward slash sign: 5'…C/CGG…3'; 3'…GGC/C…5'), following the manufacturer's procedure. The DNA was then made single stranded by heating at 95 °C for 10 min and then rapidly transferred to ice for at least 15 min. ELISA was subsequently performed by using the IgG (Total) Mouse Uncoated ELISA Kit and following the manufacture's procedure with some modifications. Briefly, a 96-well plate was pre-coated with 200 µL/well of 1% protamine sulfate (powder dissolved in dH_2O) at RT for 1 h, then removed and washed 5 times with a jet of milli-Q water. Wells were then coated with DNA solution (10 ug/mL; 100 µL/well) diluted in coating buffer 1x, and then incubated overnight on a plate shaker at RT, in the dark. Next day, the remaining solution was removed, and the wells were washed thrice with eBioscience wash buffer 1x, followed by a blocking stage with 150 µL/well of blocking buffer 2x for 2 h, at RT. Later, the solution in the wells was removed and wells were washed thrice with eBioscience wash buffer 1x, followed by incubation with 150 µL of monoclonal 1° Ab, mouse anti-human *O6*-MeG (final concentration (C2) = 0.2 µg/mL; initial concentration (C1) = 100 µg/mL) for 1.5 h at RT, in the dark. Afterwards, the solution in the wells was removed and wells were washed thrice with eBioscience wash buffer 1x, followed by incubation with 150 µL of 2° polyclonal Ab, HRP-conjugated anti-mouse IgG (1:250) for 1 h at RT, in the dark. Finally, the solution in the wells was removed and wells were washed thrice with eBioscience wash buffer 1x, followed by treatment with TMB substrate solution (100 µL) for 15 min at RT, in the dark. Subsequently, stop solution (100 µL) was added and the plates were placed on an orbital shaker for 5 min at RT, in the dark, to facilitate the quenching of the reaction. The absorbance was read at λ = 450 nm with Perkin Elmer Envision plate reader. Three replicates of each sample were performed on the same day and at least 3 independent repeats also.

2.7 Cellular characterisation

2.7.1 Western blot

Western blot was used to detect a specific protein from a mixture of proteins using a monoclonal 1° Ab.[188] The indirect method of western blot additionally includes a separate incubation step with a polyclonal 2° Ab conjugated to an enzyme, which recognises the monoclonal 1° Ab, binds to it and subsequently catalyses a substrate to a product (which produces either colour or light). Although the indirect method is slightly more time-consuming and has additional experimental steps, one advantage of this method over the direct western blot method, is that it allows one 2° Ab to be used on numerous different 1° Ab, in one setting.

A loading control must be included for every western blot gel that is run.[188] These are usually Ab directed at proteins that are highly expressed at stable levels and are ubiquitous. For this reason, housekeeping genes that are constitutively expressed and necessary for basic cell function, are typically used as loading controls, such as beta-actin or GADPH, and are used to make sure that the protein has been loaded equally across all wells of the SDS-PAGE gel. The loading control accounts for several possible variations. Firstly, it essentially ensures the reliability of the data when comparing the expression of a protein in different sample lanes. In cases where some lanes have not been evenly loaded, loading controls can be used to quantify the protein amounts in each lane by using the density of the loading control band to correct for differences in loading. In addition, loading controls can be used to check that there has been an even transfer from across the whole gel to the membrane. What's more, is that they can account for variations in Ab incubation/ signal across different samples or lanes.

Recipe:

- NP-40 lysis buffer: 100 µL NP-40, 1.5 mL NaCl (1.0 M), 500 µL Tris (1.0 M; pH 8.0), 7.9 mL dH_2O, 1 tablet of protease inhibitor and 1 tablet of phosphatase inhibitor.
- Tris-buffered saline and Tween 20 (TBST): 10 L dH_2O, NaCl (80 g), Tris (24.2 g) and 5 mL Tween20.
- Transfer buffer 10x: Make up to 1 L with dH_2O. Tris (250 mM) and glycine (1920 mM).
- Transfer buffer 1x: Make up to 1 L with dH_2O. A 1:10 dilution was carried out using 10x transfer buffer (final concentrations: Tris (25 mM) and glycine (192 mM)) and add MeOH (10%).
- Blocking solution: 5% non-fat dried milk in TBST.

For protein extraction, cells were harvested in 15 mL falcon tubes and pelleted by centrifugation (1200 rpm, 5 min, 4 °C). Cell pellets were washed thrice with ice-cold PBS and centrifugation was performed after each wash to discard the supernatant. After the wash, 300 µL of NP-40 lysis buffer was added to cells extracted from a T25/T75 cm^2 flask. Cell pellets were then disrupted with a pipette and transferred to a microcentrifuge tube, which was then placed in wet ice for 30 min to facilitate protein extraction and prevent protein degradation. The samples were then centrifuged in a Heraeus Fresco 17 centrifuge (Thermo Electron Cooperation) at 13300 rpm, for 10 min at 4 °C and the supernatant (containing protein) was retained, and pellet discarded. The protein lysate was then stored at -20 °C until use.

Protein lysates were thawed on ice and protein concentrations determined *via* Bradford assay (see section 2.4.1). Proteins lysates (50 µg) were loaded onto a 10% resolving gel and separated by SDS-PAGE (see section 2.4.4). Whilst SDS-PAGE was running, for a single gel, 8x (5 cm x 3 cm) blotting filter papers alongside 1x (5 cm x 3 cm) nitrocellulose membrane were pre-wetted for 30 min in transfer buffer 1x. This was achieved by wetting 4 filter papers in one tray and 4 other filter papers with 1 nitrocellulose membrane on top in another tray.

After the SDS-PAGE run was completed, the transfer of proteins from the gel to the nitrocellulose membrane was performed by laying out the 4 filter paper with the nitrocellulose membrane in the transfer compartment first, followed by the placement of the resolving section of the gel on top and then followed by the placement of the remaining 4 filter papers to create a sandwich. Air bubbles were gently removed by using a mini rolling pin. Subsequently, transfer took place with the Trans-Blot Turbo Transfer System (Bio-Rad) for 45 min (parameters: 2.5 A, 25 V). After transfer, the nitrocellulose membrane was transferred to a plastic bag (polythene layflat tubing) and blocking took place following the addition of 8 mL blocking buffer to the bag, which was then sealed using the Salton vacuum bag sealer and the bag was incubated on the mini orbital shaker SO5 (Stuart Scientific), at 100 rpm, for 1h at RT. The blocking solution was then removed, and the membrane was transferred to a new plastic bag. Monoclonal 1° Ab diluted with blocking buffer (8 mL; see Table 2.4) was added to the bag, which was then sealed using the bag sealer and incubated overnight on the orbital shaker in a cold room at T = 2-8 °C. After, the solution was removed and washing took place with TBST for 3 rounds, 5 min per round, on the shaker. The membrane was then transferred to a new plastic bag and incubated with polyclonal (2°) Ab diluted with blocking buffer (8 mL; see Table 2.4), for 1 h at RT on the shaker. The solution was removed and washing took place with TBST for 3 rounds, 5 min per round, on the shaker. Finally, the membrane was incubated with ECL reagent (1.5 mL; 1:1 solution A (luminol enhancer solution):solution B (peroxide solution)) for 5 min and bands were visualised on a C-DiGit blot scanner (LI-Cor Biosciences). At least 3 independent repeats for each cell line were performed.

Table 2.4. The Ab used for western blot.

Ab	Ratio	Manufacturer/Supplier
1° Ab: Rabbit anti-human TfR1	1:1000	Cell Signalling Technology
1° Ab: Rabbit anti-human MGMT	1:1000	Cell Signalling Technology
1° Ab: Rabbit anti-human glyceraldehyde 3-phosphate dehydrogenase (GAPDH)	1:1000	Cell Signalling Technology
1° Ab: Rabbit anti-human PARP-1	1:1000	Cell Signalling Technology
1° Ab: Mouse anti-human SCARA5	1:1000	R&D systems a bio-techne brand
1° Ab: Mouse anti-human TfR2	1:250	R&D systems a bio-techne brand
2° Ab: Goat anti-rabbit Ab conjugated with HRP	1:4000	Dako
2° Ab: Goat anti-mouse Ab conjugated with HRP	1:4000	Dako

2.7.2 Flow cytometry: quantification of transferrin receptor 1

U373V, U373M, HCT116 and MRC-5 cells were seeded in 6-well plates at 1 x 10^5 cells/well. Following 24 h post seeding, floating and attached cells (collected by trypsinisation) were collected into FACS tubes and pelleted by centrifugation (1200 rpm, 5 min, 4 °C). The supernatant was discarded by decantation (which applies for all other centrifugation steps in this assay). Following on, the pellet was washed once with ice-cold PBS (1 mL), and the pellet was disrupted by a rapid, short pulse (< 5 s) with a vortex and pelleted again by centrifugation (1200 rpm, 5 min, 4 °C). Cell pellets were blocked to prevent non-specific binding of Ab, through the addition of 1 mL of 1% FBS (in PBS) for 30 min incubation at RT on the mini orbital shaker SO5. After incubation, cells were collected by centrifugation and stained with 80 µL of human anti-TfR1 R-PE conjugated 1° Ab (1:50; Invitrogen), on wet ice for 45 min and then fixed with 3.7% v/v formaldehyde in PBS for 5 min. Cells were washed once with the addition of PBS (1 mL) and then pelleted. Finally, the pellet was resuspended in 500 µL of PBS. Subsequently, the fluorescence of 10000 mean gated events (single cells) was obtained using the Beckman Coulter FC500 flow cytometer. The data were processed using Weasel v3.0.2 software. Three replicates of each sample were performed on the same day and at least 3 independent repeats also.

2.8 Cell-based imaging

2.8.1 Environmental scanning electron microscopy (ESEM)

ESEM was used to scan the surface of cells and observe any morphological changes to the cell surface after 24 h test agent treatment. ESEM presents advantageous qualities over conventional electron microscopy.[189] It allows the specimen to be studied live at high magnification and resolution, with minimal cellular damage and without the need to coat the cells in conductive materials.[189]

U373V and M cells were harvested and counted. A TGS1x0.2 Gold slot grid was placed at the centre of each well (front face of the grid facing up) of a 6-well plate and cells were seeded at a density of $1x10^5$ cells/well (2 mL/well). After 24 h, medium was gently removed to not disturb the gold grid and cells were treated with TMZ or AFt-TMZ (50 μM; 2 mL/well) for 24 h. Subsequently, wells were gently washed with PBS (1 mL) and then fixed with 3.7% v/v formaldehyde (in PBS) for 5 min at RT. The grids were washed twice with PBS (1 mL) and transported in PBS for imaging. Prior to imaging, the grids were thoroughly rinsed with dH_2O (to remove salts) and mounted onto the microscope stage set at 3 °C. A droplet of water was placed on top of the front face of the grid (containing cells) and around the stage. The pressure was shifted to create a saturated water vapour environment inside the chamber before dropping the pressure to 5.15 Torr, with humidity set to 87%, to create a low vacuum environment and a thin water layer on the grid for high resolution imaging. A gaseous secondary electron detector was used for imaging at low vacuum. Resolution was achieved with a 5-nm spot size and 5 kV electron beam. Working distance was 5.8 mm, with a magnification of x1000. ESEM was performed using the FEI Quanta 650 ESEM, on pre- and post- 24 h treated

samples. Three replicates of each sample were performed on the same day and at least 2 independent repeats also.

2.8.2 Confocal microscopy

Confocal microscopy was used to observe morphological changes (via F-actin staining) to U373V and M cells following 24h test agent treatment. This technique allows us to collect serially thin optical sections from a thick specimen in a non-invasive manner, to create high resolution images.[190]

Cells were harvested, counted, and seeded in an 8 well µ-slide glass plate at $1x10^4$ cells/well (200 µL/well). The following day, medium was removed, and cells were treated for 24 h with TMZ or AFt-TMZ (50 µM; 200 µL/well). Following treatment, cells were washed with PBS (200 µL), fixed with 200 µL of 3.7% v/v formaldehyde (15 min; RT), permeabilised with 0.1% v/v triton X-100 (in PBS) and co-stained for 1 h with 200 µL of phalloidin-iFluor 633 (1x; prepared from 1000x stock using PBS) and DAPI (0.02 µg/ml) at RT in the dark. Between each step and the final step, the wells were washed twice with PBS before being left in PBS (200 µL) for imaging. Imaging was performed with Zeiss Elyra PS1 super resolution microscope with DAPI excitation at 405 nm and phalloidin excitation at 633 nm. A 63x water magnification lens was used, and z-stack imaging was performed. Images were analysed using Fiji image J. Three replicates of each sample were performed on the same day and at least 3 independent repeats also.

2.9 Statistical analyses

A two-way or three-way ANOVA analysis function on GraphPad Prism version 8.2.1 was employed to assess the significant differences between multiple groups ($n \geq 3$). Values of *P or #P <0.05, **P or ##P < 0.01, ***P or ###P < 0.001, and ****P or ####P < 0.0001 were considered as statistically significant. Data are represented as mean ± SD.

Chapter 3 – Apoferritin encapsulation of test agents to overcome temozolomide resistance

3.1 Introduction

Currently, the most common route of treatment for GBM is through a combination of surgery, to remove the tumour, followed by radiotherapy coupled with TMZ chemotherapy. This combinatorial approach to treatment confers a median survival rate of only ~ 15 months.[58] TMZ can cross the BBB relatively well by diffusion. However, there remain concerns associated with poor accumulation of TMZ at the tumour site due to the presence of active drug efflux transport proteins such as Pgp and also short TMZ plasma $t_{1/2}$.[191,192] It has been estimated that < 1% of circulating drugs reach the brain tumour.[193] Moreover, TMZ therapy is blighted by dose-limiting bone marrow toxicity, hence presenting an additional barrier to successful treatment.[194]

Nevertheless, the biggest hurdle associated with TMZ therapy is the inherent and acquired resistance mechanisms in brain cancer cells, which reduce TMZ efficacy. TMZ is a DNA methylating prodrug. The methyldiazonium cation is the active degradation product released, which subsequently reacts with DNA purine bases, methylating *N3*-adenine, *O6*-, and *N7*-guanine.[80] *O6*-MeG is the most cytotoxic product produced (Scheme 1.2).[75,195] Deficiency in DNA MMR leading to *O6*-MeG-thymine mismatch tolerance (a functioning MMR system would normally trigger G2/M cell cycle arrest), and overexpression of MGMT, which removes the methyl group from the O6-position of guanine (restoring normal guanine), are major causes of TMZ resistance *in vitro* and clinically.[196,197]

To overcome TMZ resistance, numerous approaches have been considered. One approach involves combining TMZ (Figure 3.1a) with either an MGMT inhibitor such as *O6*-BeG (Figure 3.1b; to enhance the levels of *O6*-MeG) or with a PARP-1 inhibitor such as NRP (Figure 3.1c; to enhance the levels of *N3*-MeA and *N7*-MeG).[80] Enhancing the levels of these adducts should achieve greater cytotoxicity. Also, another approach towards overcoming TMZ resistance includes the development of TMZ analogues with N3-methyl substitutions with, for example an N3-propargyl group (to generate N3P analogue; Figure 3.1d), which have allowed such analogues to evade recognition and removal by MGMT and exert activity independent of DNA MMR status.[84,91,92] Furthermore, substitutions at the C8-position of TMZ have created analogues with far superior *in vitro* PK and PD properties.[92,198] Such analogues i.e. T25 (Figure 3.1e), have shown improved drug efficacy and $t_{1/2}$ over TMZ and N3P analogue.[92]

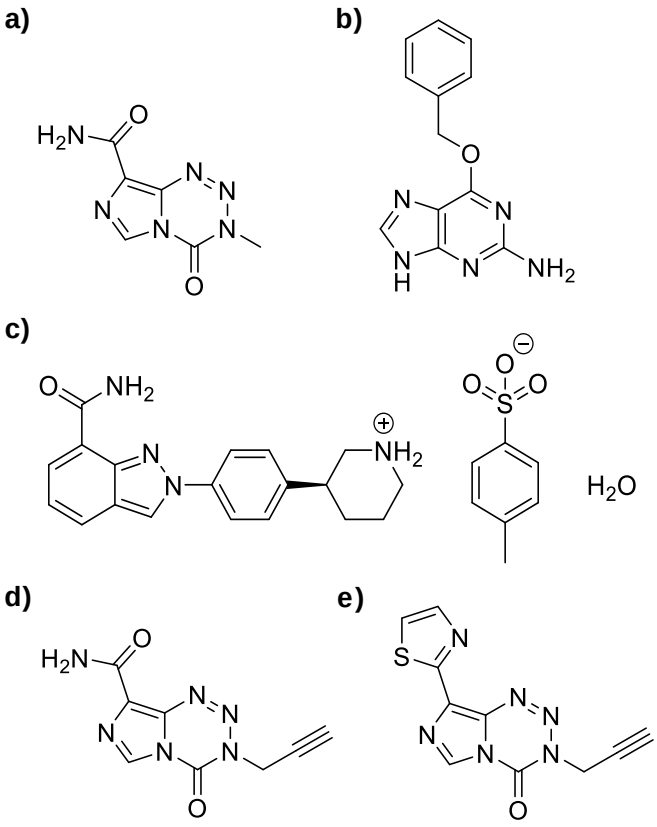

Figure 3.1. The chemical structures of test agents. (a) TMZ, (b) *O6*-BeG, (c) NRP tosylate, (d) N3P and (e) T25.

Subsequently, the next hurdle to overcome include poor drug accumulation at the brain tumour site and off-target side effects. One approach towards enhancing the specificity and selectivity of TMZ and TMZ analogues is through enhancing their targeting capabilities by enveloping them in a targeted carrier. Nanoparticle DDS are fast becoming an interesting formulation choice for enhancing the physicochemical, PK and PD profiles of drugs.[199,200] Targeted nanoparticles (1-100 nm) can reach the site of action *via* passive (EPR effect) and active targeting.[201] Ft, an Fe transport/storage protein can be converted to a hollow protein cage called AFt (480 kDa), through the removal of Fe and subsequently used as a DDS.[134,135] AFt has an external diameter of 12 nm and interior diameter of 8 nm,[202] which makes it highly suitable for passive targeting *via* the EPR effect.[100,101] In addition, the H-subunits of the AFt cage contain a binding site for TfR1.[203,204] This receptor plays a role in maintaining cellular Fe

homeostasis and is expressed in small quantities on most types of cells of the human body, and expression is regulated by Fe levels.[205] However, it is overexpressed on many cancers (including GBM) due to their Fe hungry nature.[205] It is also found on the BBB, allowing for selective and specific accumulation of the DDS at the tumour site.[206,207] Once bound to TfR1, AFt is internalised by clathrin dependent endocytosis and is destined to the lysosomes.[203,208] There the protein undergo degradation allowing the cargo to be released directly into the cytoplasm. Some additional advantages of AFt include its biocompatibility, stability and non-toxic properties, as well the ability to be biodegradable. It can also be used as a theragnostic agent, for example to carry both drugs and imaging agents for the purpose of treating the disease and imaging at the same time.[160,209] As well as this, the surface of AFt can be further functionalised to introduce enhanced targeting by genetic or chemical means, making AFt quite a versatile DDS.[153,210]

We envisage that due to the rapid proliferation rate of cancer cells due to their high Fe demand, the uptake of exogenous Ft will be welcome. *In vivo*, it is postulated that Fe is released from Ft by lysosomal degradation, yet further studies will need to be carried out to explore other potential avenues of Fe release from Ft i.e. physiological reducing agents.[145,146] *In vitro*, chemical removal of Fe from Ft (such as with thioglycolic acid) have been successfully carried out either *via* reductive dissolution of Fe^{3+} to Fe^{2+} followed by chelation and removal of Fe^{2+} by dialysis or direct chelation of Fe^{3+} and removal by dialysis.[147,150]

There are numerous applications for Fe-free AFt. Some examples include the use of AFt as a nanomedicine or as a diagnostic tool.[211] AFt used as a nanomedicine can be used to encapsulate drug by a variety of manners. The

two most commonly reported methods of encapsulation are the so-called 'nanoreactor' method,[212,213] which involves the use of the AFt channels of 0.3-0.4 nm in diameter, for entry of small molecules by diffusion, and the disassembly-reassembly method,[214,215] which involves the disassembly of the AFt quaternary structure into monomeric subunits at pH = 2, then reformation of the AFt quaternary structure around the drugs at pH > 7.

Herein, we report the use of horse spleen Ft to generate AFt for the encapsulation of TMZ, TMZ analogues: N3P and T25, *O6*-BeG (MGMT inhibitor) and NRP (PARP-1 inhibitor), for GBM-targeted drug delivery *via* TfR1 uptake. Combination mixtures of AFt-TMZ with AFt-*O6*-BeG or AFt-NRP were also explored. AFt was generated *via* the reductive demineralisation of Ft using thioglycolic acid. Subsequently, we characterised the protein, determining its concentration, purity, and stability before drug encapsulation. We then explored the use of the nanoreactor method for the encapsulation of the test agents. All test agents have MW < 300 Da (except for NRP, which in its salt form has a MW < 550 Da but is a linear molecule with a similar width to all the other test agents). Therefore, due to their small size these molecules were able to diffuse across the channels of the AFt cage. To assess the success of test agent encapsulation, encapsulation efficiencies were determined by UV-vis spectroscopy and Bradford assay and the stability of protein and test agent as well as test agent release was monitored for all formulations.

3.2 Results and Discussion

3.2.1 Preparation of AFt from horse spleen Ft

AFt, a hollow protein capsule derived from the iron storage/transport protein called Ft is devoid of Fe through either the genetic expression of AFt in bacteria or chemical removal of Fe from Ft. Outsourced Ft from Sigma-Aldrich, which was extracted from horse spleen, was used in our studies. Fe was removed by reductive demineralisation of the Fe-mineral core. Fe^{3+} was converted to Fe^{2+} and subsequently cleared away from the protein cage by dialysis. A colour change from red/brown to pale yellow marks the shift of Ft to AFt and the successful removal of Fe, see Figure 3.2.

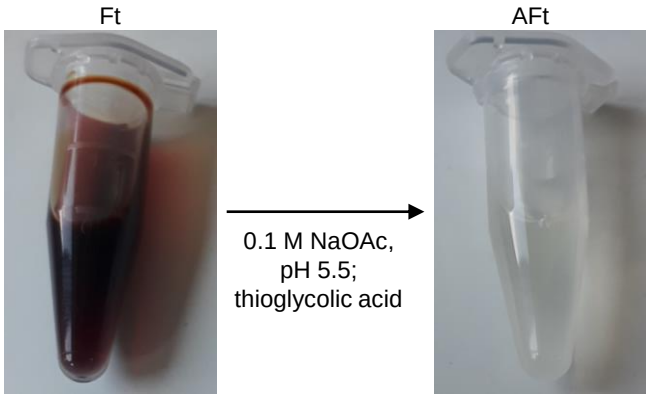

Figure 3.2. Conversion of Ft to AFt. Change in colour of Ft (red/brown) to AFt (pale yellow) after loss of Fe with thioglycolic acid.

To determine total protein concentration in solution and quantify protein yield following purification of Fe from the protein, a colorimetric assay called the Bradford assay was employed.[167] A BSA standard curve was first performed. BSA is commonly used in Bradford assays to quantify relative rather than absolute concentrations of protein in solution. Although it is ideal to use the same protein to the one we attempt to measure (to create a standard curve), in some cases this is not always practically achievable.

As such, to quantify the concentration of AFt in solution a few approaches were considered. Figure 3.3 demonstrates the standard curves obtained from the Bradford assay using either the commonly used relative reference standard - BSA (Figure 3.3a) or an absolute reference standard - AFt, purchased from Sigma-Aldrich (Figure 3.3b). The concentration range of the standards were selected to cover a linear absorbance range and background was subtracted from protein samples to avoid any interference readings from the matrix. A linear regression equation was obtained with a coefficient of determination (R^2) > 0.99. This indicated that the regression model was a good fit for the observed data and as such allowed us to use the model equation to determine the unknown concentration of samples. Following removal of Fe from the protein by dialysis, the protein concentration was determined to be 4.51 ± 0.32 mg/mL (protein yield: 87 ± 6%), using the linear regression equation from the BSA standard curve, and 4.69 ± 0.34 mg/mL (protein yield: 89 ± 6%), using the linear regression equation from the AFt standard curve. It was apparent that the concentration of AFt obtained using the BSA standard curve was like the concentration obtained using the AFt standard curve. This means that BSA was henceforth used to prepare standard curves for the Bradford assay to calculate AFt concentration, because BSA is inexpensive and can be bought in huge quantities to make many standard curves unlike AFt, which is expensive and can only be purchased in very small quantities in its pure Fe-free form (from Sigma-Aldrich).

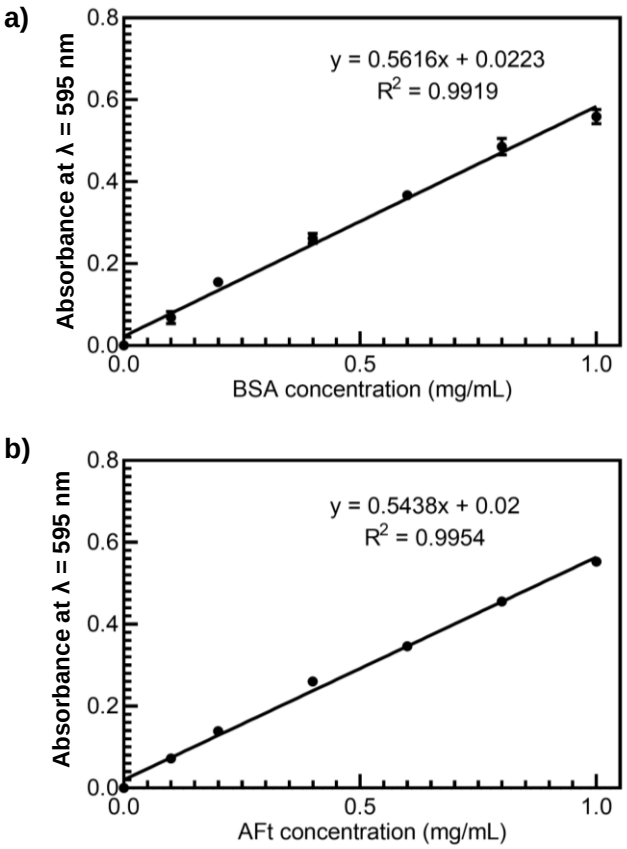

Figure 3.3. Standard curves from Bradford assay. (a) Standard curve of BSA. (b) Standard curve of AFt (purchased from Sigma-Aldrich). Absorbance values were obtained at λ = 595 nm. Values are reported as mean ± SD (n = 3).

Next, we attempted to determine the concentration of AFt by UV-vis spectroscopy and compare the measured concentration to that obtained from the Bradford assay. To obtain the concentration of AFt by absorbance readings, the Beer-Lambert equation (see Equation (2.2)) was employed. Using Equation (2.2), the concentration of AFt was 3.54 ± 0.35 mg/mL (protein yield: 84 ± 7%). Compared to values obtained using the Bradford assay, we can see that the concentration of AFt obtained from absorbance at 280 nm was slightly lower. However, since UV-vis spectroscopy can be a less sensitive technique for protein concentration determination compared to the Bradford assay, despite one advantage being that samples can be reused after analysis, we continued to measure sample concentrations using the Bradford assay.

In addition, UV-vis spectroscopy was used to assess the loss of Fe from Ft. Figure 3.4 demonstrates a wavelength scan plot of Ft and AFt with absorbance readings from wavelengths 200 – 1000 nm. The Ft plot displayed peaks at ~ 280 (protein absorbance) and 400 (Fe absorbance) nm whereas for AFt, only peak x was present with loss of peak y, indicating the loss of Fe. This study further confirmed the successful loss of Fe following reductive demineralisation of Ft by dialysis and the purity of AFt; suggesting no residual Fe was left, which was essential for drug encapsulation and in solely assessing the activity of encapsulated drug.

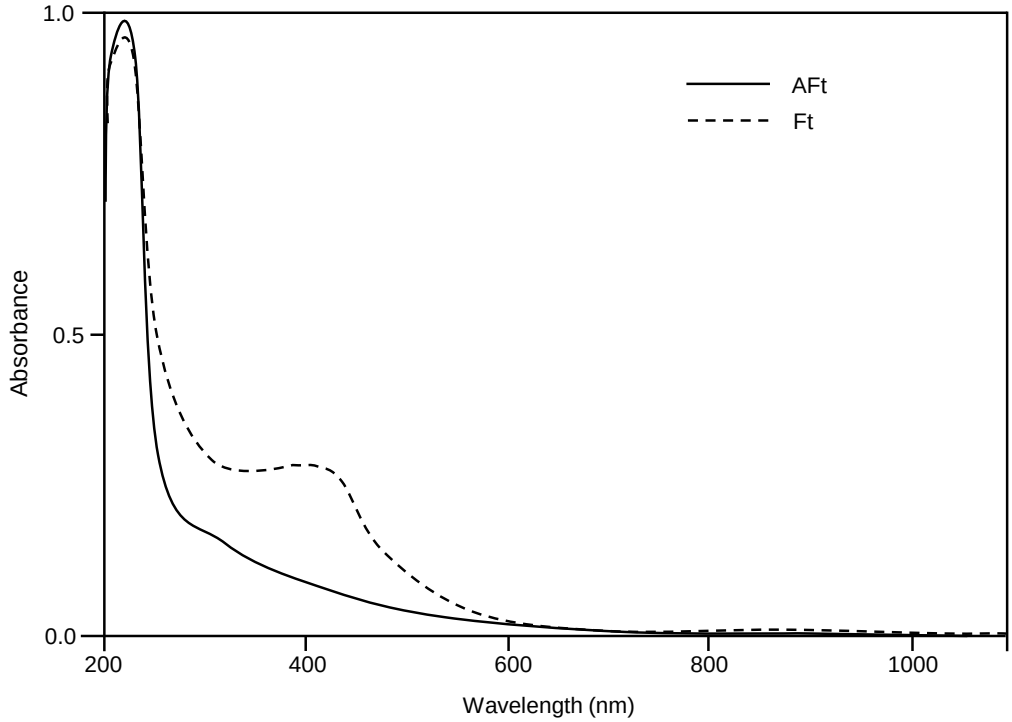

Figure 3.4. UV-vis spectra of Ft and AFt showing the presence and absence of the Fe peak (at ~ 400 nm). Absorbance reading range was taken from λ = 200 – 1000 nm.

Subsequently, SDS-PAGE and native-PAGE were employed to assess the purity and stability of AFt by confirming the protein MW and composition. Figure 3.5 demonstrates Ft and AFt samples separated by SDS-PAGE (Figure 3.5a) and red native-PAGE (Figure 3.5b). According to Figure 3.5a, both Ft and AFt samples displayed the L-subunit band (19 kDa), which makes up 92% of the composition of horse spleen AFt cage. We also see bands below 15 kDa, and near 55 kDa (for the Sigma purchased AFt). According to previous reports, similar results were seen, with bands below 15 kDa potentially indicative of proteolysis in the commercial Ft batch and bands near 55 kDa potentially indicative of subunit dimerisation.[216] Results from native-PAGE (Figure 3.5b) confirm the presence of the monomeric form of Ft and AFt at bands near the 480 kDa marker with some additional bands present at ≥ 720 kDa to indicate the presence of oligomers.[216] Despite some degree of protein instability both PAGE techniques establish the presence of intact Ft protein cages. Indeed, further methods would need to be employed to further confirm that the molecular composition of each band belongs to that of Ft. It has been reported that dimerisation may possibly arise from the homogenisation process during Ft extraction from horse spleen and therefore a change in extraction methods may improve the purity and stability profiles of horse spleen Ft.[217]

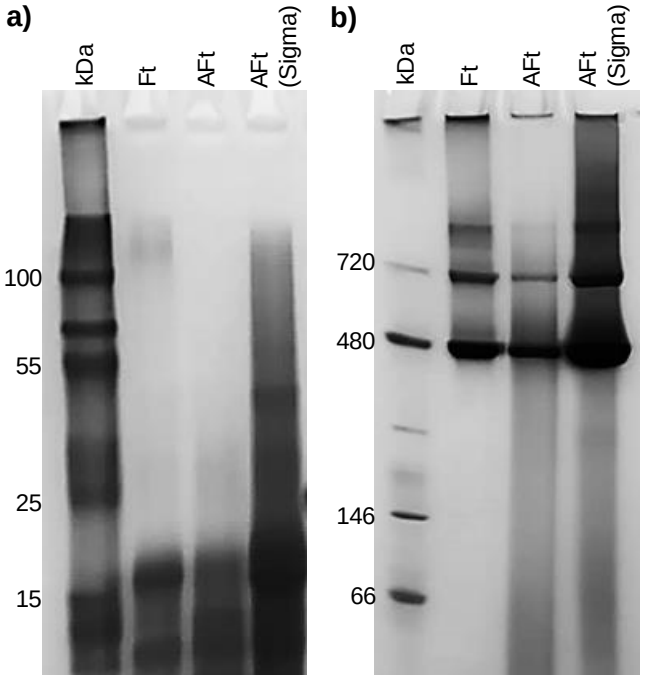

Figure 3.5. Protein separation by PAGE. (a) SDS-PAGE was performed on a 10% resolving gel. (b) Native-PAGE was performed on a 4−16% gradient gel.

Moreover, to corroborate the findings from SDS- and native-PAGE, further analyses into the stability of AFt were carried out. Hydrodynamic size by DLS and ζ-potential were measured for protein samples diluted from stocks using dH_2O water.[175]

For small nanoparticles in the presence of a few aggregate particles, the intensity-based size distribution plot is often skewed to show another large intensity peak for a large sized particle alongside the intensity peak for the smaller sized nanoparticle. This was apparent for Ft and AFt samples (Figure 3.6a). The reason behind this can be due to the sensitivity of intensity-based sizing to the presence of large particles, aggregates, or dust, as the larger the particle the more intense the scattered light. However, the polydispersity index (PDI), which ranges from 0-1, was averaged to be 0.326 ± 0.08, which suggested that the sample was not too polydisperse, as the closer the PDI is to 1 the greater the degree of polydispersity in solution. Figure 3.6b-c shows the

volume and number-based size distribution plots of Ft, AFt and ready-made AFt purchased from Sigma-Aldrich. A different profile was seen with volume- and number-based size distributions to that of the intensity size profiles. Here, the plots show a more monomeric profile for the protein in solution with an average hydrodynamic diameter of 13.1 ± 0.5 nm, like the literature quoted size of 12 nm. Some degree of aggregation was seen in the volume-based plot with an average hydrodynamic diameter of 185.3 ± 3.2 nm, which does corroborate the findings seen with native-PAGE and confirms what was seen with the intensity size profiles, that some aggregates were present in solution.

Furthermore, ζ-potential measurements were carried out, which tells us the net charge of the protein surface in solution. The surface charge of proteins in solution gives us an indication of its physical state in liquids e.g. stability, and their potential interactions with biological systems e.g. protein corona formation.

Figure 3.6d represents the ζ-potential values of Ft, AFt and AFt from Sigma-Aldrich. ζ-potential readings were carried out in dH_2O (pH measured at 7.32). Thus, the protein should still assume a net negative charge (isoelectric point (IEP) of horse spleen AFt is ~ 5.36 calculated using Expasy). The ζ-potential of Ft was marginally more negative than AFt possibly due to the presence of the mineralised Fe core. Ft has a ζ-potential of – 27 ± 0.6 mV close to ± 30 mV, which is a threshold indicator for colloidal stability, whilst ζ-potentials of AFt (-12.6 ± 0.4 mV) were further away from this threshold, which may indicate a tendency for the particles to aggregate over time.[175]

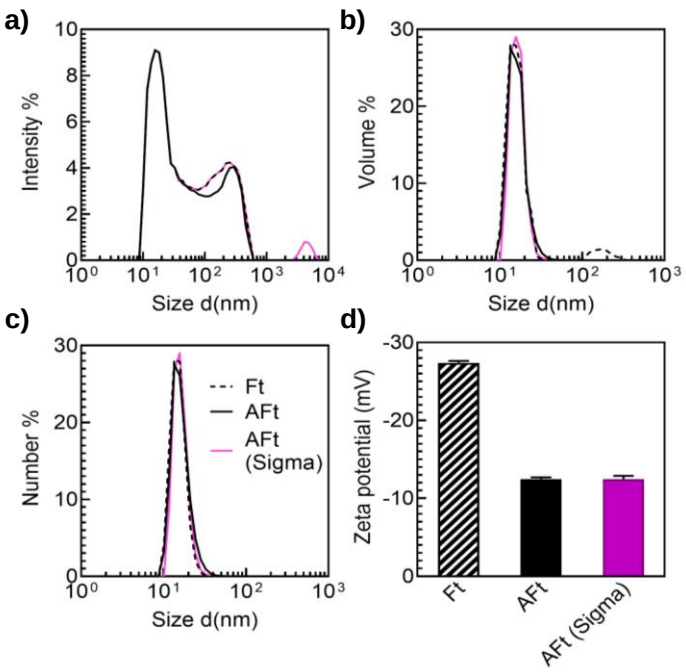

Figure 3.6. The stability of Ft, AFt and AFt (Sigma-Aldrich) protein cages monitored through hydrodynamic size (by DLS) and ζ-potential measurements. (a) Intensity-based size distribution. (b) Volume-based size distribution. (c) Number-based size distribution. (d) ζ-potential. Values are reported as mean ± SD (n = 3).

3.2.2 Drug stock preparation and characterisation

TMZ is the first-in-line chemotherapeutic agent available for the treatment of high-grade brain tumours such as GBM, following surgery and radiotherapy. Since GBM tumours have inherent and acquired resistance to TMZ, analogues of TMZ bearing an N3-propargyl group instead of the traditional N3-methyl group have been developed and combinations of TMZ with *O6*-BeG (MGMT inhibitor) or NRP (PARP-1 inhibitor) have been explored.[80,84,91,92,196,197] The goal of encapsulating the test agents into AFt to achieve selective accumulation in brain tumours first required the solubilisation of test agents in an appropriate medium. All test agents have limited solubility in aqueous solvents. DMSO is widely used as a solubilising reagent for compound screening. The test agents were found to be soluble in DMSO and 50 mM stocks were prepared for *in vitro* compound screening assays. Additionally, DMSO was a suitable solvent when mixed with AFt, as it did not cause the protein to precipitate out of solution,

which would be the case if AFt was mixed with solvents such as MeOH and acetonitrile (ACN). Initially, UV-vis spectroscopy was carried out on TMZ, N3P, T25, *O6*-BeG and NRP to create standard curves for concentration determination following drug encapsulation (Figure 3.7), whereby each test agent absorbed maximally at slightly different wavelengths. The extinction coefficients determined experimentally for each test agent from the standard curves were 9800 M^{-1} cm^{-1} for TMZ, 11100 M^{-1} cm^{-1} for N3P, 4000 M^{-1}, 17900 M^{-1} cm^{-1} for T25, 8100 M^{-1} cm^{-1} for *O6*-BeG and 20000 M^{-1} cm^{-1} for NRP. T25 unlike the other imidazotetrazine agents was found to emit at 475 nm. *O6*-BeG and NRP have not yet been measured by fluorescence microscopy.

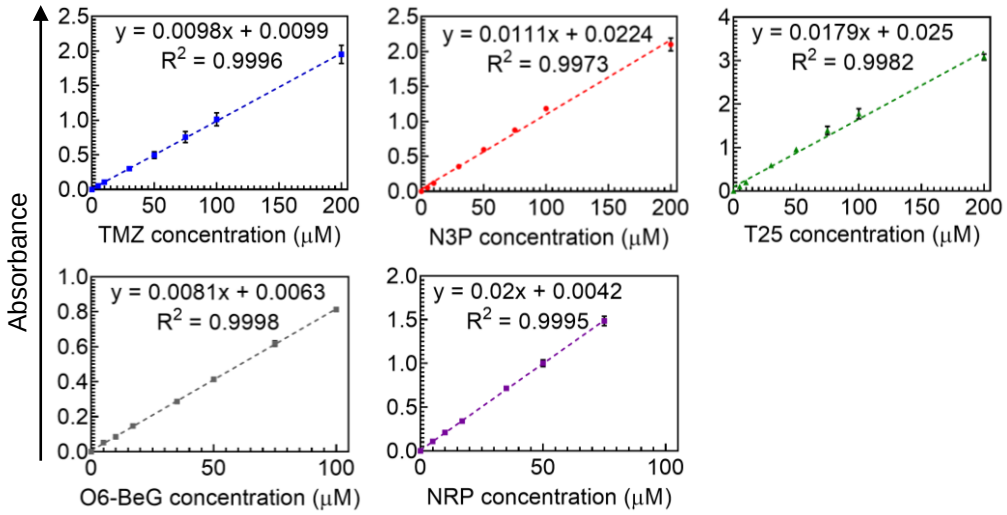

Figure 3.7. The standard curves of TMZ and TMZ analogues (N3P and T25), as well as *O6*-BeG and NRP obtained by UV-vis spectroscopy. Values are reported as mean ± SD (n = 3).

Furthermore, according to previous studies the *in vitro* $t_{1/2}$ of the imidazotetrazine test agents (which are designed to be prodrugs): TMZ, N3P and T25, at 37 °C pH 7.4, are 92, 49 and 173 min, respectively.[92] The imidazotetrazine agents are far more stable at acidic pH and T < 8 °C ($t_{1/2}$ > 100 h). Much like TMZ, the analogues also break down to release their active product at pH > 7 and 37 °C; therefore, under these conditions, the test agents

are not chemically stable for very long. As such, drug encapsulation was carried out under acidic pH and *T* = 2-8 °C, to avoid rapid test agent degradation, and similar conditions were adopted for *O6*-BeG and NRP encapsulation.

3.2.3 AFt encapsulation of test agents

Prior to the encapsulation of the test agents into AFt, some physicochemical properties of the test agents were identified to determine the route of drug encapsulation for the test agents. All test agents except for NRP possessed MW < 300 Da, whilst the salt form of NRP has a MW < 550 Da. However, NRP is a linear molecule with roughly a similar width to the others test agents, so it should be able to cross the channels of the AFt cage. There were no ionisable groups identified in the imidazotetrazine agents and *O6*-BeG, meaning that the drugs were not charged under any pH conditions. As for NRP, it has a pKa value of 9.66, meaning that it should be positively charged at pH values below its pKa. Due to their small size, the test agents were encapsulated into AFt by the 'nanoreactor' i.e. the passive diffusion method, crossing the channels (0.3-0.4 nm in diameter) of the AFt cage, rather than *via* the disassembly-reassembly route. However, once inside the AFt cage, the uncharged agents unlike NRP do not undergo any ionic interactions with the negative interior of the AFt cage and hence would not be retained in the interior core through ionic interactions. Potentially, the larger sized, hydrophobic agents may be better retained in the core due to their larger size and through other interactions such as hydrophobic interactions. So far, test agents in DMSO were added to AFt in 0.1 M NaOAc, pH 5.5, at initial D:A ratios of 800:1 for TMZ:AFt, 700:1 for analogue:AFt, 700:1 for *O6*-BeG and 100:1 for NRP. The initial D:A ratio and initial test agent concentration of 10 mM was deemed to be the ideal initial ratio and test agent concentration to maintain good test agent solubility and loading. The test agent solution was added to AFt gradually (every 30 min) over a time span of 4.5 h to

prevent the test agent from precipitating out of solution. Subsequently, to remove any unencapsulated agents, ultracentrifugation was carried out using a filter MWCO that retains AFt but with large enough pores to release the test agents. Table 3.1 summarises the results following the encapsulation of the test agents into AFt and subsequent purification. For all formulations but AFt-NRP, the final D:A ratio was > 510 molecules per AFt cage, whereas for AFt-NRP it was > 80 molecules per AFt cage. Overall, the EE values were > 60% and DL values > 8%. In addition, the yield of AFt, which looks at how much AFt was retained after purification was > 96%, suggesting very little protein was lost following purification by ultracentrifugation, compared to the protein yields achieved after removal of Fe from the protein by dialysis. Except for NRP, we achieved considerably improved levels of test agents encapsulated inside AFt with the nanoreactor route compared to other previously reported values of up to 100−350 molecules of GW610 and its derivatives and 185 molecules of MTIC.[154,212] Even compared to reports of drugs encapsulated *via* the disassembly-reassembly method our method encapsulated a higher load of the test agents e.g. ~ 91 curcumin or 2 cisplatin molecules were encapsulated per AFt cage *via* the disassembly-reassembly route.[214,215] The enhanced DL can be attributed to the method of gradual step wise addition of test agents, small drug size and decent solubility profiles. In addition, it has been shown that with the method of AFt disassembly at pH 2 and reassembly around pH 7, the AFt cage does not completely reform to the original 24-mer, with defects detected in the AFt cage; so, protein yields are expected to be lower with this method.[218] Therefore, the method of passive diffusion of test agents through the AFt channels remains preferable.

Table 3.1. Summary of the AFt encapsulation of test agents. The mean values for drug:AFt (D:A) ratio, encapsulation efficiency (EE), drug loading (DL) and protein yield are shown along with the standard deviation (n = 3).

	D:A ratio (molecules per AFt)	EE (%)	DL (w/w %)	Protein yield (%)
AFt-TMZ	527 ± 14	84.3 ± 5.2	18.7 ± 2.3	97.0 ± 2.7
AFt-N3P	525 ± 20	70.5 ± 3.3	20.5 ± 3.1	97.3 ± 1.4
AFt-T25	523 ± 26	67.2 ± 6.2	23.3 ± 0.9	96.5 ± 1.5
AFt-*O6*-BeG	550 ± 25	79.1 ± 5.4	23.1 ± 2.2	96.9 ± 3.1
AFt-NRP	82 ± 17	79.3 ± 7.2	8.6 ± 2.1	97.1 ± 1.9

3.2.4 Characterisation of formulations by DLS, ζ-potential and native-PAGE

To assess the integrity of the AFt cage following test agent encapsulation, protein size, charge and MW were assessed before and after drug encapsulation by a combination of DLS, ζ-potential and native-PAGE. Figure 3.8a demonstrates the hydrodynamic size and ζ-potential (inset) of AFt formulations (AFt-TMZ, AFt-N3P, AFt-T25, AFt-*O6*-BeG and AFt-NRP) alongside AFt vehicle alone. According to DLS and ζ-potential measurements, the hydrodynamic size and ζ-potential for all formulations were comparable to that of AFt alone. Average hydrodynamic diameter was 13.3 ± 0.9 nm and average ζ-potential was −12.7 ± 0.3 mV. Since the size and charge of the AFt cage remained the same after test agent encapsulation, this suggested that the protein cage remained stable and intact after test encapsulation and that there was a likely absence of test agent attachment to the AFt exterior, which suggests that the test agents were likely encapsulated within the AFt cage, essential to ensure cellular recognition of the AFt cage.

Next, to lend support to the DLS measurements, native-PAGE was carried out to further confirm the stability of the AFt cage after test agent encapsulation. Through this technique, the MW of the AFt cage was assessed (Figure 3.8b). Native PAGE of AFt formulations revealed protein bands at MWs ~ 480

(monomer) and 720 (dimer) kDa, which are comparable to bands seen for AFt alone samples. This substantiates the results seen with DLS, confirming that the quaternary structure of the protein cage remains stable and intact after test agent encapsulation and that the presence of oligomers was present before test agent encapsulation rather than a by-product from the encapsulation process.

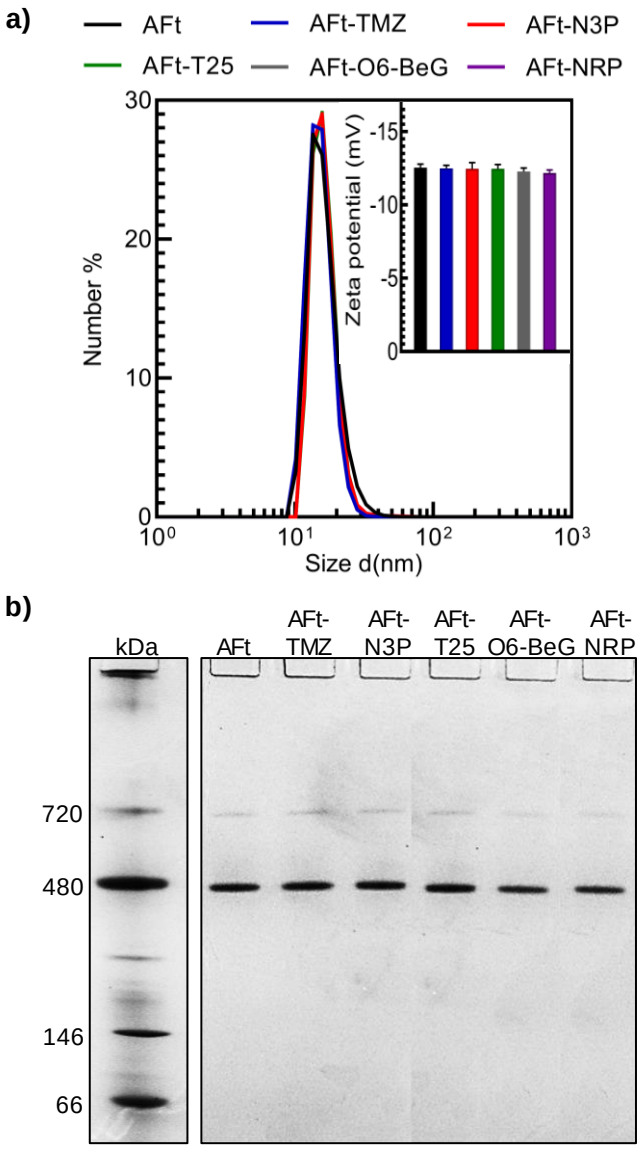

Figure 3.8. AFt size, charge and MW characterisation. (a) Hydrodynamic size distribution of AFt, AFt-TMZ, AFt-N3P, AFt-T25, AFt-*O6*-BeG and AFt-NRP measured by DLS and corresponding ζ-potential values (inset). (b) Native-PAGE of AFt, AFt-TMZ, AFt-N3P, AFt-T25, AFt-*O6*-BeG and AFt-NRP performed on a 4−16% gradient gel. Values are reported as mean ± SD (n = 3).

3.2.5 *In vitro* test agent release studies for AFt formulations

Following encapsulation, we evaluated the release of only the imidazotetrazine agents (TMZ, N3P and T25) from AFt, *in vitro,* under physiologically relevant conditions (*T* = 37 °C; pH 7.4 and pH 5.5). Test agent release from AFt was studied at physiological pH 7.4 and pH 5.5 conditions to mimic the environment of systemic and endosomal/lysosomal compartments, respectively. Figure 3.9 represents the test agent release profiles at two different pH values, from 0 to 24 h. At pH 7.4, slower test agent release was observed during the first three hours of dialysis compared to that seen under pH 5.5 conditions: advantageous for systemic delivery of AFt formulations. This observation was expected considering the AFt channels are narrower at more alkaline pH and widen slowly as the capsule is exposed to increasing acidity.[218] At time *t* > 3 h, chemical degradation of the test agents (a ring-opening event of the imidazotetrazine agents to release the active product) was apparent at pH 7.4, as demonstrated by the downward decline of the curves. Test agent release at pH 5.5, was continuous for 24 h. For all formulations, 60 – 82% maximum test agent release was observed at pH 5.5 compared to a maximum release of 24 – 48% at pH 7.4. Maximum release of test agents occurs after 5 h of dialysis when samples were under pH 5.5 conditions.

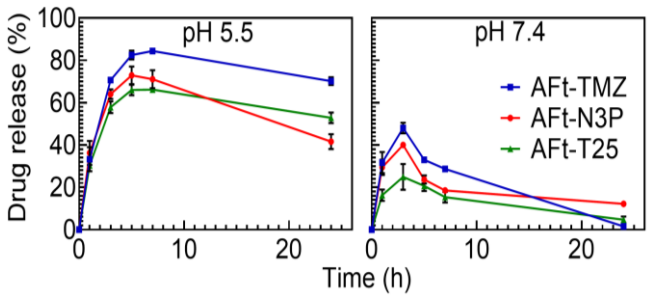

Figure 3.9. Time-dependent test agent release at 37 °C under two buffered conditions, pH 5.5 (0.1 M NaOAc) and pH 7.4 (1X PBS). Values are reported as mean ± SD (n = 3).

When translating observed *in vitro* results to an *in vivo* setting, discrepancies are likely to appear. Many factors affecting the outcome of test agent release *in vivo* would need to be considered. One example would be the difference in the release medium used in the *in vitro* experiments compared to the components of the blood and endosomal/lysosomal milieu, which would lead to different test agent release rates.[219] Important to consider, the rapid rate of the ring-opening imidazotetrazine molecule activation has prevented us from continuing the study beyond 24 h. The fast test agent release from the AFt cage contrasted with some who have reported slower test agent release with larger molecules.[220] Nevertheless, it has been reported that the presence of additional components in the blood may lead to the formation of a protein corona on the nanocages, which may slow down test agent release.[221] As such, a biologically simulated release study to confirm or contradict the test agent release rates seen in our study would be an essential experiment to carry out. On the other hand, selective active targeting may negate the concerns associated with fast test agent release. Targeted therapies would allow for rapid and precise accumulation of test agents in the tumour, preventing unnecessary long circulation around the body and misgivings associated with early test agent leakage e.g. toxicity.

3.2.6 Storage stability of AFt formulations

After test agent encapsulation and purification, AFt formulations were stored in the fridge (2-8 °C). Samples were monitored every day for 7 days to assess the protein and test agent stability. Hydrodynamic size and ζ-potential were measured to observe any changes in protein size and charge over time, and to monitor changes in the aggregation status of AFt. In addition, UV-vis spectroscopy and Bradford assay were used to measure test agent and protein concentration, respectively. Subsequently, the D:A ratio was calculated to show any changes in the number of test agents encapsulated per AFt cage and to show whether a loss of test agent or protein due to ring-opening molecule activation or protein precipitation, affects this parameter. Figure 3.10 summarises the stability of AFt formulations: AFt-TMZ, AFt-N3P and AFt-T25 (currently no data available for AFt-*O6*-BeG and AFt-NRP) during storage. The results demonstrated stable AFt capsules during storage, as indicated by stable and consistent hydrodynamic sizes and ζ-potential values over time compared to samples measured at t = 0 h. The D:A ratio was also similar over time, which indicated that the number of test agent encapsulated per capsule remained the same and that both test agent and protein were not lost due to chemical activation or protein precipitation at the following conditions of pH 5.5, T = 2-8 °C, in the dark. In all, the formulations were stable for a period of 7 days and therefore samples were prepared and used within 7 days. Longer timescales and different storage conditions for the AFt formulations have yet to be investigated.

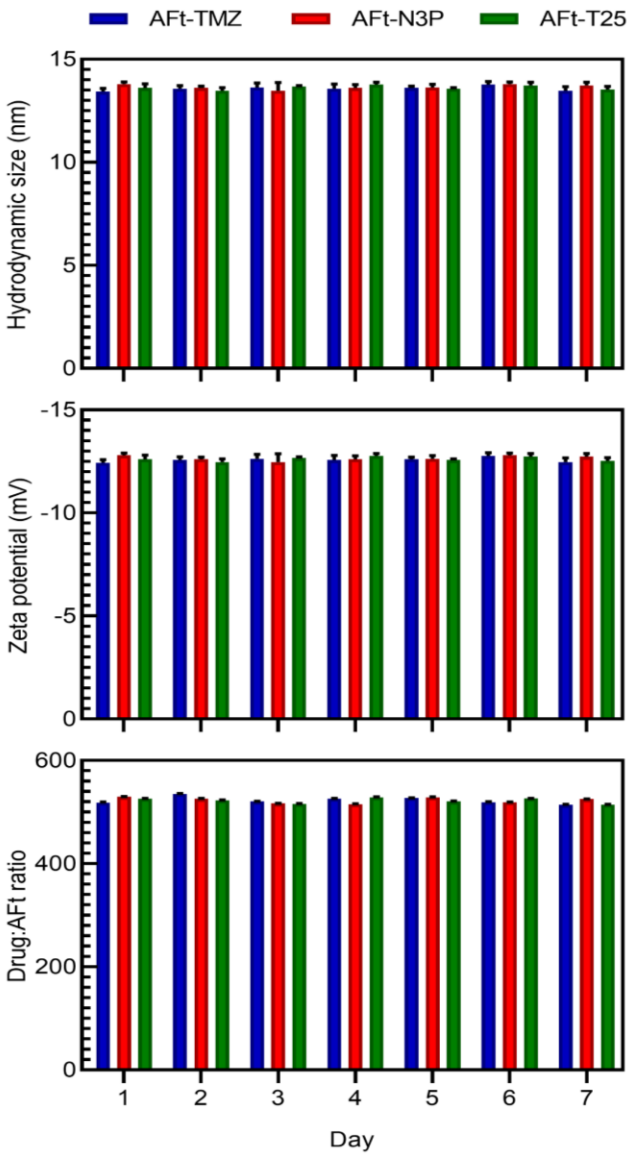

Figure 3.10. AFt-TMZ, AFt-N3P and AFt-T25 stability monitored at storage conditions (*T* = 4 °C; pH 5.5). Hydrodynamic size and ζ-potential were measured by DLS. Test agent and protein concentrations were determined by UV-Vis spectroscopy and Bradford assay, respectively, to estimate the D:A ratio. Values are reported as mean ± SD (n = 3).

3.3 Conclusions

In summary, we have successfully generated Fe-free AFt from Ft using thioglycolic acid as a reducing agent. Six rounds of dialysis with the acid and an additional acid-free buffer exchange round was sufficient to eradicate Fe with little loss of the protein. Various methods were employed to quantify protein concentration. It was concluded that the Bradford assay, despite some disadvantages, was the simplest, most consistent, and cost-efficient method to employ, due to its 96-well setup. Standard curves for the Bradford assay using BSA or outsourced AFt demonstrated comparable concentration values of AFt. However, the BSA standard was still used to calculate the concentration of AFt, due to its cost efficiency and because it can be purchased in large quantities unlike the outsourced Fe-free AFt. Protein yields were > 85% and a loss of the Fe peak was seen by UV-vis spectroscopy, which after many rounds of dialysis was quite efficient; therefore, thioglycolic acid was continually used *via* the dialysis method to generate AFt from outsourced horse spleen Ft.

Subsequently, we successfully loaded > 510 TMZ, N3P, T25 or *O6*-BeG and > 80 NRP molecules per AFt cage, with encapsulation efficiencies > 60%. The test agent load per AFt cage was much higher than the loads reported by various other groups using the nanoreactor method. It was assumed that the small size and favourable solubility and stability profiles of the test agents at the encapsulation conditions of pH 5.5, 4 °C, contributed to the successfully high, test agent load by diffusion. In addition, the stability of the protein capsules was assessed and corroborated by various methods, which included DLS, ζ-potential and native-PAGE. All methods show that the protein remains stable after test agent encapsulation. Size, charge, and MW of the capsules after test agent encapsulation was comparable to AFt alone (before encapsulation).

The storage stability tests so far carried out for AFt-TMZ, AFt-N3P and AFt-T25 only, showed stable formulations under storage (at pH 5.5, 4 °C), which was maintained for a period of 7 days post-encapsulation. Finally, *in vitro* test agent release studies (for AFt-TMZ, AFt-N3P and AFt-T25 only) at pH 7.4 demonstrated slower test agent release in the first 3 h compared to pH 5.5. This is advantageous, since delayed release of test agents from the capsules during systemic administration is desirable to avoid systemic toxicities and to ideally achieve release once inside the cancer cells. Therefore, the trends seen with the release studies were ideal, but will need to be further corroborated with an *in vivo* buffer solution mimic.

Chapter 4 – *In vitro* activity of horse spleen apoferritin encapsulated-temozolomide

4.1 Introduction

AFt is a nanosized (12 nm in diameter) protein that can deliver drugs to cancerous cells *via* passive and active uptake routes.[201] Our work will investigate the suitability of AFt formulations for parenteral (systemic) administration. Like other protein therapeutics a lot of the reasons against the enteral route of administration include instability at low pH, protein degradation by proteases in the GI tract and poor permeability across GI tract mucosal surfaces.[222,223]

TfR1 is a receptor highly expressed on a variety of cancer cells (including GBM) due to their high Fe consumption.[205,224] Transcription factors such as Myc and HIF-1α promote the transcription of TfR1 in many cancers.[225] A study assessing the survival of grade 2 and 3 glioma patients with high TfR1 expression demonstrated that there was a poor survival outcome and that TfR1 played a negative role in the prognosis of glioma.[226]

As such, targeting TfR1 for cancer treatment presents a therapeutic potential. TfR1 targeted treatments include the reduction of TfR1 expression and presentation on cellular surfaces (thus reducing iron uptake) with molecules such as ferristatin II or monoclonal antibodies (directed against TfR1).[227,228] TfR1 can also be a source of targeting for nanomedicines to achieve specificity and selectivity.[207] AFt is one such DDS where naturally its H-subunits can bind to TfR1.[203] This allows for selective accumulation of drugs in cancer cells with high expression of TfR1 over normal cells (with very low numbers of the

receptor). Such selectivity would prevent off-target, negative side effects. Recent interest in using AFt to target the brain has gained momentum. Research groups have been able to show that AFt can successfully traverse the BBB and accumulate in brain tumours.[152,153,229] By using AFt as a carrier for anti-cancer drugs and utilising TfR1 as the point of entry into cancer cells, we can encapsulate more effective drugs for more comprehensive eradication of cancer cells. We propose to encapsulate test agents that directly target the DNA such as TMZ, TMZ analogues and inhibitors of MGMT and PARP-1 (as we have carried out in chapter 3), for targeted treatment of GBM.

TMZ remains the drug of choice for the treatment of GBM. Once hydrolysed at pH > 7, the active product (methyldiazonium cation) then goes onto to alkylate various positions on the DNA.[80] The alkylation product - *O6*-MeG, is the most cytotoxic despite it only accounting for 5-7% of the alkylation products by TMZ.[75,79-82,84,195] Mostly, this is because the other adducts are quickly removed by BER, effectively minimising the consequences of these lesions.[80]

However, the effectiveness of TMZ is diminished in the presence of MGMT. MGMT is an enzyme capable of removing the methyl group specifically from the O6-position of guanine, by transferring the methyl group to Cys145 (of MGMT).[85,197] However, this process harbours consequences for the enzyme, as upon accepting a methyl residue, immediate inactivation of MGMT takes place, and as such, the protein has been dubbed a suicidal enzyme.[230] Therefore, for TMZ to exert cytotoxic action, the cells require an intact MMR system (to detect the *O6*-MeG:thymine base mispairing and alert the DNA damage response to achieve G2/M cellular arrest) and deficient MGMT

expression, because in an environment where MMR is deficient and/or MGMT expression is high, TMZ tolerance or resistance follows.

Herein, we first attempted to examine the potency of TMZ and AFt-TMZ in TMZ sensitive and resistant human cancer and non-cancer cell lines. Such cell lines include an isogenic GBM cell line pair: U373V (MGMT -ve) and U373M (MGMT +ve), and another GBM cell line: LN-18 (MGMT +ve), which is capable of forming tumours in nude mice, as well as CRC cell lines: HCT116 (MMR deficient: MLH1 -ve; MGMT +ve) and HCT116-VR (MMR deficient: MLH1 -ve; MGMT +ve; Pgp +ve) and lastly a non-tumourigenic lung fetal fibroblast cell line, MRC-5. The combination of cell lines selected were employed to assess whether AFt can successfully deliver TMZ to cells in a selective manner and overcome drug efflux by Pgp for enhanced intracellular drug accumulation. If possible, we wanted to see if enhanced drug accumulation with AFt in cancer cells, translated to a greater potency over drug alone, and establish that AFt itself does not exert any form of cytotoxicity. To assess this, multiple *in vitro* growth inhibitory and cytotoxicity assays were employed.

4.2 Results and Discussion

4.2.1 Preliminary assessment of cellular growth inhibition by TMZ and AFt-TMZ *via* MTT assay

TMZ is a DNA alkylating prodrug which is capable of inducing GBM cell death by either apoptosis and/or autophagy, following DNA *O6*-MeG lesion formation and G2/M-phase cellular arrest.[84] To assess the potency of TMZ following its encapsulation within AFt and comparing its cytotoxic activity against TMZ and AFt alone, a variety of sensitive and resistant cancer cell lines, as well as a non-cancer cell line was employed for test agent treatment. Cellular growth inhibition was assessed by utilising a colorimetric assay called MTT assay.[176]

We initially assessed the possibility of MTT reduction being carried out by the test agents or solvent/buffer system used to dissolve the test agents, in the absence of cells. We found that the test agents and solvent/buffer systems did not reduce MTT (no absorbance was seen at 570 nm), at concentrations ≤ 1000 μM for test agents, ≤ 1 μM for AFt alone, ≤ 1% DMSO and ≤ 500 μM NaOAc (0.1 M; pH 5.5).

Next, the anti-cancer activity of unencapsulated (naked) TMZ and TMZ delivered within AFt (AFt-TMZ) was assessed in a panel of cancer and non-cancer cell lines. The MTT assay was employed, and the following cell lines utilised for our studies were: U373V (MGMT −ve), U373M (MGMT +ve) and LN-18 (MGMT +ve) GBM; HCT116 (MMR deficient; MGMT +ve), HCT116-VR (Pgp +ve; MMR deficient; MGMT +ve) CRC, and non-cancerous MRC-5 fibroblasts. The cells were exposed to test agents ranging from a concentration of 0.001 – 1000 μM for 6 days. A 6-day treatment period (which is at least 2 cell cycle rounds) ensured that enough time was given for DNA methylation, MMR

activation and cellular arrest to take place. The absorbance of formazan measured at 570 nm was subsequently plotted against the concentrations of the test agents (Figure 4.1). Treatment of cancer cells with AFt-TMZ demonstrated a greater shift of the curve to the left over naked TMZ treatment, which meant that lower concentrations of AFt-TMZ were required to achieve 50% cellular growth inhibition. Whereas in non-cancerous MRC-5 cells, the difference between AFt-TMZ and TMZ treatment was not as great. Treatment with AFt alone however, did not display growth inhibitory activity and appeared on the plots to remain stable at values similar to those from cells without treatment.

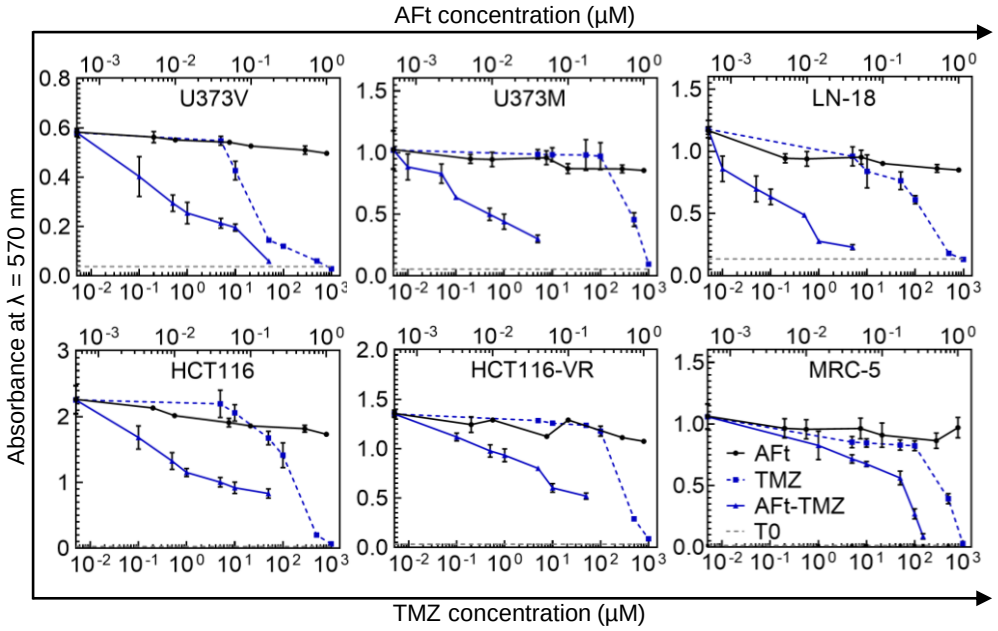

Figure 4.1. Concentration-dependent growth inhibition profiles from MTT assays. The following cells used in the assay include GBM cell lines: U373V (MGMT -ve), U373M (MGMT +ve) and LN-18 (MGMT +ve), CRC cell lines: HCT116 (MGMT +ve; MMR-deficient) and HCT116-VR (MGMT +ve; MMR-deficient; Pgp +ve) and non-cancerous MRC 5 fibroblasts. Cells were exposed to different concentrations of TMZ, AFt-TMZ (the data points on the graph are based on the absorbance against the TMZ concentration of these samples) and AFt (of which the concentration ranges between the lowest and highest concentration of AFt found in AFt-TMZ data points, of the graphs) for 6 days. Values are reported as mean ± SD (n > 3 trials (5 repeats per trial)).

Subsequently, the estimated 50% cellular growth inhibition (GI_{50}) values were determined for each test agent (Figure 4.2). Estimated GI_{50} is defined as the concentration that is required to achieve 50% of the maximal inhibition of cell proliferation. To determine growth inhibition, experimental controls like cells without treatment at treatment time = 0 h (T0) and cells without treatment at treatment endpoint: day 6, enabled GI_{50} values to be calculated. Having a T0 in place (as shown in Figure 4.1) allows us to deduce whether the test agent was slowing the growth of cells (cytostatic effect) or killing the cells (cytotoxic effect). The T0 is also important when there are multiple cell lines present, as it considers for differences in growth rates.

We considered the effects of TMZ and AFt-TMZ in non-resistant (MGMT -ve) and resistant (MGMT +ve) GBM cell lines (Figure 4.2). U373V cells displayed greater sensitivity to TMZ treatment (GI_{50} = 35 µM), in contrast to resistant GBM cell lines where TMZ activity was markedly lower: in U373M GI_{50} = 376 µM and in LN-18 GI_{50} = 181 µM. The enhanced sensitivity to TMZ in U373V was likely due to its low MGMT expression. Even so, all these GI_{50} values are quite high, demonstrating the poor activity of this drug. Remarkably, AFt-TMZ demonstrated significantly lower GI_{50} values in the isogenic GBM cell lines and LN-18 cells, with values < 1.5 µM, suggesting TMZ delivered within AFt to GBM cells conferred a greater advantage to the drug by enhancing its potency over naked TMZ delivery.

Contrary to expectations, AFt-TMZ displayed enhanced activity compared to naked TMZ in all cell lines that showed resistance to TMZ:

(i) Cells where resistance was conferred by MGMT: 532-fold enhanced activity was observed in U373M and 947-fold enhanced activity was observed in LN-18.

(ii) Cells where resistance was conferred by MMR loss: 22-fold enhanced activity was observed in HCT116.

(iii) Cells where resistance was conferred by Pgp expression: 24-fold enhanced activity was observed in HCT116-VR.

It is worth pointing out that TMZ activity was significantly lower in the Pgp expressing HCT116-VR cell line compared to HCT116, confirming the possibility and supporting previously reported studies of Pgp drug efflux as another source of TMZ resistance - where despite that TMZ was not found to be a substrate for Pgp, preferential accumulation was seen in mice brains with Pgp mutated or inhibited cells over wild type.[191] In our case, since HCT116-VR has high Pgp expression, some TMZ molecules may simply efflux out of these cells *via* the Pgp channels, reducing intracellular TMZ levels and thus activity. Whereas delivering TMZ within AFt possibly prevents this, which could explain the difference in activity between TMZ and AFt-TMZ in HCT116-VR cells. Of additional interest, cancer-selective activity was seen, with AFt-TMZ demonstrating enhanced activity in cancer cells over fibroblasts by ~ 5-fold, suggesting AFt may be advantageously employed to reduce off-target side effects. We envisage that the selective activity was imparted due to the differences in the expression of TfR1 between cancer and non-cancer cell lines, allowing AFt to be honed specifically to cells expressing high levels of TfR1 – the cancer cells. Also, the higher activity of AFt-TMZ over naked TMZ was postulated to be due its different mode of cellular uptake (i.e. *via* TfR1 recognition). Consequently, enhanced intracellular accumulation of TMZ should

result in greater potency, as seen in Figure 4.2. Alone, AFt did not display growth inhibitory activity against any of the cell lines at concentrations ≤ 1 µM (Figure 4.1), indicating that any activity seen with AFt-TMZ was imparted by the drug itself.

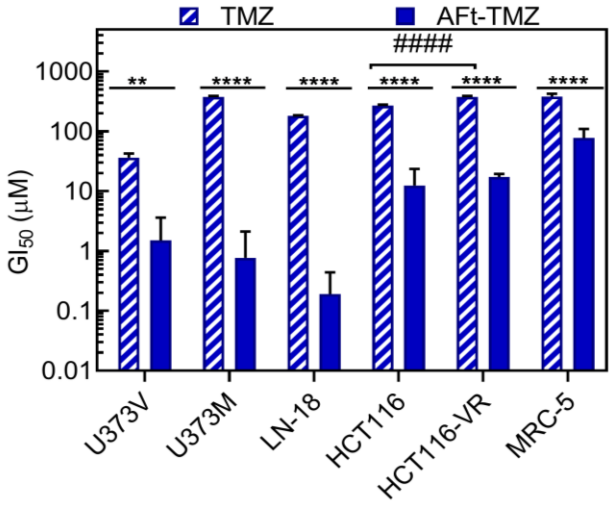

Figure 4.2. A summary of estimated GI_{50} values for TMZ and AFt-TMZ (6-day treatment exposure) in all studied cell lines. Cell used in the assay includes GBM cell lines: U373V (MGMT -ve), U373M (MGMT +ve) and LN-18 (MGMT +ve), CRC cell lines: HCT116 (MGMT +ve; MMR-deficient) and HCT116-VR (MGMT +ve; MMR-deficient; Pgp +ve) and non-cancerous MRC 5 fibroblasts). Values are reported as mean ± SD (n > 3). Significant differences from TMZ are expressed as **P < 0.01 and ****P < 0.0001. Significant differences from HCT116 (TMZ) are expressed as ####P < 0.0001.

Additionally, to observe the effect of DMSO and NaOAc (0.1 M; pH 5.5) on the cells, we have treated cells with a range of different concentrations of DMSO and NaOAc (0.1 M; pH 5.5); the lowest and highest concentration of DMSO/NaOAc mimicking the amount of DMSO/NaOAc found in the lowest and highest concentration of TMZ and AFt-TMZ samples (when diluted with media) used to treat cells. DMSO solvent did not display growth inhibitory activity against any of the cell lines with the concentrations range tested (GI_{50} values > 1%), and NaOAc (0.1 M; pH 5.5) buffer did not display growth inhibitory activity against any of the cell lines with the concentration range tested (GI_{50} values > 500 µM).

4.2.2 Assessment of the number of live/dead GBM cells following exposure to TMZ and AFt-TMZ

In support of the MTT assay study and to assess the cytotoxic potential of encapsulated TMZ, the live cell count assay was carried out on isogenic GBM U373V & M cell lines. A single concentration was selected: 50 µM, to compare naked and encapsulated TMZ. The concentration of 50 µM is below the GI_{50} value of naked TMZ in U373M (in the MTT assay); therefore, it should not be very effective, whereas it is above the GI_{50} value of AFt-TMZ.

From this study, AFt-TMZ treatment demonstrated significantly greater loss of viable U373V & M cells compared to naked TMZ ($P < 0.0001$), whilst AFt alone (concentration equal to protein concentration in AFt-TMZ 50 µM solution) demonstrated little to no loss of viable cells (Figure 4.3). Therefore, the live cell count study lends support to the trends seen in the MTT assay. Interestingly, Fang et al. demonstrated that conjugation of TMZ to chitosan nanoparticles could partially overcome TMZ resistance.[231] Kumari et al. also reported this phenomenon with TMZ loaded lactoferrin nanoparticles.[232] Recently reported was the AFt-encapsulation of combined TMZ-intermediate, MTIC, with copper.[154] All studies have shown that encapsulating TMZ or its product, enhances its potency in cancer cells.

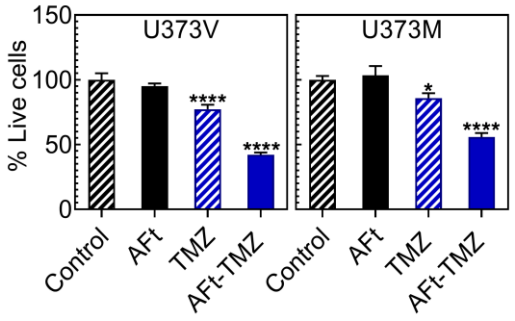

Figure 4.3. *In vitro* cell viability assessment of U373V (MGMT -ve) and U373M (MGMT +ve). Live cells were counted using a haemocytometer with dead cells excluded *via* trypan blue staining following treatment with TMZ (50 μM), AFt-TMZ (50 μM), AFt (0.057 μM; equivalent to the AFt concentration in the AFt-TMZ 50 μM solution) or media alone for 6 days. Values are reported as mean ± SD (n = 5). Significant differences from the control are expressed as *P < 0.05 and ****P < 0.0001.

4.2.3 Assessing the expression levels of cellular protein

To test the hypothesis that the enhanced drug accumulation, potency and selectivity associated with AFt-TMZ was due to greater TfR1 expression in cancer cells, we next examined, by an indirect western blot method, the cellular expression of proteins responsible for AFt uptake and resistance to TMZ.

Henceforth, whole cell protein lysates were prepared from cancer and non-cancer cell lines (used in our studies) and analysed by western blot (Figure 4.4). We first investigated the expression of TfR1 (which binds the H-subunit of AFt) and revealed TfR1 expression for all cancer cell lines, whereas in MRC-5 lysates, expression was below the limit of detection. Since the expression of SCARA5 (which binds the L-subunit of AFt) and TfR2 (whose role is yet unknown) were not observed, we concluded that TfR1 was the receptor responsible for AFt uptake and provided some selective anti-cancer activity for our formulation. Western blot also confirmed the presence of PARP-1 expression in all cell lines, which is an important component of BER and is involved in TMZ resistance; as well as a high presence of MGMT, which confers

TMZ resistance, in U373M, some expression in LN-18 and CRC cell lines and its absence in U373V.

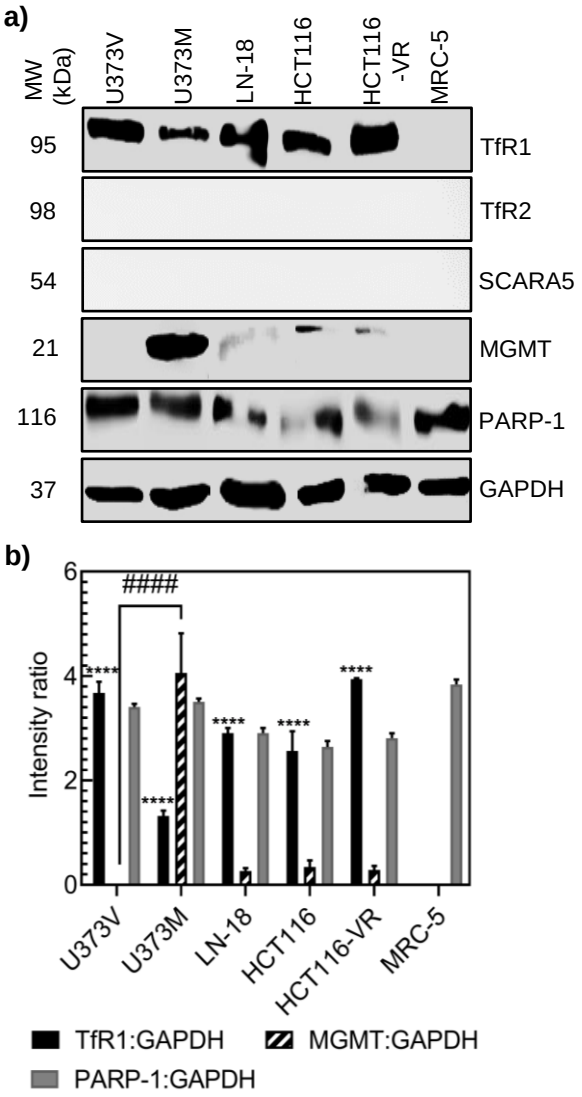

Figure 4.4. Cellular characterisation of protein expression. (a) Western blot analysis of membrane bound receptors responsible for AFt uptake and intracellular proteins responsible for TMZ resistance. (b) Quantification of target protein band intensity expressed as a ratio of target protein to loading control (GAPDH) band intensity using the LICOR software. Values are reported as mean ± SD (n = 3). Significant differences from MRC-5 are expressed as ****P < 0.0001; Significant difference from U373V is expressed as ####P < 0.0001.

To further corroborate the western blot data on TfR1 expression - flow cytometric analyses of TfR1 cell surface expression was conducted on cells sampled during their logarithmic growth phase.

Hereafter, cells were stained with a human anti-TfR1 R-PE conjugated 1° Ab and the fluorescence intensity was quantified from 10000 single cells (Figure 4.5). In contrast to MRC-5 fibroblasts, abundant TfR1 expression was detected in cancer cells (LN-18 and HCT116-VR were not measured), complementing the trends seen in our western blot studies (Figure 4.4). Interestingly, as observed by western blot, reduced TfR1 expression was seen in U373M (transfected with MGMT) compared to U373V cells. This phenomenon is not unusual, often the overexpression of any protein can (and does) occur at the expense of other proteins and may even be destructive, as to make and transport proteins can exhaust the resources of the cells.[233]

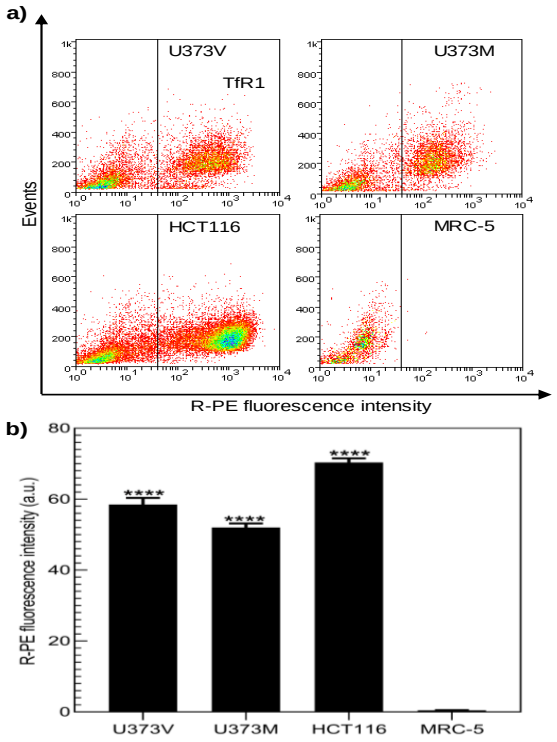

Figure 4.5. Flow cytometric quantification of cell surface TfR1 expression (through quantification of the fluorescence of R-PE conjugated on an anti-TfR1 1° Ab) in U373V, U373M, HCT116 and MRC-5 cells. (a) Dot plot representing a shift of TfR1-(R-PE) signal to the right to signify bound Ab and presence of TfR1. (b) Bar graph summary of the fluorescence intensity of TfR1-(R-PE) conjugated Ab bound to TfR1. Values are reported as mean ± SD (n = 3). Significant difference from MRC-5 are expressed as ****P < 0.0001.

4.2.4 The effect of TMZ and AFt-TMZ on GBM colony formation

To substantiate the intriguing results from the MTT assay for AFt-TMZ activity against TMZ-resistant U373M, clonogenic assays were employed. Figure 4.6 illustrates the survival fraction of U373V and U373M colonies after 24 h and 6-day exposure to naked and encapsulated TMZ (see also Appendix I, Figure 8.1). AFt alone had a negligible effect on colony numbers confirming the non-toxicity of this DDS; however, AFt encapsulation of TMZ augmented the drug's inhibition of colony formation in both U373V and U373M GBM cells. TMZ alone (50 μM) potently inhibited U373V colony formation by 68% and 55% after 24 h and 6 days of exposure, respectively; whereas, U373M cells demonstrated much greater resistance to naked TMZ challenge (colony formation was inhibited by 14% and 47% after 24 h and 6 days of exposure, respectively). In

contrast, 24 h and 6 days of AFt-TMZ (50 μM) exposure potently inhibited U373M colony formation by 35% and 76%, respectively. U373M cells were significantly less able to survive the AFt-TMZ challenge (compared to naked TMZ) and form progeny colonies; supporting MTT assays and cell counts and further demonstrating that AFt delivery of TMZ was able to weaken tumour resistance to TMZ mediated by MGMT. However, since TMZ degrades rapidly at pH 7.4 and 37 °C, it was surprising to see greater loss in colony fractions after 6 days over 24 h. Hypothetically one would assume the results should be similar between the two timepoints considering that this experiment involved only a single dose challenge. Therefore, further investigations will need to be carried out to clarify the mechanism behind the differences in the percentage of survival fractions between the two timepoints.

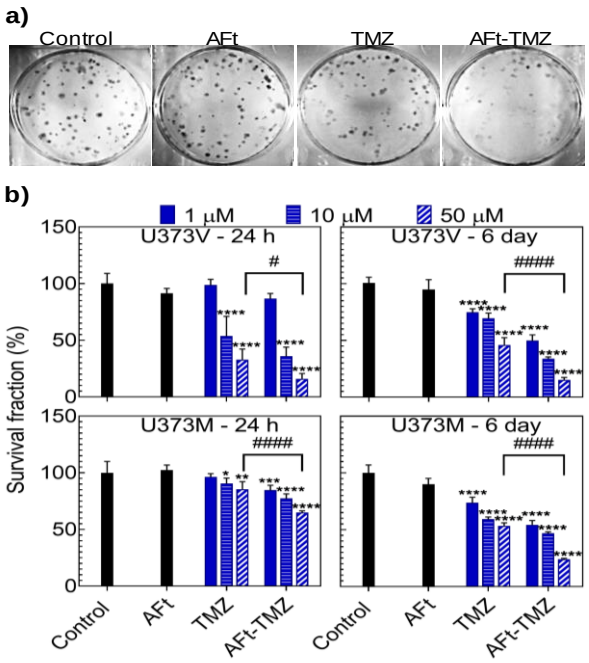

Figure 4.6. *In vitro* characterisation of cell proliferation proficiency following treatment. (a) Representative images of the clonogenic assay conducted on U373M for a 6-day treatment (TMZ 50 μM, AFt-TMZ 50 μM, AFt 0.057 μM, or media alone) exposure. (b) Percentage survival fraction of GBM: MGMT +/−ve cells following either a 24 h or 6-day treatment regimen with 1, 10, or 50 μM TMZ/AFt-TMZ and 0.057 μM AFt (equivalent to AFt concentration of AFt-TMZ 50 μM sample). Values are reported as mean ± SD (n = 5). Significant differences from the control are expressed as *P < 0.05, **P < 0.01, ***P < 0.001, and ****P < 0.0001. Significant differences from TMZ are expressed as #P < 0.05. ####P < 0.0001.

4.2.5 Monitoring the changes to cell cycle and DNA damage status of GBM cells following exposure to TMZ and AFt-TMZ

After adopting several *in vitro* assays to assess the anti-cancer activity of AFt-TMZ, it was evident that encapsulated TMZ demonstrated enhanced anti-cancer activity over naked TMZ and this trend was unexpectedly seen in TMZ resistant cancer cell lines. Therefore, we wanted to further probe the reason for this greater activity associated with AFt-TMZ over TMZ. We hypothesise that there are greater intracellular concentrations of TMZ following AFt-TMZ over naked TMZ treatment. If this is the case, we predict to see greater cell cycle perturbations, DNA damage and DNA *O6*-MeG levels. So, we first proceeded to assess GBM cell cycle progression after 72 h exposure of cells to TMZ and AFt-TMZ (50 μM). Cells were stained with the nuclear stain, PI, and the fluorescence intensity measured by flow cytometry.

The treatment exposure period of 72 h was used to allow cells to complete at least one division for the detection of putative cell cycle perturbation by AFt-TMZ. It is known that TMZ (in the absence of MGMT) alkylates DNA causing S and G2/M arrest.[79,81] G2/M arrest can be seen following treatment with TMZ in U373V cells only; whilst, both U373V and U373M cells expressed greater G2/M- and S-phase arrest following exposure to AFt-TMZ (Figure 4.7a and Appendix II, Figure 8.2). Compared to U373V control populations, S-phase arrest was increased by ~ 2.5- and 2.6-fold with TMZ and AFt-TMZ treatment, respectively; G2/M-phase arrest was increased by ~ 2.3- and 2.8-fold, respectively. As for U373M, S- and G2/M-phase arrest was increased by ~ 1.87- and 2-fold, respectively, following treatment with AFt-TMZ; minimal cell cycle perturbations were seen following TMZ alone treatment at 50 μM. In support of previous studies, both cell lines displayed non-perturbed cell cycle profiles when exposed to AFt alone.

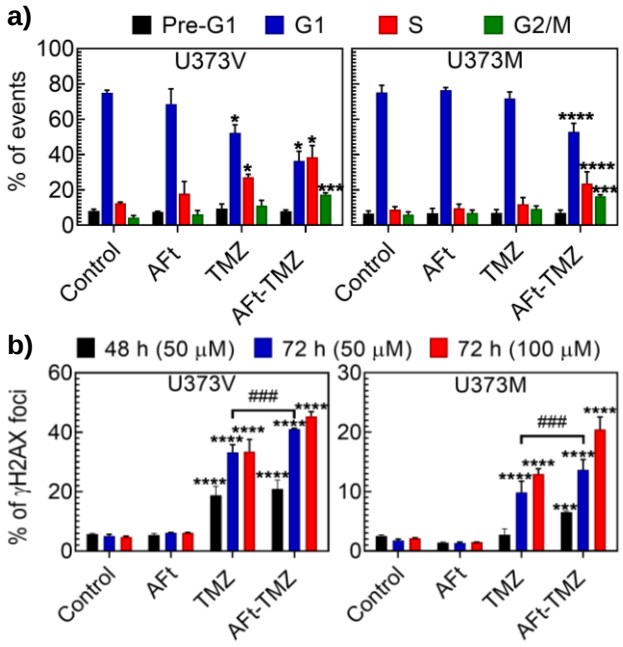

Figure 4.7. Mechanism of action of TMZ compared to AFt delivered TMZ (AFt-TMZ) in GBM: MGMT +/−ve cells, as assessed by flow cytometry. (a) Summary of the number of gated events (single cells), expressed as a percentage from 10,000 gated events, arrested in different phases of the cell cycle (using PI DNA stain), after 72 h treatment (TMZ 50 μM, AFt-TMZ 50 μM, AFt 0.057 μM, or media alone) exposure. (b) Summary of the fluorescence intensity of γH2AX foci (expressed as a percentage from 10,000 gated events), after a 48 or 72 h treatment exposure to 50 or 100 μM TMZ and AFt-TMZ and 0.057 or 0.1 μM AFt. Values are reported as mean ± SD (n = 3). Significant differences from the control are expressed as *P < 0.05, ***P < 0.001, and ****P < 0.0001. Significant differences from TMZ are expressed as ###P < 0.001.

It was reported that cell cycle arrest at the S- and G2/M-phase occurs following repeated production of DNA strand breaks after futile mismatch repair, which signals the ATR/CHK1 system and triggers cellular arrest.[79,81] Therefore, we sought to establish whether the increased S- and G2/M-phase arrest seen with AFt-TMZ, which has so far shown to transcend the resistance systems in GBM cells, evoking significantly enhanced activity over TMZ alone, translated to greater DNA damage following treatment for 48 and 72 h. We attempted to quantify the presence of γ-H2AX foci, which is indicative of DNA double strand breaks, by flow cytometry.[234] As such, our studies have demonstrated that greater levels of γ-H2AX foci were observed following treatment of U373V and

U373M cells with AFt-TMZ (compared to TMZ alone; Figure 4.7b and Appendix III, Figure 8.3). These levels were shown to increase in both time- and concentration-dependent manners. In U373V and U373M, 72 h exposure to 50 μM AFt-TMZ yielded ~ 1.2- and 1.4-fold significantly more DNA double strand breaks over TMZ alone ($P < 0.001$), respectively. This corroborated well with the trends observed in cell cycle analyses.

4.2.6 Quantifying differences in the levels of DNA *O6*-MeG following exposure to TMZ and AFt-TMZ

A follow up study was next carried out to assess the reasoning behind the greater S- and G2/M-phase arrest, and γ-H2AX foci levels from AFt-TMZ over naked TMZ treatment, irrespective of the MGMT status of GBM cells. We proceeded to quantify the DNA *O6*-MeG levels by indirect ELISA, following treatment with TMZ and AFt-TMZ (50 μM) for multiple time durations (4−144 h). The time range was selected to cover all treatment time points used for all assays so far, with 4 h decided arbitrarily as the point by which AFt uptake by endocytosis should be completed, most of the TMZ molecules broken down and methyldiazonium cations released for DNA alkylation.

Hereby, ELISA was employed to confirm the presence and compare the levels of DNA *O6*-MeG in single-stranded, digested DNA samples. As such, Figure 4.8 demonstrates a plot of absorbance (signalling absorbance from antibody bound to DNA *O6*-MeG) versus time for both isogenic GBM cell lines, following treatment. The results suggest that AFt-TMZ delivered significantly more ($P < 0.001$) methyl groups to *O6*-guanine then TMZ alone, for all treatment exposure periods. It was also apparent that the levels start to slowly decline after 24 h. Further studies are required to investigate why levels decline after 24 h. In addition, we have yet to quantify the levels of DNA *O6*-MeG and to do this we

would require a standard curve, possibly prepared by high performance liquid chromatography (HPLC).

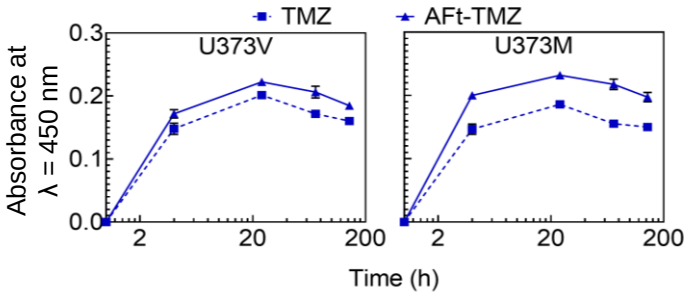

Figure 4.8. Indirect ELISA, DNA *O6*-MeG quantification in GBM: MGMT +/−ve cells following exposure of cells to 50 μM TMZ or AFt-TMZ. Values are reported as mean ± SD (n = 3).

4.2.7 Monitoring the morphological changes to GBM cells after short treatment exposure

We further evaluated the effects of AFt-TMZ treatment on GBM cells using ESEM in order to observe morphological changes to the cell surface after brief exposure to test agents. By exploiting the surface scanning capabilities of this technique, pit formation may be visualised to help support the hypothesis that AFt is internalized by clathrin-mediated endocytosis. However, GBM cells were quite flat and not very 3-dimensional, and so the resolution required to scrutinise the levels of change apparent on the cell surface during uptake was not achievable. Nevertheless, it was apparent that the size and shape of the cell was greatly affected by AFt-TMZ, more so than by naked TMZ after 24 h of treatment (Figure 4.9a). In contrast to the control cells, those treated with AFt-TMZ appeared more shrunken, with obvious membrane blebbing on U373M.

Additionally, confocal microscopy studies were carried out on stained actin filaments (using phalloidin) to further corroborate the ESEM work. This technique provided an added advantage towards scrutinising morphological changes to cells by fluorescently tagging the cytoskeleton and subsequently

allowing us to collect serially thin optical sections from a thick specimen in a non-invasive manner, to create high resolution images.[190] Herein, we can see that the intensity of the phalloidin stain was at its lowest with AFt-TMZ; a more shrunken cellular morphology most likely indicates reduced uptake of F-actin stain (Figure 4.9b). Cell shrinkage and blebbing may signify apoptosis. The F-actin cytoskeleton is an essential component in the regulation of cell shape, migration, and division, and its reduction infers loss of these capabilities.[235] Therefore, these methodologies have demonstrated that AFt-TMZ affected cellular morphology as early as 24 h post treatment.

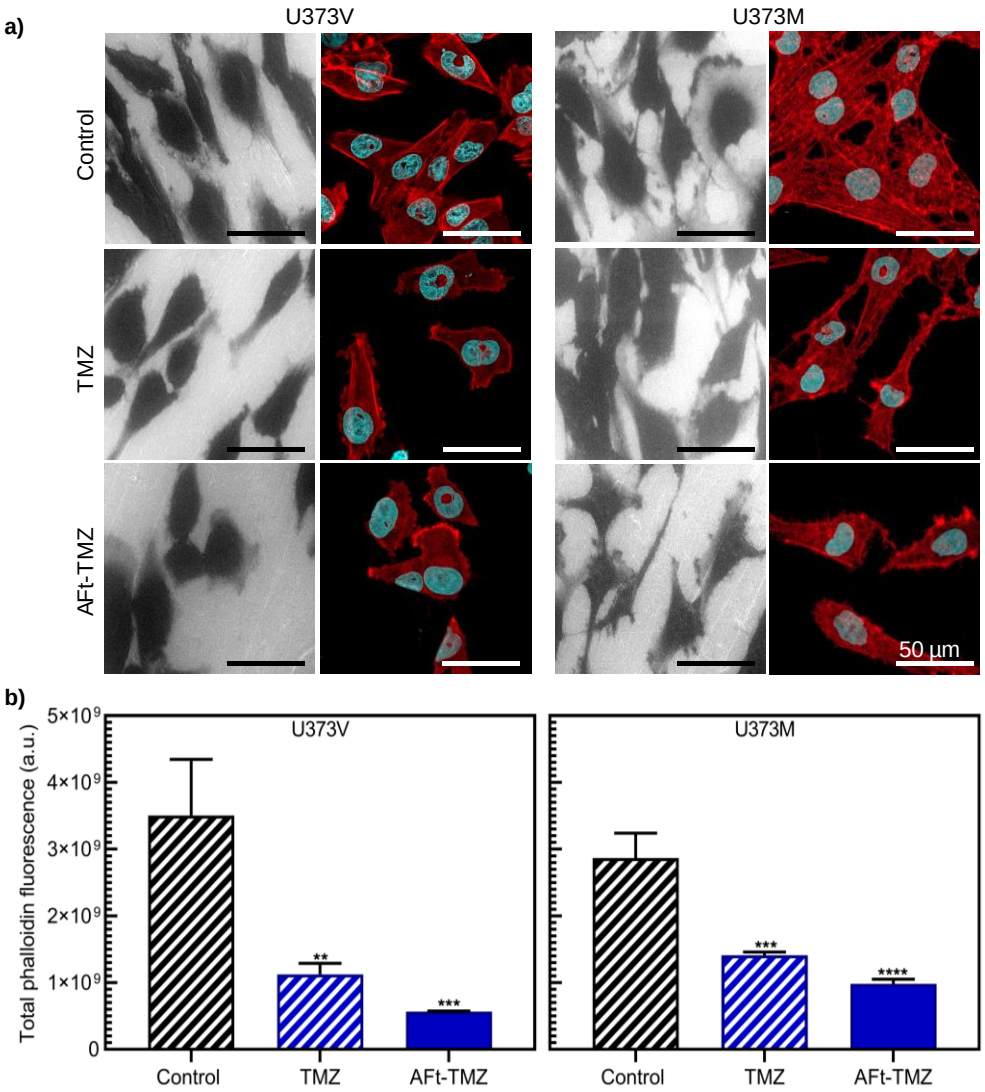

Figure 4.9. Morphological changes to GBM cells (MGMT +/-ve) following 24 h treatment exposure (TMZ/AFt-TMZ; 50 µM). (a) Cell morphology was imaged by a combination of ESEM and confocal microscopy (phalloidin (red) − F-actin stain; DAPI (blue) − nucleus stain). The scale bar is 50 µm. (b) Plot summarising total phalloidin fluorescence in GBM cells. Values are reported as mean ± SD (n = 3). Significant differences from the control are expressed as **P < 0.01, ***P < 0.001 and ****P < 0.0001.

4.3 Conclusions

In summary, we have successfully demonstrated through initial *in vitro* assays that the delivery of TMZ within AFt (AFt-TMZ formulation) was able to overcome various modes of TMZ resistance. *In vitro* studies intriguingly demonstrated that in contrast to naked TMZ, the AFt nano-formulation displayed significantly enhanced activity against MGMT +/−ve GBM cell lines and MMR deficient and Pgp +/-ve CRC cell lines. In fact, where AFt-TMZ displayed good growth inhibitory activity in Pgp overexpressing CRC cell line, treatment with TMZ alone faced more resistance compared to Pgp -ve CRC cell line. Furthermore, clonogenic and live cell count assays further corroborated the MTT assays by establishing that AFt-TMZ was indeed able to by-pass MGMT resistance and exhibit a greater decrease in colony fractions and live cells compared to naked TMZ treatment. In addition, we were able to see some selectivity with AFt-TMZ treatment between cancer and non-cancer cell lines. We attributed this selectivity to the differences in the expression of TfR1, with MRC-5 not showing TfR1 expression, according to western blot and flow cytometry analyses.

We next probed the intriguing activity associated with AFt-TMZ further and conclusively demonstrated that there was greater accumulation of *O6*-MeG DNA adducts, enhanced S- and G2/M-phase cell cycle arrest, and γ-H2AX levels in U373M, with AFt-TMZ over naked TMZ treatment. This supports the hypothesis that TfR1, expressed by cancer cell lines used in our studies, possibly enables greater AFt-TMZ uptake and avoids recognition by Pgp, allowing enhanced intracellular accumulation of TMZ and possibly overwhelming the suicide repair protein MGMT; conferring sensitivity to TMZ in MGMT (+ve) GBM cells. If *O6*-guanine methylation outpaces MGMT protein synthesis, MGMT depletion would ensue.[236]

Finally, in support of previous assays we have carried out imaging *via* ESEM and confocal microscopy and established a loss in cell size and shape and added presence of morphological markers of apoptosis in U373M, following treatment with AFt-TMZ. Importantly, it was demonstrated through various assays that AFt alone treatment was non-toxic. These findings lay the foundations for AFt, a biocompatible, species specific, nanosized biomaterial with built-in targeting, to deliver concentrated amounts of anti-cancer small molecules to tumours in a tolerable and potent manner.

Chapter 5 – *In vitro* assessment of alternative horse spleen AFt encapsulated-test agents that overcome TMZ resistance

5.1 Introduction

Despite the enhanced activity demonstrated with AFt-TMZ in all cancer cells, it remains ideal that alternative agents are explored, to ensure inherent and acquired TMZ resistance in GBM tumours is overcome. Therefore, one approach has been to explore the encapsulation of TMZ analogues, using AFt, to overcome MGMT- and MMR-mediated TMZ resistance.

Additionally, other approaches for overcoming TMZ resistance include combination treatment. Two examples include the co-delivery of TMZ with MGMT or with PARP inhibitors, which would aim to sensitise GBM cells to TMZ and achieve enhanced accumulation of *O6*-MeG or *N7*-MeG and *N3*-MeA, respectively.[86] PARP inhibition is more effective in cells that have mutated breast cancer genes 1/2 (BRCA genes 1/2), which lead to homologous recombination (HR)-deficient cells.[237] PARP is a component of BER and is actively involved in diminishing the effects of *N7*-MeG and *N3*-MeA adduct formation.[237-239] In addition, PARP inhibition also leads to another mode of cytotoxicity; it can block auto polyADP-ribosylation (PARylation) by PARP, which is required for PARP dissociation from DNA.[237] This can lead to the formation of cytotoxic PARP-DNA complexes and the accumulation of DNA double strand breaks.[237]

Combinations of TMZ with MGMT- or PARP-inhibitors have been previously explored, even in the clinical setting for GBM treatment, with some success.[237-

[241] However, one underlying issue remains, is the adverse side effects associated with these combinations. If the drugs are not specifically targeted towards cancer cells and these drugs end up also in healthy cells, then inhibiting important protective cellular mechanism such as DNA damage repair will sensitise those cells to the DNA damage associated with TMZ chemotherapy, and so adverse side effects like myelosuppression arise. This has been a particular issue with the combination of TMZ with *O6*-BeG (an MGMT inhibitor). Therefore, in our project, we aim to co-deliver such agents inside AFt, to achieve specific accumulation of the test agents in GBM cells and overcome issues of unwanted toxicity.

5.2 Results and Discussion

5.2.1 Preliminary assessment of cellular growth inhibition by AFt encapsulated N3P or T25 analogues *via* MTT assay

The anti-cancer activity of naked N3P/T25 and N3P/T25 delivered within AFt (AFt-N3P and AFt-T25, respectively) was assessed in a panel of cancer and non-cancer cell lines. The MTT assay (see section 2.6.1) was employed, and the following cell lines were utilised for our studies: U373V (MGMT −ve), U373M (MGMT +ve) and LN-18 (MGMT +ve) GBM; HCT116 (MMR deficient; MGMT +ve) CRC, and non-cancerous MRC-5 fibroblasts. These cell lines were selected to see if the treatment with encapsulated analogues (like with naked analogue treatment) establishes good anti-cancer activity irrespective of the MGMT or MMR status of cancer cells. The cells were exposed to test agents with a concentration ranging from 0.01 μM to 500 μM for 6 days. The absorbance of formazan at 570 nm was determined and plotted against the concentrations of test agents (Figure 5.1). The curves for AFt-N3P and AFt-T25 both demonstrate a greater shift to the left, over naked test agent treatment; meaning that encapsulated test agents demonstrated greater potency compared to naked agents. This effect was less pronounced in MRC-5, which suggests that some degree of selectivity for AFt formulation was achieved between cancer and non-cancer cells. Also, AFt alone treatment does not appear to cause much growth inhibition when compared to untreated control; further cementing its biocompatibility as a DDS.

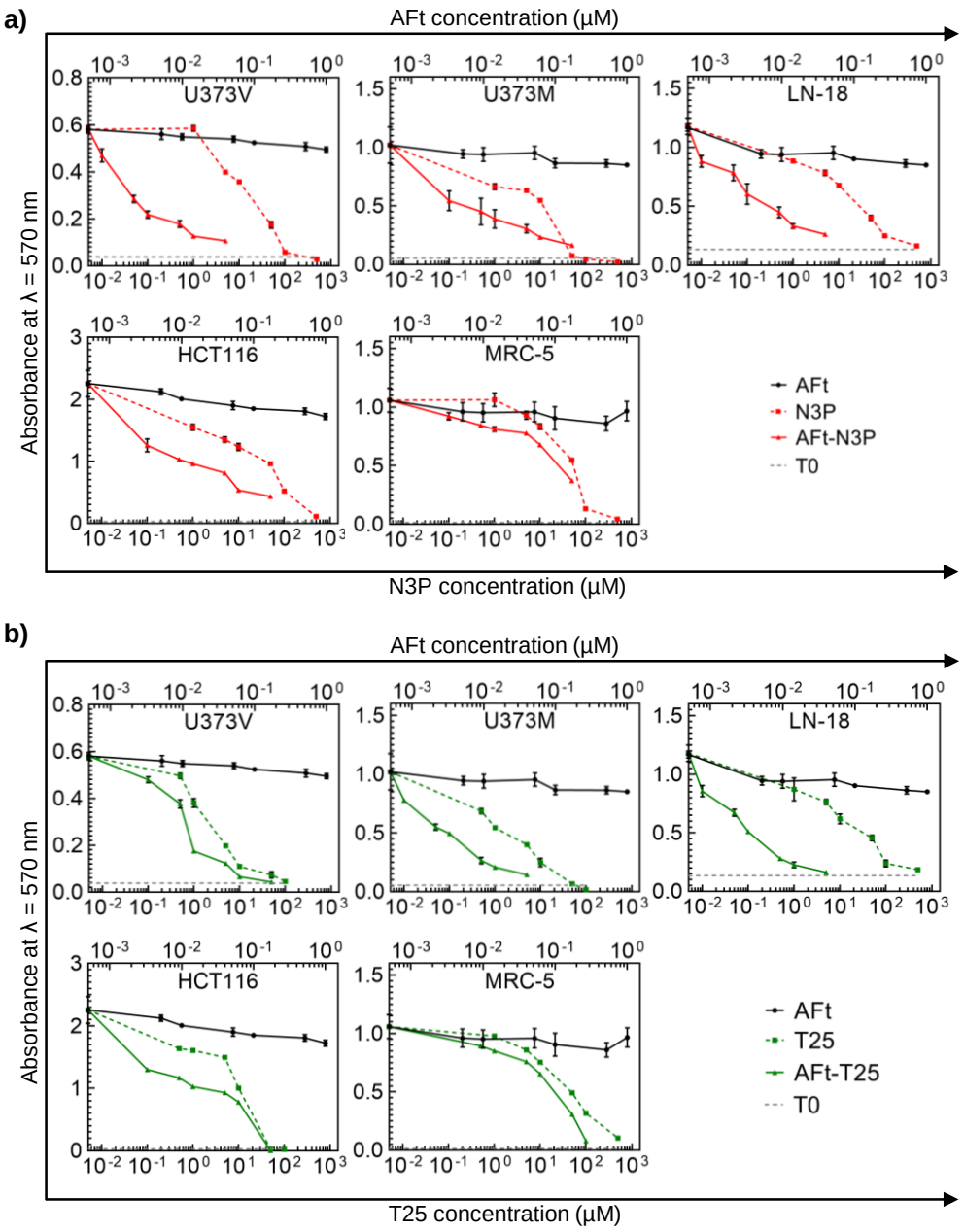

Figure 5.1. *C*oncentration-dependent growth inhibition profiles from MTT assays. Cells used in the assay includes GBM cell lines: U373V (MGMT -ve), U373M (MGMT +ve) and LN-18 (MGMT +ve); CRC cell line: HCT116 (MGMT +ve; MMR-deficient) and non-cancerous MRC 5 fibroblasts. (a) Cells were exposed to different concentrations of AFt, N3P, and AFt-N3P for 6 days. (b) Cells were exposed to different concentrations of AFt, T25, and AFt-T25 for 6 days. Values are reported as mean ± SD (n > 3 trials (5 repeats per trial)).

Estimated GI_{50} values were determined for each test agent (Figure 5.2). First, we assessed the activities of N3P/T25 and AFt-N3P/AFt-T25 in non-resistant (MGMT -ve) and resistant (MGMT +ve) GBM cell lines. U373V cells displayed greater sensitivity to N3P (GI_{50} = 30.88 µM) and T25 (GI_{50} = 3.47 µM) over TMZ

(GI_{50} = 35 µM) treatment (see section 4.2.1 for TMZ results). Interestingly, this was also the case in resistant GBM cell lines where treatment with N3P in U373M (GI_{50} = 28.06 µM) and LN-18 (GI_{50} = 19.62 µM) cells, as well as with T25 in U373M (GI_{50} = 6.87 µM) and in LN-18 (GI_{50} = 15.27 µM) cells demonstrated far greater activity compared to treatment with TMZ in U373M (GI_{50} = 376 µM) and in LN-18 (GI_{50} = 181 µM) cells. Therefore, the analogues appear to impart greater anti-cancer activity over TMZ by overcoming MGMT repair.

Again, both analogues delivered within AFt demonstrated significantly lower GI_{50} values in the isogenic U373 cell lines and LN-18 GBM cells, with values < 1 µM; suggesting TMZ analogues delivered within AFt to GBM cells, conferred a greater advantage to the test agents by enhancing its potency over naked TMZ analogue delivery.

Of interest, cancer-selective activity was also seen, with AFt-N3P and AFt-T25 demonstrating enhanced activity in cancer cells over fibroblasts (GI_{50} values < 8 µM in cancer cells and > 27 µM in fibroblast cells, which accounts for > 152-fold with AFt-N3P and > 31-fold with AFt-T25 treatment when taking into consideration only GBM cells), suggesting AFt may be favourably employed to reduce off-target side effects. The selective activity was likely imparted due to the differences in the expression of TfR1 between cancer and non-cancer cell lines. AFt rapidly enters and accumulates inside the lysosomes following TfR1 receptor mediated endocytosis; therefore, evasion of Pgp efflux may be possible. We envisage that the enhanced intracellular accumulation of TMZ analogues with AFt delivery, as well as the added capability of the analogues to impart activity irrespective of the MGMT and/or MMR status of cancer cells, resulted in greater potency. Exposure to AFt alone did not result in growth

inhibitory activity against any of the cell lines at concentrations ≤ 1 μM, indicating that any activity seen with AFt-N3P/AFt-T25 was imparted by the test agent itself.

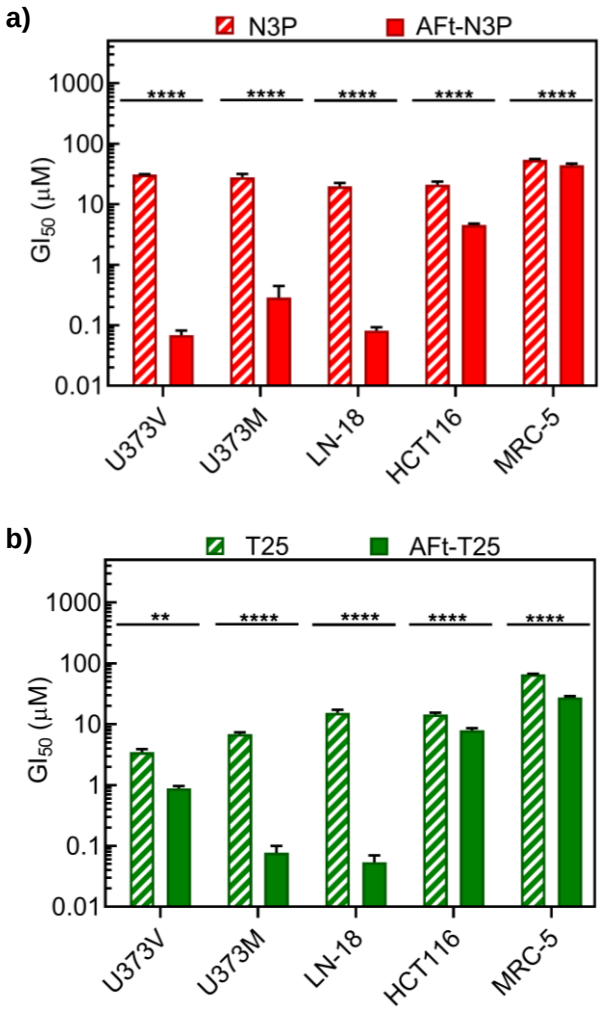

Figure 5.2. Bar graphs of estimated GI_{50} values following a 6-day treatment of all studied cell lines. Cells used in the assay includes GBM cell lines: U373V (MGMT -ve), U373M (MGMT +ve) and LN-18 (MGMT +ve); CRC cell line: HCT116 (MGMT +ve; MMR-deficient) and non-cancerous MRC 5 fibroblasts). (a) Represents the estimated GI_{50} values following treatment of cells with N3P and AFt-N3P. (b) Represents the estimated GI_{50} values following treatment of cells with T25 and AFt-T25. Values are reported as mean ± SD (n > 3). Significant differences from TMZ analogue alone are expressed as **P < 0.01 and ****P < 0.0001.

5.2.2 Effect of MGMT or PARP inhibitors on AFt-TMZ activity assessed *via* MTT assay

Next, we attempted to assess the effect of combining TMZ with a commonly investigated MGMT inhibitor called *O6*-BeG (see Figure 3.1b), whose roles is to deplete MGMT levels and thereby allow DNA *O6*-MeG levels to accumulate following TMZ treatment. Studies have been conducted by other research groups exploring such combination treatments and have reported myelosuppression as a dose-limiting size effect (due to low MGMT levels in the bone marrow).[242] Therefore, to overcome this issue we encapsulated *O6*-BeG within AFt and assessed its anti-cancer activity versus naked *O6*-BeG *via* the MTT assay, prior to assessing the anti-cancer activity of combined TMZ and *O6*-BeG; assays were also conducted to determine the anti-cancer activity of combined TMZ and *O6*-BeG. The anti-cancer activity was assessed in U373M (MGMT +ve) GBM and non-cancerous MRC-5 fibroblast cell lines. The cells were exposed to test agents with concentration in the range 0.01 – 500 μM for 6 days. The absorbance of formazan at 570 nm was determined and plotted against the concentrations of test agents (Figure 5.3a) and estimated GI_{50} values were determined for each test agent (Figure 5.3b).

Alone, the anti-cancer activity of *O6*-BeG was low in U373M (GI_{50} = 90.80 μM) and far lower in MRC-5 (GI_{50} = 244.72 μM) but was potentiated in U373M when *O6*-BeG was delivered inside AFt (AFt-*O6*-BeG), by 277-fold. Additionally, cancer-selective activity was seen. AFt-*O6*-BeG demonstrated enhanced activity in U373M over MRC-5 (GI_{50} = 0.33 μM in U373M and 218.06 μM in MRC-5), suggesting that AFt may reduce off-target side effects. Note, that exposure to AFt alone did not result in any growth inhibitory activity up to concentrations of ≤ 1 μM, confirming that the observed activity seen with AFt-*O6*-BeG was imparted by the test agent itself.

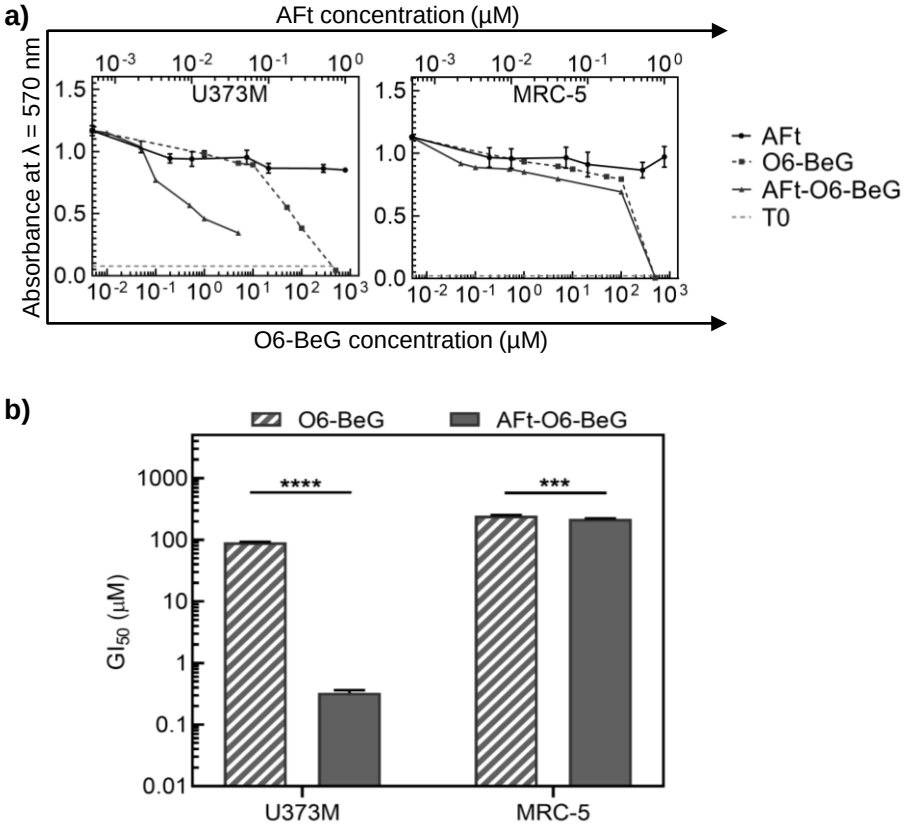

Figure 5.3. MTT assay to assess cellular growth inhibition. (a) *C*oncentration-dependent growth inhibition profiles from MTT assays for GBM cell line: U373M (MGMT +ve) and non-cancerous MRC 5 fibroblasts. Cells were exposed to different concentrations of AFt, *O6*-BeG, and AFt-*O6*-BeG for 6 days. Values are reported as mean ± SD (n > 3 trials (5 repeats per trial)). (b) A summary of estimated GI_{50} values. Values are reported as mean ± SD (n > 3 trials). Significant differences from *O6*-BeG alone are expressed as ***P < 0.001 and ****P < 0.0001.

We then sought to determine the potential of combining TMZ solution with *O6*-BeG solution (TMZ+*O6*-BeG) and AFt-TMZ solution with AFt-*O6*-BeG solution (AFt-TMZ+AFt-*O6*-BeG), in a 1:1 molar ratio. The aim with this combination approach was to inhibit MGMT, to enhance DNA *O6*-MeG levels from TMZ alkylation. Figure 5.4 demonstrates the MTT plots of naked and encapsulated TMZ+*O6*-BeG combinations, with Table 5.1 summarising the estimated GI_{50} values from both test agents in the combination. Treating U373M with encapsulated TMZ+*O6*-BeG demonstrated greater growth inhibitory activity over naked agents by 216-fold. Cancer-selective activity was also seen. AFt-

TMZ+AFt-*O6*-BeG demonstrated enhanced activity in U373M over MRC-5 by 251-fold (see Table 5.1), suggesting AFt may be favourably employed to reduce off-target side effects. AFt alone did not display growth inhibitory activity against any of the cell lines at concentrations ≤ 1 μM, indicating that any activity seen with the AFt-TMZ+AFt-*O6*-BeG combination was imparted by the test agents.

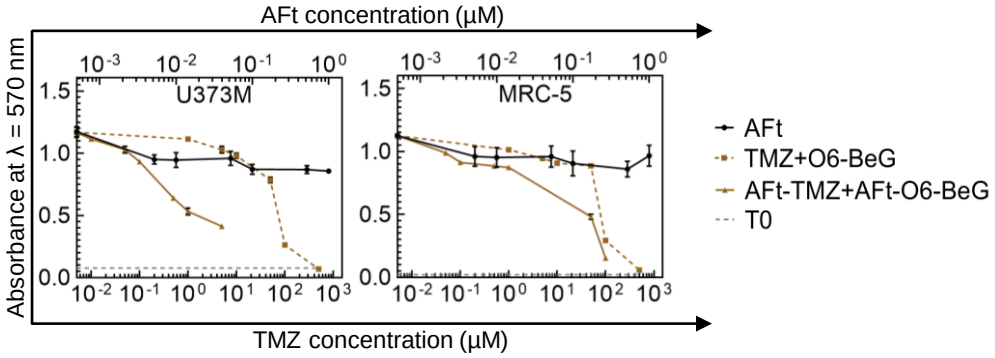

Figure 5.4. *C*oncentration-dependent growth inhibition profiles from MTT assays. Cells used in the assay includes GBM cell line: U373M (MGMT +ve) and non-cancerous MRC 5 fibroblasts. Cells were exposed to different concentrations of AFt, TMZ+*O6*-BeG (based on the TMZ concentration), and AFt-TMZ+AFt-*O6*-BeG (based on the TMZ concentration) for 6 days. Values are reported as mean ± SD (n > 3 trials (5 repeats per trial)).

Table 5.1. A summary of the estimated GI_{50} values following a 6-day treatment exposure (1:1 molar ratio of TMZ+*O6*-BeG or 1:1 molar ratio AFt-TMZ+AFt-*O6*-BeG) in GBM cell line: U373M (MGMT +ve) and non-cancerous MRC 5 fibroblasts). GI_{50} values were determined for each test agent in the combination administered to cells. Values are reported as mean ± SD (n > 3).

	TMZ+*O6*-BeG		AFt-TMZ+AFt-*O6*-BeG	
	TMZ GI_{50} (μM)	*O6*-BeG GI_{50} (μM)	TMZ GI_{50} (μM)	*O6*-BeG GI_{50} (μM)
U373M	62.46 ± 2.35	62.46 ± 2.43	0.28 ± 0.01	0.28 ± 0.01
MRC-5	84.01 ± 3.56	84.01 ± 3.78	72.49 ± 4.35	72.49 ± 4.78

Furthermore, we assessed the effect of combining TMZ with an inhibitor of PARP (a component of BER) i.e. NRP (an inhibitor of both PARP-1 and -2; see Figure 3.1c), to enhance the levels of DNA *N7*-MeG (70% of methylated

adducts produced by TMZ) and *N3*-MeA (approximately 10% of methylated adducts produced by TMZ) following TMZ treatment, which are normally rapidly removed by BER.[76] To enhance specificity and reduce potential dose-limiting toxicity, NRP was encapsulated inside AFt and its anti-cancer activity assessed versus naked NRP *via* the MTT assay, prior to assessing the combination of TMZ with NRP. The anti-cancer activity was assessed in U373M (MGMT +ve) GBM and non-cancerous MRC-5 fibroblast cell lines. According to our western blot study, both cell lines expressed PARP-1 (see section 4.2.3). The cells were exposed to test agents with concentration in the range 0.00172 – 86 μM for 6 days. The results of MTT studies are presented in Figure 5.5a and estimated GI_{50} values were determined for each test agent (Figure 5.5b).

The anti-cancer activity of NRP alone was high in U373M (GI_{50} = 3.77 μM) and marginally lower in MRC-5 (GI_{50} = 6.171 μM). The activity of NRP was further potentiated in U373M when delivered inside AFt (AFt-NRP), by 50-fold. Additionally, cancer-selective activity was seen. AFt-NRP demonstrated enhanced activity in U373M over MRC-5 (GI_{50} values = 0.076 μM in U373M and 3.262 μM in MRC-5), again suggesting AFt may be favourably employed to reduce off-target side effects. Additionally, the activity difference between AFt-NRP and NRP in MRC-5 was not as pronounced like that seen in U373M. In fact, the activity was only enhanced by 2-fold; likely due to the absence of TfR1 expression in MRC-5. AFt alone did not display growth inhibitory activity against any of the cell lines at concentrations ≤ 1 μM, indicating that any activity seen with AFt-NRP was imparted by the test agent itself.

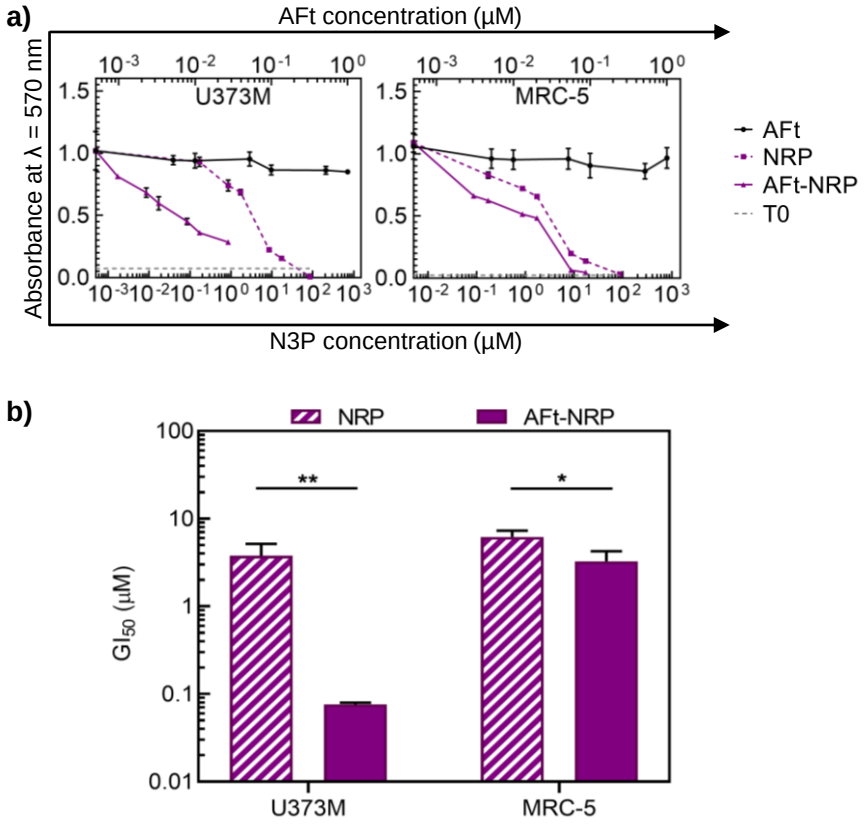

Figure 5.5. MTT assay to assess cellular growth inhibition. (a) *C*oncentration-dependent growth inhibition profiles from MTT assays for GBM cell line: U373M (MGMT +ve) and non-cancerous MRC 5 fibroblasts. Cells were exposed to different concentrations of AFt, NRP, and AFt-NRP for 6 days. Values are reported as mean ± SD (n > 3 trials (5 repeats per trial)). (b) A summary of estimated GI_{50} values. Values are reported as mean ± SD (n > 3 trials). Significant differences from NRP alone are expressed as *P < 0.05 and **P < 0.01.

Moreover, the combinations of TMZ solution with NRP solution (TMZ+NRP) and AFt-TMZ solution and AFt-NRP solution (AFt-TMZ+AFt-NRP), in a 5.8:1 molar ratio, respectively, were assessed. The aim was to inhibit PARP and enhance DNA *N7*-MeG and *N3*-MeA levels from TMZ alkylation. Figure 5.6 demonstrates the MTT plots of naked and encapsulated TMZ+NRP combinations, with Table 5.2 summarising the estimated GI_{50} values from both test agents in the combination. Treating U373M with encapsulated TMZ+NRP demonstrated greater growth inhibitory activity over naked agents by 97-fold, according to the GI_{50} value of TMZ, but for NRP the potency was somewhat lower in the

combination mixture when delivered by AFt (GI_{50} values for NRP in TMZ+NRP = 0.0012 µM and in AFt-TMZ+AFt-NRP = 0.0124 µM, in U373M). Cancer-selective activity was also seen. AFt-TMZ+AFt-NRP demonstrated enhanced activity in U373M over MRC-5 (see Table 5.2), again suggesting AFt may be favourably employed to reduce off-target side effects. AFt alone did not display growth inhibitory activity against any of the cell lines at concentrations ≤ 1 µM, indicating that any activity seen with the AFt-TMZ+AFt-NRP combination was imparted by the test agents.

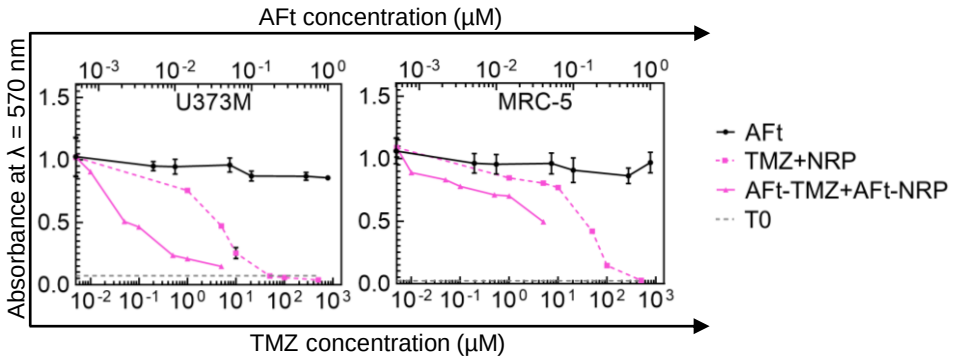

Figure 5.6. Concentration-dependent growth inhibition profiles from MTT assays. Cells used in the assay includes for GBM cell line: U373M (MGMT +ve) and non-cancerous MRC 5 fibroblasts. Cells were exposed to different concentrations of AFt, TMZ+NRP, and AFt-TMZ+AFt-NRP for 6 days. Values are reported as mean ± SD (n > 3 trials (5 repeats per trial)).

Table 5.2. A summary of the estimated GI_{50} values following a 6-day treatment exposure (5.8:1 molar ratio of TMZ+NRP or AFt-TMZ+AFt-NRP) in GBM cell line: U373M (MGMT +ve) and non-cancerous MRC 5 fibroblasts). GI_{50} values were determined for each test agent in the combination administered to cells. Values are reported as mean ± SD (n > 3).

	TMZ+NRP		AFt-TMZ+AFt-NRP	
	TMZ GI_{50} (µM)	NRP GI_{50} (µM)	TMZ GI_{50} (µM)	NRP GI_{50} (µM)
U373M	6.958 ± 0.562	0.001 ± 0.000	0.072 ± 0.039	0.012 ± 0.007
MRC-5	19.759 ± 0.652	0.003 ± 0.000	4.453 ± 0.457	0.766 ± 0.042

To determine whether the combination of TMZ with *O6*-BeG or TMZ with NRP would garner synergistic or antagonistic drug interactions, the combination index was determined for each naked and encapsulated combinations in both U373M and MRC-5 cell lines (Table 5.3). From the data, it appears that the combination of TMZ with NRP was synergistic, suggesting that the combination of test agents led to a larger effect than expected.[243] If two test agents act synergistically, this means that lower doses of each test agent may be used, which could limit the adverse side effects and allow good efficacy to be achieve.[243]

As for the combination of TMZ with *O6*-BeG, the effect was less synergistic than the combination of TMZ with NRP. In U373M (MGMT +ve) cells, TMZ with *O6*-BeG displayed an additive effect, in contrast to non-cancerous MRC-5 cells where the effect of the combination was synergistic. This may be explained by the differences in the levels of MGMT in the two cells; whereby MGMT levels are very low (and readily depleted) in MRC-5 cells. On the other hand, the combination delivered in AFt demonstrated antagonistic behaviour in both cell lines, suggesting that the combination of test agents led to a smaller effect than expected.[243]

According to other research groups, whether anti-cancer drug combinations interact synergistically or antagonistically is dependent on the ratio of the combined agents and so cells were likely exposed to antagonistic ratios in the case of AFt-co-delivered TMZ and *O6*-BeG formulation.[244,245] In future, it would be worth exploring other ratios, starting by setting the ratio approximately equivalent to the GI_{50} of the two test agents. Alas, there is an unmet need to further understand the principles governing antagonistic drug-drug interactions.

Computer modelling is an important tool that could aid in the prediction of drug-drug synergy or antagonism.[246] In clinical trials, *O6*-BeG was mainly delivered prior to TMZ, by ~ 1 h, to deplete MGMT.[247] In our study TMZ was delivered simultaneously with *O6*-BeG to see if we can achieve good activity with fewer treatment steps. Whether anti-cancer activity would be enhanced if cells were treated with AFt-*O6*-BeG prior to AFt-TMZ should also be investigated.

Table 5.3. Combination indices calculated for different combination treatments administered to U373M and MRC-5 cells to determine synergistic, additive, or antagonistic drug interactions (using the bottom table as a key).

Cells	Combination treatment	Combination index	Graded symbol
U373M	TMZ+*O6*-BeG	0.97	±
	AFt-TMZ+AFt-*O6*-BeG	1.59	- - -
	TMZ+NRP	0.02	+ + + + +
	AFt-TMZ+AFt-NRP	0.27	+ + + +
MRC-5	TMZ+*O6*-BeG	0.64	+ + +
	AFt-TMZ+AFt-*O6*-BeG	1.58	- - -
	TMZ+NRP	0.05	+ + + + +
	AFt-TMZ+AFt-NRP	0.31	+ + +

Range of combination index	Description	Graded symbol
0.10	Very strong synergism	+ + + + +
0.10-0.30	Strong synergism	+ + + +
0.30-0.70	Synergism	+ + +
0.70-0.85	Moderate synergism	+ +
0.85-0.90	Slight synergism	+
0.90-1.10	Nearly additive	±
1.10-1.20	Slight antagonism	-
1.20-1.45	Moderate antagonism	- -
1.45-3.30	Antagonism	- - -
3.30-10.00	Strong antagonism	- - - -
10.00	Very strong antagonism	- - - - -

5.3 Conclusions

In summary, we have successfully demonstrated through preliminary *in vitro* studies that the delivery of TMZ analogues: N3P and T25 within AFt (AFt-N3P and AFt-T25, respectively) displayed enhanced growth inhibitory activity over naked agents in MGMT +/−ve GBM and MMR-deficient CRC cell lines. This is in line with what was observed with AFt-TMZ versus TMZ treatment. In addition, we were able to visualise some degree of selectivity with AFt-N3P and AFt-T25 treatment between cancer and non-cancer cell lines. We attributed this selectivity to the differences in the expression of TfR1, with MRC-5 displaying undetectable levels of TfR1 expression, according to western blot and flow cytometry analyses. Importantly, it was demonstrated that AFt alone did not display growth inhibitory activity at the studied concentration range, according to the MTT assay. Again, these findings lay the foundations for AFt, a biocompatible, species-specific, nanosized biomaterial with built-in targeting, to deliver concentrated amounts of anti-cancer small molecules to tumours.

In addition, combination treatments were explored as alternative approaches to overcoming TMZ resistance in GBM tumours. Naked and encapsulated combinations of TMZ with *O6*-BeG (an inhibitor of MGMT) and TMZ with NRP (an inhibitor of PARP) were studied for growth inhibitory activity *via* MTT assay. Again, AFt formulations demonstrated enhanced growth inhibitory activity over naked agents in MGMT +ve GBM cell line and some degree of selectivity was seen between cancer and non-cancer cell lines. The combination index was subsequently determined to assess synergy, demonstrating that naked and encapsulated TMZ+NRP displayed synergy in all cell lines tested, yet encapsulated TMZ+*O6*-BeG did not. We suggest that further studies will need to be carried out to determine the correct ratio of TMZ and *O6*-BeG required to

achieve synergy and whether *O6*-BeG will need to be administered prior to TMZ treatment. However, since we did not see antagonistic activity with the combination of naked TMZ and *O6*-BeG, perhaps with the AFt agents, different amounts of AFt-TMZ and AFt-*O6*-BeG were entering the cells - i.e. more of one and less of the other. It may be worth attempting to find the correct ratio of TMZ and *O6*-BeG and then encapsulating both agents (in that ratio) into a single AFt capsule.

Chapter 6 – Conclusions and future directions

6.1 Conclusions

The overarching objective of this project was to develop chemotherapies for GBM tumour treatment, which ensure enhanced drug specificity and selectivity to minimise adverse side effects and to overcome inherent and acquired resistance in GBM tumours. The protein shell of AFt was proposed as a natural, biocompatible nano-sized DDS with built-in targeting (TfR1 binding site on H-subunits), for the delivery of TMZ and its analogues, N3P and T25. Potential benefits of the co-delivery of TMZ with MGMT inhibitor *O6*-BeG or with PARP inhibitor NRP were also investigated.

In summary, all test agents were encapsulated into AFt *via* the nanoreactor route, in which small molecules accumulate inside AFt by diffusion across the channels of the AFt cage. The test agents were successfully loaded inside AFt with > 510 molecules of TMZ, N3P, T25 or *O6*-BeG and > 80 molecules of NRP per AFt cage, with encapsulation efficiencies > 60%. In addition, the stability of the protein capsules was assessed by various methods, including DLS, ζ-potential and native-PAGE, which have all shown that the protein remains intact after test agent encapsulation and that the size, charge and MW of the capsules was comparable to that of AFt alone (before encapsulation).

Storage stability was also monitored for AFt-TMZ, AFt-N3P and AFt-T25. The results demonstrated that the test agent and protein cage remained stable for at least 7 days post-encapsulation, under storage (at pH 5.5, 4 °C), and that the D:A ratio was continually maintained. As it stands, the *in vitro* test agent release

studies for AFt-TMZ, AFt-N3P and AFt-T25, at pH 7.4, demonstrated slower test agent release in the first 3 h compared to pH 5.5; however, under both conditions, most of the test agents were released across the AFt channels to the exterior environment within 7 h. This was probably because the small size and neutral charge of the test agents meant that they do not interact appreciably with the negative interior of the AFt cage and can readily diffuse out (across the channels) because of their small size. Currently, the stability and release studies are on-going for AFt-*O6*-BeG and AFt-NRP.

The activity of the AFt formulations was probed by various *in vitro* 2D cell culture assays and the AFt nano-formulations displayed significantly enhanced activity against MGMT +ve and −ve GBM cell lines, and MMR deficient and Pgp +ve and -ve CRC cell lines, compared to the activity of naked agents. Out of all the imidazotetrazine agents, the T25 analogue demonstrated the greatest potency, which was further enhanced when delivered inside AFt. Clearly, the C8 modification of the imidazotetrazine molecule not only extended the $t_{1/2}$ of the test agent but also imparted greater growth inhibitory activity in TMZ-resistant cancer cells lines. Even so, it was apparent that the combination of AFt-TMZ with AFt-NRP was the most effective formulation amongst all the treatments tested in TMZ-resistant U373M cells. As such, this likely proves that multiple test agents may be required to tackle TMZ resistance in GBM.

Furthermore, the combination index values demonstrated that naked and encapsulated TMZ+NRP displayed synergy in all cell lines tested, yet encapsulated TMZ+*O6*-BeG did not. In addition, some cancer-selective activity was seen with AFt formulated treatments. This may be explained by the fact that MRC-5 does not show TfR1 expression, whereas TfR1 expression was

observed in all cancer cell lines, as demonstrated by western blot and flow cytometry. Since the expression of SCARA5 (which binds L-subunit of AFt) and TfR2 (whose role is yet unknown) were not observed, we concluded that TfR1 was the receptor most likely responsible for AFt uptake and in the selective anti-cancer activity seen with our formulations. Since AFt alone did not display any growth inhibitory activity, all observed affects were attributed to the encapsulated agents.

During this project, we spent significant time trying to assess and further corroborate the intriguing result seen with AFt-TMZ, which demonstrated significantly enhanced activity over TMZ alone, even in TMZ resistant cancer cell lines (MGMT +ve GBM cell lines and MMR deficient and Pgp +ve and -ve CRC cell lines). Our results confirmed that AFt encapsulation of TMZ amplified TMZ ability to inhibit colony formation in both U373V and U373M GBM cells and that a significantly greater loss of viable U373V and U373M cells was seen with AFt-TMZ over naked TMZ treatment ($P < 0.0001$). Moreover, we demonstrated that there was greater accumulation of *O6*-MeG DNA adducts, enhanced S- and G2/M-phase cell cycle arrest, and greater γH2AX levels in U373M, with AFt-TMZ over naked TMZ treatment. Additionally, imaging U373M cells *via* ESEM and confocal microscopy showed greater loss in cell shape and presence of morphological markers of apoptosis following treatment with AFt-TMZ. Importantly, all assays further established the non-toxicity of AFt alone treatment.

Overall, the encapsulation of anti-cancer agents (so far explored) within AFt has proven to be advantageous. The use of AFt as a DDS has allowed us to achieve greater anti-cancer activity in a cancer-specific and selective manner.

Additionally, it has proven to be non-toxic and even play an added role in overcoming drug resistance by Pgp drug efflux. Therefore, further studies should be carried out to pave way towards clinical trials for the use of AFt, as a DDS, in GBM treatment. Currently, ongoing studies are taking place with the AFt-N3P formulation, for CED delivery to certain paediatric brain tumours like diffuse intrinsic pontine glioma. Our aim is to further branch out the application of our AFt formulation for treatment of a variety of different high-grade brain tumours and explore different routes of administration.

6.2 Future directions

Before the AFt encapsulation can be taken forward as an alternative treatment option, further studies are needed to fully understand the *in vitro* results and to corroborate them with *in vivo* studies. Some of the proposed studies yet to be carried out in the future are listed below:

- Control the release and improve the AFt retention of TMZ and TMZ analogues like N3P, by chemically modifying the C8-position of the imidazotetrazine molecules with positively charged groups that can electrostatically interact with the negative interior of the AFt cage. With an intermediary linker, one can also introduce specific and controlled release of the imidazotetrazine molecules from the AFt cage, under certain cellular conditions such as by the acidic pH of lysosomes or by esterases.[248] This work would ensure that the drug release is prolonged and timed to release only at the site of action; minimising off-target side effects and enhancing cancer intracellular drug accumulation.

- The *in vitro* drug release and storage stability study for AFt-*O6*-BeG and AFt-NRP have yet to be carried out and are important studies for deciding the suitability and efficiency of using AFt as a DDS for these test agents.

- Additionally, it would be interesting to monitor possible protein corona formation around AFt in biological fluids, *in vitro*, to predict how AFt would look and behave when administered intravenously (which is

another route of administration for AFt formulations, besides CED, that we aim to investigate).

- To achieve co-delivery of TMZ with *O6*-BeG or NRP in a single AFt cage. Currently, TMZ and *O6*-BeG/NRP are encapsulated inside separate AFt cages and subsequently mixed in a 1:1 (TMZ:*O6*-BeG) or 5.8:1 (TMZ:NRP) molar ratio. Firstly, a suitable analytical technique would need to be optimised for the quantification of two test agents loaded inside the AFt cage; HPLC is one example of such techniques. Secondly, an experimental study would need to be carried out to determine the most appropriate test agent ratio for the dual test agent encapsulation, to achieve synergistic test agent interactions.[180]

- Further studies are required to prove that test agent molecules are indeed encapsulated inside the AFt cage and is retained during storage. This has proven to be challenging so far. To ensure one mimics the storage conditions, there should be no purification to separate out free molecules from encapsulated molecules, as usually during storage there is no external mechanical force applied, like mixing. Also, by applying a force to separate free molecules from encapsulated molecules, any weakly bound molecules inside the AFt cage may simply diffuse out of the cage (across the channels), which we suspect may be the case with TMZ and TMZ analogues. One suggestion would be to adopt an analytical technique whereby samples can be stored in a chamber mimicking the storage conditions and simultaneously measuring the change in the MW of AFt-test agent particles in solution over time. Alternatively, a study could be carried out to attempt to close

the channels of the AFt cage through mutagenesis and rely on the disassembly-reassembly method of drug encapsulation. This would achieve prolonged test agent retention inside the AFt cage.

- To further corroborate the *in vitro* 2D cell culture cytotoxicity results, the generation of a high throughput 3D-spheroid and BBB co-culture model, would enable rapid screening to monitor the efficiency of AFt-drug brain tumour penetration and distribution, and slightly mimic the *in vivo* tumour environments, which 2D cell culture assays lack.[249]

- There is an important need to map the intracellular route of AFt in studied cell lines *via* time lapsed live cell confocal microscopy. Importantly, it would be worth attempting to generate a pair of TfR1 +ve and TfR1 -ve cells (*via* transient or stable knockdown) to map the route of entry of AFt and prove whether TfR1 is indeed important for AFt to gain entry into cells, and confirm its final destination inside the cells.

- Furthermore, it is imperative that we attempt to quantify the intracellular amount of TMZ following TMZ or AFt-TMZ treatment. Similarly, it is also worth looking into the distribution of naked and encapsulated test agent in a 3D-spheroid and compare the degree of penetration and distribution between the two treatments. This would lend support and explain the reasoning behind the greater potency associated with AFt-TMZ compared to naked TMZ treatment. We propose radiolabelling TMZ or for research novelty purposes using orbiSIMS to quantify TMZ levels and observe the distribution of the drug. OrbiSIMS is a label-free imaging tool, which allows for metabolites to be visualised in 3D with

subcellular resolution, by combining the high spatial resolution of secondary ion mass spectrometry (SIMS; < 200 nm for inorganic species and < 2 μm for biomolecules), with the high mass-resolving power of an Orbitrap (> 240,000 at *m/z* 200).[250]

- In addition to quantifying the intracellular levels of TMZ, it would also be intriguing to assess the protein expression levels of MGMT (by western blot) or MGMT activity *via* the MGMT activity assay (which uses a distinct chemical substrate with a radiolabel for the detection of very low levels of repair activity), over time, following treatment with TMZ and AFt-TMZ.[251] This experiment would shed light on the hypothesis of whether enhanced intracellular accumulation of TMZ by AFt overwhelms the suicide repair protein MGMT; conferring sensitivity to TMZ in MGMT (+ve) GBM cells. If *O6*-guanine methylation outpaces MGMT protein synthesis, MGMT depletion would ensue.[236]

- Similarly, for the combination treatments, it would be useful to assess the degree of MGMT or PARP inhibition by western blot, following treatment with naked and encapsulated combination agents, to see between the two, which results in greater loss of the proteins. Alternatively, we could change the schedule of administration of these test agents to examine whether saturation or inhibition of repair mechanisms is occurring.

- Further *in vitro* studies such as clonogenic assays, cell cycle and γ-H2AX detection assays, as well as possible 3D spheroid size measurements should be carried out to corroborate the MTT assay

results, for TMZ analogues and TMZ with *O6*-BeG/NRP combination treatments; to further confirm and corroborate the good anti-cancer activity profiles of these test agents and add insight behind why these test agents are performing well against resistant cancer cell lines.

- Modify the exterior surface of the AFt cage with additional targeting, to enhance BBB penetration and tumour-specific accumulation of the AFt cage; further avoiding unwanted accumulation of AFt in the liver, spleen and kidney. We propose to modify the surface of AFt with EGFR affibodies (already produced by researcher - Isobel Holden, from the University of Nottingham), for specific and targeted treatment. Affibodies are small and physically resilient peptides, comprised of only 58 amino acids.[252] Affibodies have a MW of 6 kDa, while antibodies have a MW of around 150 kDa. Despite its smaller size, the binding site and affinity of an affibody is like that of an antibody. Figure 8.4 (Appendix IV) demonstrates how all cancer cells in our studies and most importantly GBM cells, express EGFR, so in addition to TfR1 targeting, we could target EGFR for greater tumour accumulation and penetration. We would also be increasing the hydrodynamic size of the AFt cage, which would minimise the possible risk of AFt elimination *via* the kidneys.

- Finally, an *in vivo* PK and PD study, using LN-18 as our GBM model in mice, is underway to corroborate our *in vitro* results. We propose to assess the effect of intravenous administration of AFt-TMZ and AFt-T25, due to their intriguing *in vitro* results. It would also be important to carry out PK and PD studies on AFt alone.

7 - References

1. Rashid, S. *Cancer and Chemoprevention: An Overview*; Springer Nature: Singapore, 2017.

2. Bray, F.; Ferlay, J.; Soerjomataram, I.; Siegel, R. L.; Torre, L. A.; Jemal, A. Global Cancer Statistics 2018: GLOBOCAN Estimates of Incidence and Mortality Worldwide for 36 Cancers in 185 Countries. *CA. Cancer J. Clin.* **2018**, *68*, 394–424.

3. Cancer Research UK. Cancer Statistics for the UK. https://www.cancerresearchuk.org/health-professional/cancer-statistics-for-the-uk (accessed Jun 28, 2020).

4. World Cancer Research Fund. Cancer statistics. https://www.wcrf-uk.org/uk/preventing-cancer/cancer-preventability-statistics (accessed Jun 28, 2020).

5. Hanahan, D.; Weinberg, R. A. The Hallmarks of Cancer. *Cell* **2000**, *100*, 57-70.

6. Hanahan, D.; Weinberg, R. A. Hallmarks of Cancer: The next Generation. *Cell* **2011**, *144*, 646–674.

7. Giancotti, F. G.; Ruoslahti, E. Integrin Signaling. *Science* **1999**, *285*, 1028–1033.

8. Li, L.; Zhao, G. D.; Shi, Z.; Qi, L. L.; Zhou, L. Y.; Fu, Z. X. The Ras/Raf/MEK/ERK Signaling Pathway and Its Role in the Occurrence and Development of HCC (Review). *Oncol. Lett*. **2016**, *12*, 3045–3050.

9. Weinberg, R. A. The Retinoblastoma Protein and Cell Cycle Control. *Cell* **1995**, *81*, 323-330.

10. Foley, K. P.; Eisenman, R. N. Two MAD Tails: What the recent knockouts of Mad1 and Mxi1 tell us about the MYC/MAX/MAD network. *Biochim. Biophys. Acta, Rev. Cancer* **1999**, *1423*, M37–M47.

11. Elmore, S. Apoptosis: A Review of Programmed Cell Death. *Toxicol. Pathol*. **2007**, *35*, 495–516.

12. Evan, G.; Littlewood, T. A Matter of Life and Cell Death. *Science*. **1998**, *281*, 1317–1322.

13. Green, D. R.; Reed, J. C. Mitochondria and Apoptosis. *Science* **1998**, *281*, 1309–1312.

14. Thornberry, N. A.; Lazebnik, Y. Caspases: Enemies Within. *Science* **1998**, *281*, 1312–1316.

15. Harris, C. C. P53 Tumor Suppressor Gene: From the Basic Research Laboratory to the Clinic-an Abridged Historical Perspective. *Carcinogenesis* **1996**, *17*, 1187-1198.

16. Hayflick, L. Mortality and Immortality at the Cellular Level. A Review. *Biochemistry* **1997**, *62*, 1180-1190.

17. Wright, W. E.; Pereira-Smith, O. M.; Shay, J. W. Reversible Cellular Senescence: Implications for Immortalization of Normal Human Diploid Fibroblasts. *Mol. Cell. Biol.* **1989**, *9*, 3088–3092.

18. Counter, C. M.; Avilion, A. A.; Lefeuvre, C. E.; Stewart, N. G.; Greider, C. W.; Harley, C. B.; Bacchetti, S. Telomere Shortening Associated with Chromosome Instability Is Arrested in Immortal Cells Which Express Telomerase Activity. *EMBO J.* **1992**, *11*, 1921-1929.

19. Varner, J. A.; Cheresh, D. A. Integrins and Cancer. *Curr. Opin. Cell Biol.* **1996**, *8*, 724–730.

20. Hanahan, D.; Folkman, J. Patterns and Emerging Mechanisms Review of the Angiogenic Switch during Tumorigenesis. *Cell* **1996**, *86*, 353-364.

21. Aplin, A. E.; Howe, A.; Alahari, S. K.; Juliano, R. L. Signal Transduction and Signal Modulation by Cell Adhesion Receptors: The Role of Integrins, Cadherins, Immunoglobulin-Cell Adhesion Molecules, and Selectins. *Pharmacol. Rev*. **1998**, *50*, 197–263.

22. Christofori, G.; Semb, H. The Role of the Cell-Adhesion Molecule E-Cadherin as a Tumour-Suppressor Gene. *Trends Biochem. Sci*. **1999**, *24*, 73–76.

23. Negrini, S.; Gorgoulis, V. G.; Halazonetis, T. D. Genomic Instability - an Evolving Hallmark of Cancer. *Nat. Rev. Mol. Cell Biol*. **2010**, *11*, 220–228.

24. Jackson, S. P.; Bartek, J. The DNA-Damage Response in Human Biology and Disease. *Nature* **2009**, *461*, 1071–1078.

25. DeNardo, D. G.; Andreu, P.; Coussens, L. M. Interactions between Lymphocytes and Myeloid Cells Regulate Pro-versus Anti-Tumor Immunity. *Cancer Metastasis Rev*. **2010**, *29*, 309–316.

26. Grivennikov, S. I.; Greten, F. R.; Karin, M. Immunity, Inflammation, and Cancer. *Cell* **2010**, *140*, 883–899.

27. Jones, R. G.; Thompson, C. B. Tumor Suppressors and Cell Metabolism: A Recipe for Cancer Growth. *Genes Dev*. **2009**, *23*, 537–548.

28. Heiden, M. G. V.; Cantley, L. C.; Thompson, C. B. Understanding the Warburg Effect: The Metabolic Requirements of Cell Proliferation. *Science* **2009**, *324*, 1029–1033.

29. Hardee, M. E.; Dewhirst, M. W.; Agarwal, N.; Sorg, B. S. Novel Imaging Provides New Insights into Mechanisms of Oxygen Transport in Tumors. *Curr. Mol. Med.* **2009**, *9*, 435–441.

30. Teng, M. W. L.; Swann, J. B.; Koebel, C. M.; Schreiber, R. D.; Smyth, M. J. Immune-Mediated Dormancy: An Equilibrium with Cancer. *J. Leukocyte. Biol.* **2008**, *84*, 988–993.

31. Pagès, F.; Galon, J.; Dieu-Nosjean, M. C.; Tartour, E.; Sautès-Fridman, C.; Fridman, W. H. Immune Infiltration in Human Tumors: A Prognostic Factor That Should Not Be Ignored. *Oncogene* **2010**, *29*, 1093–1102.

32. Yang, L.; Pang, Y.; Moses, H. L. TGF-β and Immune Cells: An Important Regulatory Axis in the Tumor Microenvironment and Progression. *Trends Immunol*. **2010**, *31*, 220–227.

33. Shields, J. D.; Kourtis, I. C.; Tomei, A. A.; Roberts, J. M.; Swartz, M. A. Induction of Lymphoidlike Stroma and Immune Escape by Tumors That Express the Chemokine CCL21. *Science* **2010**, *328*, 749–752.

34. Mougiakakos, D.; Choudhury, A.; Lladser, A.; Kiessling, R.; Johansson, C. C. Regulatory T Cells in Cancer. *Adv. Cancer Res*. **2010**, *107*, 57–117.

35. Ostrand-Rosenberg, S.; Sinha, P. Myeloid-Derived Suppressor Cells: Linking Inflammation and Cancer. *J. Immunol.* **2009**, *182*, 4499–4506.

36. Patel, A. P.; Fisher, J. L.; Nichols, E.; Abd-Allah, F.; Abdela, J.; Abdelalim, A.; Abraha, H. N.; Agius, D.; Alahdab, F.; Alam, T.; Allen, C. A.; Anber, N. H.; Awasthi, A.; Badali, H.; Belachew, A. B.; Bijani, A.; Bjørge, T.; Carvalho, F.; Catalá-López, F.; Choi, J. Y. J.; Daryani, A.; Degefa, M. G.; Demoz, G. T.; Do, H. P.; Dubey, M.; Fernandes, E.; Filip, I.; Foreman, K. J.; Gebre, A. K.; Geramo, Y. C. D.; Hafezi-Nejad, N.; Hamidi, S.; Harvey, J. D.; Hassen, H. Y.; Hay, S. I.; Irvani, S. S. N.; Jakovljevic, M.; Jha, R. P.; Kasaeian, A.; Khalil, I. A.; Khan, E. A.; Khang, Y. 36. H.; Kim, Y. J.; Mengistu, G.; Mohammad, K. A.; Mokdad, A. H.; Nagel, G.; Naghavi, M.; Naik, G.; Nguyen, H. L. T.; Nguyen, L. H.; Nguyen, T. H.; Nixon, M. R.; Olagunju, A. T.; Pereira, D. M.; Pinilla-Monsalve, G. D.; Poustchi, H.; Qorbani, M.; Radfar, A.; Reiner, R. C.; Roshandel, G.; Safari, H.; Safiri, S.; Samy, A. M.; Sarvi, S.; Shaikh, M. A.; Sharif, M.; Sharma, R.; Sheikhbahaei, S.; Shirkoohi, R.; Singh, J. A.; Smith, M.; Tabarés-Seisdedos, R.; Tran, B. X.; Tran, K. B.; Ullah, I.; Weiderpass, E.; Weldegwergs, K. G.; Yimer, E. M.; Zadnik, V.; Zaidi, Z.; Ellenbogen, R. G.; Vos, T.; Feigin, V. L.; Murray, C. J. L.; Fitzmaurice, C. Global, Regional, and National Burden of Brain and Other CNS Cancer, 1990–2016: A Systematic Analysis for the Global Burden of Disease Study 2016. *Lancet Neurol.* **2019**, *18*, 376–393.

37. Tandel, G. S.; Biswas, M.; Kakde, O. G.; Tiwari, A.; Suri, H. S.; Turk, M.; Laird, J. R.; Asare, C. K.; Ankrah, A. A.; Khanna, N. N.; Madhusudhan, B. K.; Saba, L.; Suri, J. S. A Review on a Deep Learning Perspective in Brain Cancer Classification. *Cancers* **2019**, *11*, 111-143.

38. Johns Hopkins Medicine. Metastatic Brain Tumors. https://www.hopkinsmedicine.org/health/conditions-and-diseases/metastatic-brain-tumors (accessed Sep 25, 2020).

39. National Brain Tumor Society. Tumor types: understanding brain tumors. https://braintumor.org/brain-tumor-information/understanding-brain-tumors/tumor-types/ (accessed Sep 25, 2020).

40. Louis, D. N.; Perry, A.; Reifenberger, G.; von Deimling, A.; Figarella-Branger, D.; Cavenee, W. K.; Ohgaki, H.; Wiestler, O. D.; Kleihues, P.; Ellison, D. W. The 2016 World Health Organization Classification of Tumors of the Central Nervous System: A Summary. *Acta Neuropathol*. **2016**, *131*, 803–820.

41. Gupta, A.; Dwivedi, T. A Simplified Overview of World Health Organization Classification Update of Central Nervous System Tumors 2016. *J. Neurosci. Rural Pract*. **2017**, *8*, 629–641.

42. McKinney, P. A. Brain Tumours: Incidence, Survival, and Aetiology. J. Neurol., Neurosurg. Psychiatry **2004**, *75*, ii12–ii17.

43. Cancer Research UK. Brain, Other CNS and Intracranial Tumours Incidence Statistics. https://www.cancerresearchuk.org/health-professional/cancer-statistics/statistics-by-cancer-type/brain-other-cns-and-intracranial-tumours/incidence#heading-Zero (accessed Sep 25, 2020).

44. Arora, R. S.; Alston, R. D.; Eden, T. O. B.; Estlin, E. J.; Moran, A.; Birch, J. M. Age–Incidence Patterns of Primary CNS Tumors in Children, Adolescents, and Adults in England. *Neuro. Oncol.* **2009**, *11*, 403–413.

45. Hanif, F.; Muzaffar, K.; Perveen, K.; Malhi, S. M.; Simjee, S. U. Glioblastoma Multiforme: A Review of Its Epidemiology and Pathogenesis through Clinical Presentation and Treatment. *Asian Pac. J. Cancer Prev*. **2017**, *18*, 3–9.

46. Nørøxe, D. S.; Poulsen, H. S.; Lassen, U. Hallmarks of Glioblastoma: A Systematic Review. *ESMO Open* **2016**, *1*, e000144.

47. Nakada, M.; Kita, D.; Watanabe, T.; Hayashi, Y.; Teng, L.; Pyko, I. V.; Hamada, J. I. Aberrant Signaling Pathways in Glioma. *Cancers*. **2011**, *3*, 3242–3278.

48. Holland, E. C. Glioblastoma Multiforme: The Terminator. *Proc. Natl. Acad. Sci.* **2000**, *97*, 6242–6244.

49. Zong, H.; Verhaak, R. G. W.; Canolk, P. The Cellular Origin for Malignant Glioma and Prospects for Clinical Advancements. *Expert Rev. Mol. Diagn*. **2012**, *12*, 383–394.

50. Jäkel, S.; Dimou, L. Glial Cells and Their Function in the Adult Brain: A Journey through the History of Their Ablation. *Front. Cell. Neurosci*. **2017**, 11, 24-40.

51. Children Brain Tumour Drug Delivery Consortium. The Brain's Drug Delivery Challenge. http://www.cbtddc.org/news/blog-bbb.aspx (accessed Sep 25, 2020).

52. Wikimedia Commons. Neuron with Oligodendrocyte and Myelin Sheath. https://commons.wikimedia.org/wiki/File:Neuron_with_oligodendrocyte_and_myelin_sheath.svg (accessed Sep 25, 2020).

53. Arizona Stata University. What Are the Regions of the Brain and What Do They Do? https://askabiologist.asu.edu/brain-regions (accessed Sep 25, 2020).

54. Cedars Sinai. Glioblastoma Multiforme. https://www.cedars-sinai.org/health-library/diseases-and-conditions/g/glioblastoma-multiforme.html (accessed Sep 25, 2020).

55. Das, K. K.; Kumar, R. Pediatric Glioblastoma; Exon Publications: India, 2017.

56. Adamson, C.; Kanu, O. O.; Mehta, A. I.; Di, C.; Lin, N.; Mattox, A. K.; Bigner, D. D. Glioblastoma Multiforme: A Review of Where We Have Been and Where We Are Going. *Expert Opin. Invest. Drugs*. **2009**, *18*, 1061–1083.

57. D'Alessio, A.; Proietti, G.; Sica, G.; Scicchitano, B. M. Pathological and Molecular Features of Glioblastoma and Its Peritumoral Tissue. *Cancers* **2019**, *11*, 469-487.

58. Brodbelt, A.; Greenberg, D.; Winters, T.; Williams, M.; Vernon, S.; Collins, V. P. Glioblastoma in England: 2007-2011. *Eur. J. Cancer* **2015**, *51*, 533–542.

59. Urbanska, K.; Sokolowska, J.; Szmidt, M.; Sysa, P. Glioblastoma Multiforme - An Overview. *Wspolczesna Onkol*. **2014**, *18*, 307–312.

60. Libre Pathology. Glioblastoma. https://librepathology.org/wiki/Glioblastoma (accessed Sep 25, 2020).

61. Nakada, M.; Nakada, S.; Demuth, T.; Tran, N. L.; Hoelzinger, D. B.; Berens, M. E. Molecular Targets of Glioma Invasion. *Cell. Mol. Life Sci*. **2007**, *64*, 458–478.

62. Sasmita, A. O.; Wong, Y. P.; Ling, A. P. K. Biomarkers and Therapeutic Advances in Glioblastoma Multiforme. *Asia-Pac. J. Clin. Oncol*. **2018**, *14*, 40–51.

63. Verhaak, R. G. W.; Hoadley, K. A.; Purdom, E.; Wang, V.; Qi, Y.; Wilkerson, M. D.; Miller, C. R.; Ding, L.; Golub, T.; Mesirov, J. P.; Alexe, G.; Lawrence, M.; O'Kelly, M.; Tamayo, P.; Weir, B. A.; Gabriel, S.; Winckler, W.; Gupta, S.; Jakkula, L.; Feiler, H. S.; Hodgson, J. G.; James, C. D.; Sarkaria, J. N.; Brennan, C.; Kahn, A.; Spellman, P. T.; Wilson, R. K.; Speed, T. P.; Gray, J. W.; Meyerson, M.; Getz, G.; Perou, C. M.; Hayes, D. N. Integrated Genomic Analysis Identifies Clinically Relevant Subtypes of Glioblastoma Characterized by Abnormalities in PDGFRA, IDH1, EGFR, and NF1. *Cancer Cell* **2010**, *17*, 98–110.

64. Phillips, H. S.; Kharbanda, S.; Chen, R.; Forrest, W. F.; Soriano, R. H.; Wu, T. D.; Misra, A.; Nigro, J. M.; Colman, H.; Soroceanu, L.; Williams, P. M.; Modrusan, Z.; Feuerstein, B. G.; Aldape, K. Molecular Subclasses of High-Grade Glioma Predict Prognosis, Delineate a Pattern of Disease Progression, and Resemble Stages in Neurogenesis. *Cancer Cell* **2006**, *9*, 157–173.

65. Jiao, Y.; Killela, P. J.; Reitman, Z. J.; Rasheed, B. A.; Heaphy, C. M.; De Wilde, R. F.; Rodriguez, F. J.; Rosemberg, S.; Mieko Oba-Shinjo, S.; Kazue,

S.; Marie, N.; Bettegowda, C.; Agrawal, N.; Lipp, E.; Pirozzi, C. J.; Lopez, G. Y.; He, Y.; Friedman, H. S.; Friedman, A. H.; Riggins, G. J.; Holdhoff, M.; Burger, P.; Mclendon, R. E.; Bigner, D. D.; Vogelstein, B.; Meeker, A. K.; Kinzler, K. W.; Papadopoulos, N.; Diaz, L. A.; Yan, H. Frequent ATRX, CIC, FUBP1 and IDH1 Mutations Refine the Classification of Malignant Gliomas. *Oncotarget* **2012**, *3*, 709-722.

66. Inda, M. del M.; Bonavia, R.; Seoane, J. Glioblastoma Multiforme: A Look inside Its Heterogeneous Nature. *Cancers* **2014**, *6*, 226–239.

67. Bergmann, N.; Delbridge, C.; Gempt, J.; Feuchtinger, A.; Walch, A.; Schirmer, L.; Bunk, W.; Aschenbrenner, T.; Liesche-Starnecker, F.; Schlegel, J. The Intratumoral Heterogeneity Reflects the Intertumoral Subtypes of Glioblastoma Multiforme: A Regional Immunohistochemistry Analysis. *Front. Oncol.* **2020**, *10*, 494-505.

68. Davis, M. E. Glioblastoma: Overview of Disease and Treatment. *Clin. J. Oncol. Nurs.* **2016**, *20*, 1–8.

69. American Brain Tumor Association. About Brain Tumors a Primer for Patients and Caregivers; American Brain Tumor Association: Chicago, IL, USA, 2015.

70. Fernandes, C.; Costa, A.; Osorio, L.; Lago, R. C.; Linhares, P.; Carvalho, B.; Caeiro, C. Current Standards of Care in Glioblastoma Therapy; Exon Publications: Portugal, 2017.

71. Pubchem. Temozolomide. https://pubchem.ncbi.nlm.nih.gov/compound/temozolomide#section=Drug-Indication (accessed Sep 29, 2020).

72. Agarwala, S. S.; Kirkwood, J. M. Temozolomide, a Novel Alkylating Agent with Activity in the Central Nervous System, May Improve the Treatment of Advanced Metastatic Melanoma. *Oncologist* **2000**, *5*, 144–151.

73. Food & Drug Association. Temodar (temozolomide) label. https://www.accessdata.fda.gov/drugsatfda_docs/label/2016/021029s031lbl.pdf (accessed Sep 29, 2020).

74. Stevens, M. F. G. Temozolomide: From Cytotoxic to Molecularly Targeted Agent. In *Cancer Drug Design and Discovery*; Elsevier: Amsterdam, The Netherlands, 2008.

75. Denny, B. J.; Wheelhouse, R. T.; Stevens, M. F.; Tsang, L. L.; Slack, J. A. NMR and molecular modeling investigation of the mechanism of activation of the antitumor drug temozolomide and its interaction with DNA. *Biochemistry* **1994**, *33*, 9045-9051.

76. Barciszewska, A. M.; Gurda, D.; Głodowicz, P.; Nowak, S.; Naskręt-Barciszewska, M. Z. A New Epigenetic Mechanism of Temozolomide Action in Glioma Cells. *PLoS One* **2015**, *10*, e0136669.

77. Strobel, H.; Baisch, T.; Fitzel, R.; Schilberg, K.; Siegelin, M. D.; Karpel-Massler, G.; Debatin, K.-M.; Westhoff, M.-A. Temozolomide and Other Alkylating Agents in Glioblastoma Therapy. *Biomedicines* **2019**, *7*, 69-85.

78. Trivedi, R. N.; Almeida, K. H.; Fornsaglio, J. L.; Schamus, S.; Sobol, R. W. The Role of Base Excision Repair in the Sensitivity and Resistance to Temozolomide-Mediated Cell Death. *Cancer Res.* **2005**, *65*, 6394–6400.

79. Quiros, S.; Roos, W. P.; Kaina, B. Processing of O6-Methylguanine into DNA Double-Strand Breaks Requires Two Rounds of Replication Whereas Apoptosis Is Also Induced in Subsequent Cell Cycles. *Cell Cycle* **2010**, *9*, 168–178.

80. Zhang, J.; Stevens, M. F. G.; Bradshaw, T. D. Temozolomide: Mechanisms of Action, Repair and Resistance. *Curr. Mol. Pharmacol*. **2012**, *5*, 102-114.

81. Stojic, L.; Brun, R.; Jiricny, J. Mismatch Repair and DNA Damage Signalling. *DNA Repair* **2004**, *3*, 1091–1101.

82. Mojas, N.; Lopes, M.; Jiricny, J. Mismatch Repair-Dependent Processing of Methylation Damage Gives Rise to Persistent Single-Stranded Gaps in Newly Replicated DNA. *Genes Dev.* **2007**, *21*, 3342–3355.

83. Yan, Y.; Xu, Z.; Dai, S.; Qian, L.; Sun, L.; Gong, Z. Targeting Autophagy to Sensitive Glioma to Temozolomide Treatment. *J. Exp. Clin. Cancer Res*. **2016**, 35, 23–36.

84. Zhang, J.; Hummersone, M.; Matthews, C. S.; Stevens, M. F. G.; Bradshaw, T. D. N3-Substituted Temozolomide Analogs Overcome Methylguanine-DNA Methyltransferase and Mismatch Repair Precipitating Apoptotic and Autophagic Cancer Cell Death. *Oncology* **2015**, *88*, 28–48.

85. Daniels, D. S.; Woo, T. T.; Luu, K. X.; Noll, D. M.; Clarke, N. D.; Pegg, A. E.; Tainer, J. A. DNA Binding and Nucleotide Flipping by the Human DNA Repair Protein AGT. *Nat. Struct. Mol. Biol.* **2004**, *11*, 714–720.

86. Jiapaer, S.; Furuta, T.; Tanaka, S.; Kitabayashi, T.; Nakada, M. Potential Strategies Overcoming the Temozolomide Resistance for Glioblastoma. *Neurologia Medico-Chirurgica* **2018**, *58*, 405–421.

87. Palma, J. P.; Rodriguez, L. E.; Bontcheva-Diaz, V. D.; Bouska, J. J.; Bukofzer, G.; Colon-Lopez, M.; Guan, R.; Jarvis, K.; Johnson, E. F.; Klinghofer, V.; Liu, X.; Olson, A.; Saltarelli, M. J.; Shi, Y.; Stavropoulos, J. A.; Zhu, G.-D.; Penning, T. D.; Luo, Y.; Giranda, V. L.; Rosenberg, S. H.; Frost, D. J.; Donawho, C. K. The PARP Inhibitor, ABT-888 Potentiates Temozolomide: Correlation with Drug Levels and Reduction in PARP Activity in Vivo. *Anticancer Res.* **2008**, *28*, 2625–2636.

88. Nakada, M.; Furuta, T.; Hayashi, Y.; Minamoto, T.; Hamada, J. ichiro. The Strategy for Enhancing Temozolomide against Malignant Glioma. *Front. Oncol*. **2012**, *2*, 98–102.

89. Kanzawa, T.; Germano, I. M.; Komata, T.; Ito, H.; Kondo, Y.; Kondo, S. Role of Autophagy in Temozolomide-Induced Cytotoxicity for Malignant Glioma Cells. *Cell Death Differ.* **2004**, *11*, 448–457.

90. Matsuda, K. I.; Sato, A.; Okada, M.; Shibuya, K.; Seino, S.; Suzuki, K.; Watanabe, E.; Narita, Y.; Shibui, S.; Kayama, T.; Kitanaka, C. Targeting JNK for Therapeutic Depletion of Stem-like Glioblastoma Cells. *Sci. Rep.* **2012**, *2*, 516–526.

91. Cousin, D.; Zhang, J.; Hummersone, M. G.; Matthews, C. S.; Frigerio, M.; Bradshaw, T. D.; Stevens, M. F. G. Antitumor Imidazo[5,1-d]-1,2,3,5-Tetrazines: Compounds Modified at the 3-Position Overcome Resistance in Human Glioblastoma Cell Lines. *Medchemcomm* **2016**, *7*, 2332–2343.

92. Summers, H. S. Synthesis and Biological Evaluation of Novel Imidazotetrazines. Ph.D. Thesis, University of Nottingham, UK, January 2019.

93. Toniatti, C.; Jones, P.; Graham, H.; Pagliara, B.; Draetta, G. Oncology Drug Discovery: Planning a Turnaround. *Cancer Discov.* **2014**, *4*, 397–404.

94. Wong, C. H.; Siah, K. W.; Lo, A. W. Estimation of Clinical Trial Success Rates and Related Parameters. *Biostatistics* **2019**, *20*, 273–286.

95. Patel, A. G.; De Lorenzo, S. B.; Flatten, K. S.; Poirier, G. G.; Kaufmann, S. H. Failure of Iniparib to Inhibit Poly(ADP-Ribose) Polymerase in Vitro. *Clin. Cancer Res.* **2012**, *18*, 1655–1662.

96. Liu, X.; Shi, Y.; Maag, D. X.; Palma, J. P.; Patterson, M. J.; Ellis, P. A.; Surber, B. W.; Ready, D. B.; Soni, N. B.; Ladror, U. S.; Xu, A. J.; Iyer, R.; Harlan, J. E.; Solomon, L. R.; Donawho, C. K.; Penning, T. D.; Johnson, E. F.; Shoemaker, A. R. Iniparib Nonselectively Modifies Cysteine-Containing Proteins in Tumor Cells and Is Not a Bona Fide PARP Inhibitor. *Clin. Cancer Res.* **2012**, *18*, 510–523.

97. Bornstein, S. R.; Licinio, J. Improving the Efficacy of Translational Medicine by Optimally Integrating Health Care, Academia and Industry. *Nat. Med*. **2011**, *17*, 1567–1569.

98. Smietana, K.; Siatkowski, M.; Møller, M. Trends in Clinical Success Rates. *Nat. Rev. Drug Discovery* **2016**, *15*, 379–380.

99. Tran, S.; DeGiovanni, P.-J.; Piel, B.; Rai, P. Cancer Nanomedicine: A Review of Recent Success in Drug Delivery. *Clin. Transl. Med.* **2017**, *6*, 44-64.

100. Matsumura, Y.; Maeda, H. A New Concept for Macromolecular Therapeutics in Cancer Chemotherapy: Mechanism of Tumoritropic Accumulation of Proteins and the Antitumor Agent Smancs. *Cancer Res.* **1986**, *46*, 6387–6392.

101. Fox, M. E.; Szoka, F. C.; Fréchet, J. M. J. Soluble Polymer Carriers for the Treatment of Cancer: The Importance of Molecular Architecture. *Acc. Chem. Res.* **2009**, *42*, 1141–1151.

102. Wikimedia Commons. Enhanced permeability and retention (EPR) effect and passive targeting. https://commons.wikimedia.org/wiki/File:Enhanced_permeability_and_retention_(EPR)_effect_and_passive_targeting.svg (accessed Oct 10, 2020).

103. Ageitos, J. M.; Chuah, J. A.; Numata, K. Design Considerations for Properties of Nanocarriers on Disposition and Efficiency of Drug and Gene Delivery. In *RSC Drug Discovery Series*; Royal Society of Chemistry: United Kingdom, 2016.

104. Cainelli, F.; Vallone, A. Safety and Efficacy of Pegylated Liposomal Doxorubicin in HIV-Associated Kaposi's Sarcoma. *Biologics* **2009**, *3*, 385–390.

105. Salatin, S.; Maleki Dizaj, S.; Yari Khosroushahi, A. Effect of the Surface Modification, Size, and Shape on Cellular Uptake of Nanoparticles. *Cell Biol. Int*. **2015**, *39*, 881–890.

106. Sukhanova, A.; Bozrova, S.; Sokolov, P.; Berestovoy, M.; Karaulov, A.; Nabiev, I. Dependence of Nanoparticle Toxicity on Their Physical and Chemical Properties. *Nanoscale Res. Lett.* **2018**, *13*, 44-64.

107. Brandelli, A. The Interaction of Nanostructured Antimicrobials with Biological Systems: Cellular Uptake, Trafficking and Potential Toxicity. *Food Science and Human Wellness* **2020**, *9*, 8–20.

108. Hoshyar, N.; Gray, S.; Han, H.; Bao, G. The Effect of Nanoparticle Size on in Vivo Pharmacokinetics and Cellular Interaction. *Nanomedicine* **2016**, *11*, 673–692.

109. Huo, S.; Jin, S.; Ma, X.; Xue, X.; Yang, K.; Kumar, A.; Wang, P. C.; Zhang, J.; Hu, Z.; Liang, X. J. Ultrasmall Gold Nanoparticles as Carriers for Nucleus-Based Gene Therapy Due to Size-Dependent Nuclear Entry. *ACS Nano* **2014**, *8*, 5852–5862.

110. Moghimi, S. M.; Hunter, A. C.; Andresen, T. L. Factors Controlling Nanoparticle Pharmacokinetics: An Integrated Analysis and Perspective. *Annu. Rev. Pharmacol. Toxicol.* **2012**, *52*, 481–503.

111. Baimanov, D.; Cai, R.; Chen, C. Understanding the Chemical Nature of Nanoparticle-Protein Interactions. *Bioconjugate Chem.* **2019**, *30*, 1923–1937.

112. Kim, J. A.; Aberg, C.; Salvati, A.; Dawson, K. A. Role of Cell Cycle on the Cellular Uptake and Dilution of Nanoparticles in a Cell Population. *Nat. Nanotechnol.* **2012**, *7*, 62–68.

113. Šamec, N.; Zottel, A.; Videtič Paska, A.; Jovčevska, I. Nanomedicine and Immunotherapy: A Step Further towards Precision Medicine for Glioblastoma. *Molecules* **2020**, *25*, 490–522.

114. Hadjipanayis, C. G.; Machaidze, R.; Kaluzova, M.; Wang, L.; Schuette, A. J.; Chen, H.; Wu, X.; Mao, H. EGFRvIII Antibody-Conjugated Iron Oxide Nanoparticles for Magnetic Resonance Imaging-Guided Convection-Enhanced

Delivery and Targeted Therapy of Glioblastoma. *Cancer Res.* **2010**, *70*, 6303–6312.

115. Neuwelt, E. A.; Várallyay, C. G.; Manninger, S.; Solymosi, D.; Haluska, M.; Hunt, M. A.; Nesbit, G.; Stevens, A.; Jerosch-Herold, M.; Jacobs, P. M.; Hoffman, J. M. The Potential of Ferumoxytol Nanoparticle Magnetic Resonance Imaging, Perfusion, and Angiography in Central Nervous System Malignancy: A Pilot Study. *Neurosurgery* **2007**, *60*, 601–611.

116. Belhadj, Z.; Zhan, C.; Ying, M.; Wei, X.; Xie, C.; Yan, Z.; Lu, W. Multifunctional Targeted Liposomal Drug Delivery for Efficient Glioblastoma Treatment. *Oncotarget* **2017**, *8*, 66889–66900.

117. Zhang, Y.; Zhang, L.; Hu, Y.; Jiang, K.; Li, Z.; Lin, Y. Z.; Wei, G.; Lu, W. Cell-Permeable NF-KB Inhibitor-Conjugated Liposomes for Treatment of Glioma. *J. Controlled Release* **2018**, *289*, 102–113.

118. Jhaveri, A.; Luther, E.; Torchilin, V. The Effect of Transferrin-Targeted, Resveratrol-Loaded Liposomes on Neurosphere Cultures of Glioblastoma: Implications for Targeting Tumour-Initiating Cells. *J. Drug Target.* **2019**, *27*, 601–613.

119. Lakkadwala, S.; Singh, J. Co-Delivery of Doxorubicin and Erlotinib through Liposomal Nanoparticles for Glioblastoma Tumor Regression Using an in Vitro Brain Tumor Model. *Colloids Surf., B* **2019**, *173*, 27–35.

120. Lakkadwala, S.; dos Santos Rodrigues, B.; Sun, C.; Singh, J. Dual Functionalized Liposomes for Efficient Co-Delivery of Anti-Cancer Chemotherapeutics for the Treatment of Glioblastoma. *J. Controlled Release* **2019**, *307*, 247–260.

121. Ganipineni, L. P.; Ucakar, B.; Joudiou, N.; Bianco, J.; Danhier, P.; Zhao, M.; Bastiancich, C.; Gallez, B.; Danhier, F.; Préat, V. Magnetic Targeting of Paclitaxel-Loaded Poly(Lactic-Co-Glycolic Acid)-Based Nanoparticles for the Treatment of Glioblastoma. *Int. J. Nanomedicine* **2018**, *13*, 4509–4521.

122. Qu, J.; Zhang, L.; Chen, Z.; Mao, G.; Gao, Z.; Lai, X.; Zhu, X.; Zhu, J. Nanostructured Lipid Carriers, Solid Lipid Nanoparticles, and Polymeric Nanoparticles: Which Kind of Drug Delivery System Is Better for Glioblastoma Chemotherapy? *Drug Deliv.* **2016**, *23*, 3408–3416.

123. Quader, S.; Liu, X.; Chen, Y.; Mi, P.; Chida, T.; Ishii, T.; Miura, Y.; Nishiyama, N.; Cabral, H.; Kataoka, K. CRGD Peptide-Installed Epirubicin-Loaded Polymeric Micelles for Effective Targeted Therapy against Brain Tumors. *J. Controlled Release* **2017**, *258*, 56–66.

124. Sarisozen, C.; Dhokai, S.; Tsikudo, E. G.; Luther, E.; Rachman, I. M.; Torchilin, V. P. Nanomedicine Based Curcumin and Doxorubicin Combination Treatment of Glioblastoma with ScFv-Targeted Micelles: In Vitro Evaluation on 2D and 3D Tumor Models. *Eur. J. Pharm. Biopharm.* **2016**, *108*, 54–67.

125. Li, Y.; He, H.; Jia, X.; Lu, W. L.; Lou, J.; Wei, Y. A Dual-Targeting Nanocarrier Based on Poly(Amidoamine) Dendrimers Conjugated with

Transferrin and Tamoxifen for Treating Brain Gliomas. *Biomaterials* **2012**, *33*, 3899–3908.

126. Babincová, N.; Sourivong, P.; Babinec, P.; Bergemann, C.; Babincová, M.; Durdík, Š. Applications of Magnetoliposomes with Encapsulated Doxorubicin for Integrated Chemotherapy and Hyperthermia of Rat C6 Glioma. *Z. Naturforsch. C. J. Biosci.* **2018**, *73*, 265–271.

127. Zhang, J.; Xiao, X.; Zhu, J.; Gao, Z.; Lai, X.; Zhu, X.; Mao, G. Lactoferrin- and RGD-Comodified, Temozolomide and Vincristine-Coloaded Nanostructured Lipid Carriers for Gliomatosis Cerebri Combination Therapy. *Int. J. Nanomedicine* **2018**, *13*, 3039–3051.

128. Jiang, Y.; Lv, L.; Shi, H.; Hua, Y.; Lv, W.; Wang, X.; Xin, H.; Xu, Q. PEGylated Polyamidoamine Dendrimer Conjugated with Tumor Homing Peptide as a Potential Targeted Delivery System for Glioma. *Colloids Surf., B* **2016**, *147*, 242–249.

129. Agemy, L.; Kotamraju, V. R.; Friedmann-Morvinski, D.; Sharma, S.; Sugahara, K. N.; Ruoslahti, E. Proapoptotic Peptide-Mediated Cancer Therapy Targeted to Cell Surface P32. *Mol. Ther.* **2013**, *21*, 2195–2204.

130. Wang, H.; Mooney, D. J. Biomaterial-Assisted Targeted Modulation of Immune Cells in Cancer Treatment. *Nat. Mater*. **2018**, *17*, 761–772.

131. Lamberti, M.; Zappavigna, S.; Sannolo, N.; Porto, S.; Caraglia, M. Advantages and Risks of Nanotechnologies in Cancer Patients and Occupationally Exposed Workers. *Expert Opin. on Drug Delivery* **2014**, *11*, 1087–1101.

132. Belletti, D.; Pederzoli, F.; Forni, F.; Vandelli, M. A.; Tosi, G.; Ruozi, B. Protein Cage Nanostructure as Drug Delivery System: Magnifying Glass on Apoferritin. *Expert Opin. Drug Delivery* **2017**, *14*, 825–840.

133. Harrison, P. M. The Structure and Function of Ferritin. *Biochem. Educ.* **1986**, *14*, 154–162.

134. Ford, G. C.; Harrison, P. M.; Rice, D. W.; Smith, J. M.; Treffry, A.; White, J. L.; Yariv, J. Ferritin: Design and Formation of an Iron-Storage Molecule. *Philos. Trans. R. Soc. Lond. B. Biol. Sci.* **1984**, *304*, 551–565.

135. Bjork, I.; Fish, W. W. Native and Subunit Molecular Weights of Apoferritin. *Biochemistry* **1971**, *10*, 2844–2848.

136. Chasteen, N. D.; Harrison, P. M. Mineralization in Ferritin: An Efficient Means of Iron Storage. *J. Struct. Biol.* **1999**, *126*, 182–194.

137. Harrison, P. M.; Arosio, P. The Ferritins: Molecular Properties, Iron Storage Function and Cellular Regulation. *Biochim. Biophys. Acta* **1996**,*1275*, 161-203.

138. Theil, E. C. Ferritin: Structure, Gene Regulation, and Cellular Function in Animals, Plants, and Microorganisms. *Annu. Rev. Biochem*. **1987**, *56*, 289–315.

139. Granick, S.; Michaelis, L. Ferritin. II. Apoferritin of Horse Spleen. *J. Biol. Chem.* **1943**, *147*, 91–97.

140. Arosio, P.; Levi, S. Cytosolic and Mitochondrial Ferritins in the Regulation of Cellular Iron Homeostasis and Oxidative Damage. *Biochim. Biophys. Acta* **2010**, *1800*, 783–792.

141. Zhang, L.; Knez, M. Spherical Nanoscale Protein Templates for Biomedical Applications: A Review on Ferritin. *J. Nanosci. Lett.* **2012**, *2*, 6-18.

142. Heger, Z.; Skalickova, S.; Zitka, O.; Adam, V.; Kizek, R. Apoferritin Applications in Nanomedicine. *Nanomedicine* **2014**, *9*, 2233–2245.

143. Truffi, M.; Fiandra, L.; Sorrentino, L.; Monieri, M.; Corsi, F.; Mazzucchelli, S. Ferritin Nanocages: A Biological Platform for Drug Delivery, Imaging and Theranostics in Cancer. *Pharmacol. Res*. **2016**, *107*, 57–65.

144. Truty, J.; Malpe, R.; Linder, M. C. Iron Prevents Ferritin Turnover in Hepatic Cells. *J. Biol. Chem.* **2001**, *276*, 48775–48780.

145. Kidane, T. Z.; Sauble, E.; Linder, M. C. Release of Iron from Ferritin Requires Lysosomal Activity. *Am. J. Physiol. Cell Physiol.* **2006**, *291*, 445–455.

146. La, A.; Nguyen, T.; Tran, K.; Sauble, E.; Tu, D.; Gonzalez, A.; Kidane, T. Z.; Soriano, C.; Morgan, J.; Doan, M.; Tran, K.; Wang, C. Y.; Knutson, M. D.; Linder, M. C. Mobilization of Iron from Ferritin: New Steps and Details. *Metallomics* **2018**, *10*, 154–168.

147. Bou-Abdallah, F.; Paliakkara, J.; Melman, G.; Melman, A. Reductive Mobilization of Iron from Intact Ferritin: Mechanisms and Physiological Implication. *Pharmaceuticals* **2018**, *11*, 120-133.

148. Sirivech, S.; Osaki, S. The Release of Iron from Horse Spleen Ferritin by Reduced Flavins. *Biochem. J.* **1974**, *143*, 311-315.

149. Sakurai, K.; Nabeyama, A.; Fujimoto, Y. Ascorbate-Mediated Iron Release from Ferritin in the Presence of Alloxan. *BioMetals* **2006**, *19*, 323–333.

150. Joo, M.-S.; Tourillon, G.; Sayers, D. E.; Theil, E. C. Rapid Reduction of Iron in Horse Spleen Ferritin by Thioglycolic Acid Measured by Dispersive X-Ray Absorption Spectroscopy. *Biol. Met.* **1990**, *3*, 171-175.

151. Wang, Z.; Gao, H.; Zhang, Y.; Liu, G.; Niu, G.; Chen, X. Functional Ferritin Nanoparticles for Biomedical Applications. *Front. Chem. Sci. Eng*. **2017**, *11*, 633–646.

152. Chen, Z.; Zhai, M.; Xie, X.; Zhang, Y.; Ma, S.; Li, Z.; Yu, F.; Zhao, B.; Zhang, M.; Yang, Y.; Mei, X. Apoferritin Nanocage for Brain Targeted Doxorubicin Delivery. *Mol. Pharm.* **2017**, *14*, 3087–3097.

153. Zhai, M.; Wang, Y.; Zhang, L.; Liang, M.; Fu, S.; Cui, L.; Yang, M.; Gong, W.; Li, Z.; Yu, L.; Xie, X.; Yang, C.; Yang, Y.; Gao, C. Glioma Targeting Peptide Modified Apoferritin Nanocage. *Drug Deliv.* **2018**, *25*, 1013–1024.

154. Li, X.; Shao, F. L.; Sun, J.; Du, K.; Sun, Y.; Feng, F. D. Enhanced Copper-Temozolomide Interactions by Protein for Chemotherapy against Glioblastoma Multiforme. *ACS Appl. Mater. Interfaces* **2019**, *11*, 41935-41945.

155. Du, K.; Xia, Q.; Heng, H.; Feng, F. Temozolomide-Doxorubicin Conjugate as a Double Intercalating Agent and Delivery by Apoferritin for Glioblastoma Chemotherapy. *ACS Appl. Mater. Interfaces* **2020**, *12*, 34599–34609.

156. Wong, K. K. W.; Douglas, T.; Gider, S.; Awschalom, D. D.; Mann, S. Biomimetic Synthesis and Characterization of Magnetic Proteins (Magnetoferritin). *Chem. Mater.* **1998**, *10*, 279–285.

157. Aime, S.; Frullano, L.; Crich, S. G. Compartmentalization of a Gadolinium Complex in the Apoferritin Cavity: A Route to Obtain High Relaxivity Contrast Agents for Magnetic Resonance Imaging. *Angew. Chem.* **2002**, *41*, 1017–1019.

158. Sana, B.; Poh, C. L.; Lim, S. A Manganese–Ferritin Nanocomposite as an Ultrasensitive T2 Contrast Agent. *Chem. Commun.* **2012**, *48*, 862–864.

159. Lin, X.; Xie, J.; Niu, G.; Zhang, F.; Gao, H.; Yang, M.; Quan, Q.; Aronova, M. A.; Zhang, G.; Lee, S.; Leapman, R.; Chen, X. Chimeric Ferritin Nanocages for Multiple Function Loading and Multimodal Imaging. *Nano Lett.* **2011**, *11*, 814–819.

160. Turyanska, L.; Bradshaw, T. D.; Sharpe, J.; Li, M.; Mann, S.; Thomas, N. R.; Patanè, A. The Biocompatibility of Apoferritin-Encapsulated PbS Quantum Dots. *Small* **2009**, *5*, 1738–1741.

161. Bradshaw, T. D.; Junor, M.; Patanè, A.; Clarke, P.; Thomas, N. R.; Li, M.; Mann, S.; Turyanska, L. Apoferritin-Encapsulated PbS Quantum Dots Significantly Inhibit Growth of Colorectal Carcinoma Cells. *J. Mater. Chem. B* **2013**, *1*, 6254–6260.

162. Uchida, M.; Flenniken, M. L.; Allen, M.; Willits, D. A.; Crowley, B. E.; Brumfield, S.; Willis, A. F.; Jackiw, L.; Jutila, M.; Young, M. J.; Douglas, T. Targeting of Cancer Cells with Ferrimagnetic Ferritin Cage Nanoparticles. *J. Am. Chem. Soc.* **2006**, *128*, 16626–16633.

163. Yan, F.; Zhang, Y.; Yuan, H.; Gregas, M. K.; Vo-Dinh, T. Apoferritin Protein Cages: A Novel Drug Nanocarrier for Photodynamic Therapy. *Chem. Commun.* **2008**, *38*, 4579–4581.

164. Li, L.; Muñoz-Culla, M.; Carmona, U.; Lopez, M. P.; Yang, F.; Trigueros, C.; Otaegui, D.; Zhang, L.; Knez, M. Ferritin-Mediated SiRNA Delivery and Gene Silencing in Human Tumor and Primary Cells. *Biomaterials* **2016**, *98*, 143–151.

165. Kim, S. E.; Ahn, K. Y.; Park, J. S.; Kim, K. R.; Lee, K. E.; Han, S. S.; Lee, J. Fluorescent Ferritin Nanoparticles and Application to the Aptamer Sensor. *Anal. Chem.* **2011**, *83*, 5834–5843.

166. Kanekiyo, M.; Wei, C. J.; Yassine, H. M.; McTamney, P. M.; Boyington, J. C.; Whittle, J. R. R.; Rao, S. S.; Kong, W. P.; Wang, L.; Nabel, G. J. Self-

Assembling Influenza Nanoparticle Vaccines Elicit Broadly Neutralizing H1N1 Antibodies. *Nature* **2013**, *499*, 102–106.

167. Bradford, M. M. A rapid and sensitive method for the quantitation of microgram quantities of protein utilizing the principle of protein-dye binding. *Anal. Biochem.* **1976**, *72*, 248-254.

168. Compton, S. J.; Jones, C. G. Mechanism of dye response and interference in the Bradford protein assay. *Anal. Biochem.* **1985**, *151*, 369-374.

169. Chial, H. J.; Thompson, H. B.; Splittgerber, A. G. A spectral study of the charge forms of Coomassie blue G. *Anal. Biochem.* **1993**, *209*, 258-266.

170. Swinehart, D. F. The Beer-Lambert Law. *J. Chem. Educ.* **1962**, *39*, 333–335.

171. Garfin, D. E. One-dimensional gel electrophoresis. In Guide to Protein Purification, Second Edition, Burgess, R. R.; Deutscher, M. P., Eds. Elsevier Academic Press Inc: San Diego, **2009**; Vol.463, 497-513.

172. Drab, T.; Kracmerova, J.; Ticha, I.; Hanzlikova, E.; Ticha, M.; Ryslava, H.; Doubnerova, V.; Manaskova-Postlerova, P.; Liberda, J. Native Red Electrophoresis - A new method suitable for separation of native proteins. *Electrophoresis* **2011**, *32*, 3597-3599.

173. Schagger, H.; Vonjagow, G. Blue native electrophoresis for isolation of membrane-protein complexes in enzymatically active form. *Anal. Biochem.* **1991**, *199*, 223-231.

174. Drab, T.; Kracmerova, J.; Ticha, I.; Hanzlikova, E.; Ticha, M.; Liberda, J. Native polyacrylamide electrophoresis in the presence of Ponceau Red to study oligomeric states of protein complexes. *J Sep Sci* **2011**, *34*, 1692–1695.

175. Bhattacharjee, S. DLS and zeta potential - What they are and what they are not? *J. Controlled Release* **2016**, *235*, 337-351.

176. Mosmann, T. Rapid Colorimetric Assay for Cellular Growth and Survival: Application to Proliferation and Cytotoxicity Assays. *J. Immunol. Methods* **1983**, *65*, 55-63.

177. Liu, Y.; Peterson, D. A.; Kimura, H.; Schubert, D. Mechanism of Cellular 3-(4,5-Dimethylthiazol-2-Yl)-2,5-Diphenyltetrazolium Bromide (MTT) Reduction. *J. Neurochem.* **2002**, *69*, 581–593.

178. Lü, L.; Zhang, L.; Wai, M. S. M.; Yew, D. T. W.; Xu, J. Exocytosis of MTT Formazan Could Exacerbate Cell Injury. *Toxicol. In Vitro* **2012**, *26*, 636–644.

179. Stepanenko, A. A.; Dmitrenko, V. V. Pitfalls of the MTT Assay: Direct and off-Target Effects of Inhibitors Can Result in over/Underestimation of Cell Viability. *Gene* **2015**, *574*, 193–203.

180. Chou, T. C. Drug Combination Studies and Their Synergy Quantification Using the Chou-Talalay Method. *Cancer Res.* **2010**, *70*, 440–446.

181. Chou, T. C. Theoretical Basis, Experimental Design, and Computerized Simulation of Synergism and Antagonism in Drug Combination Studies. *Pharmacol. Rev.* **2006**, *58*, 621–681.

182. Ichite, N.; Chougule, M. B.; Jackson, T.; Fulzele, S. V.; Safe, S.; Singh, M. Enhancement of Docetaxel Anticancer Activity by a Novel Diindolylmethane Compound in Human Non- Small Cell Lung Cancer. *Clin. Cancer Res.* **2009**, *15*, 543–552.

183. Strober, W. Trypan Blue Exclusion Test of Cell Viability. *Curr. Protoc. Immunol.* **2015**, *111*, A3.B.1-A3.B.3.

184. Buch, K.; Peters, T.; Nawroth, T.; Sänger, M.; Schmidberger, H.; Langguth, P. Determination of Cell Survival after Irradiation via Clonogenic Assay versus Multiple MTT Assay - A Comparative Study. *Radiat. Oncol.* **2012**, *7*, 1-6.

185. Vembadi, A.; Menachery, A.; Qasaimeh, M. A. Cell Cytometry: Review and Perspective on Biotechnological Advances. *Front. Bioeng. Biotechnol.* **2019**, *7*, 147-166.

186. Babes, R. M.; Tofolean, I. T.; Sandu, R. G.; Baran, O. E.; Cosoreanu, V.; Ilie, M. T.; Duta, A. I.; Ceausescu, M. C.; Ciucur, P. M.; Costache, S.; Ganea, C.; Baran, I. Simple Discrimination of Sub-Cycling Cells by Propidium Iodide Flow Cytometric Assay in Jurkat Cell Samples with Extensive DNA Fragmentation. *Cell Cycle* **2018**, *17*, 766–779.

187. Stokes, R. P.; Cordwell, A.; Thompson, R. A. A Simple, Rapid ELISA Method for the Detection of DNA Antibodies. *J. Clin. Pathol.* **1982**, *35*, 566–573.

188. Bass, J. J.; Wilkinson, D. J.; Rankin, D.; Phillips, B. E.; Szewczyk, N. J.; Smith, K.; Atherton, P. J. An Overview of Technical Considerations for Western Blotting Applications to Physiological Research. *Scand. J. Med. Sci. Sports* **2017**, *27*, 4–25.

189. Collins, S. P.; Pope, R. K.; Scheetz, R. W.; Ray, R. I.; Wagner, P. A.; Little, B. J. Advantages of Environmental Scanning Electron Microscopy in Studies of Microorganisms. *Microsc. Res. Tech.* **1993**, *25*, 398–405.

190. Jonkman, J.; Brown, C. M. Any Way You Slice It—A Comparison of Confocal Microscopy Techniques. *J. Biomol. Tech.* **2015**, *26*, 54–65.

191. de Gooijer, M. C.; de Vries, N. A.; Buckle, T.; Buil, L. C. M.; Beijnen, J. H.; Boogerd, W.; van Tellingen, O. Improved Brain Penetration and Antitumor Efficacy of Temozolomide by Inhibition of ABCB1 and ABCG2. *Neoplasia* **2018**, *20*, 710-720.

192. Baker, S. D.; Wirth, M.; Statkevich, P.; Reidenberg, P.; Alton, K.; Sartorius, S. E.; Dugan, M.; Cutler, D.; Batra, V.; Grochow, L. B.; Donehower, R. C.; Rowinsky, E. K. Absorption, metabolism, and excretion of C-14-temozolomide following oral administration to patients with advanced cancer. *Clin. Cancer Res.* **1999**, *5*, 309-317.

193. Groothuis, D. R. The blood-brain and blood-tumor barriers: A review of strategies for increasing drug delivery. *Neuro-Oncology* **2000**, *2*, 45-59.

194. Newton, S. L.; Kalamaha, K.; Fernandes, H. D. Temozolomide-induced aplastic anemia treated with eltrombopag and granulocyte colony stimulating factor: a report of a rare complication. *Cureus* **2018**, *10*, e3329.

195. Tisdale, M. J. Antitumour imidazotetrazines—XV: Role of guanine O^6 alkylation in the mechanism of cytotoxicity of imidazotetrazinones. *Biochem. Pharmacol.* **1987**, *36*, 457-462.

196. Cejka, P.; Stojic, L.; Mojas, N.; Russell, A. M.; Heinimann, K.; Cannavó, E.; di Pietro, M.; Marra, G.; Jiricny, J. Methylation-induced G2/M arrest requires a full complement of the mismatch repair protein hMLH1. *EMBO J.* **2003**, *22*, 2245-2254.

197. Kitange, G. J.; Carlson, B. L.; Schroeder, M. A.; Grogan, P. T.; Lamont, J. D.; Decker, P. A.; Wu, W.; James, C. D.; Sarkaria, J. N. Induction of MGMT expression is associated with temozolomide resistance in glioblastoma xenografts. *Neuro-Oncology* **2009**, *11*, 281-291.

198. Yang, Z.; Wei, D.; Dai, X.; Stevens, M. F. G.; Bradshaw, T. D.; Luo, Y.; Zhang, J. C8-Substituted Imidazotetrazine Analogs Overcome Temozolomide Resistance by Inducing DNA Adducts and DNA Damage. *Front. Oncol.* **2019**, *9*, 485–498.

199. Kim, J.; Ahn, S. I.; Kim, Y. Nanotherapeutics Engineered to Cross the Blood-Brain Barrier for Advanced Drug Delivery to the Central Nervous System. *J. Ind. Eng. Chem.* **2019**, *73*, 8-18.

200. Oberoi, R. K.; Parrish, K. E.; Sio, T. T.; Mittapalli, R. K.; Elmquist, W. F.; Sarkaria, J. N. Strategies to improve delivery of anticancer drugs across the blood-brain barrier to treat glioblastoma. *Neuro-Oncology* **2016**, *18*, 27-36.

201. Soares, S.; Sousa, J.; Pais, A.; Vitorino, C. Nanomedicine: Principles, Properties, and Regulatory Issues. *Front. Chem.* **2018**, *6*, 360.

202. Harrison, P. M. The structure of apoferritin: molecular size, shape and symmetry from x-ray data. *J. Mol. Biol.* **1963**, *6*, 404-422.

203. Li, L.; Fang, C. J.; Ryan, J. C.; Niemi, E. C.; Lebron, J. A.; Bjorkman, P. J.; Arase, H.; Torti, F. M.; Torti, S. V.; Nakamura, M. C.; Seaman, W. E. Binding and uptake of H-ferritin are mediated by human transferrin receptor-1. *Proc. Natl. Acad. Sci. U. S. A.* **2010**, *107*, 3505-3510.

204. Zhang, L.; Li, L.; Di Penta, A.; Carmona, U.; Yang, F.; Schöps, R.; Brandsch, M.; Zugaza, J. L.; Knez, M. H-Chain Ferritin: A Natural Nuclei Targeting and Bioactive Delivery Nanovector. *Adv. Healthcare Mater.* **2015**, *4*, 1305-1310.

205. Torti, S. V.; Torti, F. M. Iron and cancer: more ore to be mined. *Nat. Rev. Cancer* **2013**, *13*, 342-355.

206. Jefferies, W. A.; Brandon, M. R.; Hunt, S. V.; Williams, A. F.; Gatter, K. C.; Mason, D. Y. Transferrin receptor on endothelium of brain capillaries. *Nature* **1984**, *312*, 162-163.

207. Johnsen, K. B.; Burkhart, A.; Melander, F.; Kempen, P. J.; Vejlebo, J. B.; Siupka, P.; Nielsen, M. S.; Andresen, T. L.; Moos, T. Targeting transferrin receptors at the blood-brain barrier improves the uptake of immunoliposomes and subsequent cargo transport into the brain parenchyma. *Sci. Rep.* **2017**, *7*, 10396.

208. Antileo, E.; Garri, C.; Tapia, V.; Muñoz, J. P.; Chiong, M.; Nualart, F.; Lavandero, S.; Fernández, J.; Núñez, M. T. Endocytic pathway of exogenous iron-loaded ferritin in intestinal epithelial (Caco-2) cells. *Am. J. Physiol. Gastrointest. Liver Physiol.* **2013**, *304*, G655-661.

209. Zhang, Y. Y.; Tang, Z. W.; Wang, J.; Wu, H.; Lin, C. T.; Lin, Y. H. Apoferritin nanoparticle: a novel and biocompatible carrier for enzyme immobilization with enhanced activity and stability. *J. Mater. Chem.* **2011**, *21*, 17468-17475.

210. Al-Ani, A. W.; Zhang, L.; Ferreira, L.; Turyanska, L.; Bradshaw, T. D.; Thomas, N. R. Listeria innocua Dps as a nanoplatform for bioluminescence based photodynamic therapy utilizing Gaussia princeps luciferase and zinc protoporphyrin IX. *Nanomedicine (N.Y., NY, U. S.)* **2019**, *20*, 102005.

211. Chiou, B.; Connor, J. R. Emerging and Dynamic Biomedical Uses of Ferritin. *Pharmaceuticals (Basel)* **2018**, *11*, E124.

212. Breen, A. F.; Scurr, D.; Cassioli, M. L.; Wells, G.; Thomas, N. R.; Zhang, J.; Turyanska, L.; Bradshaw, T. D. Protein Encapsulation of Experimental Anticancer Agents 5F 203 and Phortress: Towards Precision Drug Delivery. *Int. J. Nanomed.* **2019**, *14*, 9525-9534.

213. Kuruppu, A. I.; Zhang, L.; Collins, H.; Turyanska, L.; Thomas, N. R.; Bradshaw, T. D. An Apoferritin-based Drug Delivery System for the Tyrosine Kinase Inhibitor Gefitinib. *Adv. Healthcare Mater.* **2015**, *4*, 2816-2821.

214. Pandolfi, L.; Bellini, M.; Vanna, R.; Morasso, C.; Zago, A.; Carcano, S.; Avvakumova, S.; Bertolini, J. A.; Rizzuto, M. A.; Colombo, M.; Prosperi, D. H-Ferritin Enriches the Curcumin Uptake and Improves the Therapeutic Efficacy in Triple Negative Breast Cancer Cells. *Biomacromolecules* **2017**, *18*, 3318-3330.

215. Yang, Z.; Wang, X.; Diao, H.; Zhang, J.; Li, H.; Sun, H.; Guo, Z. Encapsulation of platinum anticancer drugs by apoferritin. *Chem. Commun.* **2007**, *33*, 3453-3455.

216. Thomas, B. R.; Carter, D.; Rosenberger, F. Effect of microheterogeneity on horse spleen apoferritin crystallization. *J. Cryst. Growth* **1998**, *187*, 499-510.

217. Saeed, S. A.; Boyde, T. R. Horse spleen ferritin: a change of crystal form during crystallisation of monomer is associated with the appearance of oligomers. *FEBS Lett.* **1981**, *123*, 111-114.

218. Kim, M.; Rho, Y.; Jin, K. S.; Ahn, B.; Jung, S.; Kim, H.; Ree, M. pH-Dependent Structures of Ferritin and Apoferritin in Solution: Disassembly and Reassembly. *Biomacromolecules* **2011**, *12*, 1629-1640.

219. Lin, Z. Q.; Zhou, D. L.; Hoag, S.; Qiu, Y. H. Influence of Drug Properties and Formulation on In Vitro Drug Release and Biowaiver Regulation of Oral Extended Release Dosage Forms. *AAPS J.* **2016**, *18*, 333-345.

220. Ruozi, B.; Veratti, P.; Vandelli, M. A.; Tombesi, A.; Tonelli, M.; Forni, F.; Pederzoli, F.; Belletti, D.; Tosi, G. Apoferritin nanocage as streptomycin drug reservoir: Technological optimization of a new drug delivery system. *Int. J. Pharm.* **2017**, *518*, 281-288.

221. Behzadi, S.; Serpooshan, V.; Sakhtianchi, R.; Muller, B.; Landfester, K.; Crespy, D.; Mahmoudi, M. Protein corona change the drug release profile of nanocarriers: The "overlooked" factor at the nanobio interface. *Colloids Surf., B* **2014**, *123*, 143-149.

222. Antosova, Z.; Mackova, M.; Kral, V.; Macek, T. Therapeutic Application of Peptides and Proteins: Parenteral Forever? *Trends Biotechnol*. **2009**, *27*, 628–635.

223. Mahato, R. I.; Narang, A. S.; Thoma, L.; Miller, D. D. Emerging Trends in Oral Delivery of Peptide and Protein Drugs. *Crit. Rev. Ther. Drug Carrier Syst.* **2003**, *20*, 153–214.

224. Daniels, T. R.; Delgado, T.; Rodriguez, J. A.; Helguera, G.; Penichet, M. L. The Transferrin Receptor Part I: Biology and Targeting with Cytotoxic Antibodies for the Treatment of Cancer. *Clin. Immunol*. **2006**, *121*, 144–158.

225. Shen, Y.; Li, X.; Dong, D.; Zhang, B.; Xue, Y.; Shang, P. Transferrin Receptor 1 in Cancer: A New Sight for Cancer Therapy. *Am. J. Cancer Res.* **2018**, *8*, 916-931.

226. Weston, C.; Klobusicky, J.; Weston, J.; Connor, J.; Toms, S. A.; Marko, N. F. Aberrations in the Iron Regulatory Gene Signature Are Associated with Decreased Survival in Diffuse Infiltrating Gliomas. *PLoS One* **2016**, *11*, e0166593.

227. Byrne, S. L.; Buckett, P. D.; Kim, J.; Luo, F.; Sanford, J.; Chen, J.; Enns, C.; Wessling-Resnick, M. Ferristatin II Promotes Degradation of Transferrin Receptor-1 In Vitro and In Vivo. *PLoS One* **2013**, *8*, e70199.

228. Moura, I. C.; Lepelletier, Y.; Arnulf, B.; England, P.; Baude, C.; Beaumont, C.; Bazarbachi, A.; Benhamou, M.; Monteiro, R. C.; Hermine, O. A Neutralizing Monoclonal Antibody (MAb A24) Directed against the Transferrin Receptor Induces Apoptosis of Tumor T Lymphocytes from ATL Patients. *Blood* **2004**, *103*, 1838–1845.

229. Kim, H. K.; Baek, A. R.; Choi, G.; Lee, J.; Yang, J.; Jung, H.; Lee, T.; Kim, D.; Kim, M.; Cho, A. E.; Lee, G. H.; Chang, Y. Highly Brain-Permeable Apoferritin Nanocage with High Dysprosium Loading Capacity as a New T2 Contrast Agent for Ultra-High Field Magnetic Resonance Imaging. *Biomaterials* **2020**, *243*, 119939.

230. Fan, C. H.; Liu, W. L.; Cao, H.; Wen, C.; Chen, L.; Jiang, G. O6-Methylguanine DNA Methyltransferase as a Promising Target for the Treatment of Temozolomide-Resistant Gliomas. *Cell Death Dis.* **2013**, *4*, e876.

231. Fang, C.; Wang, K.; Stephen, Z. R.; Mu, Q.; Kievit, F. M.; Chiu, D. T.; Press, O. W.; Zhang, M. Temozolomide Nanoparticles for Targeted Glioblastoma Therapy. *ACS Appl. Mater. Interfaces* **2015**, *7*, 6674–6682.

232. Kumari, S.; Ahsan, S. M.; Kumar, J. M.; Kondapi, A. K.; Rao, N. M. Overcoming Blood Brain Barrier with a Dual Purpose Temozolomide Loaded Lactoferrin Nanoparticles for Combating Glioma (SERP-17-12433). *Sci. Rep.* **2017**, *7*, 6602.

233. Eguchi, Y.; Makanae, K.; Hasunuma, T.; Ishibashi, Y.; Kito, K.; Moriya, H. Estimating the Protein Burden Limit of Yeast Cells by Measuring the Expression Limits of Glycolytic Proteins. *Elife* **2018**, *7*, e34595.

234. Kuo, L. J.; Yang, L.-X. γ-H2AX – A Novel Biomarker for DNA Double-Strand Breaks. *In Vivo* **2008**, *22*, 305–310.

235. Stricker, J.; Falzone, T.; Gardel, M. L. Mechanics of the F-Actin Cytoskeleton. *J. Biomech.* **2010**, *43*, 9–14.

236. Wick, W.; Platten, M.; Weller, M. New (Alternative) Temozolomide Regimens for the Treatment of Glioma. *Neuro. Oncol.* **2009**, *11*, 69–79.

237. Gill, S. J.; Travers, J.; Pshenichnaya, I.; Kogera, F. A.; Barthorpe, S.; Mironenko, T.; Richardson, L.; Benes, C. H.; Stratton, M. R.; McDermott, U.; Jackson, S. P.; Garnett, M. J. Combinations of PARP Inhibitors with Temozolomide Drive PARP1 Trapping and Apoptosis in Ewing's Sarcoma. *PLoS One* **2015**, *10*, e0140988.

238. Park, H. J.; Bae, J. S.; Kim, K. M.; Moon, Y. J.; Park, S. H.; Ha, S. H.; Hussein, U. K.; Zhang, Z.; Park, H. S.; Park, B. H.; Moon, W. S.; Kim, J. R.; Jang, K. Y. The PARP Inhibitor Olaparib Potentiates the Effect of the DNA Damaging Agent Doxorubicin in Osteosarcoma. *J. Exp. Clin. Cancer Res.* **2018**, *37*, 107-122.

239. Engert, F.; Schneider, C.; Weib, L. M.; Probst, M.; Fulda, S. PARP Inhibitors Sensitize Ewing Sarcoma Cells to Temozolomide-Induced Apoptosis via the Mitochondrial Pathway. *Mol. Cancer Ther.* **2015**, *14*, 2818–2830.

240. Hanna, C.; Kurian, K. M.; Williams, K.; Watts, C.; Jackson, A.; Carruthers, R.; Strathdee, K.; Cruickshank, G.; Dunn, L.; Erridge, S.; Godfrey, L.; Jefferies, S.; McBain, C.; Sleigh, R.; McCormick, A.; Pittman, M.; Halford, S.; Chalmers, A. J. Pharmacokinetics, Safety and Tolerability of Olaparib and Temozolomide for Recurrent Glioblastoma: Results of the Phase I OPARATIC Trial. *Neuro. Oncol.* **2020**, *noaa104*, 1-11.

241. Friedman, H. S.; Kerby, T.; Calvert, H. Temozolomide and Treatment of Malignant Glioma. *Clin. Cancer Res.* **2000**, *6*, 2585–2597.

242. Fairbairn, L. J.; Watson, A. J.; Rafferty, J. A.; Elder, R. H.; Margison, G. P. O6-Benzylguanine Increases the Sensitivity of Human Primary Bone Marrow Cells to the Cytotoxic Effects of Temozolomide. *Exp. Hematol.* **1995**, *23*, 112–116.

243. Roell, K. R.; Reif, D. M.; Motsinger-Reif, A. A. An Introduction to Terminology and Methodology of Chemical Synergy-Perspectives from across Disciplines. *Front. Pharmacol*. **2017**, *8*, 158-168.

244. Mayer, L. D.; Harasym, T. O.; Tardi, P. G.; Harasym, N. L.; Shew, C. R.; Johnstone, S. A.; Ramsay, E. C.; Bally, M. B.; Janoff, A. S. Ratiometric Dosing of Anticancer Drug Combinations: Controlling Drug Ratios after Systemic Administration Regulates Therapeutic Activity in Tumor-Bearing Mice. *Mol. Cancer Ther.* **2006**, *5*, 1854–1863.

245. Harasym, T. O.; Liboiron, B. D.; Mayer, L. D. Drug Ratio-Dependent Antagonism: A New Category of Multidrug Resistance and Strategies for Its Circumvention. *Methods mol. Biol.* **2010**, *596*, 291–323.

246. Vakil, V.; Trappe, W. Drug Combinations: Mathematical Modeling and Networking Methods. *Pharmaceutics* **2019**, *11*, 208-238.

247. Quinn, J. A.; Sara, X. J.; Reardon, D. A.; Desjardins, A.; Vredenburgh, J. J.; Rich, J. N.; Gururangan, S.; Friedman, A. H.; Bigner, D. D.; Sampson, J. H.; McLendon, R. E.; Herndon, J. E.; Walker, A.; Friedman, H. S. Phase I Trial of Temozolomide plus O6-Benzylguanine 5-Day Regimen with Recurrent Malignant Glioma. *Neuro. Oncol.* **2009**, *11*, 556–561.

248. Shervington, L.; Ingham, O.; Shervington, A. A Novel Series of Phenolic Temozolomide (TMZ) Esters with 4 to 5-Fold Increased Potency, Compared to TMZ, against Glioma Cells Irrespective of MGMT Expression. *RSC Adv.* **2020**, *10*, 17561–17570.

249. Sherman, H.; Rossi, A. E. A Novel Three-Dimensional Glioma Blood-Brain Barrier Model for High-Throughput Testing of Tumoricidal Capability. *Front. Oncol.* **2019**, *9*, 351.

250. Passarelli, M. K.; Pirkl, A.; Moellers, R.; Grinfeld, D.; Kollmer, F.; Havelund, R.; Newman, C. F.; Marshall, P. S.; Arlinghaus, H.; Alexander, M. R.; West, A.; Horning, S.; Niehuis, E.; Makarov, A.; Dollery, C. T.; Gilmore, I. S. The 3D OrbiSIMS - Label-Free Metabolic Imaging with Subcellular Lateral Resolution and High Mass-Resolving Power. *Nat. Methods* **2017**, *14*, 1175–1183.

251. Zhou, Z. Q.; Manguino, D.; Kewitt, K.; Intano, G. W.; McMahan, C. A.; Herbert, D. C.; Hanes, M.; Reddick, R.; Ikeno, Y.; Walter, C. A. Spontaneous Hepatocellular Carcinoma Is Reduced in Transgenic Mice Overexpressing Human O6methylguanine-DNA Methyltransferase. *Proc. Natl. Acad. Sci. U. S. A.* **2001**, *98*, 12566–12571.

252. Löfblom, J.; Feldwisch, J.; Tolmachev, V.; Carlsson, J.; Ståhl, S.; Frejd, F. Y. Affibody Molecules: Engineered Proteins for Therapeutic, Diagnostic and Biotechnological Applications. *FEBS Lett*. **2010**, *584*, 2670–2680.

8 - Appendices

8.1 Appendix I

Clonogenic assays were employed to corroborate MTT assays. Figure 8.1 illustrates the colonies of U373V and U373M after 24 h and 6-day exposure to naked and encapsulated TMZ. AFt alone had a negligible effect on colony numbers confirming the non-toxicity of this DDS; on the other hand, cells treated with AFt-TMZ showed greater reduction in colony numbers over naked TMZ.

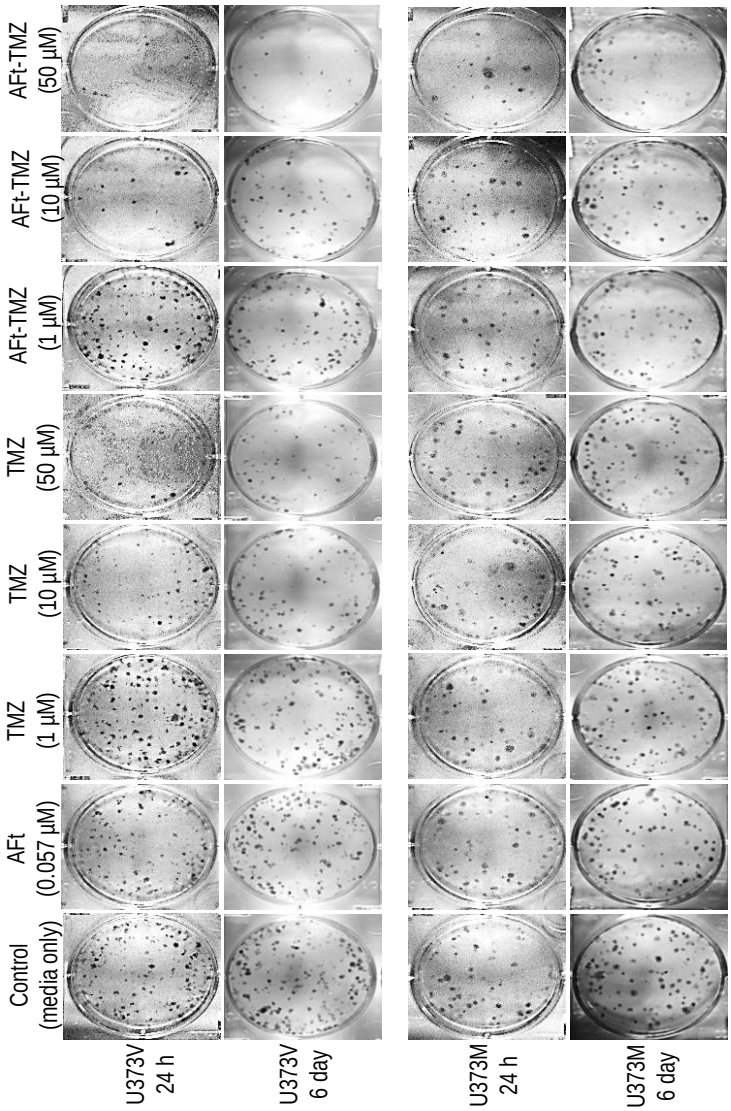

Figure 8.1. *In vitro* characterisation of cell proliferation proficiency following treatment. Representative images of the clonogenic assay conducted on U373V and U373M for a 24 h or 6-day treatment (1, 10 or 50 µM of TMZ/AFt-TMZ, 0.057 µM of AFt, or media alone) exposure.

8.2 Appendix II

To assess the alterations undergone in cells following treatment with TMZ and AFt-TMZ, cell cycle analysis by flow cytometry was carried out on U373V and U373M cells. Figure 8.2 represents the cell cycle histograms displaying the cell populations arrested in the pre-G1, G1, S and G2/M phases of the cell cycle. Following 72 h treatment exposure, the cell cycle profiles of both cell lines with AFt-TMZ treatment displays more arrest in the S and G2/M phases over TMZ alone treatment, whilst AFt alone, does not lead to any changes to the cell cycle profiles of GBM cells.

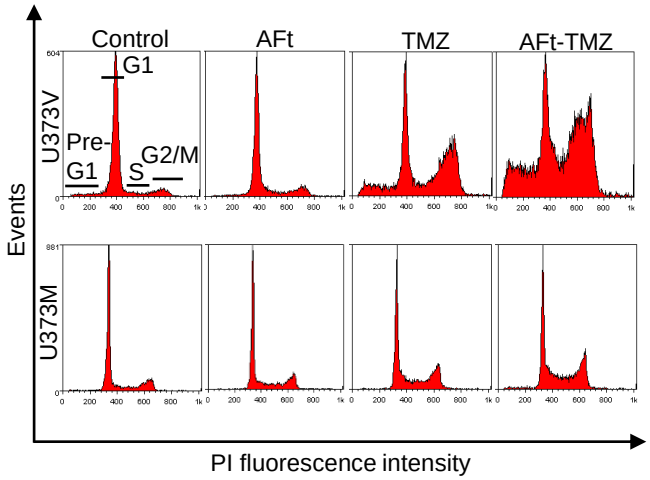

Figure 8.2. Representative flow cytometry cell cycle profiles of U373V and U373M following a 72-h treatment with TMZ (50 μM), AFt-TMZ (50 μM), AFt (0.057 μM) or media alone. Increasing PI fluorescence represents the progression of cells (from 10000 gated events i.e. cells) from the pre-G1 phase to the G2/M phase of the cell cycle.

8.3 Appendix III

The presence of γ-H2AX foci, which is indicative of DNA double strand breaks, was quantified by flow cytometry. Figure 8.3 demonstrates greater levels of γ-H2AX foci were observed following treatment of U373V and U373M cells with AFt-TMZ, compared to TMZ alone, in a time- and concentration-dependent manners.

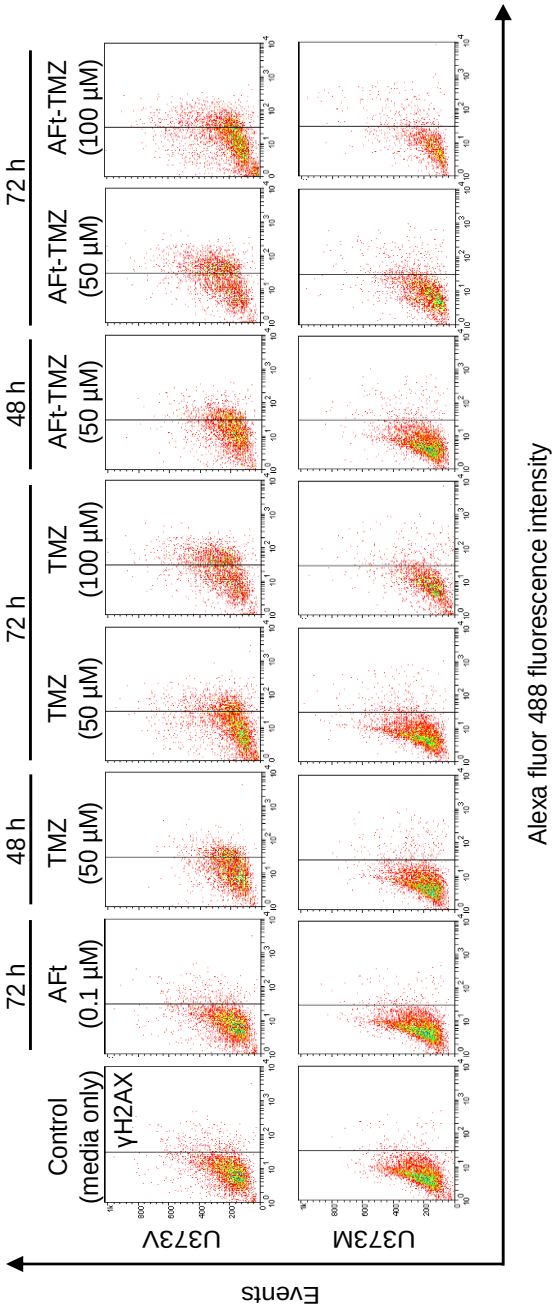

Figure 8.3. Representative U373V and U373M flow cytometry results of γ-H2AX foci from 10000 gated events i.e. cells, following 48 or 72 h exposure to test agents.

8.4 Appendix IV

Cancer and non-cancer cells were analysed by western blot for the expression of EGFR, which is commonly overexpressed in some cancers. Indeed, Figure 8.4 demonstrates that only the cancer cells expressed EGFR. Therefore, EGFR is another target that can be exploited for targeted drug delivery.

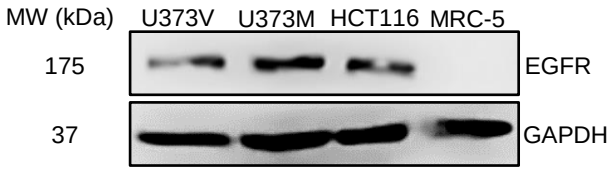

Figure 8.4. Cellular characterisation of protein expression. Western blot analysis of membrane bound EGFR in cancer and non-cancer cells.